Purkinje Cell Physiology in Health and Disease

Saša Peter

Purkinje Cell Physiology in Health and Disease

Saša Peter

The research described in this thesis was performed at the Department of Neuroscience, Erasmus Medical Centre in Rotterdam.

The research in this thesis was financially supported by the Netherlands Organisation for Scientific Research, ERC-ADV, NOW-ALW and Zon-MW grants.

Cover design by Saša Peter. The image displays Purkinje cells in the flocculus of the mouse. The green signal is derived from EAAT4-GFP. The red signal (Cy3) is derived from a biocytin filled Purkinje cell after a whole cell recording experiment.

Printing by Ridderprint BV

Purkinje Cell Physiology in Health and Disease

Purkinje cell fysiologie in gezondheid en ziekte

Proefschrift

ter verkrijging van de graad van doctor aan de

Erasmus Universiteit Rotterdam

op gezag van de

rector magnificus

Prof.dr. R.C.M.E. Engels

en volgens besluit van het College voor Promoties.

De openbare verdediging zal plaatsvinden op

dinsdag 11 december 2018 om 15:30 uur door

Saša Peter

geboren te Zenica (Joegoslavië)

Erasmus University Rotterdam

Promotiecommissie:

Promotor:	Prof.dr. C.I. De Zeeuw
Leescommissie:	Prof.dr. J.G.G. Borst
	Prof.dr. S.A. Kushner
	Prof.dr. S. Spijker
Copromotor:	Prof.dr. F.E. Hoebeek

Table of Contents

Preface

Connections between neurons in the brain have physiological and morphological properties that can be altered over time to facilitate a behavioural acquisition process known as learning. I utilised behavioural tasks, electrophysiological, and tissue imaging techniques to study the physiological and morphological characteristics of Purkinje cells: the sole cortical output of the cerebellum. This dissertation consists of two parts. The first part explores experimental evidence for cerebellar dysfunction in cognitive related disease, like autism. The second part is focused on the fundamental aspects of Purkinje cell functioning with genetic mutations that lead to altered protein expression causing lasting dysfunctional synaptic functioning and consequentially impaired learning. I have performed experiments to study different types of input to the Purkinje cell to reveal synaptic changes that are ongoing and responsible for the aberrant cerebellum dependent learning. The work done here would not have been possible without the effort of many collaborators that helped reveal how genetic modifications can cause differential physiological and behavioural phenotypes.

Chapter 1.0

Introduction

1.1 Sense to behave

In the following chapters I discuss the relevance of several synaptic proteins for normal physiology of Purkinje cells and cerebellar related behaviour in health and disease. Before explaining the function of these proteins, I begin with a holistic question regarding the central nervous system: why do we have a brain?

A body, albeit a single or multiple celled organism, requires mechanisms to integrate information from the outside world, which will need to be processed to execute short-term goals. This input of information is a limited aspect of any stimulus that the body is capable of perceiving. Through natural selection, organisms acquired the ability to process different sensory modalities like light, sound, pressure, smell, temperature and taste. Our central nervous system (CNS) computes aspects of these sensory modalities, including their intensity (stimulus amplitude), location (spatial distribution) and timing (temporal distribution) so we can process this information and respond accordingly.

Originating in periphery and progressing through the CNS, different aspects of sensory information encoded by electrical activity between specialised cells called neurons is processed both in serial as well as parallel pathways leading to spatial and temporal separation of information processing (Figure 1). Because the world is ever changing, we need to be able to reliably observe, and at the same time predict, aspects of change in order to adjust behaviour appropriately.

The ultimate function of sensory information processing can be seen as the facilitation of goal-oriented behaviour through the prediction of change. In other words, the way that a body acts upon the world is through prediction-driven motor control. To illustrate, damage to a specific area of the brain, called the cerebellum, results in impaired reaching and grasping [1]. Calibrated force amplitude, spatial distribution, and timing of control is crucial in any goal-oriented movement and depends on the current state of muscles and any sensory information relevant to the execution of the desired motion (Picture 1).

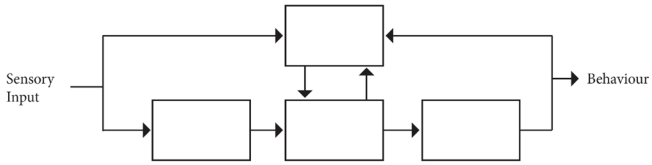

Figure 1 Conceptual diagram of information processing in the CNS. To facilitate goal-oriented behaviour, a constant stream of information progresses through the CNS in serial and parallel pathways. Both pathways represent various types of information processes that are hierarchically organised and present with complexity through feedback loops and fundamental differences in network physiology.

Picture 1 Example of complex goal-oriented behaviour. The body needs to continuously process visual, vestibular and proprioceptive sensory modalities in addition to integrating experience-based knowledge of any significant properties (e.g., weight) of the ball and baseball bat.

Thus, for a movement to be efficient in time and space, sufficient processing of the relevant sensory modalities and, in parallel, a constant feedback that predicts and corrects motor output are necessary [2].

We receive sensory information as it enters the body in serially distributed areas of the spinal cord, brainstem, thalamus and cerebral cortex (Figure 2). The sensory information that is important for maintaining and adjusting the processing of desired movements is encoded in different areas that act in parallel and can affect serial processes. Such processes are not confined to motor execution alone. It is believed that the non-motor domain (i.e., cognitive processes) of thought are subject to similar processes [3, 4].

This thesis investigates the functioning of the cerebellum, a brain area that effectively uses internal models to exert computation on top of serial processes to facilitate well-executed motor and non-motor behaviour. The following chapters describe cerebellar anatomy, physiology, and behaviour to explore various hypotheses that have arisen from decades of experimental work in an attempt to reveal cerebellar function.

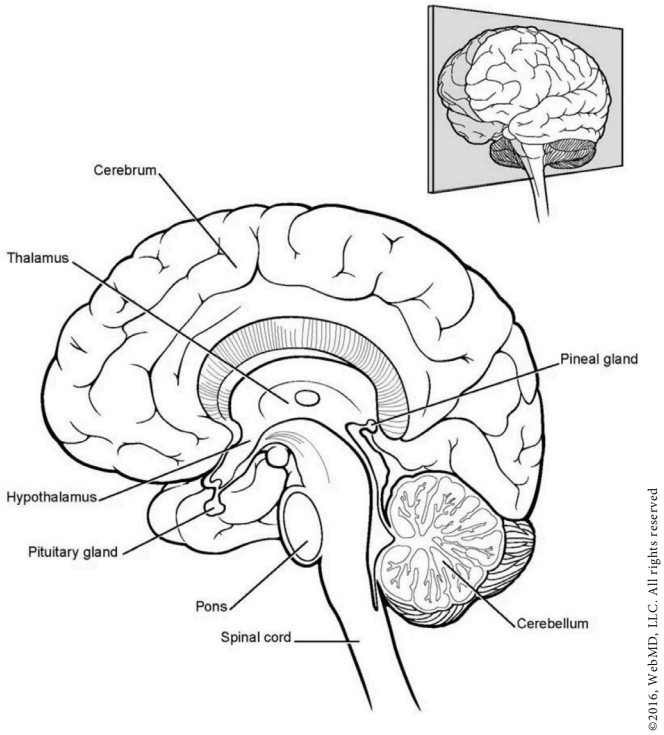

Figure 2 Sagittal mid-section of the brain.

1.2 Cerebellar macro structure

To understand how the cerebellum can modulate behaviour, we first need to consider its structure and major fibre pathways. One remarkable feature of the cerebellum, also reflected in its name ('little brain' in Latin), is its volume, which accounts to only 10% of total brain volume. However, it contains more than 50% of all the neurons in the brain. The cerebellum is positioned just dorsally of the brainstem, where it is connected to the rest of the brain through three peduncles: the inferior, middle, and superior cerebellar peduncles. The macroscopic division of the cerebellum is separated into anatomically differentiated lobes. The central vermis ('worm like') structure, running anterior to posterior across the midline, laterally positioned hemispheres and the posterior flocculondular lobe, are the major landmark structures of the cerebellum (Figure 3).

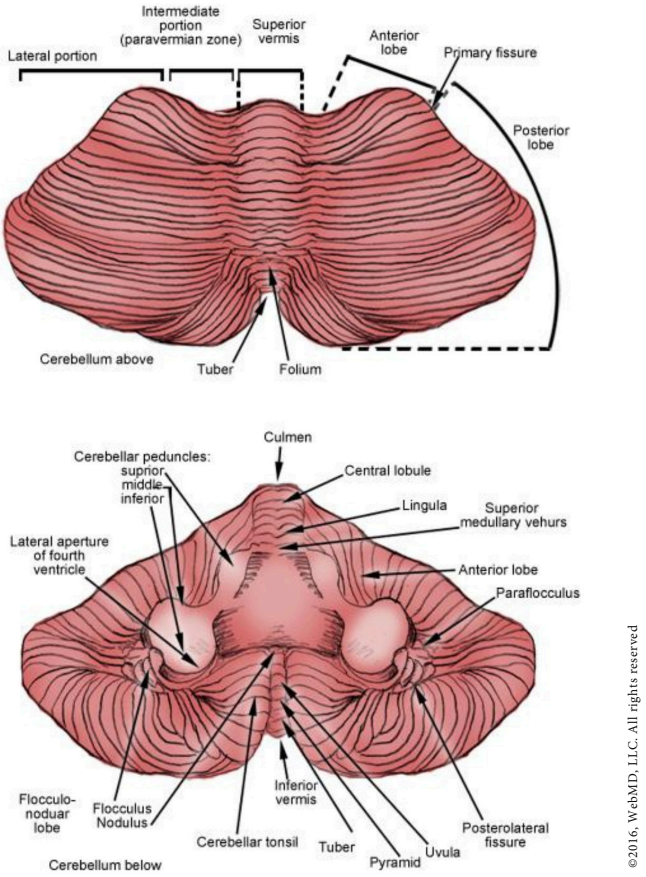

Figure 3 Macroscopic division of the cerebellum from above and below

The vermis receives primarily spinal and trigeminal sensory modalities, including visual, auditory, vestibular and somatosensory information. Outgoing projections from the vermis have synaptic connections in the fastigial nucleus and eventually target the cortical and brain stem systems that modulate proximal limbs and body muscles to establish functional locomotion and proper posture. The vermis, together with the inter-hemispheric (paravermis, important for voluntary limb movements) regions, is also termed the spinocerebellum, because this is the part of the cerebellum that receives major somatosensory information from the spinal cord. The interposed nucleus mostly receives projections from the paravermis and projects outgoing fibres to the red nucleus via the superior peduncle. By means of the rubrospinal tracts, the interpositus strongly influences the motor system. The lateral hemispheres receive significant corticopontine input and are

therefore also called the cerebrocerebellum. The hemispheres project outgoing fibres by means of the dentate nucleus towards motor and premotor cortices involved in motor planning and non-motor related aspects of behaviour. The posteriorly oriented flocculondular lobe, consisting of the flocculus and nodulus, is also called the vestibulocerebellum. The vestibular nerve projects directly to the vestibulocerebellum, while the output of the vestibulocerebellum projects to the vestibular nuclei affecting balance and eye movements.

The major incoming connections to the cerebellum are called mossy fibres. The mossy fibres terminate at granule cells of the cerebellar cortex. It is here that granule cells receive afferent excitatory input from the mossy fibres, and inhibitory input from Golgi cells. The granule cells, being the smallest neurons in the CNS, receive excitatory mossy fibre input via ~4 dendritic arms, each equipped with a claw-like structure onto which mossy fibers, but also inhibitory Golgi cells, can synapse. In turn, the axons of granule cells ascend through the Purkinje cell and molecular layer that (following bifurcation are called parallel fibres) run perpendicular through the dendritic trees of the many Purkinje cells and local interneurons. The dendritic abbreviation of Purkinje cells is remarkable as the synaptic input, mostly mediated by the parallel fibres of granule cells, can be as much as 200.000 connections for a single Purkinje cell. Each parallel fibre contacts many Purkinje cells while travelling transversely and usually makes no more than one synaptic contact per Purkinje cell. From these numbers, it should not be surprising that there are many more granule cells than Purkinje cells.

Apart from the mossy fibre-granule cell excitation the Purkinje cell also receives excitatory input from the climbing fibre. The climbing fibre originates in the inferior olive, which is located in the ventral brainstem, just caudal of the pontine nuclei. Each olivary axon innervates multiple Purkinje cells in the parasagittal plane, but only one climbing fibre per Purkinje cell. The parallel and climbing fibre innervations have profoundly different effects on Purkinje cell physiology and will be discussed in following paragraphs. The Purkinje cells are the sole output of the cerebellar cortex that projects to the deep cerebellar and vestibular nuclei. The output of Purkinje cells is GABAergic, which establishes their inhibitory post synaptic effect. It is at the level of cerebellar and vestibular nuclei that it becomes clear that the cerebellar output code lies in the exact spatiotemporal profiles of Purkinje cell inhibitory activity. However, before we delve into the physiology of Purkinje cell activity, we should first consider the functional organisation of the abovementioned projections.

1.3 Cerebellar functional organisation

Based on anatomical and molecular evidence, the cerebellum has been divided into several zones [5]. Each zone can, in turn, be subdivided into a number of rostro caudal oriented 'bands' that are defined by specific gene expression [6, 7]. One of the most studied markers is Aldolase-C (zebrin II) [8, 9], but many other genetic targets have been identified as well (Fig. 4).

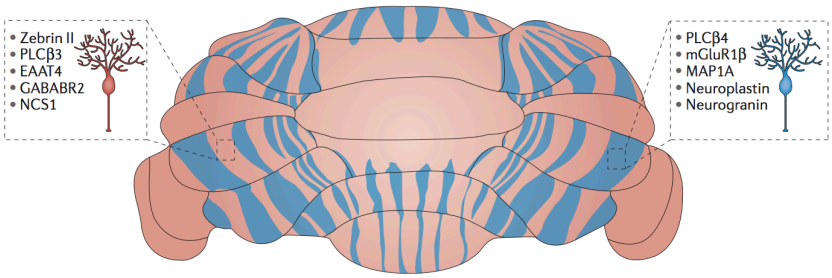

Figure 4 Patterning of zebrin II in the cerebellum. The co-localisation of zebrin II positive (orange) and negative (blue) expression in PCs with several additional molecular markers (genes/proteins) that have been identified based on the same patterning is indicated in the illustration. EAAT4, excitatory amino acid transporter 4; GABABR2, GABA B receptor subtype 2; MAP1A, microtubule-associated protein 1A; mGluR1β, metabotropic glutamate receptor 1β; NCS1, neuronal calcium sensor 1; PLCβ3, phospholipase Cβ3. Reproduced with permission from Springer: Nature Reviews Neuroscience [6].

The collection of genetic markers differentially expressed in a rostro caudal fashion in the cerebellum has strengthened the argument for non-uniform cerebellar architecture and function. A case for functional differentiation was made in recent *in vivo* electrophysiological experiments that revealed that zebrin II also strongly correlate with differential Purkinje cell activity as seen in the firing frequency [10, 11]. Furthermore, the functional organisation of the olivo cerebellar system is defined by modules. Modules have anatomically defined functional loops and can be shown to comprise of a particular sub nucleus of the inferior olive that provides climbing fibres to a set of Purkinje cells that are oriented in the sagittal plane (Figure 5). These Purkinje cells inhibit neurons in the cerebellar nuclei (CN), of which a subset inhibit the same olivary subnucleus from which the climbing fibres originated, ultimately completing the olivo-cerebello-nuclear loop.

The olivary cells are connected by means of gap junctions, which manifests itself in the so called olivary glomerulus. Here, both excitatory input (extra cerebellar regions

like the MDJ) and inhibitory input (CN feedback) exert influence on the excitability and synchrony of olivary cells [12]. The anatomically defined boundaries of the cerebellar modules are furthermore reflected in the cerebellar cortex, where both molecular layer interneurons (MLIs) and Golgi cells operate within the sagittal plane of the module. In general, the cell types that provide feed forward and back propagation are anatomically confined within these modules.

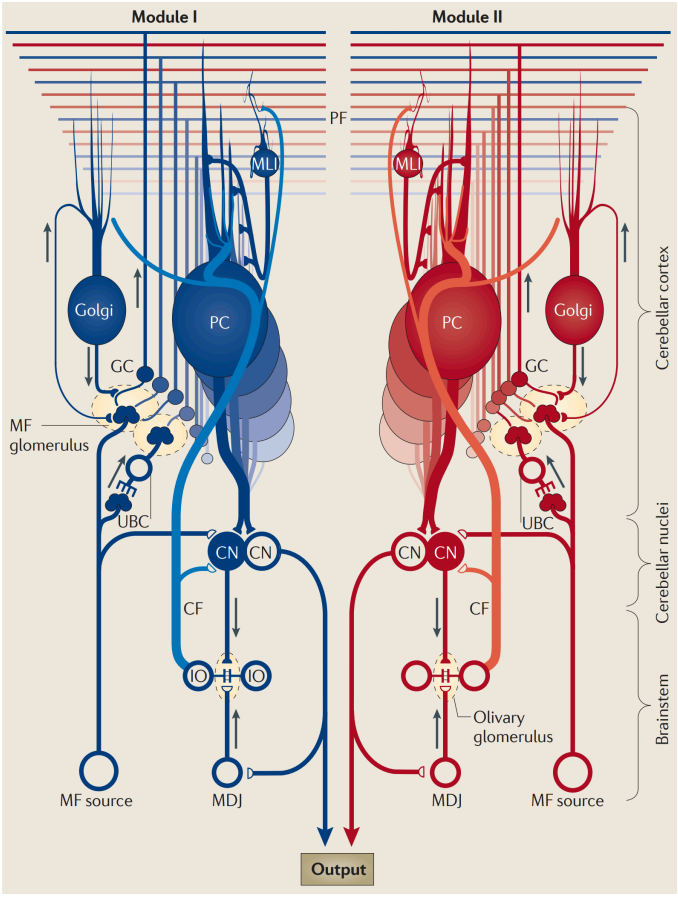

Figure 5 The cerebellum is organised in modules. The organisation of these modules is defined by an olivocerebellar loop that consists of inferior olive (IO) cells from a sub nucleus of the IO that project its output, the climbing fibres (CFs), to a set of Purkinje cells (PCs) oriented in the parasagittal plane. In turn, the output of these PCs inhibits vestibular and/or cerebellar nuclei, of which a subset inhibits the same sub nucleus of the IO that the CFs originated from. Olivary neurons are coupled by gap junctions upon which the inhibitory CN projects together with excitatory projections from brain stem areas like the mesodiencephalic junction (MDJ). The inhibitory molecular layer interneurons and the Golgi cells remain within the sagittal PC plane, thus effectively making the parallel fibres the only projections that

innervate multiple sagittal zones. Reproduced with permission from Springer: Nature Reviews Neuroscience [13].

Exception to this rule are the granule cells (GCs), which are innervated by majorly differentiated excitatory input of mossy fibres. Even though the axons of GCs are shown to project within the same modular zone of the cerebellar cortex, their parallel fibres, stretch across many sagittal zones. The parallel fibres are one of the two excitatory inputs to the PCs, but they also project to MLIs and the inhibitory Golgi cells providing a feedforward inhibition mechanism. In a sense, the major modular organisation is defined by its climbing fibre input, while the Parallel fibre input provides inputs across multiple modules.

1.4 Purkinje cell physiology

Having discussed some major characteristics of functional connectivity in the cerebellum, we now consider the physiology of the sole cerebellar cortex output: the Purkinje cell. As mentioned before, Purkinje cells have two forms of excitatory input: parallel fibres and climbing fibres [14]. In addition, Purkinje cells can be inhibited by two types of interneurons, namely stellate and basket molecular layer interneurons, and can inhibit each other through PC collaterals [15, 16]. Measured *in vivo*, the variability of excitatory and inhibitory input results in irregular patterns of firing of the Purkinje cell (Figure 6).

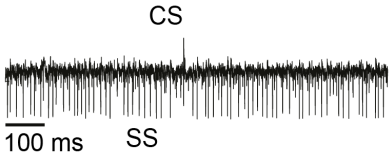

Figure 6 Purkinje cell simple spike and complex spike responses *in vivo*. The recording here was obtained from an *in vivo* experiment recoding extracellularly from one Purkinje cell. Note the high frequency simple spike (SS) firing compared to the single complex spike (CS) in this trace.

The intrinsic firing rate of Purkinje cells *in vitro* is regular when all inputs have been blocked (Figure 7). This confirms that the pacemaker activity sets the basal rate at which these cells fire and that additional excitatory and inhibitory input can modulate this firing.

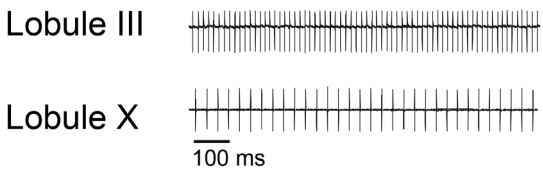

Figure 7 Purkinje cell simple spike firing *ex vivo* is regular when inputs are blocked. The firing frequency between Purkinje cells of posterior lobules is intrinsically lower than in Purkinje cells of anterior lobules. The data were obtained using cell-attached recordings in vitro with the addition of Picrotoxin, NBQX and APV to block all afferent inhibitory as well as excitatory input.

The pacemaker activity consists of simple spikes. These simple spikes are the typical Na^+ driven action potentials generated in the axon. As mentioned in the previous paragraph, the frequency of firing of simple spikes has been found to differ between lobules where specific protein expression, like that of zebrin, correlates with lower firing frequencies (see anterior mostly zebrin negative Lobule III vs. posterior mostly zebrin II positive Lobule X Purkinje cell firing frequency; Figure 7). The other characteristic type of excitatory input is driven by climbing fibres. This fibre, originating in the inferior olive, synapses onto approximately 1500 spines of the Purkinje cell and through large post synaptic depolarisation evokes a complex spike in the Purkinje cell (Figure 8).

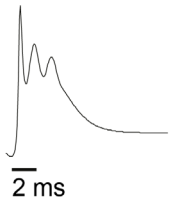

Figure 8 Purkinje cell complex spike *in vitro*. A representative complex spike from a Purkinje cell in a whole cell electrophysiological recording. Note the extra spikes generated on top of the large Ca^{2+} dependent ADP after the initital Na^+ spike.

This spike also has an initial Na^+ driven peak, but is then followed by a depolarised plateau, on which additional spikelets can be generated. Both the initial spike and the spikelets have been shown to originate from the Purkinje cell axon [17]. The occurrence of a complex spike has several pronounced consequences. A pause in the simple spike firing that occurs just after a complex spike is called a complex spike pause and is a combination of different depolarising currents that constitute the complex spike. In this sense, the complex spike occurrence has a profound short-term effect on the spiking frequency of the Purkinje cell. The spatiotemporal profile of complex spike occurrence plays major roles in cerebellar timing and motor learning functions [13].

As the synapse is the point of connectivity between cells, Hebb and others have speculated that cells that fire together wire together and that the actual strength of a connection between two cells could change in sensitivity over time [18]. Cerebellar research has been on the forefront of the study of long term changes of synaptic activity. Researchers have shown that conjunctive activity of complex spikes with PF to PC activity can depress the post synaptic PF to PC response over longer periods of time [19]. This type of long term depression (LTD) was previously hypothesised to play a crucial role in our conceptualisation of cerebellar substrates of learning [20, 21]. Beyond the demonstrations for the occurrence of LTD, long-term potentiation (LTP) has been shown to be of significance for cerebellar learning [22, 23]. Both of these processes depend on a rise in calcium levels, albeit with different sensitivities. Low calcium increases are mostly thought to be sufficient for LTP induction, whereas LTD induction requires larger calcium increase that is brought about by CF activation [24, 25]. Beyond synaptic plasticity, the PCs have also been shown to be capable of modifying their intrinsic excitability by modulating calcium activated potassium channels [26, 27].

1.5 Cerebellar dependent behaviour

To understand how the cerebellum facilitates behaviour, a quantifiable behavioural paradigm is needed. In this section, we briefly discuss two paradigms that are extensively used throughout this thesis. The first one involves compensatory eye movements, where two reflexes control eye movements: the optokinetic reflex (OKR in phase; track visual stimulus) and the vestibulo-ocular reflex (VOR out of phase; compensates for body movement). These reflexes can be generated in an experimental setting using a visual moving target for OKRs and a moving bodily stimulus for the VOR. These methodological details are further explained in the different chapter methods of this thesis.

The parameters of this paradigm are modulated by the three neuron arc of Lorente de No (Figure 9). The floccular hypothesis formulated in the 70s was based on the anatomical and physiological assumption that the flocculus might serve as a modulating system, as the VOR by itself was observed to be a feedforward system that did not have direct feedback from the eyes. The cerebellum was later shown to effectively regulate this system by modulating the activity of vestibular nuclei that in turn project to the oculomotor neurons that are responsible for the eye movements.

The relationship between floccular PC activity and the modulation of the VOR comes from several lines of evidence including genetic modifications [24]. Moreover, directly recording from PCs in the flocculus shows correlating SS modulation with head and eye velocity [28].

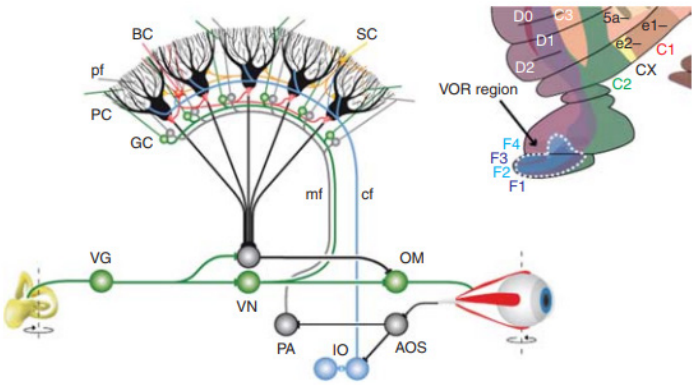

Figure 9 The circuit of the vestibulo-ocular reflex. The eye movement adaptations are modulated by the three-neuron arc of Lorente de No in the brainstem. Head rotation induces vestibular-related activity in the semicircular canals. This information is relayed by the vestibular ganglion (VG) to the vestibular nuclei (VN), which in turn sends this information to the oculomotor neurons that will initiate the movement of the eyes in the opposite direction to the vestibular movement. The PCs of the vestibulocerebellum, specifically the flocculus, send their output to the vestibular nuclei to modulate the three-arc system. The goal of this modulation is to minimise the retinal slip during head movements. The retinal slip is relayed by the accessory optic system (AOS) through the inferior olive and its CFs to the PCs. There it is integrated with vestibular and optokinetic information from the pontine nuclei (PN) and MF pathway. By integrating this information, the PCs can modulate the output of the VN to the OM such that the retinal slip is minimised (Adapted from De Zeeuw et al., 2015).

Evidence from *ex vivo* LTD- and LTP-deficient mutants [22, 23, 29-31] indicates that LTP deficiency marks greater eye movement abnormalities whereas LTD deficiency does not lead to obvious deficits in the eye movement compensatory mechanism. Overall, eye movement related motor learning, like VOR phase reversal, can be severely affected by the abnormal modulation of SS firing.

One other form of cerebellar related learning that significantly advanced our understanding of cerebellar physiology, is a form of associative and motor learning manifested through an experimental approach called eye blink conditioning. In an eyeblink experiment the conditioned stimulus (CS) is usually an auditory or visual sensory modality which is paired with a delayed unconditioned stimulus (US), which is usually an air puff in the eye (Figure

10). After sufficient CS-US pairing trails, the CS alone will serve to predict the arrival of the US and thus initiate a timed eye blink US response [32, 33].

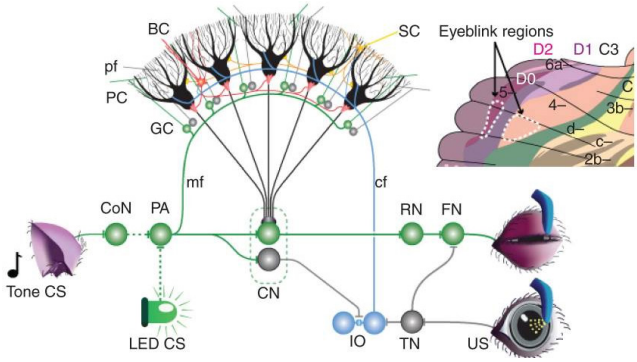

Figure 10 The circuit of the eyeblink reflex. For eyeblink conditioning, we pair a conditioned stimulus, represented by light or sound, with an unconditioned stimulus, usually an air puff. The PCs have been shown to modulate the cerebellar nuclei by inducing a timed response to disinhibit the CN and thus evoke an eyeblink through the CN to red nucleus (RN) to facial nucleus (FN) pathway. A well-rehearsed CS-US constant interval will lead to the timed reduction of PC SS output upon CS presentation, which is determined by the US related complex spike mediated by the CF originating in the IO (adapted from De Zeeuw et al., 2015).

The US blink response is thought to be facilitated by the disinhibition through lower SS firing from the PCs to the CN. The disinhibition starts before the onset of the CR [34], and it is as of yet unknown how the increase in CN firing temporally affects the occurrence of the eyeblink response. However, rebound activity of CN has been shown to be capable of modulating behaviour and is a plausible mechanism that could be facilitated by PC to CN disinhibition [35]. By now, the eye blink conditioning paradigm has become a standard in the field of neuroscience research as it reveals a PC output relationship with the timing as well as amplitude of the conditioned response. However, more research is needed to reveal the exact functional relationship between PC to CN disinhibition and eyeblink kinetics.

ASD and related cognitive evidence

As discussed in the previous paragraphs, cerebellar physiology is usually linked to the timing, coordination and learning of motor related behaviours. However, reports for cerebellar abnormalities affecting patient's planning of serial movements have been known for a while [36]. These initial observations led to further research into the realm of cognitive effect by cerebellar damage. Word association tasks and mental rehearsal have also been

shown to be affected in patients with damage to the lateral cerebellar hemispheres. The dentate nucleus has been hypothesised, through projections to the contralateral prefrontal cortex (area 46), with working memory and planning [37]. Important clues for non-sensorimotor encoding in the cerebellum has recently been revealed in cerebellar granule cells of mice in that it was shown that they could encode expectation of reward [38].

Evidence for cerebellar lesion involvement in non-motor deficits has indicated cognitive and affective changes. Recent evidence has even indicated that such abnormalities could affect social behaviour, and thus be present in autism spectrum disorder (ASD). Particularly pronounced dysfunctionalities have been reported in the cerebella of autism patients. These abnormalities often also reflect in the more classical cerebellar motor dysfunctionalities as identified in ASD patients for impaired eye-blink conditioning [39, 40] eye movement abnormalities [41, 42], motor learning deficits [43, 44], and balance and posture difficulties [45-47]. However, there is also evidence for the dysfunctions in ASD that stretch further than the symptoms related to motor issues. Cerebellar impairments also affect language, executive function and dysfunctional emotions, a collection of symptoms related to the cerebellar cognitive affective syndrome [48].

Patients affected with ASD often present with cerebellar pathologies like PC size reduction, density reduction and PC death [49-53]. Moreover, reduced number of GC and CN have also been reported [49, 54]. Importantly, results from genetic screening studies indicate that the ASD risk gene co-expression in the cerebellum is relatively high [55] thus increasing the possibility of abnormalities during hypothesized sensitive periods. The importance of the cerebellum during sensitive developmental periods is reflected by early-stage isolated cerebellar damage in infants that can lead to motor, cognitive, language and social deficits [56]. These results have been implicated in the hypothesis for a role of the cerebellum in the development of cerebral cortical networks, which in turn could play an important role in the aetiology of ASD [57].

1.6 Thesis outline

Having introduced some facets of cerebellar functioning and the importance of normal PC physiology, the following chapters present evidence for the role of several proteins in the function of PC physiology crucial for cerebellum related behaviour in both health and disease.

In **chapter 2.1**, the focus is on ASD in cerebellar and striatal ASD mouse models. In this chapter, we explore the many lines of evidence for the anatomical, morphological and

physiological abnormalities found in various genetic ASD-related mice models. In **chapter 2.2**, we expand on these arguments for the role of cerebellum in ASD by presenting evidence on cerebellar dysfunction caused by the deletion of a human risk genes for ASD shank2 in a Purkinje cell specific KO model. In this chapter, we gain more insight into the relevance of cerebellum dysfunction in ASD and how Purkinje cell aberrant physiology might play a role. **Chapter 2.3** evaluates the relevance of the cerebellum in a human language deficit caused by the mutation of the transcription factor Foxp2. Here, we report specific motor coordination problems and Purkinje cell increased excitability in a PC specific KO model for Foxp2.

Chapter 3.1 focusses on the function of potentiation at the PF to PC synapse. Here, the absence of shisa6, an AMPA receptor auxiliary protein, results in less spontaneous and evoked post-synaptic depolarisation of the Purkinje cells and impaired long-term potentiation, leading to aberrant baseline motor behaviour and learning. Depreciating excitation at both the baseline level and the long-term plasticity level strongly affects behaviour, unsurprisingly, more so than is expected from mere synaptic plasticity abnormalities. In this section, we discuss these results in light of the other plasticity deficient mutants. **Chapter 3.2** further discusses how long-term potentiation can be affected by adding NMDA receptors that facilitate additional calcium influx at the PF to PC synapse. These experiments reveal that LTP is impaired, but LTD is not, supporting the hypothesis that very precise calcium threshold management is crucial for the type of long-term changes that can be brought about at the PF to PC synapse. **Chapter 3.3** goes beyond the potentiation of the PF to PC synapse and evaluates how a combination of aberrant LTD and feed-forward inhibition can affect the cerebellar dependant learning process more than impaired LTD or feed forward inhibition alone. These results provide support for the synergistic plasticity hypothesis, which dictates that multiple sites of information processing need to be affected for the severity of the behavioural phenotypes to increase.

In **chapter 4.1**, we review the current state of chloride mediated function in the CNS and more specifically the olivocerebellar network. In **chapter 4.2**, this subject is further disentangled in an ongoing project on the function of Ano2, a calcium activated chloride channel in the inferior olive. In this chapter evidence is presented for a role of Ano2 in inferior olive cell physiology and motor function. Finally, **chapter 5** provides a general discussion on the findings in this thesis.

Chapter 2.1

Cerebellar and Striatal Pathologies in Mouse Models of Autism Spectrum Disorder

Saša Peter ¶, Chris I. De Zeeuw, Tobias M. Boeckers, Michael J. Schmeisser ¶

¶ Corresponding author(s)

Advances in Anatomy, Embryology and Cell Biology (2018)

Abstract

Autism spectrum disorder (ASD) is a complex neurodevelopmental condition with a strong genetic component. To date, several hundred different genetic mutations have been identified to play a role in its aetiology. The heterogeneity of genetic abnormalities combined with the different brain regions where aberrations are found makes the search for causative mechanisms a daunting task. Even within a limited number of brain regions, a myriad of different neural circuit dysfunctions may lead to ASD. Here, we review mouse models that incorporate mutations of ASD risk genes causing pathologies in the cerebellum and striatum and highlight the vulnerability of related circuit dysfunctions within these brain regions in ASD pathophysiology.

Introduction

The definition of autism spectrum disorder (ASD) as we know today originates from behavioural observations done by Kanner [58] and Asperger [59]. Abnormal motor behaviour and social functioning characterised these earliest observations. Modern evaluations based on the Diagnostic and Statistical Manual of Mental Disorders (DSM-V) include persistent difficulties in the social use of verbal and non-verbal communication, impaired social interaction as well as restricted and/or repetitive behaviours. Even though hundreds of abnormal genes have been identified that are correlated with the presence of ASD, understanding of the aetiology has not advanced much further since these earliest behavioural characterisations. Still, enough experimental insights have been gathered to establish the following: ASD is a heterogeneous neurodevelopmental condition most probably caused by dysfunctional neural circuits involving multiple brain areas. Within these circuits, the timing and location of insult, being of genetic nature or otherwise, are of great importance for the progress of the pathology. This temporal aspect has recently been proposed to be critical during postnatal development in the cerebellum [57]. Abnormalities in striatal circuits, being an integral brain region for sensory input and reward-related behaviour, have also been put forward as a critical area in the aetiology of ASD phenotypes [60]. In this review, we discuss several major findings of both cerebellar and striatal abnormalities found in ASD mouse models.

Human Cerebellum in ASD

Cerebellar functioning has traditionally been linked to the timing, coordination and learning of motor tasks. Contributions of cerebellum-related motor impairments to ASD have been identified in patients through impaired eye-blink conditioning [39, 40] eye movement abnormalities [41, 42], motor learning deficits [43, 44], and balance and posture difficulties [45-47]. Still, an accumulating amount of evidence points towards dysfunctions that reach beyond the readily observable symptoms of motor problems. For instance, damage in the adult cerebellum has also been shown to lead to deficits in language, executive function and impaired emotions, a condition termed cerebellar cognitive affective syndrome [48]. ASD patients commonly show cerebellar pathologies like widely distributed reduction of Purkinje cells (PCs) from early on [49-51]. Apart from the cell loss during development, there is also evidence for reduced size and density of PCs [52, 53]. In addition to the PC abnormalities, there is proof for a developmental reduction of granule cells (GCs) and abnormal cerebellar nuclei [49, 54]. Beyond the body of work on the contribution of cerebellum-related behaviour in ASD, there is support for a crucial role during

development that ranges from ASD risk gene co-expression in the cerebellum [55] and early-stage isolated cerebellar damage in infants, leading to motor, language, cognitive as well as social behaviour deficits [56]. Finally, emerging evidence also points towards a role of the cerebellum in the maturation of cerebral cortical networks that could play a crucial role in the development of ASD [57].

Cerebellum in ASD Mouse Models

Given the extensive behavioural and pathological changes in ASD that can be associated with the cerebellum, we still have relatively little understanding as to how these contribute to the aetiology of ASD. To tackle this issue, different cerebellar mouse models have been generated and tested in recent years; these include models of both syndromic (i.e. part of a set of symptoms that characterise the disease) and non-syndromic forms of ASD.

Mouse Models for Syndromic ASD

One of the well-known syndromes associated with ASD is fragile X syndrome (FXS). Approximately 5% of FXS patients fit within the ASD classification [61, 62]. FXS is associated with abnormalities in the cerebellum, including decreased cerebellar volume [63] and PC loss [64, 65]. Additionally, cerebellum-dependent eye-blink conditioning is impaired in FXS patients [66, 67]. Morphological changes in the *Fmr1* KO cerebellum have been described as a reduction of volume, cell loss in the cerebellar nuclei (CN) [68] and longer dendritic spines have been identified among PC dendrites [66]. Further evidence for cerebellum-related pathophysiology includes cerebellar-prefrontal deficient dopamine release [69], enhanced LTD induction at the parallel fibre to PC synapse [66], and abnormal pre-synaptic vesicle dynamics [70]. In addition, pathology of non-neuronal cerebellar cells such as increased expression of myelination proteins in astrocytes may also contribute to the phenotype of ASD [71]. Such phenomena may partially reflect compensation for decreased myelination in the cerebellum as occurs in *Fmr1* KO mice.

Another syndromic disorder regularly presenting with ASD is Rett syndrome (RTT), which is primarily caused by a mutation in the *MECP2* gene [72]. Assessment of these individuals has shown motor impairments during the developmental phase [73]. A significant body of evidence points towards cerebellar pathology in RTT including loss and abnormal size of PCs [54, 74, 75]. In *Mecp2* KO mice, motor coordination and learning, as assessed by rotarod, are impaired [76]. Additionally, a reduced cerebellar volume [77] and smaller and more dense GCs have been reported in these mutants [78]. *Mecp2* exhibits a defined

cerebellar expression pattern with early expression in PCs and relatively late expression in GCs [79]. In line with the finding that *Mecp2* has been shown to regulate hundreds of genes in the cerebellum [80], this temporal expression pattern in PCs and GCs could reveal sensitive periods that are crucial for key developmental processes of the cerebellar network.

Mutations in the maternal *UBE3A* gene lead to Angelman syndrome (AS), a developmental disease with a high prevalence of ASD [81]. In addition to the observations that AS and RTT have similar behavioural abnormalities, there is evidence for functional pathway overlap between *Ube3a* and *Mecp2* at the molecular level [82]. Cerebellar involvement is probably also implicated in AS, as revealed by the abnormal motor behaviour of AS patients [83] and abnormal GABA-receptor functioning in their cerebellum [84]. In mice, *Ube3a* maternal deficiency leads to phenotypes that include impaired motor coordination [85, 86] and orofacial activity [86]. These behavioural impairments are in line with deficits found in the morphology [87] and firing rates of their PCs [88], possibly further causing abnormal functioning in the cerebellar cortical network. However, recent evidence indicates that the motor-related impairments in maternal *Ube3a* might not be due to impairments in PCs alone, as PC-specific *Ube3a* ablation did not result in significant motor phenotypes [89]. Other physiological impairments may be explained by decreased tonic inhibition due to a deregulation of GABA transporter 1 (GAT1) in the GCs [90]. The results of this study show that due to excessive GAT1 expression there is more GABA re-uptake from the extra synaptic space resulting in less inhibition of the GCs. The motor deficits resulting from these physiological impairments could be reversed by applying the THIP $GABA_A$ receptor agonist, suggesting a possible therapeutic strategy [90].

The dup15q syndrome, another ASD-related disease that has been modelled in mice, involves chromosome 15q11-13 duplication. This duplication is of particular interest as it has a high prevalence in the ASD population [91]. A mouse line modelling the 15q11-13 duplication, the *patDp*/+ mutant, shows impaired social interaction, behavioural inflexibility and abnormal communication [92]. In a recent study, *patDp*/+ mutants were used to evaluate possible cerebellar phenotypes. Intriguingly, these mice indeed show impairments in motor coordination, learning and eye blink conditioning [93]. Disruption of cerebellar physiology was supported by impaired LTD at the parallel fibre to PC synapse and abnormal climbing fibre elimination of the PCs.

Tuberous sclerosis (TSC) is caused by mutations in *TSC1* or *TSC2* and results in benign tumour growth across the body, including the brain. A large portion of TSC patients is diagnosed with ASD [94]. The extent of TSC-related ASD has been shown to correlate with

the severity of cerebellar pathology [95]. The *TSC* gene products hamartin and tuberin both inhibit mTOR activity and can thereby regulate protein biosynthesis. Because of their relatively high expression in the murine cerebellum [96], it was hypothesized that mutations in *TSC1* or *TSC2* could have a major impact on cerebellar function. Tsai et al. created a PC-specific *Tsc1* mutantmouse model to assess the importance of cerebellar dysfunction in TSC (Tsai et al., 2012). This was the first study to show that a PC-specific mutation of a syndromic ASD gene results in social, repetitive and communicative impairments in mice, mimicking the human condition. The behavioural deficits are furthermore supported by reduced excitation, abnormal spine density and apoptosis of PCs. Similarly to the *Tsc1* mouse model, a PC-specific mutation of *Tsc2* shows comparable results [97, 98]. Interestingly, in both the *Tsc1* and *Tsc2* mutants the behavioural and PC-specific abnormalities can be rescued using the mTOR inhibitor rapamycin [97-99]. Another ASD-related gene involved in mTOR signaling is *PTEN* [100]. In support of the central role of PC dysfunction in ASD, a recent study investigated PC-specific deletion of *Pten* and found that mutants show abnormalities of PC structure, disrupted climbing and parallel fibre synapses, and death of PCs [101]. These mutant mice exhibited impaired sociability, repetitive behaviour and deficits in motor learning.

Mouse Models for Non-syndromic ASD

The *SHANK* family of postsynaptic scaffolding proteins comprises three main genes with homologous functional domains that have alternative splicing variants. They are crucial for the morphology, transmission and plasticity of glutamatergic synapses [102, 103]. Genetic disruption of the three different *SHANK* genes has been related to ASD, whereas cerebellum-related motor problems were predominantly occurring in individuals with mutations in the *SHANK2* gene [104]. A mouse model based on global and PC-specific *Shank2* deletion was recently investigated for physiological and behavioural phenotypes in two different studies [29, 105].) In one of the studies [29] the authors reported deficits in motor learning, social interaction and task-specific repetitive behaviour. Interestingly, the latter phenotype was also reflected in a lack of flexibility and adaptability on the ErasmusLadder, while the baseline motor performance during locomotion appeared intact. Physiological experiments indicated impaired LTP at the parallel fibre to PC synapse and dysfunctional intrinsic plasticity. Moreover, a notable increase in simple spike PC firing irregularity can be seen in posterior lobules. This increase in irregularity was accompanied by increased inhibition. The differentiation between anterior and posterior phenotypes in the cerebellum is of particular interest as posterior abnormalities have been reported in

patients [106] and could therefore indicate a biological vulnerability in the aetiology of ASD. In the second study [105] the authors report that PC-specific deletion of Shank2 results in reduced PSD number within the molecular layer as well as motor coordination, repetitive and anxiety-like behavioural phenotypes. However, these mutants do not show any impaired social interaction. The differences between the studies, as noted by the authors, could be due to different exon deletion strategies and genetic backgrounds of the mice used.

Mutations in *NLGN3* and *NLGN4* encoding the postsynaptic cell adhesion molecules Neuroligin3 and 4, have been identified in individuals with ASD [107]. Through their role as cell adhesion molecules (CAMs), which bind Neurexins and thereby physically connect pre- and postsynaptic terminals, they are crucially involved in different aspects of synapse function. Recently, similarities were reported between syndromic and non-syndromic ASD by analysing molecular phenotypes in the Neuroligin3-deficient cerebellum [108]. In this study, the authors show that *Nlgn3* KO mice exhibit cerebellum-related motor impairments and impaired cerebellar mGluR-dependent synaptic plasticity – a phenotype that is similar to the one found in *Fmr1* KO [66].

Converging Cerebellar Phenotypes Among Several Mouse Models

ASD patients have deficient processing of multiple sensory stimuli, which might contribute to their characteristic social and cognitive abnormalities. In a recent report Kloth et al., (2015) investigated five different ASD mouse models including *Shank3+/ΔC*, *Mecp2*$^{R308/Y}$, *Cntnap2*$^{-/-}$, *patDp/+* and *L7-Tsc1* mutants in their ability to acquire conditioned eye-blink responses; a form of associative learning where proper integration of sensory information is crucial, the acquisition and expression of which depends on the cerebellum [109]. They provided data showing that dysfunctional sensory integration in ASD could be related to various genetic mutations that result in cerebellar dysfunction [110]. In the light of these results, and the relatively high expression of ASD-related genes in the cerebellum [55], it is quite plausible that the sensory integration problems in ASD may be caused by a dysfunctional cerebellar circuit, appearing early in life and preventing proper functional development of downstream structures like the thalamus and sensorimotor cerebral cortex (Fig. 2.1).

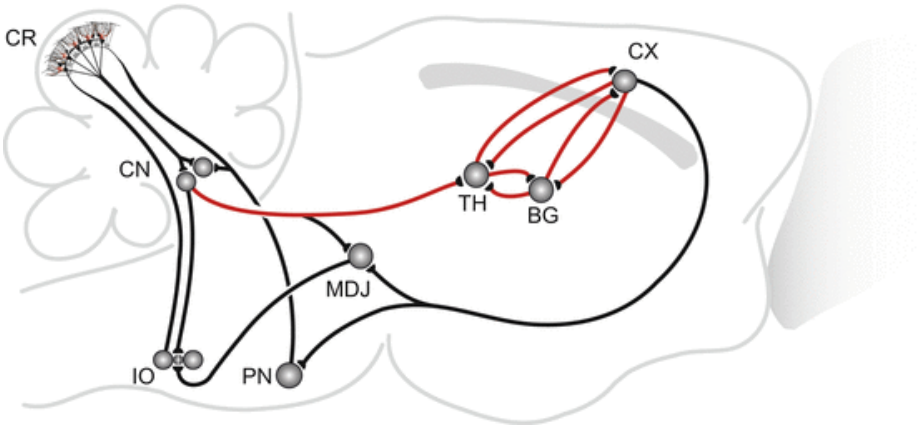

Figure 2.1 Simplified illustration of several key connections that are implicated in ASD. Here, the cerebellar output through cerebellar nuclei and the reciprocating connections between the thalamus, basal ganglia and the cerebral cortex are central. These connections require in-depth investigation that focuses on timed circuit insults as well as cell specificity of these insults. Both of these aspects (i.e. location and timing) are believed to be at the core of ASD aetiology. *CR* cerebellar cortex, *CN* cerebellar nuclei, *MDJ* mesodiencephalic junction, *PN* pontine nuclei, *IO* inferior olive, *TH* thalamus, *BG* basal ganglia, *CX* cerebral cortex

Human Striatum in ASD

Similarly to the cerebellum, the striatum, a relatively large structure that is part of the basal ganglia, has been functionally related to different aspects of motor control [111, 112]. Just like the cerebellum, the striatum receives input from both cortical and thalamic structures and is also implicated in control of cognitive processes, reaching beyond motor control functions [113]. Considering that ASD has such a complex aetiology involving multiple brain areas, the striatum has also been recognised as a promising target for further investigation. Differential abnormal changes in the volume of the striatum in ASD have been reported previously [114-116]. In support of these changes, a longitudinal study provided evidence for a developmental correlation of striatal volume change and repetitive behaviour in ASD patients [117]. The idea that the striatum is involved in repetitive behaviours is not new; in fact, over the years different lines of evidence have been accumulated in favour of dysfunctional cortico-striatal pathways in mice [118, 119], which could well be related to impulsive and stereotypical behaviours in humans [120, 121]. To advance our understanding of the underlying mechanisms in the striatum-related to dysfunctional behavioural phenotypes in ASD several different mutant mouse models have been utilized over the years.

Striatum in ASD Mouse Models

One major group of mouse models that has provided insight into striatum-related pathology in ASD are the different *Shank* mutants. As mentioned above, genetic disruptions of *SHANK* genes are highly relevant for ASD, especially mutations in *SHANK3* [104]. Interestingly, Shank3 is highly expressed in striatum and several different *Shank3* mutant lines exhibit core ASD-like behaviour and various deficits at corticostriatal synapses [118, 122-124]. Importantly, re-introducing *Shank3* has recently been shown to rescue both certain behavioural phenotypes and cortico-striatal deficits, indicating a certain degree of flexibility in the adult mutant brain [125]. In addition, recent work also suggests promise for the use of the pharmacological enhancement of metabotropic glutamate receptor 5 in the reversal of behavioural and physiological cortico-striatal abnormalities in another *Shank3* mutant [126]. Two lines of *Shank2* mutants also show ASD-like behavioural deficits [127, 128]. Interestingly, Schmeisser et al. (2012) indicate in their model that absence of *Shank2* in the striatum results in striatal up-regulation of *Shank3*, while absence of major *Shank3* isoforms results in striatal up-regulation of *Shank2*. In terms of circuit pathology, an important role for early cortical hyperactivity has been revealed in *Shank3B*$^{-/-}$ mutants [129]. Here, the authors provide evidence for a surprising early maturation of excitatory inputs of striatal spiny projection neurons in *Shank3B*$^{-/-}$ mutants, and propose that this cortico-striatal hyperactivity during development could be central in ASD models where dysfunctional cortical activity could be part of the aetiology implicating cognitive impairment. Because *SHANK3* mutations have been associated with both ASD and schizophrenia, differential mutations of the *SHANK3* gene have recently been attributed to different disorder associated symptoms in mice [130]. This work provides important clues as to how different alleles of the same *SHANK3* gene could in fact be responsible for ASD and schizophrenia-related symptoms, where distinct phenotypes can be found for striatal (ASD) and cortical (schizophrenia) impairments in physiology.

Apart from the above discussed cerebellar findings in *Nlgn3* KO, these mice have also been instructive in unravelling the striatal role in ASD. Specific deletion of *Nlgn3* in medium spiny neurons (MSNs) of the direct, but not indirect, pathway of the ventral striatum (i.e. nucleus accumbens), resulted in enhanced repetitive behaviours [131]. Deletion of *Nlgn3* in the dorsal striatum did not induce repetitive behaviours, which is surprising, as dysfunction of the dorsal striatum has been implicated in the development of repetitive behaviour in related ASD models, such as those of *Shank3* [118]. The Rothwell (2014) study therefore sheds light on the complexity of circuit involvement in the generation of behavioural

phenotypes and adds insight into the role of a specific cell type within both a defined circuit and defined subregion of the brain in this context.

An additional feature of ASD is impaired communication. As the basal ganglia are in general strongly implicated in the process of language [132], aberrations of striatal functions have also been suggested as one of the prime causes for the communication problems in ASD. Mouse models that could prove useful involve genetic abnormalities of the *Foxp* genes, which seem to be strongly associated with language. *FOXP1* and *FOXP2* encode transcriptional factors and their genetic disruption is involved in lower IQ, verbal dyspraxia and ASD in humans [133-138]. Interestingly, a recent report on the ablation of the *Foxp1* gene selectively in the mouse brain has shown a substantial reduction of striatal volume in an early postnatal phase, disrupted learning and memory, reduction of social interest and a higher occurrence of repetitive behaviours [139]. Furthermore, *Foxp2* mutants show impaired motor function and ultrasonic vocalisations (USV) abnormalities [140, 141]. Possibly, impairments in striatal LTD [142] and negative modulation of firing rates in striatal neurons [143] contribute to the behavioural phenotype in these *Foxp2* mutants.

Conclusions

The cerebellar and striatal morphological and physiological abnormalities found in ASD-related mouse models are not uniform of character [144]. Experimental data indicates that different gene dysfunctions can lead to differential, and sometimes opposing, physiological and morphological abnormalities in the same brain areas, while the impaired behavioural consequences appear to be similar. This indicates that the underlying nature of the insult is probably not overly informative in the unravelling of ASD aetiology, even though it might provide therapeutic intervention strategies in those specific insults. Instead, for the purpose of unravelling ASD aetiology it seems prudent to investigate two major questions: Which neuronal circuits are core suspects in the development of ASD? And during what time are these circuits especially vulnerable? The cerebellum and striatum have traditionally been viewed as structures controlling motor function. Yet, over the years multiple lines of evidence provide support for a functionally relevant interaction of both areas in non-motor-related tasks. Evidence from functional imaging and viral tracing studies [145] further indicates a strong interaction between both brain regions, which could have significant implications for neuropsychiatric diseases. Importantly in this context, physiologically relevant data have been published that underline a short latency modulation of the basal ganglia through deep cerebellar nuclei stimulation [146]. Given the evidence of

striatal involvement in repetitive behaviours in ASD [117], it seems parsimonious to hypothesize that the striatum-related phenotypes of repetitive and cognitive behaviours may be modulated by cerebellar output and vice versa. Indeed, together they could derail coherent activity in the cerebral cortex from early on (Fig. 2.1), which is one of the hallmarks of autism [147-149]. The ASD mouse models discussed here (Table 2.1) give potential insight into the pathology that could result from neural circuit dysfunction. However, one of the main obstacles in elucidating the contribution of a brain region to specific behavioural phenotypes is the lack of cell specificity in the targeting strategies. Future studies need to utilize cell specific mutants in both brain regions and investigate circuit morphology and physiology. *Shank* mutants are a promising model for that purpose, as global KO have already been used to evaluate either cerebellar or striatal abnormalities [29, 105, 118, 127, 128]. Cell specific *Shank* mutants should provide further insights into both behavioural and neurobiological abnormalities that might directly derive from dysfunction of specific cerebellar or striatal cell types. This type of approach will offer key insight in both motor and cognitive abnormalities in ASD and more specifically, this might lead to the identification of the major circuits involved.

Table 1 **A short list of some of the more frequently used ASD mouse models and their main morphological and physiological impairments in cerebellum and striatum**

Model	Morphology		Physiology		References
Cerebellar phenotypes in ASD mouse models					
Fmr1	N/R	Increased PC spine length	P15–P30	Increased PF-PC LTD	Koekkoek et al. (2005)
	P30	Reduced volume and cell loss in DCN	–	N/I	Ellegood et al. (2010)
	–	N/I	N/R	Reduced cerebellar-mediated PFC dopamine release	Rogers et al. (2013)
	–	N/I	P98	Increased synaptic vesicle unloading	Broek et al. (2016)
Mecp2	P10–P70	Smaller and more dense GCs	–	N/I	Chen et al. (2001)
	P21	Reduced cerebellar volume	–	N/I	Belichenko et al. (2008)
Ube3a	–	N/I	P300–P390	Increased oscillations in the cerebellar cortex	Cheron et al. (2005)
	P49–P56	Reduced PC spine density	–	N/I	Dindot et al. (2008)
	–	N/I	P25–P28	Decreased tonic inhibition in GCs	Egawa et al. (2012)
	–	N/I	P30–P32	Decreased tonic inhibition in GCs	Bruinsma et al. (2015)
***Patdp*/+**	P10–P12 and	Reduced developmental elimination of	P25–P120	Absent PF-PC LTD, restored after initial LTP induction	Piochon et al. (2014)

	P63–P70	CFs			
L7-Tsc1	P30–P120	Increased PC spine density and degeneration	P42	Reduced PC excitability	Tsai et al. (2012)
L7-Tsc2	P30–P280	PC degeneration	–	N/I	Reith et al. (2011, 2013)
L7-Pten	P180–P270 P30–P270	Reduced number of PCs Increased PC size	P84–P126	Reduced PC excitability	Cupolillo et al. (2016)
L7-Shank2	P30–P90	No abnormalities	P20–P60 P90–P150	Reduced PF-PC LTP Increased irregular firing of PCs in posterior lobules	Peter et al. (2016)
Nlgn3	P60–P90	No abnormalities	P21–P28	Reduction in PC mEPSCs and absent PF-PC LTD	Baudouin et al. (2012)
Striatal phenotypes in ASD mouse models					
Shank3 ex13–16	P35	Reduced MSN spine density	P42–P49	Reduced corticostriatal transmission	Peça et al. (2011)
Shank3 ex13	–	N/I	P90–P120	Decreased NMDAR/AMPAR ratio	Jaramillo et al. (Jaramillo et al. 2016a, b)
Shank3 ex13–16	–	N/I	P10–P14	Increased corticostriatal transmission	Peixoto et al. (2016)
Shank3 ex11	–	N/I	N/R	Reduced mGluR5 transmission in MSNs	Vicidomini et al. (2016)
Shank3 ex4–22	P56	Reduced MSN spine density, PSD length and thickness	P60–P150	Reduced sEPSCs and MSN LTD	Wang et al. (2016)
Shank3 InsG3680		Reduced MSN spine	P14 P240	Reduced field population spikes dorsolateral striatum	Zhou et al. (2016)

		density		Reduced mEPSCs in MSNs	
Nlgn3	–	N/I	P120	Reduced inhibitory synaptic currents in D1 MSNs	Rothwell et al. (2014)
Foxp1	P1–P300	Reduced striatal volume	–	N/I	Bacon et al. (2015)
Foxp2	–	N/I	P90–P180	Absent LTD in MSNs	Groszer et al. (2008)
	–	N/I	P60–P180	Decreased firing rate modulation	French et al. (2012)

Chapter 2.2

Dysfunctional cerebellar Purkinje cells contribute to autism-like behaviour in Shank2-deficient mice

Saša Peter ¶, *, Michiel M. ten Brinke *, Jeffrey Stedehouder, Claudia M. Reinelt, Bin Wu, Haibo Zhou, Kuikui Zhou, Henk-Jan Boele, Steven A. Kushner, Min Goo Lee, Michael J. Schmeisser, Tobias M. Boeckers, Martijn Schonewille, Freek E. Hoebeek and Chris I. De Zeeuw ¶

* First-Co-author(s)

¶ Corresponding author(s)

Nature Communications (2016)

Abstract

Loss-of-function mutations in the gene encoding the postsynaptic scaffolding protein *SHANK2* are a highly penetrant cause of autism spectrum disorders (ASD) including cerebellum-related motor problems. Recent studies have implicated cerebellar pathology in etiology of ASD. Here, we evaluate the possibility that cerebellar Purkinje cells represent a critical locus of ASD pathophysiology in *Shank2*-related ASD. Absence of *Shank2* impairs both Purkinje cell intrinsic plasticity and induction of long-term potentiation at the parallel fiber to Purkinje cell synapse. Moreover, inhibitory input onto Purkinje cells is significantly enhanced, most prominently in the posterior lobe where simple spike regularity is most affected. Using Purkinje cell-specific *Shank2*-knockouts, we replicate alterations of simple spike regularity *in vivo* and establish cerebellar-dependence of ASD-like behavioural phenotypes in motor learning and social interaction. These data highlight the importance of *Shank2* for Purkinje cell function, and support a model by which cerebellar pathology is prominent in certain forms of ASD.

Introduction

Autism spectrum disorders (ASD) are neurodevelopmental disease entities primarily defined by deficits in social interaction and repetitive behaviour [150]. In addition, individuals with autism often suffer from motor skill deficiencies [58], many of which manifest early in the disease [151]. The aetiology of ASD is complex with reported pathophysiological alterations encompassing multiple brain regions, including the cerebellum [150]. Cerebellum-related motor symptoms of ASD patients have been observed by impairments in eyeblink conditioning [39, 40], eye movement abnormalities [41, 42], general motor learning deficits [43, 44] as well as balance and postural difficulties [45, 46]. Patients with cerebellar lesions emerging later in development are often diagnosed with cerebellar cognitive affective syndrome, a condition characterized by deficits in language, executive function and impaired emotions which overlaps considerably with symptoms in ASD [48]. Anatomical evidence for cerebellar involvement in ASD includes a decrease in the number of Purkinje cells (PCs) by post-mortem brain histopathological examination [49, 50] and functional connectivity between the cerebellum, and frontoparietal and sensorimotor regions in resting-state fMRI studies of ASD [106]. Moreover, the cerebellum is among the most prominent brain regions demonstrating high co-expression of ASD-associated genes [152].

Emerging data indicate that neurodevelopmental disorders including ASD result from dysfunctional synaptic networks [153, 154]. The postsynaptic density (PSD) in particular represents a critically important proteomic hub for a considerable proportion of neurodevelopmental disease-causing mutations, including ASD [155]. A prominent example is the Shank family of postsynaptic scaffolding proteins, which has gained wide attention because of their strong link to ASD [125, 156-159]. To date, two studies have independently reported generating *Shank2* knockout (KO) mice with ASD-like behaviour and abnormal hippocampal processing [127, 128]. However, in addition to the forebrain, *Shank2* is also highly expressed in cerebellar PCs [160, 161]. Moreover, patients with *Shank2*-related ASD exhibit motor impairments consistent with cerebellar dysfunction [162]. However, the causal influence of cerebellar dysfunction on *Shank2*-related ASD has never been established.

We therefore used both global germ-line *Shank2* knock-out (KO; *Shank2*$^{-/-}$) and PC-specific *Shank2* KO (*L7-Shank2*$^{-/-}$) mouse models to investigate the causal influence of *Shank2* on cerebellar function and ASD-related behaviours. Notably, *Shank2*$^{-/-}$ mice have impairments in plasticity at the parallel fiber (PF) to PC synapse, increased inhibitory input onto PCs,

and significant irregularities in PC simple spike activity. Moreover, *L7-Shank2*$^{-/-}$ mice show deficits in social interaction and exhibit task-specific repetitive behaviour. Together, these results provide novel insight into the pathophysiological mechanisms by which *Shank2* mutations cause impairments in cerebellar function that may contribute to ASD.

Results

Reduction of functional cerebellar AMPAR in *Shank2*$^{-/-}$ mice

A divergent role of the *Shank2* scaffolding protein has been hypothesized for PSD function and cellular morphology [163]. To evaluate the morphology of *Shank2*-deficient postsynaptic specializations along PC dendrites, we quantified the structural characteristics of dendritic spines and PSDs in the distal molecular layer of global *Shank2*$^{-/-}$ mice using Golgi-Cox staining of PC dendrites and electron microscopy (Fig. 1). Neither spine density (WT: 1.93±0.74 spines/µm dendrite; *Shank2*$^{-/-}$: 1.82±0.67 spines/µm dendrite; P=0.2, Mann-Whitney U-test (MWU-test, see Supplementary Table 1 for additional statistics), nor the length (WT: 1.34±0.77 µm; *Shank2*$^{-/-}$: 1.32±0.50 µm; P=0.4, MWU-test) or width of individual spines (WT: 0.72±0.45 µm; *Shank2*$^{-/-}$: 0.71±0.32 µm; P=0.9, MWU-test) was significantly affected (Fig. 1a). In addition, the length (WT: 313.3±97.1 nm; *Shank2*$^{-/-}$: 305.3±96.2 nm; P=0.3) and thickness of PSDs (WT: 26.2±6.0 nm; *Shank2*$^{-/-}$: 26.0±5.3 nm; P=0.9) were similar between genotypes (Fig. 1b,c). In contrast, biochemical analysis of cerebellar synaptosomes indicated that global *Shank2*$^{-/-}$ mice have lowered expression of AMPA receptor subunits GluA1 (WT: 1.00±0.37; *Shank2*$^{-/-}$: 0.63±0.23; P=0.041) (Fig. 1d, Supplementary Fig. 1) and GluA2 (WT: 1.00±0.32; *Shank2*$^{-/-}$: 0.58±0.11; P=0.014). In addition, we looked into the ASD pathology related cell adhesion molecule neuroligin 3 (Nlgn3), which has been shown to interact with Shank proteins **[155]**, but found no significant difference in its expression (WT: 1.00±0.37; *Shank2*$^{-/-}$ 0.84±0.33; P=0.4). Together, these findings indicate that *Shank2* is not crucial for the morphological differentiation of PC dendritic spines and PSDs, but instead may play an important role in the maintenance of cerebellar GluA1 and GluA2 levels.

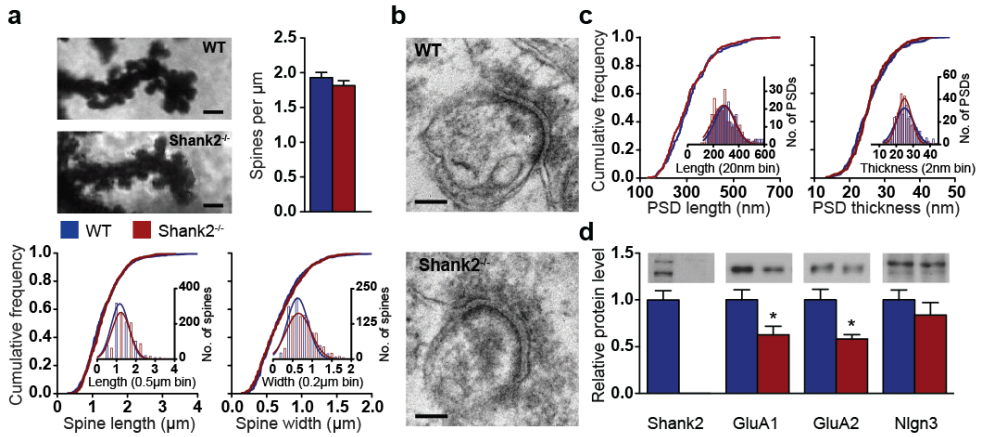

Figure 1. Reduction of AMPA receptor subunits in Shank2$^{-/-}$ cerebellar synaptosomes, but no changes in spine and PSD morphology in the distal molecular layer (DML). (A) Representative images (Golgi-Cox staining) of distal Purkinje cell dendrites in the DML, quantification of spine density (WT, n=97/4, dendrites/mice; Shank2$^{-/-}$, n=89/4, P=0.2, MWU-test) and cumulative frequency plots of spine length (P=0.4, MWU-test) and thickness (P=1, MWU-test) in WT (n=748/4 spines/mice) and Shank2$^{-/-}$ mice (n=639/4) as indicated. Scale bar: 1 µm. **(B,C)** Representative images (electron microscopy) of spine synapses in the DML and cumulative frequency plots of PSD length (WT, n=226/4, PSDs/mice; Shank2$^{-/-}$, n=243/4, P=0.3) and thickness (WT, n=223/4; Shank2$^{-/-}$, n=233/4, P=0.9) as indicated. Scale bar: 100 nm. **(D)** Biochemical analysis of *Shank2* (WT, n=12 synaptosomes; Shank2$^{-/-}$, n=6), GluA1 (WT, n=12 synaptosomes; Shank2$^{-/-}$, n=6, P=0.041) GluA2 (WT, n=11; Shank2$^{-/-}$, n=5, P=0.014), and *Nlgn3* (WT, n=12; Shank2$^{-/-}$, n=6, P=0.4) in cerebellar synaptosomes from WT and Shank2$^{-/-}$ mice as indicated. Data in bar graphs are presented as mean ± SEM; single asterisks indicates $p < 0.05$. Two-sided t-tests were used, unless stated otherwise.

Normal baseline excitability in *Shank2*$^{-/-}$ Purkinje cells

Considering that we found a reduction of cerebellar AMPA receptor expression in global *Shank2*$^{-/-}$ mice, we next examined neurotransmission at the PF-PC synapse using *ex vivo* whole-cell recordings (at 21±1°C) (**Fig. 2a**). PF-PC EPSCs, which were obtained in WT and *Shank2*$^{-/-}$ under comparable conditions (holding current: WT: -389±102 pA; *Shank2*$^{-/-}$ -388±114 pA, P=1; PC input resistance: WT: 67.2±16.8 MΩ; *Shank2*$^{-/-}$: 69.1±12.4 MΩ; P=0.8; **Fig. 2b,c**), revealed no significant differences in rise time (WT: 2.1±0.7 ms; *Shank2*$^{-/-}$: 1.7±0.6 ms; P=0.2) or decay time (WT: 9.7±0.8 ms; *Shank2*$^{-/-}$: 9.3±0.3 ms; P=0.3) (**Fig. 2d,e**). Moreover, evoking PF-EPSCs using stimulation currents varying from 3 to 15 µA resulted in similar event amplitudes (P=0.9, repeated-measures ANOVA) (**Fig. 2f,g**) and applying inter-stimulus intervals varying from 50 to 200 ms evoked comparable levels of paired-pulse facilitation (P=0.2, repeated-measures ANOVA) (**Fig. 2h**), indicating that baseline PF-PC synaptic transmission is unaltered by the lack of *Shank2*. Next, we evaluated

whether the loss of *Shank2* affected neurotransmission at the climbing fiber (CF) to PC synapse. CF stimulation induced PC complex spikes in WT and *Shank2*$^{-/-}$. These waveforms showed no significant differences in the amplitude of the initial Na^+-spike (WT: 51.8±6.4 mV; *Shank2*$^{-/-}$: 48.5±5.9 mV, P=0.3) and in the number of subsequent Ca^{2+}-spikelets (WT: 1.6±0.5; *Shank2*$^{-/-}$: 2.0±0.7; P=0.2) or the amplitude of Ca^{2+}-spikelets (WT: 31.8±11.9 mV; *Shank2*$^{-/-}$: 33.9±6.4 mV, P=0.7) (**Supplementary Fig. 2a-c**). Moreover, at P9-10 virtually all PCs of both WT and *Shank2*$^{-/-}$ were innervated by multiple CFs, while at P25-35 all converted into mono-innervation (number of CF responses P9-10: WT: 2.0±0.5; *Shank2*$^{-/-}$: 2.3±0.5; P=0.2; P25-35: WT: 1.0±0.0; *Shank2*$^{-/-}$: 1.0±0.0; P=1, MWU-test) (**Supplementary Fig. 2d,e**). Finally, the characteristic paired-pulse depression of CF-PC synaptic transmission showed no differences throughout the tested developmental stages (P9-10: WT: 0.59±0.14; *Shank2*$^{-/-}$: 0.54±0.11; P=0.5; P25-35: WT: 0.75±0.11; *Shank2*$^{-/-}$: 0.77±0.1; P=0.6) (**Supplementary Fig. 2f,g**), together indicating that the CF to PC input in *Shank2*$^{-/-}$ mice is not only normal in its baseline characteristics but also with respect to developmental elimination [164].

To examine PC kinetics, we evoked action potentials (APs) using depolarizing current steps at near-physiological temperature (33±1°C) (**Fig. 2i**). Evoked APs showed comparable thresholds (WT: -51.4±3.9 mV; *Shank2*$^{-/-}$: -51.0±3.5 mV; P=0.8), amplitudes (WT: 39.8±5.8 mV; *Shank2*$^{-/-}$: 35.9±5.8 mV; P=0.1) and half-widths (WT: 0.29±0.02 ms; *Shank2*$^{-/-}$: 0.30±0.03 ms; P=0.7), as well as after-hyperpolarization amplitudes (WT: 6.5±1.6 mV; *Shank2*$^{-/-}$: 7.5±1.7 mV; P=0.2) (**Fig. 2j-m**). In addition, PC intrinsic excitability was normal [165] in that current step injections of increasing amplitude resulted in a linear current-to-firing frequency relationship (P=0.1, repeated-measures ANOVA) (**Fig. 2n,o**) with a similar slope (WT: 16.2±2.2 Hz; *Shank2*$^{-/-}$: 16.1±2.3 Hz; P=1.0) (**Fig. 2o**). Together, these findings indicate that both the baseline transmission at PC excitatory synapses and PC intrinsic excitability remain intact in global *Shank2*$^{-/-}$ mice.

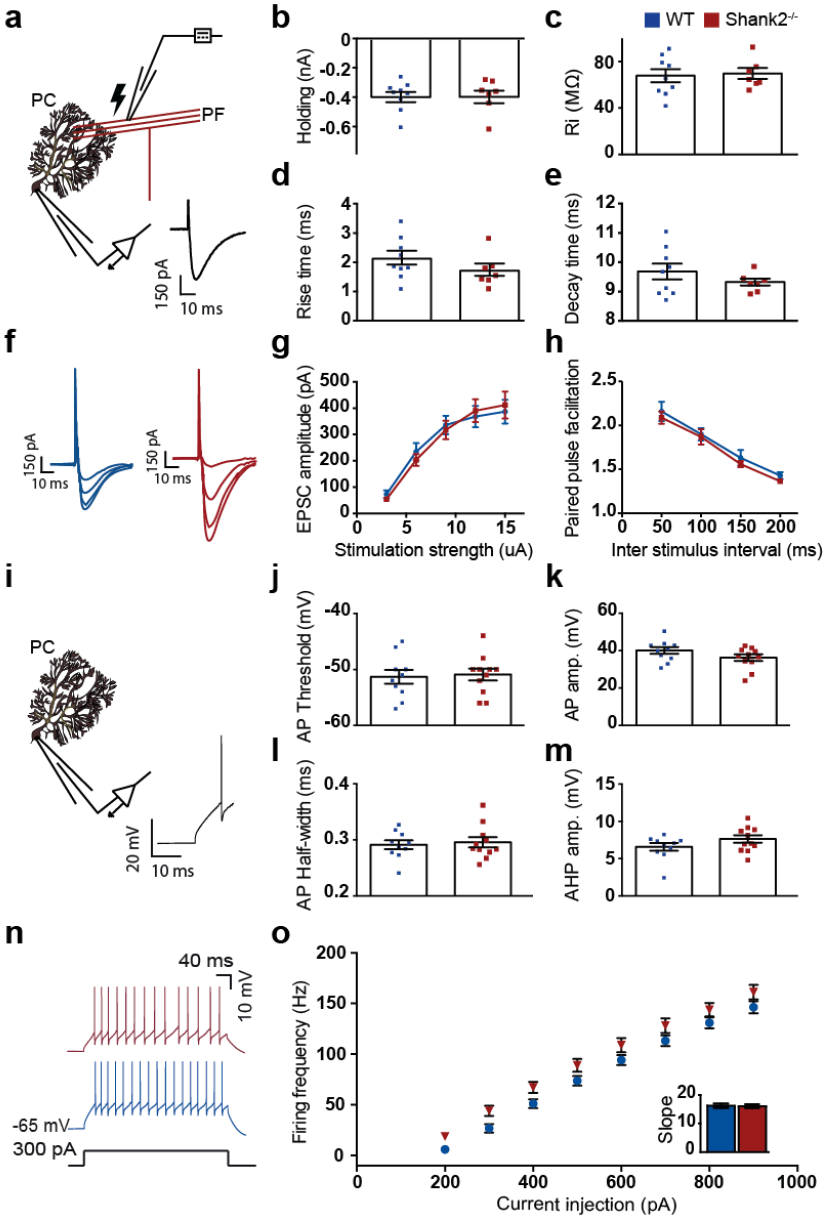

Figure 2. No changes in excited synaptic and intrinsic properties in Shank2$^{-/-}$ Purkinje cells ex vivo. (A) Recording configuration for voltage clamp recordings of PF-PC synaptic transmission. Inset: an example PF-EPSC. **(B-E)** With comparable holding current (at -65mV) (P=1) and input resistance (Ri) (P=0.8), PC EPSC rise time (P=0.2) and EPSC decay time (P=0.3) are not different between WT (n=9/6, cells/animals) and Shank2$^{-/-}$ (n=7/6). **(F)** Example EPSCs in response to 3, 6, 9, 12, and 15 uA stimulation. **(G,H)** Varying stimulation strength (P=0.9, repeated-measures ANOVA) and inter-stimulus interval (P=0.2, repeated-measures ANOVA) evoked comparable EPSC amplitude or facilitation (WT, n=11/3; Shank2$^{-/-}$ 15/3). **(I)** Recording configuration for whole

cell recording. Inset: an example action potential. **(J-M)** Action potential threshold (P=0.8), amplitude (P=0.1), half-width (P=0.7), and afterhyperpolarization (P=0.2) were not different (WT, n=10/6; Shank2$^{-/-}$, n=11/6). (n) Example traces of intrinsic Purkinje cell excitability as apparent from action potential firing evoked by 300 pA current injections. **(O)** No difference in evoked firing frequency relative to various levels of current injections (WT, n=10/5; Shank2$^{-/-}$, n=11/5, P=0.1, repeated-measures ANOVA). Inset barplot shows average slope of firing rate per current step (P=1). Data are represented as mean ± SEM. Two-sided t-tests were used, unless stated otherwise.

Increased sIPSCs and spiking irregularity in *Shank2*$^{-/-}$ PCs

To investigate inhibition of PCs in global *Shank2*$^{-/-}$ mice, we recorded spontaneous inhibitory postsynaptic currents (sIPSCs). Since PC activity can be related to the presence or absence of the glycolytic enzyme aldolase-c (referred to as zebrin) [10], we recorded from the predominantly zebrin-negative anterior lobules I-V as well as the predominantly zebrin-positive posterior lobule X of the cerebellar cortex (**Fig. 3a,b**). In both regions, we observed an increase in the frequency (lobules I-V: WT: 8.3±5.9 Hz; *Shank2*$^{-/-}$: 12.2±5.4 Hz; P=0.0295; lobule X: WT: 14.2±7.0 Hz; *Shank2*$^{-/-}$: 21.5±8.8 Hz; P=0.0079) (**Fig. 3c,e**), but not in the amplitude (for lobules I-V, WT: 53.2±24.4 pA; *Shank2*$^{-/-}$: 65.2±29.5 pA; P=0.1; for lobule X, WT: 58.9±19.0 pA; *Shank2*$^{-/-}$: 64.0±24.7 pA; P=0.5), of sIPSCs (**Fig. 3d,f**). Importantly, *Shank2*$^{-/-}$ sIPSC frequency was higher in lobule X than in the anterior lobe (P=0.0002). Given that inhibition decreases the firing frequency of PCs, but increases their irregularity [166, 167], we hypothesized that the increased frequency of sIPSCs in *Shank2*$^{-/-}$ would translate into an overall decrease of *in vivo* simple spike (SS) activity but with an increased irregularity (**Fig. 3g,h**). The global *Shank2*$^{-/-}$ mice did indeed exhibit a decrease in firing frequency in lobules I-V (WT: 88.2±18.7 Hz; *Shank2*$^{-/-}$: 76.3±11.8 Hz; P=0.0096) (**Fig. 3i**), but notably not in lobule X (WT: 52.6±12.7 Hz; *Shank2*$^{-/-}$: 50.3±12.9 Hz; P=0.6) (**Fig. 3l**). Conversely, and consistent with the relative magnitude of the change in sIPSC frequency, the irregularity of PC SS firing was increased in lobule X (CV: WT, 0.30±0.08; *Shank2*$^{-/-}$, 0.38±0.09, P=0.0086; CV2: WT, 0.29±0.07; *Shank2*$^{-/-}$, 0.40±0.11, P=0.0003), but not in lobules I-V (CV: WT, 0.48±0.06; *Shank2*$^{-/-}$, 0.49±0.12, P=0.7; CV2: WT, 0.45±0.04; *Shank2*$^{-/-}$, 0.48±0.08, P=0.1) (**Fig. 3j-n**). The complex spike frequency and the pause in SS firing following each complex spike was similar between global *Shank2*$^{-/-}$ mice and their WT littermates in both the anterior (WT: frequency 1.28±0.29 Hz; pause 9.11±1.98 ms; *Shank2*$^{-/-}$: 1.32±0.24 Hz; 10±2.9 ms; P=0.7 and P=0.2, respectively) and posterior lobules (WT: frequency 0.67±0.19 Hz; pause 19.7±5.5 ms; *Shank2*$^{-/-}$: frequency 0.84±0.37 Hz; pause 17.61±5.29 ms; P=0.1 and P=0.2, respectively) (**Supplementary Fig. 3**). Thus, in the

absence of *Shank2*, the zebrin-positive lobule X selectively exhibits a highly irregular pattern of PC simple spike firing, which is consistent with a relative increase of inhibitory input onto lobule X PCs.

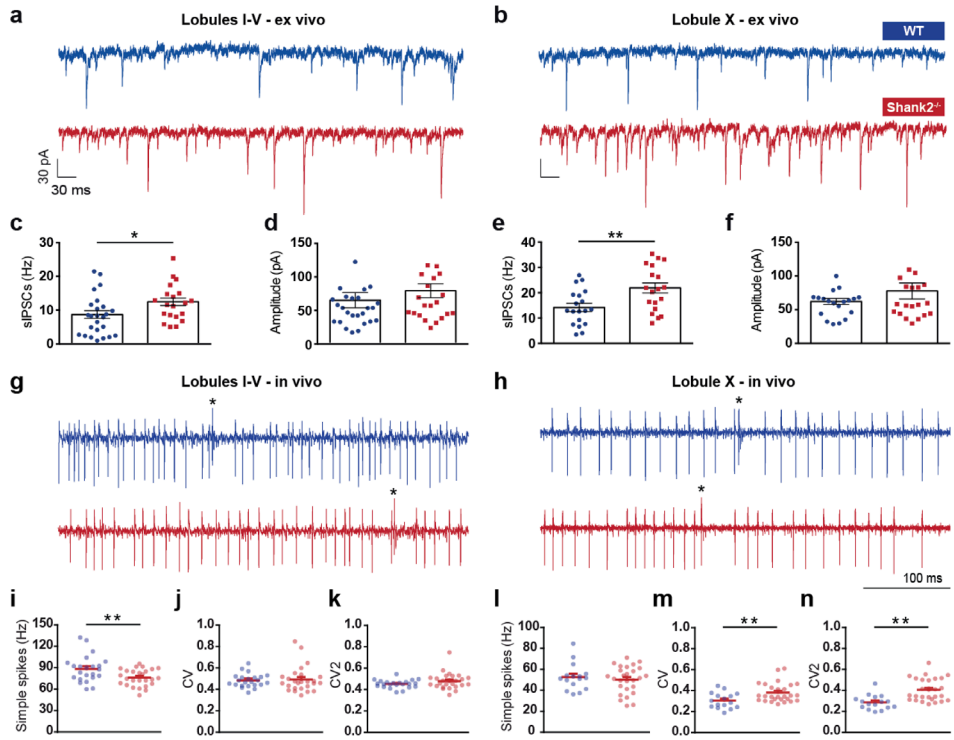

Figure 3. Increased spontaneous inhibitory events and higher simple spike irregularity in Shank2$^{-/-}$ Purkinje cells. (A,B) Example of spontaneous firing inhibitory post synaptic currents (sIPSCs) in lobules I-V and X. **(C,E)** A higher frequency of sIPSCs is found in both anterior (I-V) (P=0.0295) and posterior (X) lobules (P=0.0079) in Shank2$^{-/-}$ PCs (anterior: WT, n=25/3, cells/animals; Shank2$^{-/-}$, n=20/3; posterior: WT, n=19/3; Shank2$^{-/-}$, n=19/3). **(D,F)** There were no significant differences in sIPSC amplitudes anteriorly (P=0.1) or posteriorly (P=0.5). (g,h) Extracellular traces of PCs recorded in anterior (left) and posterior (right) lobules in the cerebellum, in WT and Shank2$^{-/-}$. Asterisks denote complex spikes. **(I-K)** Simple spike (SS) firing frequency was significantly lower (P=0.0096) in Shank2$^{-/-}$ (n=26/3) compared to wildtype (n = 23/3), whereas the coefficient of variation (CV) (P=0.7) and CV2 (P=0.1) did not differ. **(L-N)** In posterior lobule X, while SS firing frequency was similar (P=0.6), CV (P=0.0086) and CV2 (P=0.0003) were significantly higher in Shank2$^{-/-}$ (n=27/3) compared to WT (n = 16/3). Data are represented as mean ± SEM. Single and double asterisks indicate P<0.05 and P<0.01, respectively. Two-sided t-tests were used, unless stated otherwise.

Impaired synaptic and intrinsic plasticity in *Shank2*$^{-/-}$ PCs

Given that *Shank2* functions as a PSD scaffolding protein of postsynaptic receptors [153, 163] for which we observed decreased expression of both GluA1 and GluA2 in cerebellar synaptosomes of *Shank2*$^{-/-}$ mice (**Fig. 1**), we reasoned that PC synaptic plasticity might also be affected [127, 128]. Induction of long-term potentiation (LTP) (33±1˚C; 1 Hz, 5 min PF-tetanus) (**Fig. 4a**) reliably increased PF-EPSC amplitudes in WT PCs (121.1±19.8% at t=40 min; P=0.003, repeated-measures ANOVA), but not in those of global *Shank2*$^{-/-}$ mice (91.8±14.2% at t=40; P=0.3, repeated-measures ANOVA) (**Fig. 4b**). In contrast, both WT and global *Shank2*$^{-/-}$ mice exhibited robust long-term depression (LTD) of PF-EPSCs following co-activation (1 Hz) of PFs and CFs (WT: 71.4±14.9%; P<0.0001; *Shank2*$^{-/-}$: 76.9±14.6%; P=0.0009, repeated-measures ANOVA) (**Fig. 4c,d**). Since LTP has been reported to facilitate adaptation of intrinsic properties, driving spike activity [165], we next examined PC intrinsic plasticity before and after PF-LTP induction (**Fig. 4e**). Whereas WT mice readily demonstrated a potentiation of intrinsic excitability (139.7±21.3% at t=40 min; P=0.005, repeated-measures ANOVA), intrinsic plasticity was markedly impaired in global *Shank2*$^{-/-}$ mice (104.6±22.2% at t=40 min; P=0.5, repeated-measures ANOVA) (**Fig. 4f**). These results suggest that *Shank2* is a critical modulator of both synaptic and intrinsic plasticity in Purkinje cells.

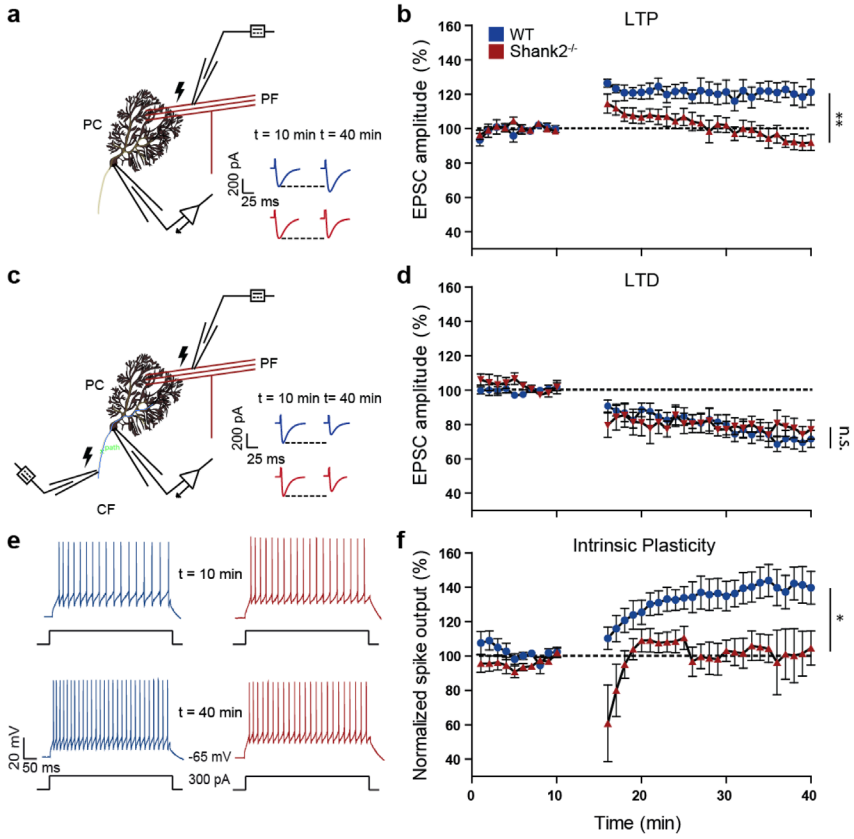

Figure 4. Impaired synaptic and intrinsic plasticity in Shank2$^{-/-}$ ex vivo. (A) Recording configuration for PF-LTP experiments. Inset: example of 5 averaged EPSCs for WT (blue) and Shank2$^{-/-}$ (red) before LTP induction (at 10 minutes) and after LTP induction (at 40 min). **(B)** LTP experiment with 5 min PF stimulation at 1Hz inducing LTP in WTs (n=7/6, cells/animals, P=0.0027) but not in Shank2$^{-/-}$ PCs (n=12/6, P=0.3), which is reflected in the difference between genotypes (P=0.0066). **(C)** Recording configuration for PF-LTD experiments. Inset: example traces as in a. **(D)** LTD is induced in both WT (n=9/6, P<0.0001) and Shank2$^{-/-}$ (n=7/6, P=0.0009) PCs, to a similar degree (P=1). **(E)** Example of traces for intrinsic plasticity with current injections of 300 pA. **(F)** LTP induction protocol induced enhanced spike output in WT PCs (n=5/4, P=0.0053), but not in Shank2$^{-/-}$ PCs (n=5/4, P=0.5), as reflected in their difference (P=0.0201). Data are represented as mean ± SEM. Single and double asterisks indicate P<0.05 and P<0.01, respectively. All tests were repeated-measures ANOVAs.

Expression of *Shank2* in *L7-Shank2*$^{-/-}$ mice

To explore the behavioural impact of the lack of *Shank2* in PCs, we generated a PC-specific knockout of *Shank2* (see methods section) using the floxed version of the *Shank2*$^{-/-}$ mutants [128] and the L7-vector [165]. Immunocytochemical analysis with the SA5193 rabbit primary *Shank2* antibody [128, 168] confirmed that *Shank2*$^{-/-}$ was specifically deleted in

PCs in the PC-specific *L7-Shank2*$^{-/-}$ mice, but not in WT littermates, whereas it was ubiquitously deleted in the global *Shank2*$^{-/-}$ (**Fig. 5**). Importantly, PC-specific deletion of *Shank2* had no discernible impact on cellular zebrin identity, or on the zonal patterns of zebrin staining across cerebellar modules (**Supplementary Fig. 4**).

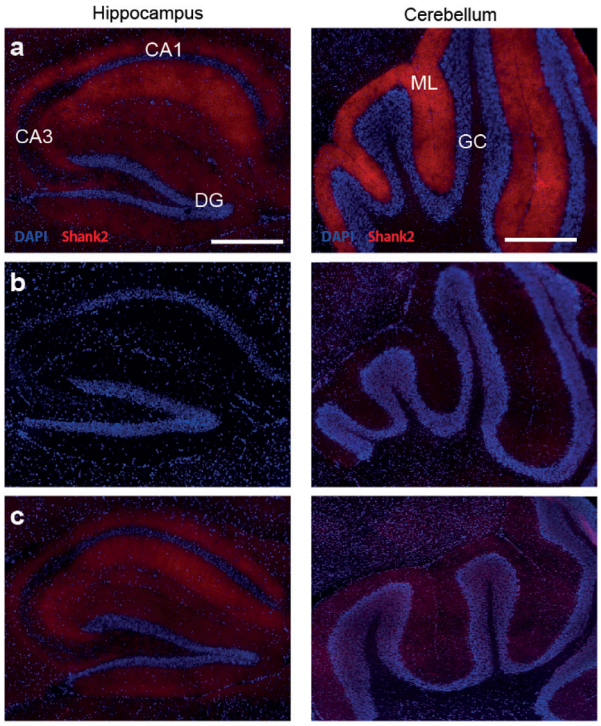

Figure 5. Immunohistological staining of the Shank2 protein in Shank2$^{-/-}$ and L7-Shank2$^{-/-}$ hippocampus and cerebellum. (A) Sagittal cryosection of hippocampal Shank2 (red) and nucleus staining (DAPI; blue) in a WT (left) L7-Shank2$^{-/-}$. Scale bar: 500 µm. Sagittal cryosection of cerebellar Shank2 staining (right). Scale bar: 200 µm. **(B)** Staining for Shank2 in the hippocampus and cerebellum of the global Shank2$^{-/-}$ shows absence of expression. **(C)** The L7-Shank2$^{-/-}$ shows expression in the hippocampus, but not in the molecular layer of the cerebellum.

Impaired motor learning in *L7-Shank2*$^{-/-}$ mice

Given the variety of electrophysiological aberrations in PCs in the global *Shank2*$^{-/-}$, we next examined motor behavior in the PC-specific *L7-Shank2*$^{-/-}$ mice. Unlike the hyperactivity exhibited by global *Shank2*$^{-/-}$ mice in an open field [127, 128], mice with PC-specific deletion of *Shank2* exhibited no evidence of hyperactivity in the open field test compared to their WT littermates (velocity: WT: 12.28±2.79 cm/s; *L7-Shank2*$^{-/-}$: 13.24±2.61 cm/s ; P=0.3; distance moved: WT: 7.37±1.68 m; *L7-Shank2*$^{-/-}$: 7.94±1.57 m; P=0.3) (**Supplementary Fig. 5a,b**). The lack of hyperactivity was confirmed using the PhenoTyper Box (Noldus), in which free exploration was quantified over a 30 min-period in a homecage-like environment (velocity: WT: 6.7±1.1 cm/s; *L7-Shank2*$^{-/-}$: 6.3±1.3 cm/s; P=0.5, distance moved: WT: 384.6±68.8 cm; *L7-Shank2*$^{-/-}$: 371.7±79.7 cm; P=0.5, repeated-measures ANOVA) (**Supplementary Fig. 5c,d**). Moreover, during the ErasmusLadder test [169] motor performance was similar

between genotypes, including the efficiency and timing of steps (2nd day efficiency, WT: 33.1±20.0%; *L7-Shank2*$^{-/-}$: 47.1±15.4 cm; P=0.3; 2nd day timing: WT: 359.2±84.2 ms; *L7-Shank2*$^{-/-}$: 330.7±49.4 ms; P=0.8, repeated-measures ANOVA) (**Supplementary Fig. 5e,f**). Finally, the amplitude (gain) and timing (phase) of baseline optokinetic (OKR) (OKR gain, P=0.6, OKR phase, P=0.9, repeated-measure ANOVA) and vestibulo-ocular reflexes (VOR) (VOR gain, P=0.4, VOR phase, P=0.2, repeated-measure ANOVA) were also similar (**Supplementary Fig. 5g-j**), further highlighting that motor performance is normal in *L7-Shank2*$^{-/-}$ mutants.

In contrast, motor learning was consistently affected in a variety of cerebellar motor learning tasks (**Fig. 6**). Using a conditioning task within the ErasmusLadder, in which mice were presented with a tone preceding the elevation of an obstructive rung at a 200 ms interval [169], *L7-Shank2*$^{-/-}$ mice were unable to successfully avoid the obstacle (*L7-Shank2*$^{-/-}$ versus WT: P=0.018, repeated-measures ANOVA) (**Fig. 6a,b**). Furthermore, *L7-Shank2*$^{-/-}$ mice failed to acquire the normal increase in VOR gain (*L7-Shank2*$^{-/-}$ versus WT: P=0.006, repeated-measures ANOVA) or shift in VOR phase (2nd day; P=0.047, 3rd P=0.0013, 4th P<0.0001, 5th P=0.0003, repeated-measures ANOVA) following visuovestibular mismatch training [170] (**Fig. 6c-f**). Finally, *L7-Shank2*$^{-/-}$ mice exhibited a significant impairment of Pavlovian eyeblink-conditioning [109] using a light pulse as the conditioning stimulus (CS) and a corneal air puff as the unconditioned stimulus at a 250 ms interval (conditioned response or CR rate: P=0.0013; CR amplitude: P=0.0009; repeated-measures ANOVA) (**Fig. 6g-i**). These findings indicate that *L7-Shank2*$^{-/-}$ mice have normal baseline motor performance, but prominent impairments in motor learning.

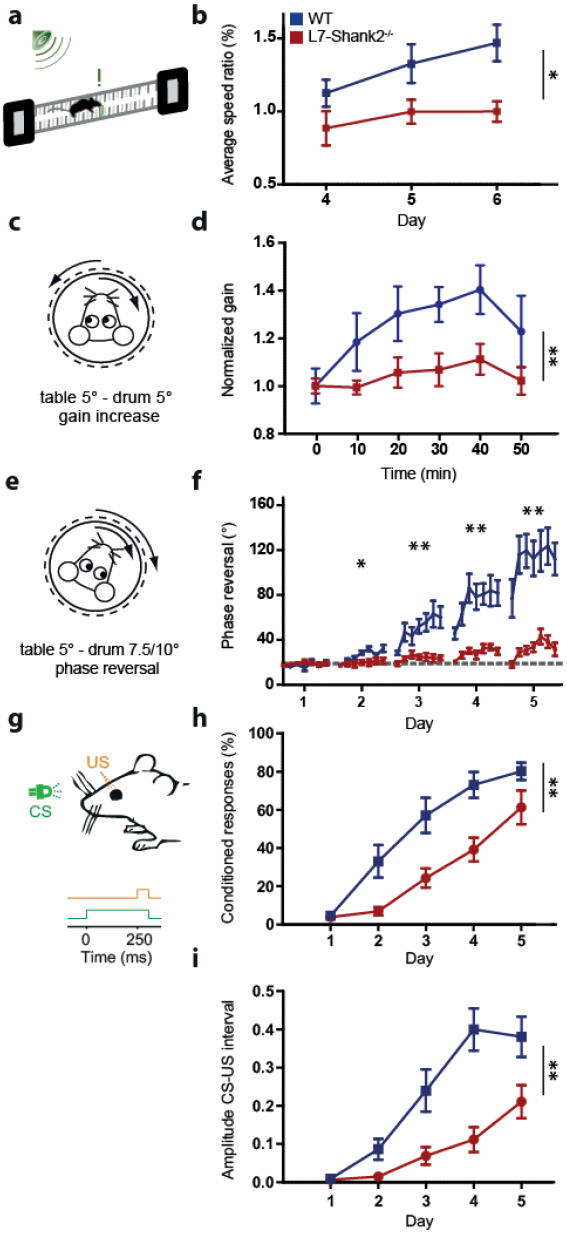

Figure 6. L7-Shank2$^{-/-}$ mice show impaired motor learning. (A,B) After three days of training, WT (n=9) but not L7-Shank2$^{-/-}$ mice (n=6) (P=0.018) learned to increase their speed during a conditioned ErasmusLadder test using tone-cued rung displacements. **(C,D)** In vestibulo-ocular reflex (VOR) gain increase training, L7-Shank2$^{-/-}$ mice (n=8) were not able to adapt their gain like WTs did (n=7) (P=0.006). **(E,F)** L7-Shank2$^{-/-}$ mutants (n=9) did not adapt their VOR phase following a reversal training paradigm, whereas WT (n=9) did (2nd day, P=0.047; 3rd, P=0.0013; 4th, P<0.0001; 5th, P=0.0003). **(G-I)** Impaired percentage (P=0.0013) and amplitude (P=0.0009) of conditioned responses (CRs) in L7-Shank2$^{-/-}$ mice (n=10) compared to WT (n=11) in an eyeblink conditioning paradigm (200 paired trials daily). Data are represented as mean ± SEM. Single and double asterisks indicate P<0.05 and P<0.01, respectively. All tests were repeated-measures ANOVAs.

Irregular *in vivo* PC simple spikes in *L7-Shank2*$^{-/-}$ mice

To investigate whether the changes in electrophysiological properties observed in PCs of the global *Shank2*$^{-/-}$ mice may contribute to the behavioural phenotypes observed, we tested to what extent the changes in simple spike activity also occurred in the *L7-Shank2*$^{-/-}$ mice. We first recorded extracellular single units *in vivo* from the largely zebrin-negative lobules I-V (**Fig. 7a-d**) and the predominantly zebrin-positive lobules IX-X (**Fig. 7e-h**). Importantly, the recordings in the *L7-Shank2*$^{-/-}$ mice fully reproduced the

increases in CV (WT, 0.35±0.07; *L7-Shank2*$^{-/-}$, 0.49±0.09; P<0.0001) and CV2 (WT, 0.36±0.06; *L7-Shank2*$^{-/-}$, 0.47±0.06; P<0.0001) (Fig. 7**g,h**) that were found in the posterior lobules of the global *Shank2*$^{-/-}$ **(Fig. 3i-n)**, confirming the higher SS irregularity. In addition, the *L7-Shank2*$^{-/-}$ mice also showed signs of SS irregularity in the anterior lobules in that their CV2 was also significantly increased (WT, 0.43±0.04; *L7-Shank2*$^{-/-}$, 0.47±0.04; P=0.0092) (**Fig. 7c,d**). The *L7-Shank2*$^{-/-}$ SS mice activity did not show higher firing frequencies in either the anterior (WT: 104.4±25.8 Hz; *L7-Shank2*$^{-/-}$: 101.2±19.7 Hz; P=0.6) or posterior (WT: 70.9±19.5 Hz; *L7-Shank2*$^{-/-}$: 76.3±23.4 Hz; P=0.4) lobules (**Fig. 7b,f**). Finally, we also recorded SS activity of PCs in the flocculus of the vestibulocerebellum, because they are known to directly control VOR adaptation [166] (**Fig. 7i-l**).

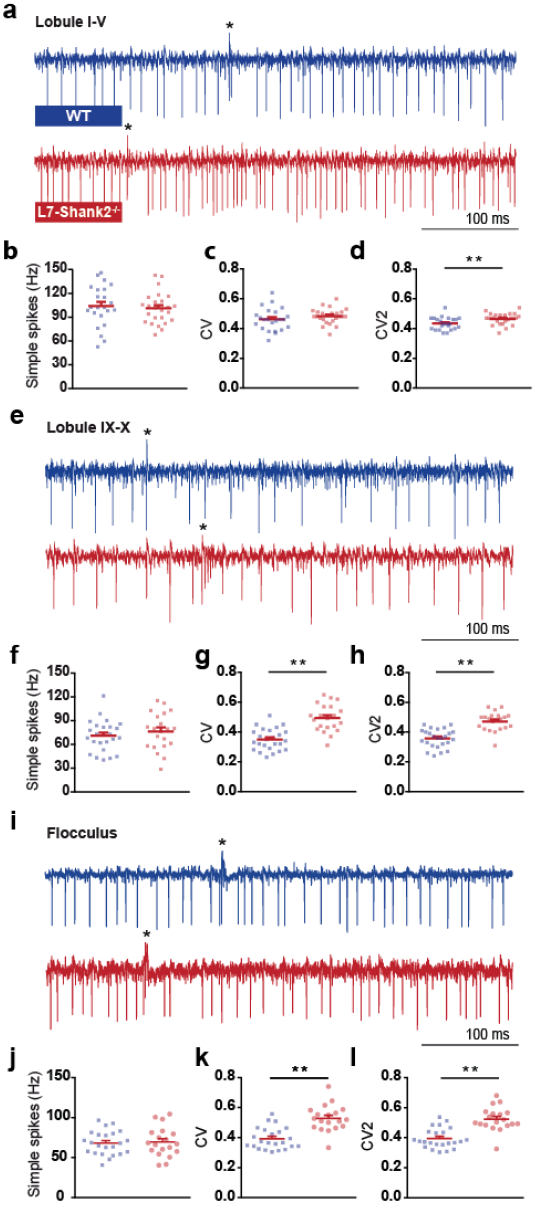

Figure 7. In vivo simple spike firing characteristics in L7-Shank2$^{-/-}$ Purkinje cells. (A) Extracellular PC traces recorded from anterior lobules (I-V) in WT (top) and L7-Shank2$^{-/-}$ (bottom) mice. **(B-D)** Firing characteristics in the anterior lobules reveal a difference in CV2 (P=0.0092) between L7-Shank2$^{-/-}$ (n=25/3, cells/animals) and WT (n=23/3). **(E)** Example PC traces from posterior lobules (IX-X). **(F-H)** PCs from the posterior cerebellum in L7-Shank2$^{-/-}$ (n=21/3) showed significantly higher CV (P<0.0001) and CV2 (P<0.0001) values compared to WT (n=25/3). **(I)** Example PC traces from posteriorly located flocculus, which is responsible for VOR learning. **(J-L)** Again, L7-Shank2$^{-/-}$ (n=19/2) shows significantly higher CV (P<0.0001) and CV2 (P<0.0001) values than WT (n=23/2). Double asterisks denote P<0.01. All tests were two-sided t-tests.

In PCs that were identified to be related to VOR-adaptation by their response to motion around the vertical axis in space, we again found a significant increase in SS irregularity (CV: WT, 0.39±0.07; *L7-Shank2*$^{-/-}$, 0.53±0.08; P<0.0001; CV2: WT, 0.39±0.07; *L7-Shank2*$^{-/-}$, 0.52±0.08; P<0.0001), while their overall firing frequency was unaffected (WT: 68.2±15.0 Hz; *L7-Shank2*$^{-/-}$: 69.6±18.8 Hz; P=0.8) (**Fig. 7j-l**). Moreover, *L7-Shank2*$^{-/-}$ showed a bigger difference with WT in SS irregularity in the posterior lobules (40.0% and 30.6% higher CV and CV2, respectively) compared to that in the anterior lobules (4.4% and 9.3% higher CV and CV2, respectively). No significant differences were observed in the duration of the complex spike-induced simple spike pause or the complex spike firing frequency in any of the recorded lobules (P>0.2 in all cases) (**Supplementary Fig. 6**). Together, *L7-Shank2*$^{-/-}$ mice demonstrate the critical importance of *Shank2* in PCs for maintaining SS regularity.

Reduced cognitive functioning in *L7-Shank2*$^{-/-}$ mice

We next examined social and repetitive ASD-like behaviours in the PC-specific *L7-Shank2*$^{-/-}$ mice. The three-chamber social interaction task is a widely used social interaction paradigm for evaluating ASD-like behaviour in mouse models of autism [127, 128]. WT mice exhibited a normal preference for the chamber in which the stranger mouse (S1) was present, compared to the empty chamber (P=0.0002, MWU-test) (**Fig. 8a**). In contrast, *L7-Shank2*$^{-/-}$ mice had no preference for either S1 or the empty chamber (P=0.7, MWU-test) (**Fig. 8b**). Comparing the preference index (stranger-empty) between WT and *L7-Shank2*$^{-/-}$ mice revealed a significantly decreased preference of *L7-Shank2*$^{-/-}$ mice for the stranger mouse

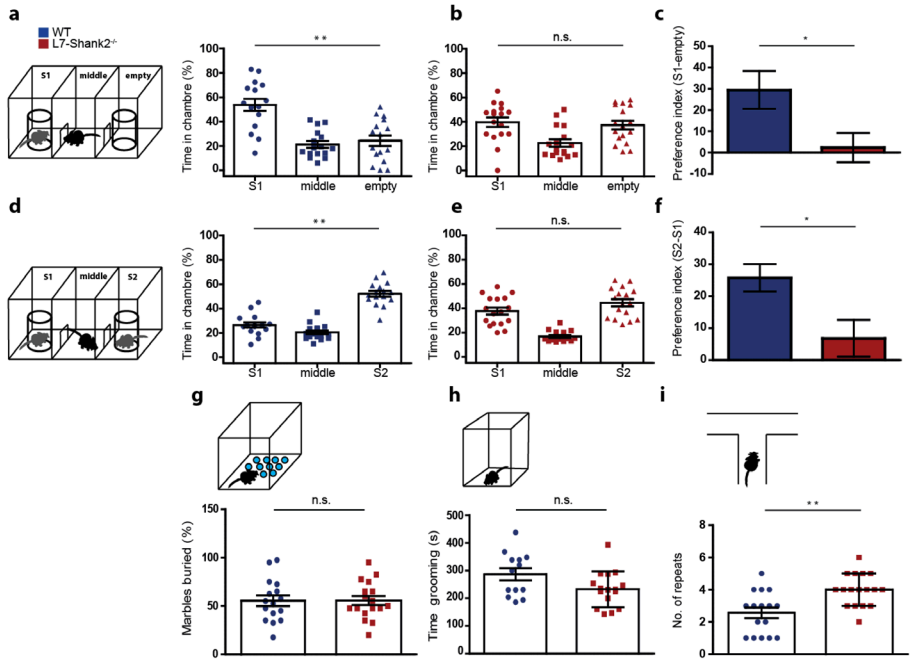

Figure 8. L7-Shank2$^{-/-}$ mice show social impairment and signs of task-specific repetitive behaviour. (A) Three-chamber social interaction evaluated by relative time spent in each chamber. WTs (n=16) prefer to spend time in the room with the stranger 1 mouse (S1), compared to the empty room (P=0.0002, MWU-test). **(B)** This was not the case for L7-Shank2$^{-/-}$ (n=17) mice (P=0.7, MWU-test). **(C)** The preference index (S1-empty) confirms the difference between genotypes (P=0.021). **(D)** Following the introduction of a second stranger (S2), WTs (n=16) prefer to spend time in the chamber with S2 compared to that with S1 (P=0.0001, MWU-test). **(E)** The L7-Shank2$^{-/-}$ mice (n=17) did not show a preference for newly introduced S2 (P=0.1, MWU-test). **(F)** The S1-S2 preference index indicates that WTs prefer S2 more than L7-Shank2$^{-/-}$ do (P=0.013). **(G)** No difference was found in a marble burying task indicative of anxious and/or repetitive behaviour (WT, n=16; L7-Shank2$^{-/-}$, n=17, P=1.0). **(H)** L7-Shank2$^{-/-}$ (n=16) seemed to trend towards less grooming than WTs (n=13) (P=0.054). **(I)** T-maze paradigm showed less consecutive alternations in L7-Shank2$^{-/-}$ (n=17) compared to WT (n=16) (P=0.0023, MWU-test) indicating repetitive decision-making. Data are presented as mean ± SEM. Single and double asterisks indicate P<0.05 and P<0.01, respectively. Two-sided t-tests were used, unless stated otherwise.

(P=0.0213) (**Fig. 8c**), indicating their social interaction deficits. With the introduction of a second stranger in the previously empty chamber, WT mice again demonstrated an increased preference for the novel stranger (S2), this time compared to the familiar mouse (S1) (P=0.0001, MWU-test) (**Fig. 8d**), whereas *L7-Shank2*$^{-/-}$ mice showed no preference for either the familiar or the novel stranger mice (P=0.1, MWU-test) (**Fig. 8e**). Comparing the preference index (S2-S1) between WT and *L7-Shank2*$^{-/-}$ confirmed the impairment of social interaction in *L7-Shank2*$^{-/-}$ mice (P=0.0136) (**Fig. 8f**). Because of previously reported compulsive grooming [128] and jumping [127] in global *Shank2*$^{-/-}$ mice, we next examined

repetitive behaviour. We observed no significant differences between WT and *L7-Shank2*$^{-/-}$ mice in the percentage of buried marbles in the marble-burying task (P=1.0) (**Fig. 8g**) or in the duration of grooming over a 15 min-period (P=0.054) (**Fig. 8h**). However, the *L7-Shank2*$^{-/-}$ mice did show an increase of repetitive behaviour in the T-maze through an increased perseveration, highlighting a reduction in cognitive flexibility (P=0.0023, MWU-test) (**Fig. 8i**). Finally, we observed no significant difference in anxiety (P=0.7, χ^2-test) or olfactory sensitivity (P=0.6) of *L7-Shank2*$^{-/-}$ mice that could have potentially biased the social behaviour assessments (**Supplementary Fig. 7**). Together, these results indicate that *L7-Shank2*$^{-/-}$ mice exhibit ASD-like social impairments and task-specific repetitive behaviour.

Discussion

Severe loss-of-function mutations in *SHANK2* have been firmly established as conferring a high genetic risk for ASD and intellectual disability [156, 158, 162]. Children with disruptive *SHANK2* mutations exhibit motor impairments, language delay and cerebellar dysfunction including dysmetria and dysdiadochokinesis [162]. Considering the increasing evidence for cerebellar involvement in ASD [171], we investigated anatomical, molecular and physiological consequences of global *Shank2* ablation in the cerebellum. In addition, we analyzed *L7-Shank2*$^{-/-}$ mice with cerebellar PC-specific deletion of *Shank2* to evaluate the extent to which the ASD-related behavioural findings in global *Shank2*$^{-/-}$ mice can be attributed to cerebellar dysfunction.

In recent years, several genetic mouse models for ASD have been used for the study of cerebellar abnormalities. The first study to implement a Purkinje cell-specific model related to ASD involved the deletion of FMR1, the fragile X mental retardation 1 protein [66]. In this study, the authors reported eye-blink abnormalities and increased LTD in both global and Purkinje cell-specific deletion of FMR1. Furthermore, global Nlgn3-KO mutants exhibited deficits in cerebellum-related motor performance as assessed by the ErasmusLadder [108]. A more recent model examining the 15q11-13 duplication ASD syndrome demonstrated impaired cerebellar synaptic plasticity and motor learning deficits as assessed by eye-blink conditioning [93]. Perhaps the most definitive study implicating cerebellar dysfunction as etiologic for ASD-like behaviour involved a Purkinje cell-specific deletion of *Tsc1* [99]. This study was the first to demonstrate that Purkinje cell-specific deletion of an ASD-associated gene results in ASD-like behaviour. Finally, a very recent study using multiple mouse models of syndromic ASD found a consistent pattern of

impaired sensorimotor integration [172]. These studies have established the foundation by which the cerebellar synaptic pathophysiology underlying ASD can be mechanistically investigated [154].

Given the general importance of *Shank2* in the regulation of neuronal plasticity [127, 128], we investigated both synaptic and intrinsic plasticity of cerebellar Purkinje cells **(Fig. 4)**. Our results indicate that *Shank2* is crucial for PF-PC LTP, but not LTD. Additionally, we show that *Shank2* is important for intrinsic plasticity of neuronal excitability [26]. In contrast to a recent study of the 15q11-13 duplication ASD syndrome in which PC synaptic plasticity deficits were limited to LTD [93], our results now highlight LTP impairments as a candidate mechanism underlying the cerebellar pathophysiology of ASD. *Shank2* is a dedicated scaffolding protein, which has a major role in the regulation of glutamate receptor integration, synaptic transmission and plasticity [153, 173]. Future molecular and functional studies will have to elucidate the exact mechanisms by which *Shank2* mediates plasticity in the Purkinje cell, but it may well include a suboptimal integration of GluR subunits as the expression levels of GluA1 and GluA2 were both reduced in the *Shank2*$^{-/-}$ mice. Since GluR subunit levels were analysed in synaptosomes from whole cerebella, it remains to be further investigated to what extent these changes are limited to the PF to PC synapse.

Because of the cerebellar physiological impairments and the previously reported motor hyperactivity in *Shank2*$^{-/-}$ mice [127, 128], we examined activity levels during both baseline exploration and motor learning. To our surprise we did not find motor performance abnormalities in the PC-specific *L7-Shank2*$^{-/-}$ mice during various assessments including five separate locomotion and eye movement tests (**Supplementary Fig. 2**). However, we did observe substantial impairments of cerebellar motor learning including conditioning of locomotion and eyeblink responses as well as adaptation of compensatory eye movements (**Fig. 6**). It might seem counterintuitive that baseline motor performance can be intact while the capacity for motor learning is reduced, but this combination has been observed in many different mutant lines over the last few decades [174]. Most likely, it reflects the indispensable role of PC plasticity for the acquisition of new behaviours within relatively short periods of time as occurs during the experimental training paradigms (i.e. in the order of hours) and the ability of the motor performance control system to compensate upstream and/or downstream of the affected synapse when prolonged adaptation periods are available as occurs during postnatal development (i.e. in the order of weeks) [175]. The potential causality of the identified electrophysiological abnormalities as underlying the

motor learning impairments is strengthened by our independent findings in another Purkinje cell-specific mouse mutant (L7-PP2B$^{-/-}$), in which also both synaptic LTP and intrinsic plasticity were affected [165]. Together, these phenotypes point towards a PC-dependent contribution to the behavioural motor impairments frequently observed in ASD.

In addition to changes in plasticity, we also found that inhibition of PCs was enhanced in the global *Shank2*$^{-/-}$ mutants. Since reduced inhibition of PCs increases regularity of SS activity [166], we hypothesized that PCs of the global *Shank2*$^{-/-}$ mutants should have a higher level of irregularity of SS firing **(Fig. 3)**. Indeed, this hypothesis was not only consistent with the *in vivo* extracellular recordings in lobule X of the global *Shank2*$^{-/-}$, but also confirmed in three different areas (Lobules I-V, Lobules IX-X and the flocculus) of the *L7-Shank2*$^{-/-}$ mice (**Fig. 7**). Moreover, this correlation was also in line with the fact that the differences in sIPSCs, CV and CV2 had bigger effect sizes in the posterior lobules than the anterior lobules.

The increased frequency of inhibition in the global *Shank2*$^{-/-}$ did not occur concomitantly with increased amplitude of sIPSCs in PCs, indicating that the observed effect could be of pre-synaptic origin. The PC irregularity in the *L7-Shank2*$^{-/-}$ would then have to originate from a pre-synaptic effect of the postsynaptic absence of *Shank2*. Indeed, recent evidence indicates the possibility of Shank-mediated transsynaptic signalling through transmembrane proteins affecting both post and pre-synaptic processes important for vesicle release probability [176]. This type of transsynaptic signalling could manipulate the inhibitory input to PCs either directly or indirectly, e.g. through altered glutamate spillover from the climbing fiber to Purkinje cell synapse [177]. Future research aimed at pinpointing the sites relevant to the effects described above should thus focus not only on Purkinje cell specific mouse mutants, but also on those in which their afferents are specifically affected [178, 179]. In doing so, important consideration in studies implementing cell-specific deletions should be given to germline analyses, given the sensitivity of the *L7*-cre [99, 180] and *Shank2* lines (Supplementary Table 1) [181, 182].

We observed a significant decrease in SS frequency in the anterior lobules of global *Shank2*$^{-/-}$ mice, but not in their posterior lobules, nor in the anterior or posterior lobules of *L7-Shank2*$^{-/-}$ mice. We believe that this inconsistency may reflect the fact that the spontaneous SS firing frequency of PCs is probably largely due to their intrinsic properties rather than the synaptic efficacy of their inhibitory or excitatory inputs [10]. Indeed, blocking inhibitory or excitatory synaptic input to PCs by deleting their GABA-A-gamma2 receptor-

subunits or abolishing voltage gated calcium channels at their parallel fiber input primarily affects the regularity of SS firing, rather than their firing frequency [166, 179]. Thus, the consistent irregularity of SS in PCs, particularly in the posterior lobe, of the *Shank2*$^{-/-}$ mutants underlines the putative importance of precise SS regularity for behavioural output [174]. Although abnormalities in the anterior and posterior lobules have both been proposed as relevant sites of cerebellar pathology in ASD [183], our converging data obtained in the posterior lobe suggest that the mechanisms governing the regularity of SS firing reveal a common biological vulnerability in the etiology of ASD.

Here, we report impaired social and task specific repetitive behaviour due to the Purkinje cell-specific deletion of *Shank2* (**Fig. 8**). This result is particularly interesting as, to our knowledge, it is the first Purkinje cell-specific mouse model for a non-syndromic form of autism in which ASD-like behaviour has been established. The impaired social behaviour, late-onset ataxia and reduced excitability of Purkinje cells previously observed in L7-Tsc1 mice [99] were due to the absence of a protein that inhibits mTOR signalling through which the translation of a wide variety of proteins is regulated. In contrast, we here show that disruption of the synapse through the absence of a single postsynaptic scaffolding protein in the Purkinje cell is sufficient to show impaired ASD-related motor learning and social behavioural impairments. In addition to the social impairments, we found signs of enhanced repetitive behaviour in the T-maze paradigm, but not the marble burying task or grooming tasks. Since the T-maze task reveals the level of cognitive inflexibility following decision making over consecutive trials rather than the level of repetitious behaviour dominated by high-frequency motor activity that characterizes the other two tasks and that may well be confounded by deficits in cerebellar motor learning, these results highlight the importance of the Purkinje cell synaptic function for ASD beyond the classically ascribed motor-related behaviour.

One of the main challenges remaining is to mechanistically explain the contribution of impaired Purkinje cell physiology to the observed ASD behavioural phenotypes. As previously mentioned, the Shank family of postsynaptic scaffolding proteins has many different interacting proteins in the postsynaptic density through which they could contribute to the functional establishment of regulatory mechanisms for plasticity. The translational challenge from synapse to behaviour brings about two main questions: How does an impaired Purkinje cell mediate ASD-related behaviour? And how might Purkinje cell impairments lead to abnormal brain function beyond the cerebellum with regards to neurodevelopmental critical periods? The first question has been extensively addressed by

the accumulating evidence regarding the contribution of ASD-related cerebellar dysfunction to impaired motor learning, as apparent from the eye movement adaptation, ErasmusLadder, and eyeblink conditioning findings examined here and by other investigators [172]. It is indeed possible that the increased inhibition and irregularity of SS firing, in addition to impaired cerebellar plasticity mechanisms, may contribute to social and repetitive behaviour-related phenotypes in ASD. We believe that the answer to how the cerebellum can essentially contribute to socially impaired behaviour could reside in various mechanisms. The idea that disruption of a certain brain area during development could affect the development and consequently the function of other inter-connected areas, also termed developmental diaschisis, has recently been put forward as a prime mechanism for the cerebellum in its ability to influence other cortical areas in critical developmental periods [57]. In the future, the latter hypothesis can for example be tested with Purkinje cell specific *Shank2* ablation at different stages during development using inducible mouse models, as has recently been employed for other ASD-related genes [125, 184]. These experiments will help to further elucidate the mechanisms by which differential genes, such as *Shank2*, regulate cerebellar function and ultimately ASD-like behaviour.

Methods

Experiments and analyses were performed with the experimenters blinded to the genotype. Mice used were global germ-line *Shank2*$^{-/-}$ and their littermate WTs all bred on a mixed C57BL6/N and C57BL6/J background. The generation of these mice has previously been described in detail [127, 128]. The *L7-Shank2*$^{-/-}$ was generated by crossing Purkinje specific L7(Pcp2)-Cre [180] with *Shank2*$^{flxd/flxd}$ [128]. Genotyping was performed on postnatal day (P)7-10 using primers 1700 S (TCCATGGTT TCGCGAGAGCG), 1842 AS (TCCCTATTGGGACGCAGTGG) and 2394 AS (CAGCATCATGACAATGTCTCCA). For all experiments we used mice from both genders, unless indicated otherwise. The mice were individually housed with food and water available *ad libitum* and in 12:12 hrs light/dark cycles. All experiments were approved by local and national ethical committees.

Primary antibodies

The anti-*Shank2* SA5193 antibody has been characterized previously [128] the following antibodies were from commercial suppliers: anti-GluA1 (Cat. No. 182 003), anti-GluA2 (Cat. No. 182 103), anti-Nlgn3 (Cat. No. 129 113) (all Synaptic Systems, Goettingen, Germany), anti-β3-Tubulin (Cat. No. MRB-435P) (Covance, Brussels, Belgium) and Aldolase C (Cat. No. 12065) (Santa Cruz, Dallas, U.S.A.)

Golgi stainings

Adult mouse cerebella were dissected and prepared using the FD Rapid GolgiStain Kit (NeuroTechnologies, Vilnius, Lithuania). Serial coronal sections of 150 µm were collected from WTs and global *Shank2*$^{-/-}$ mice and Z-stack images were taken using an upright Axioscope (Carl Zeiss, Jena, Germany). Distal dendrites of Purkinje cells were traced for spine analysis.

Electron microscopy

Adult mice were transcardially perfused with fixative (2 % paraformaldehyde, 2.5 % glutaraldehyde, 1 % saccharose in 0.1 M cacodylate buffer, pH 7.3) and their cerebella were dissected and post-fixed overnight at 4 °C. After dehydration and staining with 2 % uranyl acetate, the material was embedded in epoxy resin. Ultrathin sections were cut using an ultramicrotome (Ultracut UCT, Leica). After lead citrate staining, sections from WTs and global *Shank2*$^{-/-}$ mice were examined using an electron microscope (JEM 1400 TEM, Jeol). For ultrastructural PSD analysis, spine synapses have been selected in the distal molecular layer where the parallel fiber-Purkinje cell (PF-PC) contacts greatly outnumber other types of synapses.

Biochemistry

Adult mouse cerebella were homogenized on ice in HEPES-buffered sucrose (320 mM sucrose, 5 mM HEPES, pH 7.4) containing protease inhibitor mixture (Roche, Mannheim, Germany). The homogenate was centrifuged (1.000 x g, 4 °C) to remove cell debris and nuclei. The supernatant was further centrifuged (12.000 x g, 4 °C) to obtain a pellet containing the cerebellar synaptosomes. Equal amounts of 10-20 µg protein per lane were separated by SDS-polyacrylamide gel electrophoresis and blotted onto polyvinylidene fluoride membranes using standard protocols. After incubation with primary antibodies (1:1.000 for anti-Shank1, anti-GluA1, anti-GluA2, anti Nlgn3; 1:10.000 for anti- β3-Tubulin), immunoreactivity was visualized on X-ray film (GE Healthcare, Freiburg, Germany) using HRP-conjugated secondary antibodies (Dako; Hamburg, Germany) and the SuperSignal detection system (Thermo Scientific). For quantification, the films were scanned, the grey value of each band was analysed by ImageJ (National Institutes of Health, Bethesda, MD, USA) and normalized to the grey value of β3-Tubulin.

Immunohistochemistry

Mouse brains were snap-frozen after removal without perfusion. Tissue was sectioned at 7 µm using a cryostat at -20°C and a knife temperature of -14°C. Sections were air-dried on superfrost glass and stored at -80°C. For staining sections were defrosted at room temperature (RT) for 60 min and subsequently washed with -20°C MeOH for 3 min followed by 3X 10 min of PBS wash. To permeabilize membranes, sections were incubated for 60 min in 0.5% Triton X-100 in PBS at RT and washed 3X in PBS for 10 min. Following a 60 min incubation in 5% BSA (in PBS) at RT and subsequent PBS washing, sections were incubated in SA5193 antibody (1:1000, dissolved in 2% bovine-serum albumin, see [168]) O/N at 4°C. The sections were then washed for 3X 10 minutes in PBS followed by 120 min of fluorescent antibody staining (1:200, Donkey anti goat-Cy3) in 2% BSA at RT. After the fluorescent antibody a wash of 3X 10 min of PBS was followed by 2X 10 min wash with PB. The sections were then put for 10 min in DAPI (200 µl in 50 ml 0.1 M PB). This was concluded by a 2x 10 min PB wash. For Zebrin (Adolase C) we used a different approach after the defrosting of sections at RT. These slices were washed with 10 min 4% PFA followed by 20 min of methanol and subsequently by 2 min PBS and 30 min 100 ml PBS (with 2 ml 30% H_2O_2 + 0.8 ml sodium azide). Here after a wash of 2 min PBS and 2X 2 min in PBS (with 1 L PBS, 5 g protifar and 1.5 g glycine, sections were incubated in the primary antibody for Adolase C (1:1000; Santa Cruz, Dallas, U.S.A., Cat. No. 12065) O/N at 4°C. The sections were then washed for 3X 10 minutes in PBS followed by 90 min of fluorescent antibody staining (1:200, donkey anti goat-Cy3; The Jackson Laboratory, Sacramento, U.S.A., Cat. No 705-165-147) in 2% BSA at RT. After the fluorescent antibody a wash of 3X 10 min of PBS was followed by 2X 10 min wash with PB. The sections were then put for 10 min in DAPI (ThermoFisher Scientific, Waltham, U.S.A., Cat. No. D3571; 200 µl in 50 ml 0.1 M PB). This was concluded by a 2X 10 min PB wash. Following PBS washing, the sections were thionin-stained and permount-covered using standard protocols. All immunohistological stainings have successfully been replicated on multiple occasions.

Ex vivo electrophysiology

Following decapitation of mice under isoflurane anaesthesia, the cerebellum was removed into an ice-cold 'slicing medium', containing (in mM) 240 sucrose, 2.5 KCL, 1.25 Na_2HPO_4, 2 $MgSO_4$, 1 $CaCl_2$, 26 $NaHCO_3$ and 10 D-Glucose, that was carbogenated continuously (95% O_2 and 5% CO_2). Sagittal slices, 250 µm thick, of the cerebellar vermis were cut using a vibrotome (VT1200S, Leica) and put in carbogenated artificial cerebrospinal fluid (ACSF) containing (in mM): 124 NaCl, 5 KCL, 1.25 Na_2HPO_4, 2 $MgSO_4$, 2 $CaCl_2$, 26 $NaHCO_3$ and 20 D-Glucose, for at least one hour at 34±1°C before the start of the experiment. Slice

physiology was done at room temperature 21±1°C or 33±1°C as indicated in the results section and in the presence of 100 μM picrotoxin except for the sIPSCs recordings. Whole-cell patch clamp recording were performed with an EPC9 amplifier (HEKA Electronics, Lambrecht, Germany). Recordings were excluded if the series (Rs) or input resistances (Ri) changed by more than 15% during the experiment, which was determined using a hyperpolarizing voltage step relative to the -65 mV holding potential. Data analysis (rise times (10-90% for EPSC and action potentials)), decay time (tau) for EPSC and IPSC amplitudes, action potential threshold (identified by steepest slope in membrane potential prior to action potential) and AHP amplitude (minimal membrane potential relative to the action potential threshold)) was performed using Clampfit software (Molecular Devices).

For whole-cell recordings Purkinje cells (PCs) were visualized using an upright microscope (Axioskop 2 FS, Carl Zeiss) equipped with a 40X objective. Recording electrodes (3-5 MΩ, 1.65 mm OD and 1.11 mm ID, World Precision Instruments, Sarasota, FL, USA) were filled with an intracellular solution containing (mM): 120 K-Gluconate, 9 KCL, 10 KOH, 4 NaCL, 10 HEPES, 28.5 Sucrose, 4 Na_2ATP, 0.4 Na_3GTP (pH 7.25-7.35 with an osmolarity of 295±5). Note that we adjusted the osmolarity using sucrose [25, 26]. For the recording of sIPSCs we used an intracellular solution containing (mM): 150 CsCl, 1.5 $MgCl_2$, 0.5 EGTA, 4 Na_2ATP, 0.4 Na_3GTP, 10 HEPES, 5 QX314 (pH 7.25-7.35 with an osmolarity of 295 ± 5). For extracellular stimulation of parallel fibers (PFs), similar patch electrodes were filled with ACSF and positioned in the upper third of the molecular layer lateral to the patched Purkinje cell. The stimulation intensity was set to evoke an EPSC of 300±50 pA (typically 3-6 μA stimulation intensity). For PF-PC transmission we used various inter-stimulus intervals (50-200 ms) (see Fig. 2). For recordings of spontaneously occurring IPSCs (sIPSCs) we used the previously mentioned K^+-based internal and recorded their occurrence during at least 120 s.

For climbing fiber stimulation similar electrodes (filled with ACSF) were positioned near the patched Purkinje cell soma in the surrounding granule layer. We selected those recordings in which climbing fiber stimuli elicited clear all-or-none responses and lacked the co-activation of Purkinje cell axons (identifiable by backpropagating action potentials) for further analysis. For CF elimination experimental tissue was prepared in a similar way for all age groups. We systematically scanned the granule cell layer to elicit CF responses and recorded PC responses (using an intracellular solution containing (in mM): 115 $CsMeO_3$, 20 CsCl, 2.5 $MgCl_2$ 10 HEPES, 0.6 EGTA, 4 Na_2ATP, 0.4 Na_3GTP, 10 Na-phosphocreatine) at -20 mV holding potential to prevent voltage escape during the CF-

responses. For CF-PC transmission we evaluated the paired pulse ratio at 50 ms stimulus interval. To evaluate the complex spike waveforms we analysed the amplitude of the Na^+-spike and the amplitude of the first Ca^{2+}-spikelet evoked during the LTD-tetanus [185]. Current clamp recordings were corrected off-line for the calculated liquid junction potential (-10.2 mV).

The synaptic (LTP, LTD) and intrinsic plasticity protocols were recorded from lobules 5/6 and conducted as described previously [26, 165]. In short, for synaptic plasticity all recordings were done in voltage-clamp, except for the tetanus, which consisted of single-pulsed PF-stimulation at 1 Hz for 5 min (LTP) or single-pulsed PF + single-pulsed CF stimulation (5 ms interval) at 1 Hz for 5 min (LTD). We evaluated the synaptic plasticity by the change in PF-EPSC (presented at 0.05 Hz) relative to the mean value calculated during the last 5 min pre-tetanus. For intrinsic plasticity we utilized the PF-LTP tetanus (but without bias currents, i.e., I=0 pA) and evaluated the impact on the number of action potentials evoked by 300 pA current injections during 500 ms (presented at 0.05 Hz).

Extracellular Purkinje cell recordings

In vivo recordings were performed as recently described [10]. An immobilizing pedestal was fixed on the skull and a craniotomy (Ø 3 mm) was performed on the occipital bone. After recovery of 5 days, mice were head-fixed and body restrained for recordings. Single unit recording was identified by the presence of a short simple spike pause (>6 ms) after each complex spike. Purkinje cells were recorded from vermal lobules I-V and X using single barrel (2.0 mm OD, 1.16 mm ID, Harvard Apparatus, MA, USA) and double barrel (theta septum, 1.5 OD, 1.02 ID; World Precision Instruments) boroscilate glass pipettes. *In vivo* recordings were analysed offline using Spiketrain (Neurasmus BV, Rotterdam, The Netherlands, **www.neurasmus.com**) and custom scripts in MatLab (Mathworks, Natick, MA, USA). The CV is calculated by dividing the SD by the mean of the interspike intervals, whereas CV2 is calculated as $2 * |ISIn+1 - ISIn| / (ISIn+1 + ISIn)$.

Compensatory eye movements

Mice between 8 and 10 weeks of age were prepared for head-restrained recordings of compensatory eye movements. These types of recordings have been described in detail previously [165]. In order to head restrain the mice during the eye movement task, a small pedestal was attached using Optibond primer and adhesive (Kerr, Bioggio, Switzerland) under isoflurane anaesthesia in O_2 (induction with 4% and maintained at 1.5%

concentration). After a recovery period of two to three days, mice were head-restrained by fixation using the pedestal in the experimental setup. A round screen with a random dotted pattern ('drum') surrounded the mouse during the experiment. The optokinetic reflex (OKR), vestibulo-ocular reflex (VOR) and the light-guided vestibulo-ocular reflex (VVOR) were induced using a sinusoidal rotation of the drum in light (OKR), rotation of the table in the dark (VOR) or the rotation of the table (VVOR) in the light. The motor behaviour was assessed by rotating the table and/or drum at 0.1 to 1 Hz with a fixed 5° amplitude. In order to evaluate motor learning, a mismatch between visual and vestibular input was created. Rotating both the visual and vestibular stimuli in phase (at the same amplitude) induced a decrease of gain; rotating the drum at greater amplitude relative to the table induced the so-called phase reversal of the VOR (day 1, 5° phase difference; day 2, 7.5°; day 3-4, 10°). Rotating the visual and vestibular stimuli out of phase (at the same amplitude) induced the VOR gain increase. All training protocols were induced at 0.6 Hz with table rotation amplitude of 5°. For eye illumination during the experiments two table-fixed infrared emitters (output 600 mW, dispersion angle 7°, peak wavelength 880 nm) and a third emitter, which produced the tracked corneal reflection (CR), were mounted to the camera and aligned horizontally with the optical axis of the camera. Eye movements were recorded with eye-tracking software (ETL-200, ISCAN systems, Burlington, NA, USA). Gain and phase values of eye movements were calculated using Matlab (MathWorks).

Eyeblink conditioning

Mice of 12-15 weeks of age were prepared for head-restrained eyeblink conditioning [109]. In short, a small brass pedestal was attached to the skull using Optibond primer and adhesive (Kerr) and Charisma (Heraeus Kulzer, Armonk, NY, USA), under isoflurane anaesthesia. Three to five days after surgery, mice were habituated during two short (30-45 min) sessions on two days in a sound- and light-isolating chamber which houses the eyeblink set up. During these sessions mice were head-fixed and suspended over a foam cylindrical treadmill. While no stimuli were presented, a 27.5 gauge needle through which US air-puffs are delivered was positioned at 5 mm from the center of the left cornea, a green LED (ø 5 mm) that delivers the CS was placed 5 cm in front of the mouse, and an GMR magnetometer (NVE, Eden Prairie, MN, USA) was fixed above the left eye. During five subsequent acquisition training days, this sensor measured the distance of a miniscule magnet (1.5x0.7x0.5 mm) that was placed on the left lower eyelid with high accuracy, while 200 paired trials were presented, usually spaced 10 ± 2 s apart, plus the time needed for a sporadic unstable eyelid to stabilize in open position. Each paired trial consisted of a 280 ms

green LED CS, co-terminating with a 30 ms airpuff (30 psi, through an MPPI-3 pressure injector; ASI, Eugene, OR, USA). All experiments were performed at approximately the same time of day by the same experimenter. Individual eyeblink traces were analyzed using custom LabVIEW (National Instruments, Austin, TX, USA) or MATLAB (Mathworks, Natick, MA, USA) scripts. Trials with significant activity in a 500 ms pre-CS baseline period were regarded as invalid for further analysis. Valid trials were aligned by making the mean of their baseline activity zero, and the average amplitude of all post-US unconditioned blink responses was used to denote 100% eyelid closure. From this, the average eyelid closure as a percentage from baseline to full closure at the end of the CS-US interval was calculated over all valid trials. To calculate percentage of CRs, trials were judged to contain a CR if the eye closed for more than 5% between 50-250 ms after CS and the CR reached its peak after 100 ms.

ErasmusLadder

The ErasmusLadder (Noldus, Wageningen, Netherlands) is a fully automated system consisting of a horizontal ladder between two shelter boxes. It has 37 rungs on each side, spaced 15 mm apart, and attached to custom-made pressure sensors that are continuously monitored. In order to create a left-right alternating pattern, even rungs on one side and odd rungs on the other side are elevated by 6 mm. Prototype testing revealed that optimum forepaw displacement for mice is about 6 cm in a single step at medium high velocity, which is the distance between 3 consecutive elevated rungs and is defined as efficient step in the text (for more details, see [169]). It is clear from previous studies that mice improve their walking efficiency over training sessions by increasing the number of efficient steps relative to steps of lower sizes [169]. In the current study, mice (male, 15-18 weeks old) were tested in 6 daily sessions consisting of 2 unperturbed sessions, 1 session with a fixed obstacle in the middle of the ladder and 3 perturbed sessions. During the first three sessions, mice were trained to walk between two shelter boxes for 50 trials each day. In the perturbed sessions, a sudden appearance of a rising rung on the right side of the mouse was used as the unconditional stimulus (US). A 15 kHz tone was used as the conditional stimulus (CS) and preceded the US by 200 ms in CS-US paired trials. CS-only trials and paired trials were randomly distributed among 50 trials. There were twice as many paired trials as CS-only trials. Step length and step time were defined as the distance and time between two consecutive touches from the right front limb. To estimate motor adaptation in CS-only trials, we calculated step speed (step length/step time) using only the steps

within 1 s before and 1 s after the CS. The speed ratio during conditioning was defined as the speed post-CS divided by the speed pre-CS.

General behavioural analyses

Behavioural experiments were performed using *L7-Shank2*$^{-/-}$ and WT littermate controls aged 8-16 weeks during the light period of their diurnal cycle. The mice used in the general behavioural experiments described here underwent multiple tests.

For the PhenoTyper test, mice were placed in a homecage-like apparatus (Noldus) with *ad libitum* access to food and water, and left to explore for 30 minutes. Locomotion was recorded using the automated software Noldus Ethovision XT 11 and distance and speed were calculated.

For the open field test, mice were placed in a novel circular, brightly-lit 110-cm-diameter open arena for 10 min. Locomotion was recorded using the automated software Noldus Ethovision XT 11 and total distance travelled, as well as average speed were calculated. During analysis the arena was subdivided in three concentric zones named the inner (25 cm), middle (15 cm) and outer zone (15 cm), and percentage of time in each zone was calculated.

For the three-chamber social interaction test, age and gender-matched WT target subjects (Stranger 1 and 2) were habituated for 5 consecutive days before beginning of testing by being placed inside round metal-wired cages. On the test day, experimental mice were placed in the central chamber of a clear Plexiglas box (60 x 35 cm) divided into three interconnected chambers. After habituation for 5 min. an unfamiliar mouse (Stranger 1; S1) was introduced into a wire cage in one of the side-chambers and an empty wire cage in the other side-chamber. The dividers were then raised and the test mouse was allowed to freely explore all three chambers over a 5-minute session. Next, the mouse remained in the chamber with stranger 1 for an additional 5–minute session. Subsequently, a novel stranger mouse (Stranger 2; S2) was placed in the previously empty wire cage and again the test mouse was left to explore for 5 min. Time spent in each chamber, as well as overall locomotion, was calculated using the automated software Noldus Ethovision XT 11. Preference indices were calculated by subtracting the time spent with the empty wire cage from the time spent with stranger 1 (S1 – E), and subtracting the time spent with stranger 1 from time spent with stranger 2 (S2 – S1).

For the T-maze spontaneous alternation test, mice were placed at the base of a T-maze (arm length 50 cm) and were given the choice to freely explore either the right or left arm of the maze for 10 consecutive trials. A choice was assumed to be made when mice stepped into an arm with all four paws. At that moment the gate to that arm was closed and the animal was allowed to explore the arm for 5 s. Then, the mouse was gently placed back at the base of the T-maze for the next trial. When the mouse chose a similar arm at two consecutive trials, this was scored as number of repeats, indicative of repetitive behaviour.

For the grooming test, mice were removed from their homecage, received a single puff of water spray and placed in clean transparent cages (15 x 15 x 20 cm) under bright light for 15 min. Behaviour was recorded with a high-speed camera (30Hz full frame rate), and time spent grooming was scored by two independent raters. All types of grooming – paw licking, nose and head self-grooming, body grooming, leg grooming and tail/genital grooming – were scored.

For the marble burying test, Makrolon cages (50 x 26 x 18 cm) were filled with 4 cm of bedding material and 20 glass marbles, which were arranged in an equidistant 4 x 5 grid. Animals were given access to the marbles for 30 min. Marbles 100% covered by bedding were scored as buried and marbles covered partially contributed 50% to the total score.

For the olfactory test, a piece (1.25 g) of cookie was put into the subject's cage each day for three consecutive days, and checked for complete consumption the following day. For 24 hrs before the test phase, mice were completely food-deprived. Subjects were placed in a clean Makrolon cage (50 x 26 x 18 cm) with 4 cm of clean bedding, and allowed to habituate for 5 min. Then, a piece of cookie (1.25 g) was hidden in a random corner in the cage at 1 cm depth. Latency to find the cookie was recorded for a maximum of 15 mins (900 s).

Data analysis

In the text, mean ± SD values are presented, in the figures SEM-values are reported, and p-values smaller than 0.05 are considered significantly different. Two-sided Student's *t*-tests were performed, unless stated otherwise. For a complete representation of the data we have included a detailed overview of all statistics in Supplementary Table 1. Additionally, since the L7-Cre line was shown to reveal germline deletions (see also [44]) and since the potential impact of cerebellar Purkinje cells on general cognitive tests is widely

debated[186, 187], we have checked for heterozygous germline deletions in our L7-Shank2 mice and statistically excluded the possibility they could have influenced our conclusions on the non-cerebellar paradigms (Supplementary Table 1).

Supplementary Figures

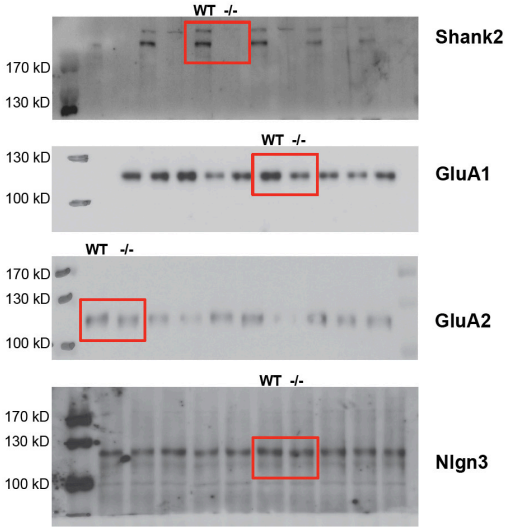

Supplementary Figure 1 Full western blots with size markers.

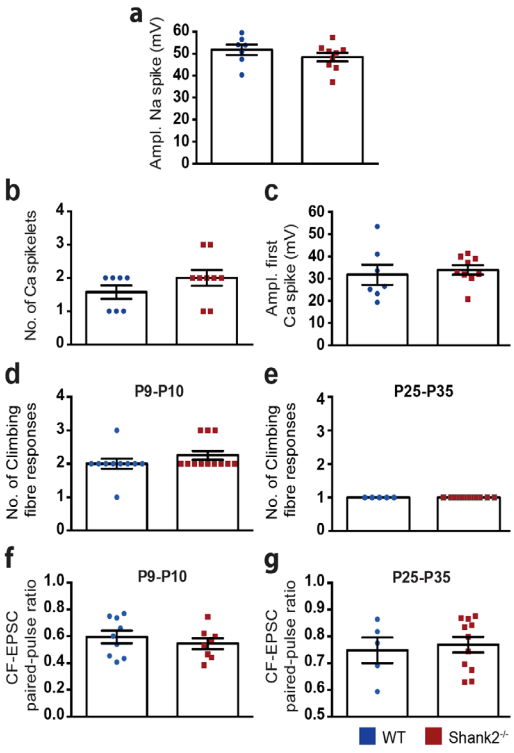

Supplementary Figure 2 Ex vivo climbing fibre activity shows no significant differences between Shank2-/- and WT mice. (a-c) No difference in Na spike amplitude (P=0.3) (a), nor in number of Ca spikelets (P=0.2) (b) or amplitude of the first Ca spike (P=0.7) (c), between WT (n=7/6) and Shank2-/- (n=9/4). (d,e) Number of climbing fibre responses was similar between Shank2-/- and WT mice at P9-10 (WT, n=10/3; Shank2-/-, n=12/3, P=0.2)) and at P25-35 (WT, n=5/3; Shank2-/-, n=12/3, P=1.0). (f,g) Complex spike paired pulse depression was similar between Shank2-/- and WT mice at P9-10 (WT, n=9/3; Shank2-/-, n=8/3, P=0.5) and at P25-35 (WT, n=5/3; Shank2-/-,n=11/3, P=0.6).Statistical test used was a two-sided t-test unless stated
otherwise.

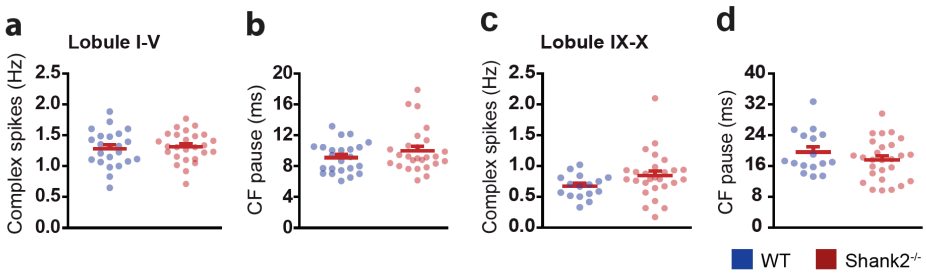

Supplementary Figure 3 In vivo complex spike activity shows no significant differencesbetween Shank2-/- and WT mice. (a,b) Complex spike firing frequency (P=0.7) and CFpause (P=0.2) were not different between Shank2-/- and WT mice in anterior lobules I-V (WT, n=23/3, cells/animals; Shank2-/-, n=26/3). (c,d) Similarly, complex spike firing rate(P=0.1) and CF pause (P=0.2) did not differ between mutant (n=27/3) and WT (n=16/3) in posterior lobules IX-X. Error bars denote SEM. Statistical test used was a two-sided t-test unless stated otherwise.

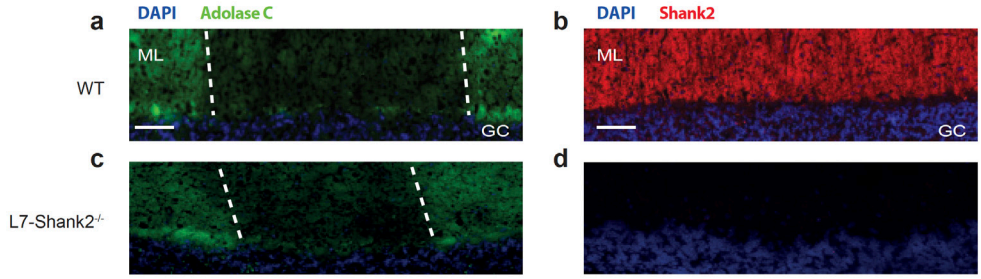

Supplementary Figure 4 Cerebellar Zebrin and Shank2 immunohistology. (a,c) Coronal section of Crus 1 showing distinctive Zebrin patterning in both WT and L7-Shank2-/-. (b,d) Coronal section of Crus 1 showing a uniform presence of Shank2 in WT, but a complete absence of Shank2 in L7-Shank2-/-. Scale bar: 50 µm.

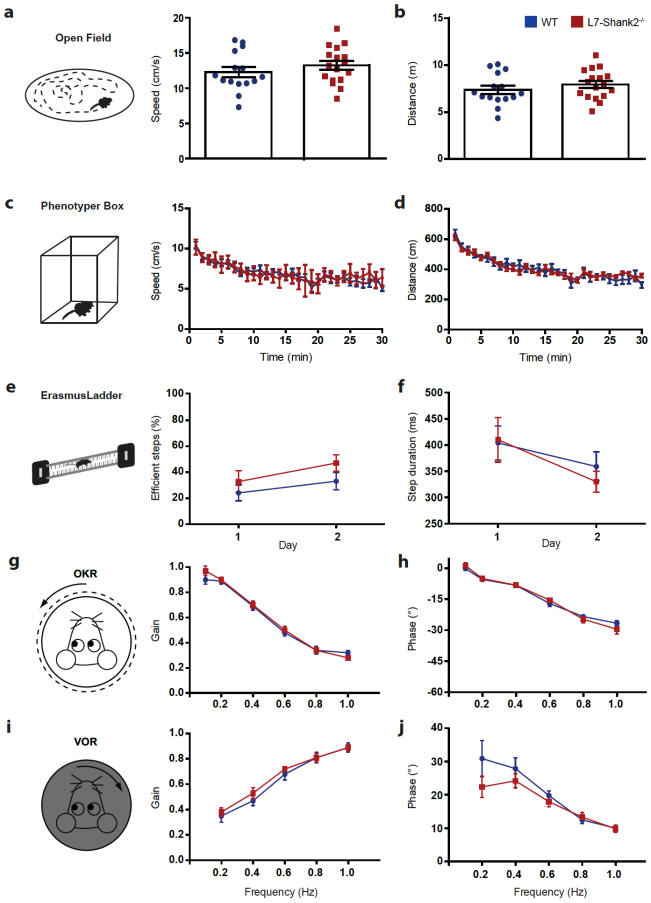

Supplementary Figure 5 L7-Shank2-/- mice have normal basic motor performance. (a) In the open field experiment mice were allowed to move around freely. The speed of movement (P=0.3, t-test) and (b) distance travelled (P=0.3, t-test) during 10 min was not different (WT, n=15; L7-Shank2-/-, n=17). (c,d) These results were confirmed in the phenotyper box for both speed (P=0.5) and distance (P=0.5) (WT, n=16; L7-Shank2-/-, n=16). (e) ErasmusLadder revealed no difference in the percentage of efficient steps (P=0.3) or (f) the duration of these steps (P=0.8) over the course of two days (WT, n=10; L7-Shank2-/-, n=6). (g,h) Optokinetic reflex (OKR) using different frequencies of drum movement revealed no differences in gain (P=0.6) or phase (P=0.9) (WT, n=9; L7-Shank2-/-, n=9). (i,j) Similarly, the vestibulo-ocular reflex (VOR) was not affected in either gain (P=0.4) or phase (P=0.2) (WT, n=8; L7-Shank2-/-, n=9). Data are represented as mean ± SEM. Statistical test used was a repeated-measures ANOVA unless stated otherwise.

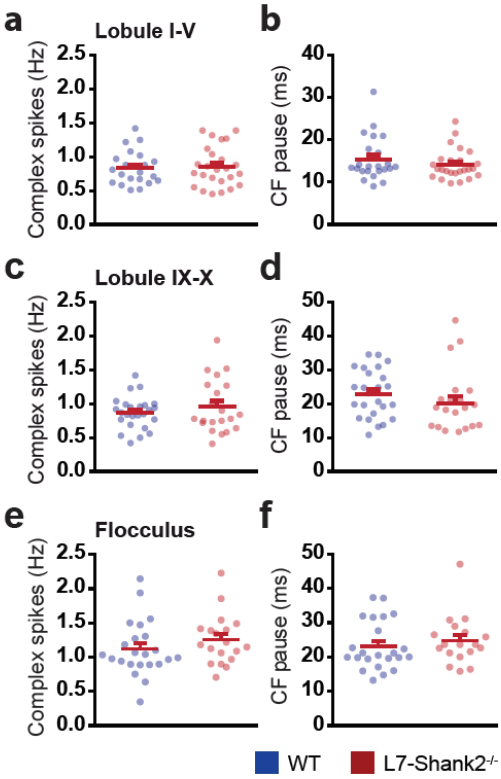

Supplementary Figure 6 In vivo complex spike firing characteristics in L7-Shank2-/- Purkinje cells. (a,b) No significant differences in complex spike firing frequency (P=0.6) or climbing fibre pause (P=0.3) in anterior lobules (I-V) between WTs (n = 23/3, cells/animals)and L7-Shank2-/- mice (n = 25/3). (c,d) Similarly, in posterior lobules IX-X, complex spike firing frequency (P=0.3) and climbing fibre pause (P=0.3) was not different between WTs (n=25/3) and mutants (n=21/3). (e,f) Also located in the posterior cerebellum, Purkinje cells from flocculus showed neither firing rate (P=0.3) nor climbing fibre pause (P=0.5) differences between L7-Shank2-/- (n=19/2) and WTs (n=23/2). Error bars denote SEM. Statistical test used was a two-sided t-test unless stated otherwise.

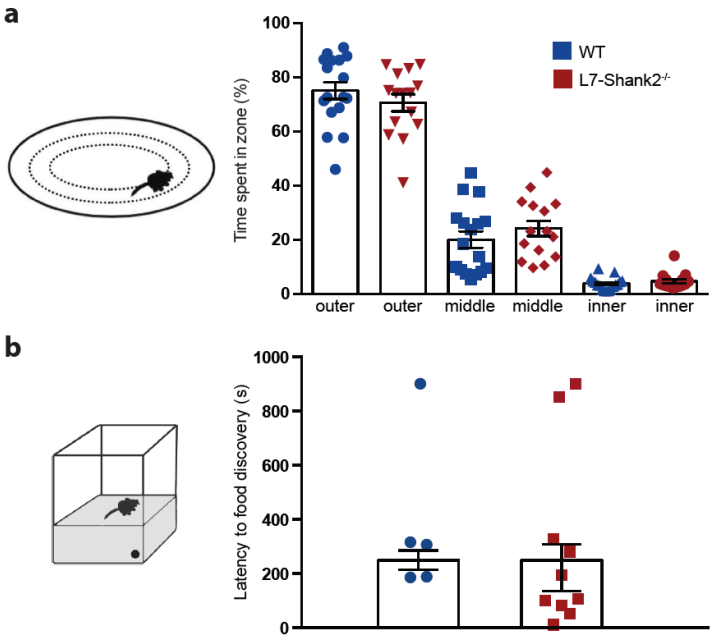

Supplementary Figure 7 (a) In the open field test, WT (n=17) and L7-Shank2-/- mice (n=15) showed no differences (P=0.7, Chi-square) in time spent in the inner, middle, or outer zones. (b) In the olfaction test, WT (n=5) and L7-Shank2-/- mice (n=10) showed no significant differences (P=0.6, t-test) in time taken to find buried food. Error bars denote SEM.

Chapter 2.3

Differential effects of Foxp2 disruption in distinct motor circuits

Catherine A. French *, María F. Vinueza Veloz *, Kuikui Zhou *, **Saša Peter** *, Simon E. Fisher ¶, Rui M. Costa ¶ and Chris I. De Zeeuw

* First-Co-author(s)

¶ Corresponding author(s)

Molecular Psychiatry (2018)

Abstract

Disruptions of the *FOXP2* gene cause a speech and language disorder involving difficulties in sequencing orofacial movements. FOXP2 is expressed in cortico-striatal and cortico-cerebellar circuits important for fine motor skills, and affected individuals show abnormalities in these brain regions. We selectively disrupted *Foxp2* in the cerebellar Purkinje cells, striatum or cortex of mice and assessed the effects on skilled motor behaviour using an operant lever-pressing task. Foxp2 loss in each region impacted behaviour differently, with striatal and Purkinje cell disruptions affecting the variability and the speed of lever-press sequences respectively. Mice lacking Foxp2 in Purkinje cells showed a prominent phenotype involving slowed lever pressing as well as deficits in skilled locomotion. In vivo recordings from Purkinje cells uncovered an increased simple spike firing rate and decreased modulation of firing during limb movements. This was caused by increased intrinsic excitability rather than changes in excitatory or inhibitory inputs. Our findings show that Foxp2 can modulate different aspects of motor behaviour in distinct brain regions, and uncover an unknown role for Foxp2 in the modulation of Purkinje cell activity that severely impacts skilled movements.

Introduction

The discovery that disruptions of one copy of the *FOXP2* gene cause a severe speech and language disorder has generated substantial interest in elucidating the neural functions of the encoded protein. Initial findings came from a large multigenerational family (the KE family) where a heterozygous *FOXP2* mutation was found to be responsible for deficits in many facets of speech and language [188-190]. A number of other familial and *de novo* cases of *FOXP2*-related disorders have since broadened the mutational and clinical spectrum [191-194], but the KE family remains the most well characterised. Affected individuals display wide-ranging impairments in oral and written language, which impact on both receptive and expressive skills. Less severe deficits are evident in aspects of non-verbal cognition [190]. A core phenotype of the disorder is developmental verbal dyspraxia (also known as childhood apraxia of speech), where imprecise and inconsistent neural control of sequences of orofacial movements impedes development of fluent speech [189, 190]. Gross motor functions outside of the orofacial region, such as limb praxis, appear relatively spared, but affected KE family members do also show reduced performance when tapping out rhythms.

FOXP2 is highly conserved in many vertebrates and functions as a transcription factor, modulating expression of target gene networks that regulate processes such as neural development, synaptic plasticity and neurite outgrowth [195-198]. Its expression pattern in the brain is broadly concordant across species and shows some intriguing overlaps with circuits that have known motor-related functions. Most FoxP2 functional studies have been carried out in humans, rodents and songbirds where the protein is found in neuronal subpopulations of the cerebral cortex, basal ganglia and thalamus, as well as in the deep nuclei and Purkinje cells of the cerebellum and the inferior olive of the medulla oblongata [199-201] (here, we use the standard nomenclature FOXP2 for humans, Foxp2 for mice and FoxP2 for other species, or when referring to several species; genes and RNA are italicised). Structural neuroimaging of the KE family uncovered subtle but significant alterations in grey-matter density in affected members in several of these same areas, including the caudate nucleus, ventral cerebellum and inferior frontal gyri [190]. Moreover, functional neuroimaging during language-based tasks showed reduced activation of several brain regions, including Broca's area (left inferior frontal gyrus) and the putamen [202].

Valuable insights have come from Foxp2 mouse mutants and knockouts [141, 203], as well as FoxP2 manipulations in songbirds [141, 204] (Wohlgemuth et al. 2014; Fisher & Scharff 2009). Mice that are homozygous for the KE-family mutation or for knockout alleles show

severe developmental delay, motor dysfunction and postnatal lethality, dying 3-4 weeks after birth [205-207]. These mice also have a disproportionately small cerebellum, with decreased foliation, although cellular organisation is broadly intact [205, 206]. In contrast, mice with heterozygous disruptions develop normally and have no obvious neural pathology. However, they display motor-skill learning deficits on the accelerating rotarod [143, 206] and on a tilted running-wheel system [206]. Studies of mice heterozygous for the KE-family mutation uncovered strongly impaired long-term depression at glutamatergic striatal inputs [206] and abnormally high striatal activity, which is aberrantly modulated as mice learn to run on the rotarod [143]. Interestingly, the males of this mouse line also show altered sequencing of ultrasonic vocalizations [208]. In zebra finches, FoxP2 knockdown in the striatal song nucleus Area X disrupts developmental and social modulation of song variability [209, 210]. Foxp2 function in the cerebellum has been less well studied. Subtle alterations in cerebellar plasticity at parallel fibre–Purkinje cell synapses are found in mice that are heterozygous for the KE-family mutation [206]. Recently, Foxp2 knockdown in the embryonic cerebellum was shown to lead to altered motor function (righting reflex and negative geotaxis) and reduced vocalisation in neonatal animals [211].

Learning to perform organised sequences of movements is critical for a multitude of complex behaviours including speech. Initiation and termination of motor-sequences is compromised in disorders such as Parkinson's and Huntington's disease [212], and the coordination of these sequences is affected in cerebellar ataxia [213]. The cerebellum, basal ganglia and cortex are the major brain regions implicated in the learning and performance of motor-sequences, and make complementary contributions to motor behaviour [214]. These regions are thought to make complementary contributions to motor functions: the cerebellum contributes to error correction and control of ongoing movement, whilst the striatum is important for reinforcement learning and motor "chunking" (the process by which sequences of motor actions are concatenated with training [212]. The motor cortex acts to store representations of learned sequences [214]. As noted above, FOXP2 is enriched in particular neuronal subpopulations of these brain circuits, and is likely to contribute differently to motor function depending on its expression site. In fact, neuroimaging studies of KE family members with a FOXP2 mutation have highlighted structural and functional abnormalities in these areas and thereby provided cues as to what functions FOXP2 might serve in these regions [202, 215]. However, it has not yet been possible to disentangle roles for Foxp2 in specific types of cells of these brain regions, because previous work has been restricted to human cases with global or mosaic FOXP2 disruptions, global

Foxp2 mouse mutants and regional FoxP2 knockdown in multiple cell types of the zebra finch or embryonic mice [194, 206, 210, 211].

Here we set out to dissect Foxp2 functions in skilled motor behaviour in the three brain areas of interest by using a conditional approach to generate cell-type specific, homozygous deletions of the gene, as is often done for uncovering the functions of genes that are widely expressed from early on [131, 216]. Loss of Foxp2 protein in distinct circuits impacted motor-skill learning and performance differently, with Foxp2 disruption in striatum and cerebellar Purkinje cells affecting the variability and speed of lever-press sequences, respectively. Purkinje cell mutants executed all lever-press sequences more slowly and also showed deficits in skilled walking on the ErasmusLadder, a system for testing locomotor learning [213]. Moreover, in vivo recordings from Purkinje cells in these animals during rest and locomotion uncovered changes in the rate and modulation of simple-spike activity. Whole-cell recordings revealed that synaptic excitation and inhibition levels are normal; instead, we found that increased intrinsic excitability of Purkinje cells resulting from the loss of Foxp2 protein in those neurons is the plausible mechanism for the aberrant simple spike modulation observed in vivo.

Results

Mice with selective Foxp2 disruptions in the cerebellum, striatum or cortex are viable and show grossly normal development

We disrupted Foxp2 in cerebellar Purkinje cells, striatal medium-sized spiny neurons (MSNs) or layer 5-6 neurons of the cerebral cortex by generating L7-Cre/ Foxp2-flox/flox [205], Rgs9-Cre/ Foxp2-flox/flox and Emx1-Cre/ Foxp2-flox/flox mice respectively (referred to from here on as Foxp2-PCKO, Foxp2-MSNKO and Foxp2-CTXKO). Cre expression begins postnatally in the L7-Cre and Rgs9-Cre lines and embryonically in the Emx1-Cre line (for details on spatiotemporal distribution of expression see Online Methods and in references [217-219]. Virtually no Foxp2 expression was seen in the Purkinje cells of Foxp2-PCKO mice or in the layer 5-6 neurons in the cortex of Foxp2-CTXKO mice and Foxp2 knockdown in the MSNs was substantial throughout the striatum of Foxp2-MSNKO mice (including both dorsal and ventral striatum), although some Foxp2-expressing cells were visible in the more lateral areas (Figure 1a). Importantly, Foxp2 knockdown was specific to the targeted cell types; e.g. Foxp2 expression in the cortex and striatum of Foxp2-PCKO mice was normal. No gross abnormalities in brain morphology were evident in mice with conditional Foxp2 disruptions (see e.g. Supplementary Figure 1), and all mutants appeared healthy and gained weight at the same rate as control littermates (Cre^-/ *Foxp2-flox/flox*) (effects of genotype: $Fs \leq 0.24$, $ps > 0.05$) (Figure 1b). This contrasts with constitutive Foxp2 knockout mice, which die at 3-4 weeks of age and have a disproportionately small cerebellum [205-207].

Foxp2-PCKO and Foxp2-MSNKO mice show reduced lever-press rates

An operant lever-pressing task was used to investigate the learning and performance of novel motor-sequences in Foxp2 conditional knockouts. In this task mice get a sucrose reinforcer after eight lever presses (fixed-ratio 8 schedule, FR8). Initially pressing is self-paced, but after twelve days of training a time constraint is added and the eight presses must be completed at increasingly high speeds (first day - 8 presses in 16 s, second day - 8 presses in 12 s, subsequent days - 8 presses in 8 s, 6 s, 4 s and 2 s).

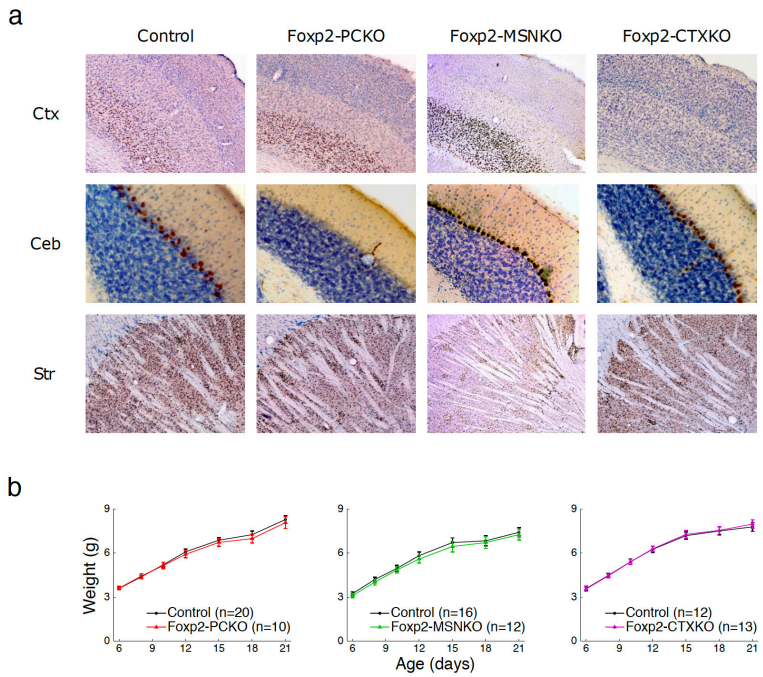

Figure 1. Conditional disruption of Foxp2. **(a)** Representative images of the cortex, cerebellum and striatum taken from adult Foxp2 stained (brown) sagittal sections of conditional knockouts and a control. **(b)** Weights of Foxp2 conditional knockouts and controls between postnatal days 6 and 21. Error bars represent ± s.e.m.

There is no signalling of the correct number of presses or the availability of the sucrose reinforcer (details in Online Methods). Foxp2-PCKO mice showed a reduced rate of reinforcer delivery throughout training compared to littermate controls ($F_{1, 22} = 4.48$, $p < 0.05$), and a reduced rate of lever pressing during the high-speed phase ($F_{1, 22} = 6.62$, $p < 0.05$) (Figure 2a). Furthermore, for these mice pressing was less efficient in the high-speed training phase ($F_{1, 22} = 8.59$, $p < 0.05$) [press efficiency % = (reinforcers delivered x 8 / lever presses) x 100]. Foxp2-MSNKO mice also showed reduced rates of reinforcer delivery and lever pressing, but only during the high-speed phase ($F_{1, 29} = 6.20$, $p < 0.05$; $F_{1, 19} = 8.55$, $p < 0.05$), and press efficiency was not affected ($F_{1, 19} = 2.41$, $p > 0.05$). No significant differences were seen between Foxp2-CTXKO mice and littermate controls (effects of genotype: $Fs_{1, 32} \leq 1.23$, $ps > 0.05$). Note that when examining reinforcer delivery and lever-press rates, the control groups for the three Foxp2 conditional knockout lines were significantly different from each other ($Fs_{1, 37} \geq 6.33$, $ps < 0.05$), meaning that mutant groups should not be compared directly with each other. Indeed, since the differences between controls are likely

caused by the varying genomic backgrounds of the Cre lines (details in Online Methods), we followed standard practice in that we only directly compared mutants with their littermates of the same genomic background. Together, these data indicate that lever-pressing behaviour is differentially affected in Foxp2 conditional knockouts.

Chunking of lever-press sequences has previously been shown to occur in the FR8 task with training, a process which is disrupted when striatal circuits are perturbed [220]. Consistent with these data, pressing in the self-paced training phase became progressively organised into discrete sequences (Figure 2b). The number of presses in a sequence increased significantly across training in all Foxp2 conditional knockouts (Fs ≥ 27.78, *ps* < 0.001) until it was close to eight (Figure 2c). However, it did not vary between any of the knockouts and their respective controls (Fs ≤ 2.43, *ps* > 0.05). Instead, an increase in sequence duration and average within-sequence inter-press interval was seen in Foxp2-PCKO ($F_{1, 22} = 4.50$, $p < 0.05$; $F_{1, 22} = 8.16$, $p < 0.01$) and Foxp2-MSNKO mice ($F_{1, 19} = 5.04$, $p < 0.05$; $F_{1, 19} = 4.45$, $p < 0.05$), likely reflecting the deficits uncovered in the initial analyses. In the high-speed training phase a similar picture emerged, with again no significant changes in sequence length between Foxp2 conditional knockouts and controls (Fs ≤ 2.06, *ps* > 0.05) (Supplementary Figure 2). Therefore, it appears that the lever-pressing deficits observed in Foxp2-PCKO and Foxp2-MSNKO mice are not caused by changes in the overall organisation of lever-press sequences, but rather by alterations in the timing of pressing.

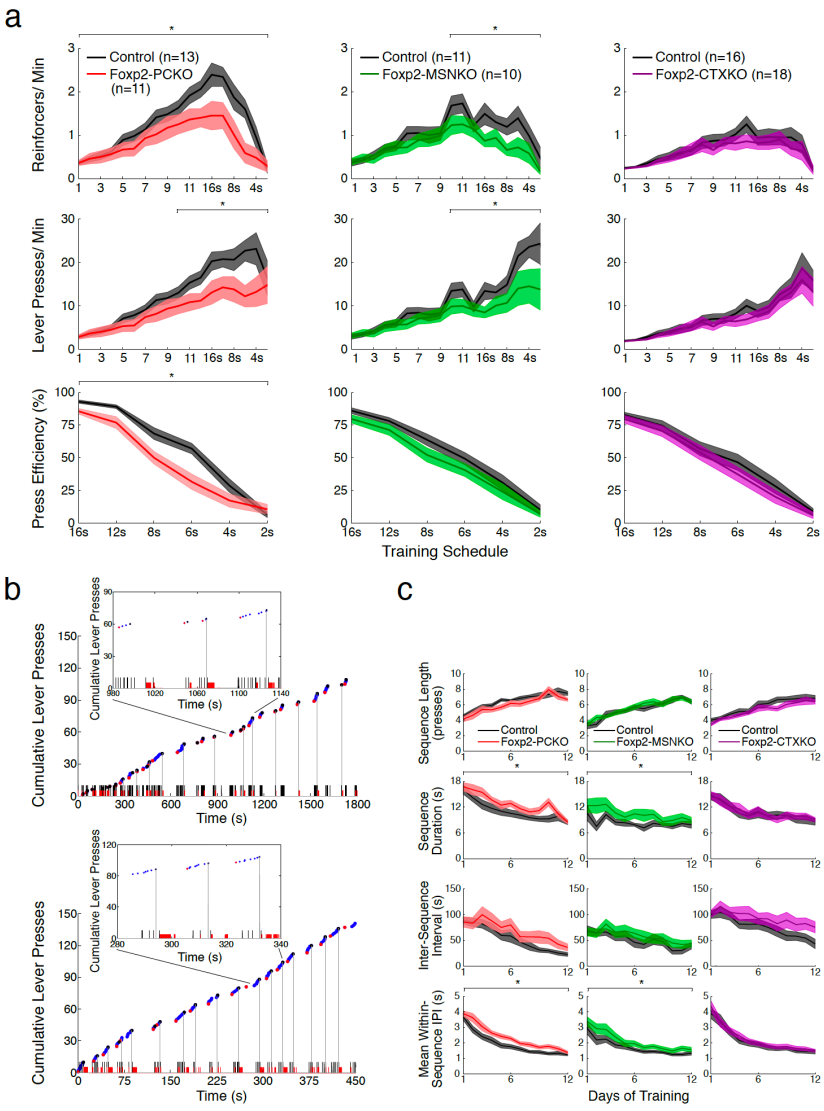

Figure 2. Operant lever-pressing in Foxp2 conditional knockouts. **(a)** Rates of reinforcer delivery (top panel) and lever pressing (middle panel) throughout the FR8 task. On the left side of the x axis numbers represent days of training completed on the self-paced FR8 schedule, and on the right side, times in which a sequence of 8 presses must be completed on the high-speed FR8 schedule. Press efficiency during the high-speed phase of the task (bottom panel) **(b)** Examples of the behavioural microstructure of a control animal from day 1 (top panel) and day 12 (bottom panel) of the self-paced phase of the FR8 task. Blue dots represent lever presses, with red and black dots indicating the first and last presses of sequences. Black and red ticks on the x axis represent head entries into the food magazine and licks in the food bowl. Grey vertical lines denote reinforcer deliveries. **(c)** Number of lever presses in a sequence (top panel), sequence duration (second panel), inter-sequence interval (third panel) and

mean within-sequence IPI (bottom panel) during the self-paced phase of the FR8 task. Error bands represent ± s.e.m.

Selective Foxp2 disruptions affect the microstructure of lever-press sequences in distinct ways

In order to look in detail at the microstructure of lever-pressing behaviour, inter-press intervals (IPIs) were divided into three types - rapid (no event between presses), check (presses separated by head entry into the food magazine), and consumption (presses separated by head entry and licking) (see Online Methods, Figure 3a). Each IPI type constituted a similar percentage of total IPIs in all Foxp2 conditional knockouts and controls (Supplementary Figure 3). All rapid IPI distributions were bimodal and a low point was consistently found at around 0.25 s throughout training. This value was used as a threshold to separate ultrafast from other rapid IPIs (Supplementary Figure 4a). Ultrafast IPI median values did not change across training ($Fs \leq 1.79$, $ps > 0.05$), indicating that these press-sequences are not learned and may reflect bouncing of the lever (Supplementary Figure 4b). They were therefore deducted from the rapid IPI groups before conducting further analyses.

Differences in IPI distributions were evident between conditional Foxp2 mutants and their respective control groups (Figure 3a, Supplementary Figure 4a, Supplementary Figure 5). Lever-pressing was slower in Foxp2-PCKO mice, which was reflected in increased median values of rapid, check and consumption IPIs compared to controls ($F_{1, 22} = 5.66$, $p < 0.05$; $F_{1, 22} = 7.08$, $p < 0.05$; $F_{1, 22} = 8.09$, $p < 0.05$) (Figure 3b). In contrast, the medians of all IPI types were unchanged in Foxp2-MSNKO mice ($Fs \leq 2.36$, $ps > 0.05$). In Foxp2-CTXKO mice, the check IPI median was increased ($F_{1, 32} = 5.78$, $p < 0.05$). The variability of IPIs of each type was assessed using the median absolute deviation (MAD) / median (Figure 3c). Notably, rapid and check IPIs were more variable in Foxp2-MSNKO mice than in controls ($F_{1, 19} = 16.47$, $p < 0.05$; $F_{1, 19} = 4.68$, $p < 0.05$), but no differences were seen in Foxp2-PCKO or Foxp2-CTXKO mice ($Fs \leq 3.42$, $ps > 0.05$). This increase in variability was not due to the influence of very long IPIs (i.e. when animals become disengaged from the task), because the result was still significant if only IPIs of 20 s or less were analysed ($F_{1, 19} = 15.94$, $p < 0.05$; $F_{1, 19} = 5.22$, $p < 0.05$) (Supplementary Figure 4c). In summary, Foxp2 disruption in cerebellar Purkinje cells and striatum has differential effects on the execution of lever-press sequences, with Foxp2-PCKO mice pressing more slowly and Foxp2-MSNKO mice more variably.

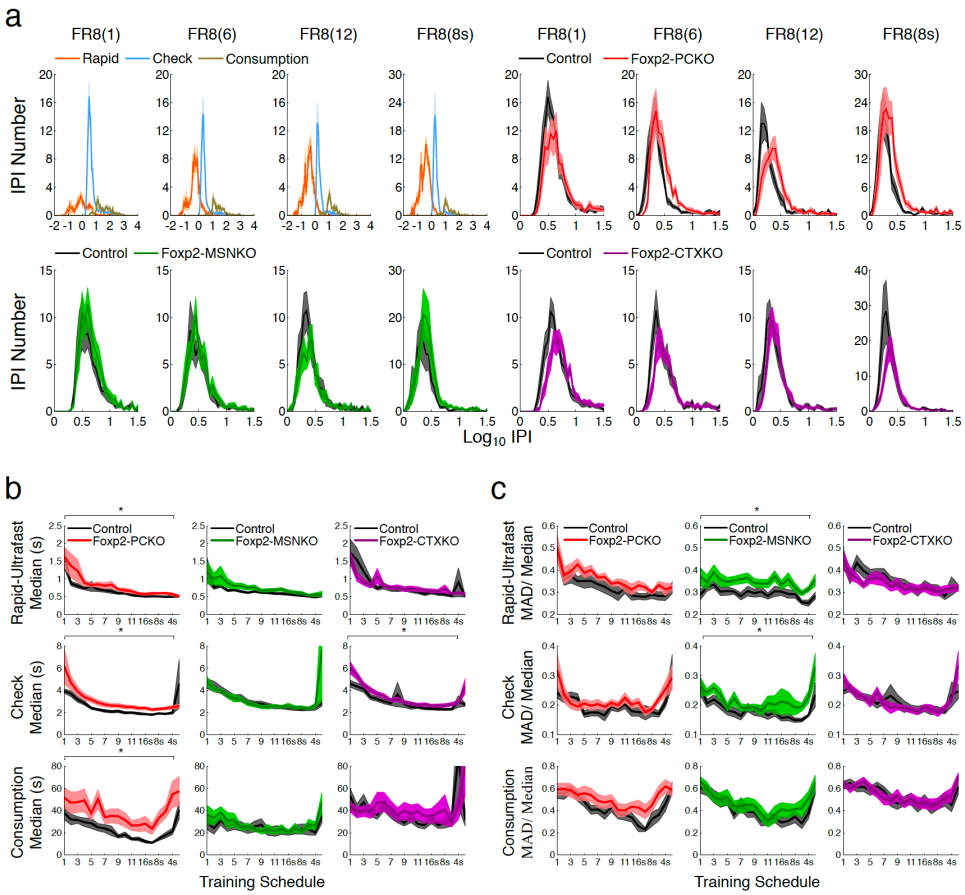

Figure 3. Microstructure of lever-pressing behaviour. **(a)** Distributions of rapid, check and consumption IPIs from Foxp2 Purkinje cell control animals at four time points during FR8 training (top left panel). Check IPI distributions of Foxp2-PCKO, Foxp2-MSNKO and Foxp2-CTXKO with controls at the same time points (top right, bottom left and bottom right panels respectively). Average **(b)** median and **(c)** MAD/ median values of the rapid, check and consumption IPI groups of Foxp2 conditional mutants and controls during FR8 training. Error bands represent ± s.e.m.

Foxp2-PCKO mice show deficits in locomotor learning

The ErasmusLadder was used to investigate sequencing of locomotor movements in Foxp2 conditional knockouts. This piece of equipment consists of two parallel sets of horizontal rungs with a shelter box at each end (see Online Methods)(Van Der Giessen et al. 2008). A light and then an air puff encourage mice to leave the shelter boxes and they are hence

trained to run back and forth across the ladder, even when motivational issues are at stake [213]. Initially, even numbered rungs on one side of the ladder and odd numbered rungs on the other were elevated to generate an alternating stepping pattern. In these unperturbed sessions, the percentage of trials with multiple missteps (touching lower rungs two or more times) was higher in Foxp2-PCKO mice than in controls ($F_{1, 27} = 8.15$, $p = < 0.05$), but unchanged in Foxp2-MSNKO and Foxp2-CTXKO mice ($F_{1, 14} = 0.46$, $p = > 0.05$; $F_{1, 27} = 0.00$, $p > 0.05$) (Figure 4). After 4 days, perturbed trials began and a tone was sounded 200 ms before a lower rung was elevated immediately in front of the mouse. An increased number of trials with multiple missteps was again observed in Foxp2-PCKO mice ($F_{1, 27} = 5.96$, $p < 0.05$), and this sensitive paradigm also uncovered increased numbers of trials with multiple missteps in Foxp2-MSNKO and Foxp2-CTXKO mice ($F_{1, 14} = 5.35$, $p < 0.05$; $F_{1, 27} = 6.38$, $p < 0.05$). We also calculated the total number of missteps in a session and saw similar but less pronounced effects (Supplementary Figure 6a).

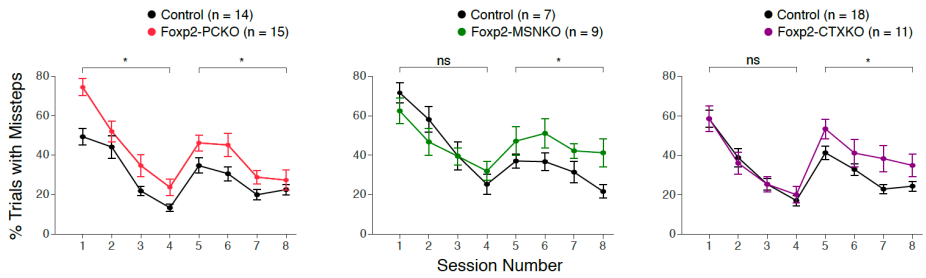

Figure 4. Skilled locomotion on the ErasmusLadder. Percentage trials with multiple missteps during unperturbed (days 1-4) and perturbed (days 5-8) sessions. Error bars represent ± s.e.m.

Taken together, the results from the operant lever-pressing and ErasmusLadder tasks suggest that finely regulated and complex motor behaviour is affected in Foxp2 conditional knockouts, whereas gross behaviour appears relatively normal. This is supported by data from the accelerating rotarod, the task first used to identify motor-skill learning deficits in global Foxp2 heterozygous mutants and knockouts [143, 206]. No differences in latency to fall were observed between Foxp2 conditional knockouts and their respective controls (Fs ≤ 0.80, *ps* > 0.05) (Supplementary Figure 6b). This indicates that none of the conditional Foxp2 knockouts by itself recapitulates the phenotype of global

Foxp2 heterozygotes, and further highlights the advantages of more detailed and sensitive motor-skill learning tasks and associated analyses in rodents for gaining more nuanced insights into gene function.

Increased intrinsic activity and decreased modulation of Purkinje cells in Foxp2-PCKO mice

Foxp2-PCKO mice displayed the most prominent deficits in the learning and performance of motor skills, so we investigated what electrophysiological changes might underlie these behavioural abnormalities. Effects of Foxp2 loss on *in vivo* Purkinje cell function were examined during limb movements. Experiments were performed in head-fixed mice while they walked on a wheel, with extracellular activity recorded from Purkinje cells in lobules III-V of the anterior lobe, an area implicated in locomotion control [221]. Locations of recording sites were confirmed by injection with Alcian blue (Supplementary Figure 7b). Purkinje cells involved in locomotion showed an increase in simple-spike activity during walking compared to rest in all animals ($F_{1,28} = 154.79$, $p < 0.001$) (Supplementary Figure 7a). However, simple-spike, but not complex-spike activity, was significantly higher in Foxp2-PCKO mice compared to controls at rest (Mann-Whitney U = 59.00, p = 0.03; Figure 5a and b) and during locomotion (Mann-Whitney U = 63.00, p = 0.04, Figure 5c and d). Furthermore, Foxp2-PCKO mice did not show characteristic epochs of reduced Purkinje cell activity when the wheel was approaching its peak velocity (Figure 5c), and the correlation between wheel velocity and simple-spike activity (see online Methods) was significantly lower than that of controls (Mann-Whitney U = 162.00, p = 0.04) (Figure 5d). In contrast, when we recorded from Purkinje cells of Foxp2-MSNKO mice and controls, no differences between genotypes were seen in complex-spike or simple-spike activity at rest, supporting the view that the electrophysiological alterations in Foxp2-PCKO mice were related specifically to loss of Foxp2 from the Purkinje cells themselves, rather than an indirection reflection of some of the motor coordination problems as also occurred in the Foxp2-MSNKO mice (Supplementary Figure 7c and d).

To elucidate the mechanisms that may underlie the abnormal *in vivo* SS firing modulation we investigated Purkinje cell activity *in vitro* using whole cell recordings. Here, we found that there was no difference in the Parallel fibre to Purkinje cell excitatory synaptic input when we varied the stimulation intensity of Parallel fibres [$F_{1, 14} = 1.30$, $p = 0.3$] (Supplementary Figure 8a). Also, paired pulse facilitation (PPF) [$F_{1, 11} = 2.99$, $p = 0.1$], input resistance [t=0.66, df=15, $p = 0.5$] and holding current [t=0.90 df=17, $p = 0.4$] (Supplementary Figure 8b-d) were not different between the Foxp2-PCKO and controls. To

investigate a possible dysfunction of inhibitory input we next focused on spontaneous inhibitory postsynaptic potentials (sIPSCs). Here too, we found no abnormalities in the frequency [t=0.19, df=23, p = 0.9] (Supplementary Figure 9a) or amplitude [t=0.05, df=21, p = 0.9] of the potentials (Supplementary Figure 9b). However, when we injected different depolarizing currents at the Purkinje cell soma, we found that the intrinsic excitability of Purkinje cells was significantly higher [$F_{1, 20}$ = 5.97, p = 0.024] (Figure 5e). The action potentials (APs) generated by current injection were not different in amplitude [t=0.88 df=20, p = 0.4], AP threshold [t=1.35 df=20, p = 0.2], after hyperpolarization [t=0.30 df=20, p = 0.8] or half-width [t=1.32, df=20, p = 0.2] (Supplementary Figure 10a-d). These findings suggest that the increased SS firing *in vivo* directly results from alterations in the intrinsic drive of Purkinje cells to fire, but that the subcellular machinery that ultimately generates the individual SS is not affected.

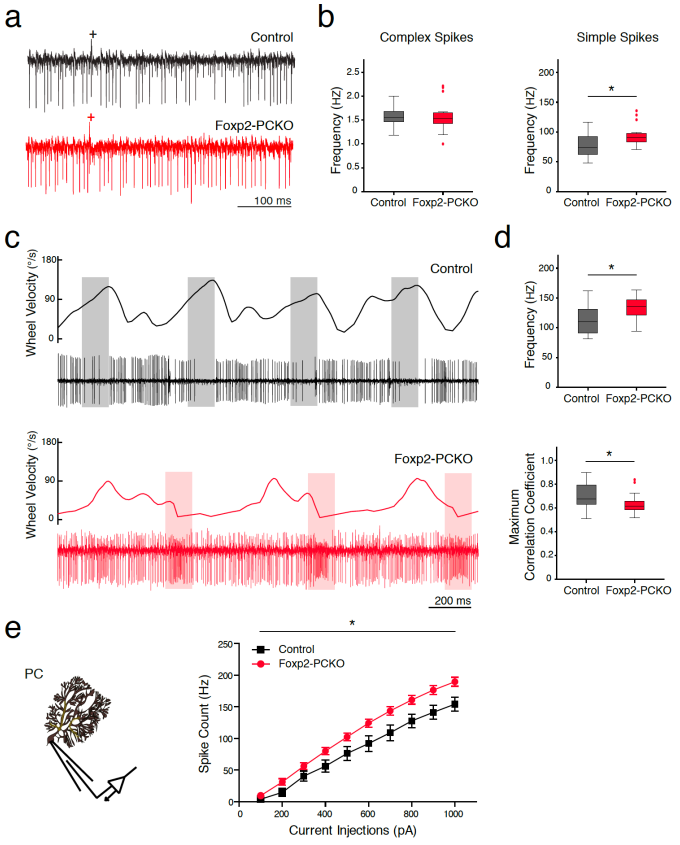

Figure 5. Electrophysiological recordings of Purkinje cells in control and Foxp2-PCKO mice. **(a)** Example traces showing simple spikes and complex spikes (+) of Purkinje cells in Foxp2-PCKO (red) and control mice (black) *in vivo*. **(b)** An increase in simple-spike firing (right panel), but normal complex spike activity, (left panel) in Foxp2-PCKO mice at rest. **(c)** Example traces with wheel motion velocity plotted in the upper panels. Transparent boxes in grey indicate epochs of reduced Purkinje cell activity in relation to pre-peak velocity in control mice, whereas boxes in red indicate increased activity at trough velocity in Foxp2-PCKO mice. **(d)** Foxp2-PCKO mice showed higher Purkinje cell firing activity (upper panel)

and lower maximum correlation coefficient between wheel velocity and simple-spike response (lower panel) during spontaneous locomotion. **(e)** Foxp2-PCKO mice showed higher output of action potentials when injecting different currents in the Purkinje cell *in vitro* (control n=11, 3 mice; Foxp2-PCKO n=11, 2 mice). Error bars represent ± s.e.m.

Discussion

In this study, we used a conditional approach to selectively remove Foxp2 from cerebellar Purkinje cells, striatal medium-sized spiny neurons or layers 5-6 cells of the cerebral cortex. These are key Foxp2 expressing areas that are also known to be involved in motor-sequence learning, and their importance has been emphasised in previous FoxP2 studies in humans, mice and songbirds. We subjected each of our region-specific Foxp2 knockouts to behavioural tasks to investigate their motor-sequence learning and performance in depth. Disrupting Foxp2 in Purkinje cells led to prominent deficits on multiple different assays of motor sequencing. Foxp2-PCKO animals executed press-sequences of all types more slowly than controls, and showed limb placement deficits during both unperturbed and perturbed conditions on the ErasmusLadder. In vivo recordings from Purkinje cells of Foxp2-PCKO mice uncovered an increase in simple-spike activity during both rest and locomotion and a reduced correlation between wheel velocity and simple-spike activity. Furthermore, whole-cell recordings showed that these electrophysiological changes in vivo may at least in part be caused by an increase in intrinsic excitability of Purkinje cells.

The increase in firing rate and reduction in correlation with the motor output are in line with a recent hypothesis on the learning mechanisms in the zebrin-negative modules of the cerebellum [170, 222]. During learning in the zebrin-negative modules, which indeed incorporate locomotion control regions [221], simple spike firing frequency is usually suppressed [223] as opposed to the zebrin-positive zones where firing frequency is increased during learning. If the intrinsic excitability is too high, the firing frequency may remain too high in zebrin-negative modules, reducing the modulation magnitude and correlation with the motor output, preventing an adequate built up of an internal model [224]. How the transcription factor Foxp2 exerts its impact on intrinsic excitability of Purkinje cells is beyond the scope of the current study, but one might speculate that factors like those of the G-protein coupled receptor protein signalling pathway, which have been shown to depend on Foxp2 [197], contribute to the excitability of Purkinje cells by affecting the efficacy of ion-conductances [225, 226].

The deficits seen in Foxp2-MSNKO mice were distinct to those seen in Foxp2-PCKO mice. Interestingly, Foxp2-MSNKO mice executed rapid and check press-sequences more

variably. This finding is consistent with independent data from zebra finches, where FoxP2 knockdown in Area X of the striatum in juvenile or adult birds increases variability of the syllables that comprise song [210]. Plasticity of striatal inputs is thought to be necessary for crystallizing new motor-skills, and disrupting plasticity in the striatum leads to more variable behaviour in mice [220]. Striatal plasticity is aberrantly modulated in mice heterozygous for the KE-family mutation [143], and although we do not know if this is the case in Foxp2-MSNKO mice, it suggests a potential mechanism that could account for the behavioural deficits that we observe.

Regulating the variability of learned motor behaviour in basal-ganglia circuits is probably modulated by dopamine [227, 228]. Dopamine levels in zebra finch Area X are elevated during directed (less variable) relative to undirected (more variable) singing [229], and infusion of a dopamine receptor 1 (D1R) antagonist can abolish these context-dependent changes in song [230]. FoxP2 knockdown in Area X also disrupts the regulation of song variability by social context, and interferes with D1R-mediated modulation of activity propagation through the anterior forebrain pathway, possibly by down-regulating expression of D1R and DARPP-32 [210]. Consistently, Area X Foxp2 knockdown also reduces the density of dendritic spines on MSNs [231], where many D1Rs are located [232]. In mice, Foxp2 is preferentially expressed in D1R compared to D2R MSNs [197, 233] and global Foxp2 heterozygous knockouts may also have altered dopamine levels in the brain [234]. Thus, it will be interesting to find out to what extent changes in the efficacy of dopamine-dependent processing in cortico-striatal circuitries contribute to the more variable behaviour seen in the Foxp2-MSNKO mice [235].

The Foxp2-CTXKO mice were characterised by relatively subtle deficits in that the check IPI median and the number of trials with multiple missteps were increased during the lever-pressing and perturbed ErasmusLadder task, respectively. Since the Foxp2-CTXKO mice were generated using a cre-line of *Emx1* [219], which is also expressed in the dorsal spinal cord, we cannot exclude the possibility that there is a difference in motor neuron development in these mutants. However, it should be noted that the Foxp2-CTXKO mice showed virtually no impairment in baseline motor performance (see e.g. results during non-perturbed sessions on the Erasmus Ladder), so it is unlikely that the potential secondary deficits of motor neurons act as a severe confound in the Foxp2-CTXKO mice. The main functional learning deficits in the Foxp2-CTXKO mice are in fact more in line with dysfunctions of higher order regions like that of the cerebral cortex [236].

The average number of lever presses in a sequence was unchanged in all region-specific Foxp2 knockouts compared with that in their respective controls. These observations suggest that sequence structure and organisation as well as the motivational drive to perform are largely unaffected by loss of Foxp2 from the targeted brain regions, although deficits could become evident with more complex heterogeneous sequences. Differences between knockouts and controls emerged only after analyses of the temporal microstructure of lever pressing, with distinct effects depending on the site of Foxp2 loss. Foxp2-PCKO mice executed all press-sequences more slowly, whereas Foxp2-MSNKO mice executed rapid and check press-sequences more variably. Consistently, a greater number of missteps were seen in Foxp2-PCKO mice during both unperturbed and perturbed conditions on the ErasmusLadder, whilst deficits in Foxp2-CTXKO and Foxp2-MSNKO were seen only in perturbed conditions. Hence, the most striking effects were seen in mice with disruption of Foxp2 specifically in Purkinje cells of the cerebellum, a region known to be involved in learning timing-sensitive processes [10, 213, 221]. Indeed, similar impairments on the ErasmusLadder have been seen in several other mouse lines with cell-type specific disruptions of cerebellar proteins [213]. In humans, patients with cerebellar lesions show impaired sequence learning on a serial reaction time task [237], whereas basal ganglia lesions result in more subtle deficits in speed and force control of finger tapping [238].

All three lines of Foxp2 conditional knockout mice still showed some degree of learning, despite the fact that they all three showed a reduced level of motor learning. This is reminiscent of cerebellar learning deficits following cell-specific deficits in the cerebellar cortex [24, 174]. Most likely, the remnant capacity for learning is partly mediated by downstream regions, such as the cerebellar and vestibular nuclei, which are engaged for compensation when prolonged periods of time are available [175, 239].

Many genetic tools and behavioural tests are nowadays available for neuroscience research in mouse models, all of which can be utilised to dissect Foxp2 function in the brain. The current study set out to determine Foxp2 functions of discrete brain regions in motor-sequence learning by subjecting conditional, homozygous region-specific Foxp2 knockouts to established behavioural tasks. To carefully examine the learning of motor-sequences we used the lever-pressing and ErasmusLadder tasks involving limb movements, rather than vocalisation tests, because mice exhibit at best limited vocal learning [240]. Indeed, this approach allowed us for the first time to detect distinct and differential roles of Foxp2 for motor learning in the cerebellum, striatum and cerebral cortex. In addition, our results

from homozygous Purkinje cell - specific knockouts provided fundamental insights into the role of Foxp2 at the cell physiological level. The relevance of deficits in Foxp2-driven cell-intrinsic processes that cannot be compensated for by synaptic inputs during development may not only apply to the pathology of the KE family, but also to that of patients with other mutations in the *FOXP2* gene [191-194]. This possibility is underscored by the fact that even heterozygous (albeit global) Foxp2 knockouts can show deficits in motor-skill learning on the accelerating rotarod and running wheel [143, 206].

The majority of brain lesions causing verbal apraxia occur in cortical and sub-cortical regions, and most functional FoxP2 work to date has focused on cortico-striatal circuits. Nevertheless, it is becoming increasingly clear that the role of the cerebellum goes beyond that of a coordinator of basic motor function [241] and extends to regulating purposeful skilled motor actions such as those required for spoken language [242]. Indeed, in line with the finding that cerebellar lesions can give rise to verbal apraxia by disrupting cerebro-cerebellar connectivity [243], patients suffering from *FOXP2* mutations show altered activity in both the cerebral cortex ánd the cerebellum when subjected to verbal tasks under the fMRI [244]. Our data highlight that reduced dosage of functional FOXP2 in different brain regions may contribute differently to the observed motor difficulties, and that in particular the cerebellum needs to be considered when thinking about FOXP2 function in motor learning and the deficits seen when it is disrupted.

Methods

Methods and any associated references are available in the online version of the paper.

Acknowledgments

We thank Vítor Paixão, Alex Gomez-Marin, Mario Negrello and Xin Jin for help with analyses and Matlab programming, and Sebastian Brandner for supplying the *L7-Cre* mouse line. We also thank Ana Vaz, Joana Almeida, Mariana Correia, Rathi Puliyadi and Sonali Darbar for mouse genotyping and colony management, and Carlos Martin Roman and Elize Haasdijk for technical support. Work in the Netherlands was supported by the Dutch Organization for Medical Sciences, Life Sciences, and Social and Behavioral Sciences, NeuroBasic, ERC-adv and ERC-POC, CEREBNET, and C7 programs of the EU (to C.I.D.Z.). Work in Portugal was funded by the Champalimaud Foundation as well as by grants from the Fundação para a Ciência e a Tecnologia (FOXNET), the European Research Council (COG 617142) and HHMI (IEC 55007415) (to R.M.C). S.E.F. is

supported by the Max Planck Society. C.F. is the recipient of a grant from the Fundação Bial (192/12).

Supplementary Figures

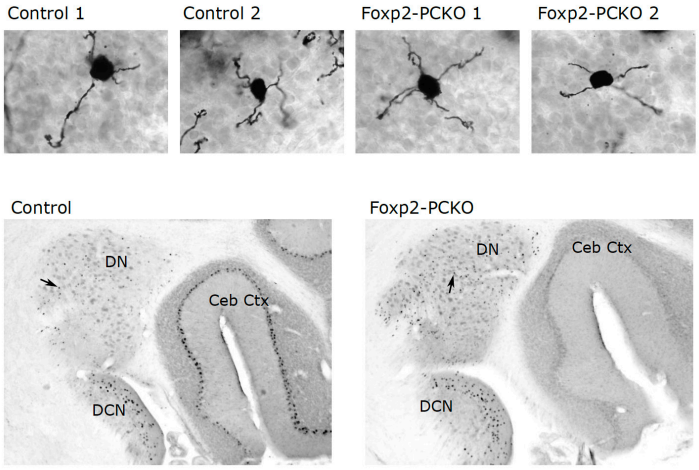

Supplementary Figure 1. The morphology of granule cells which provide input to Purkinje cells and that of cerebellar nuclei neurons which receive input from Purkinje cells appears normal in Foxp2-PCKO mice. (Top panel) Examples of Golgi stained granule cells from control animals (left) and Foxp2-PCKO animals (right). The average number of dendrites per granule cell was not significantly different ($p > 0.5$; Mann-Whitney) between controls (3.50 ± 0.14, n=2) and Foxp2-PCKO mice (3.40 ± 0.30, n=2). **(Bottom panel)** Representative cerebellar sections immunostained for Foxp2 from a control animal (left) and a Foxp2-PCKO mouse (right) (arrows show examples of labelled cells in DN). Note, that in controls all Purkinje cells and some cerebellar nuclei neurons are densely stained for Foxp2 (left), whereas in Foxp2-PCKO animals only cerebellar nuclei neurons are labelled (right). Cerebellar nuclei cells expressing Foxp2 were counted using Neurolucida software in 3-4 representative sections per animal. The average density of labelled cells was not significantly different ($p = 0.7$; Mann-Whitney) between control (512 ± 58 cells/mm^2, n=3) and Foxp2-PCKO mice (492 ± 48 cells/mm^2, n=3). The thickness of the molecular layer was also measured and no difference was found between genotypes ($p > 0.5$; Mann-Whitney) (controls: 2.05 ± 0.25 mm^2, n=3 and Foxp2-PCKO: 2.01 ± 0.12 mm^2, n=3). Abbreviations: DN = dentate nucleus; DCN = dorsal cochlear nucleus; Ceb Ctx = cerebellar cortex.

Supplementary Figure 2. Operant lever-pressing in Foxp2 conditional knockouts during the high-speed

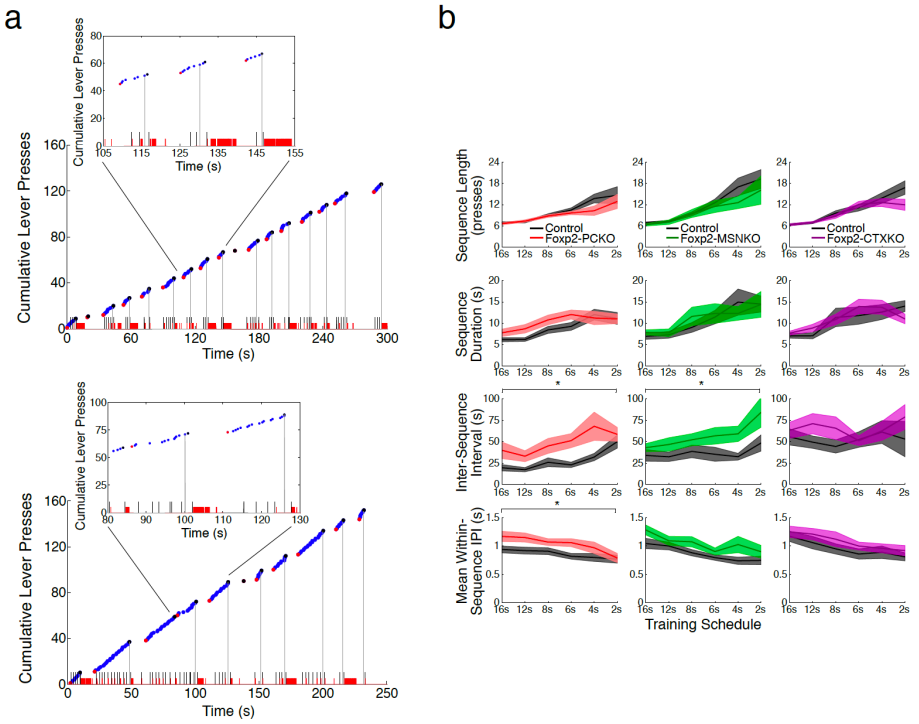

training phase. (a) Examples of the behavioural microstructure of a control animal from the high-speed phase of the FR8 task. Mice must presses 8 times in 16 s (top panel) or 6s (bottom panel). Blue dots represent lever presses, with red and black dots indicating the first and last presses of sequences. Black and red ticks on the x axis represent head entries into the food magazine and licks in the food bowl respectively. Grey vertical lines denote reinforcer deliveries. **(b)** Number of lever presses in a sequence (top panel), sequence duration (second panel), inter-sequence interval (third panel) and mean within-sequence IPI (bottom panel) during the high-speed phase of the FR8 task. Sequence length increased as the task became progressively harder, but there were no differences between Foxp2 conditional knockouts and controls. Increases in inter-sequence interval and mean within-sequence IPI were seen in Foxp2-PCKO mice with the former also elevated in Foxp2-MSNKO mice. Error bands represent ± s.e.m.

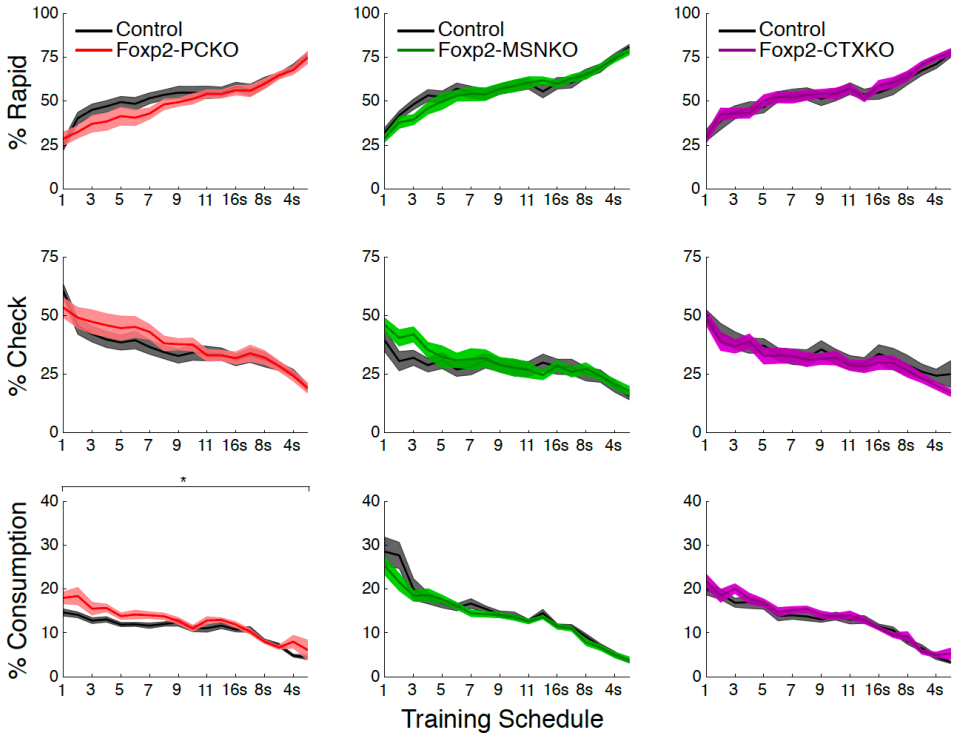

Supplementary Figure 3. Proportion of presses in each of the three inter-press interval groups. Percentage of total IPIs in the rapid, check and consumption groups of Foxp2 conditional knockouts and controls during FR8 training. The proportion of IPIs classed as rapid increased as training progressed and a corresponding decrease was seen in check and consumption IPIs. However, there were no differences between Foxp2 conditional knockouts and controls, with the exception of a small increase in the proportion consumption IPIs in Foxp2-PCKO mice. Error bands represent ± s.e.m.

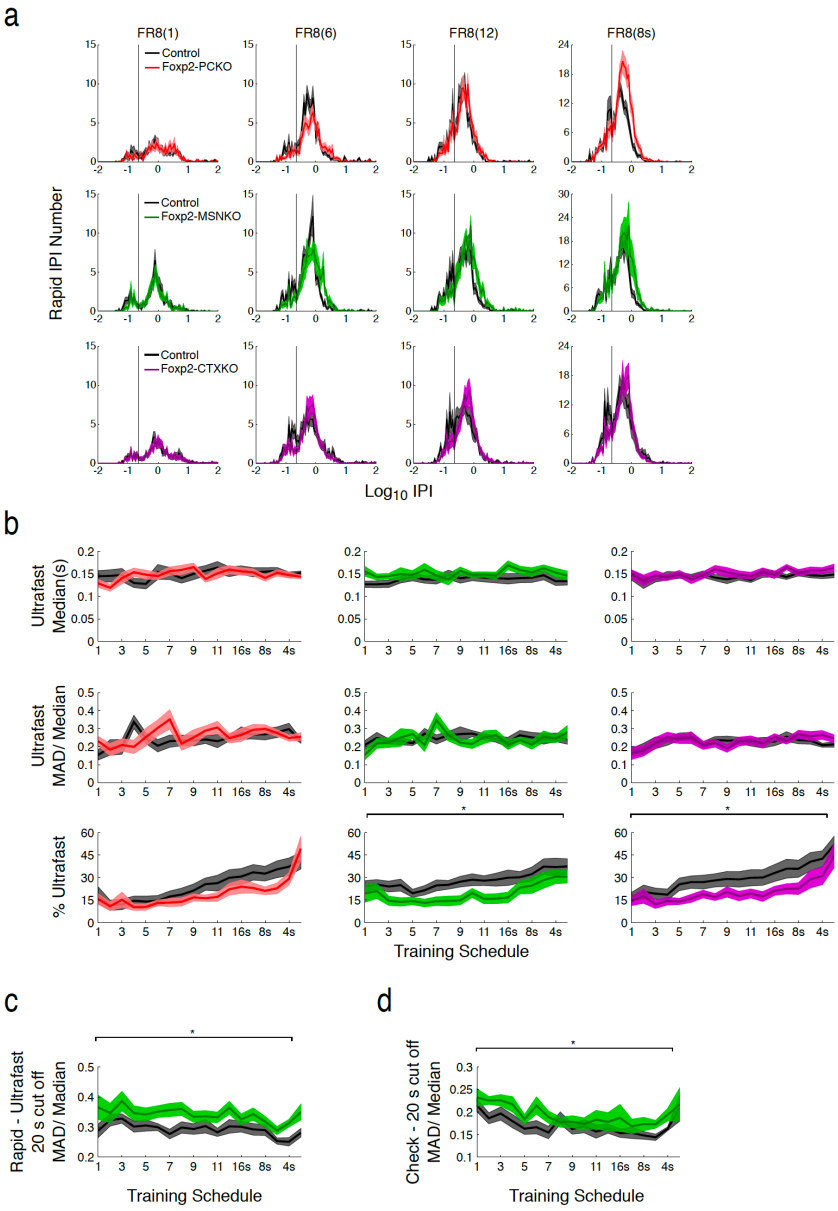

Supplementary Figure 4. Analyses of rapid lever-pressing. (a) Distribution of rapid IPIs from Foxp2 conditional knockouts and controls at four time points during FR8 training. The vertical black line at 0.25 s thresholds ultrafast IPIs. **(b)** Average median (top panel) and MAD / median (middle panel) values of ultrafast IPIs in Foxp2

conditional knockouts and controls during FR8 training. Percentage of rapid IPIs that are ultrafast (bottom panel). Average MAD / median values of **(c)** check IPIs and **(d)** rapid IPIs after ultrafast IPIs were removed in Foxp2-MSNKO mice and controls. Error bands represent ± s.e.m.

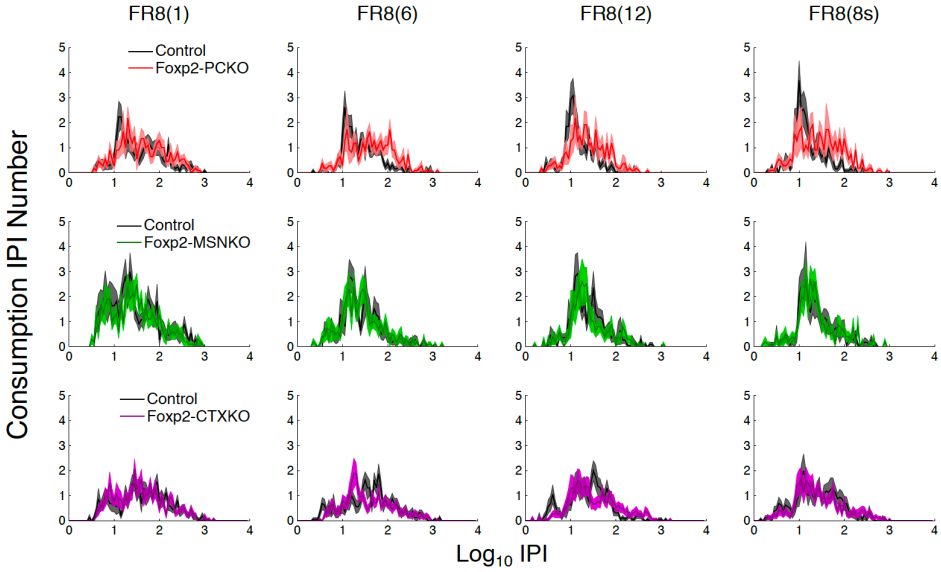

Supplementary Figure 5. Distribution of consumption IPIs. Consumption IPIs of Foxp2 conditional knockouts and controls at four time points during FR8 training. Error bands represent ± s.e.m.

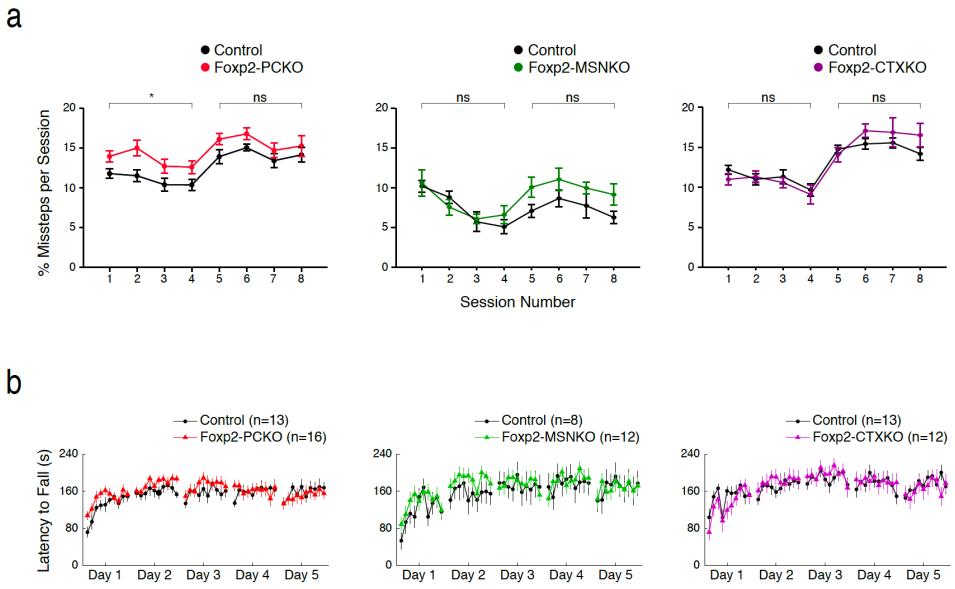

Supplementary Figure 6. Motor-skill learning on the ErasmusLadder and the accelerating rotarod. (a) Percentage missteps during unperturbed (days 1-4) and perturbed (days 5-8) sessions on the ErasmusLadder. **(b)** Latency to fall from a rotarod accelerating from 6-60 rpm over a 5 min period. Mice received 10 trials per day for 5 consecutive days. Error bars represent ± s.e.m.

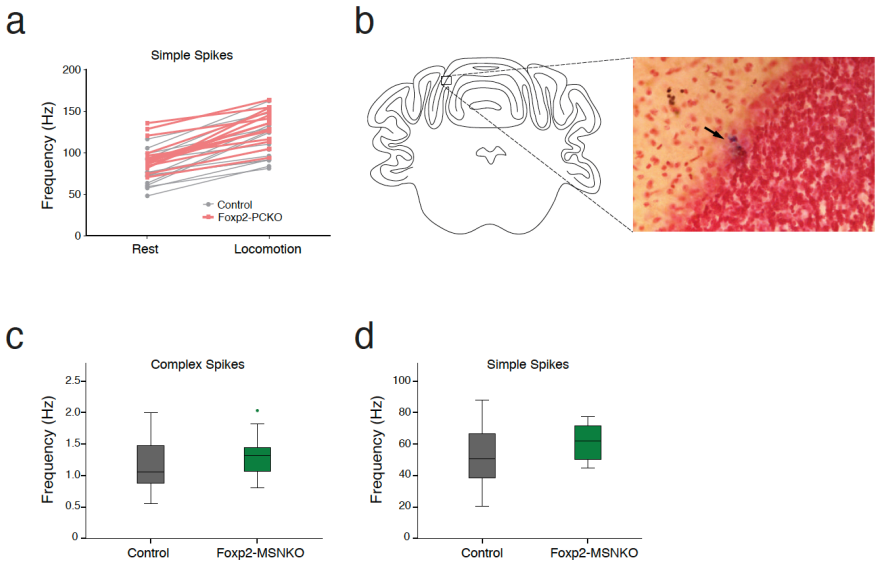

Supplementary Figure 7. Extracellular single-unit recordings of Purkinje cells. (a) Increased simple spike activity during locomotion compared to rest in control and Foxp2-PCKO mice (n = 15 for both genotypes). **(b)** Locations of recording sites were confirmed by injection with Alcian blue, which was visualised against a neutral red stained background. No differences in the firing frequency of **(c)** complex spikes or **(d)** simple spikes was seen in Foxp2-MSNKO mice compared to controls at rest (Foxp2-MSNKO: n = 15; control: n = 18).

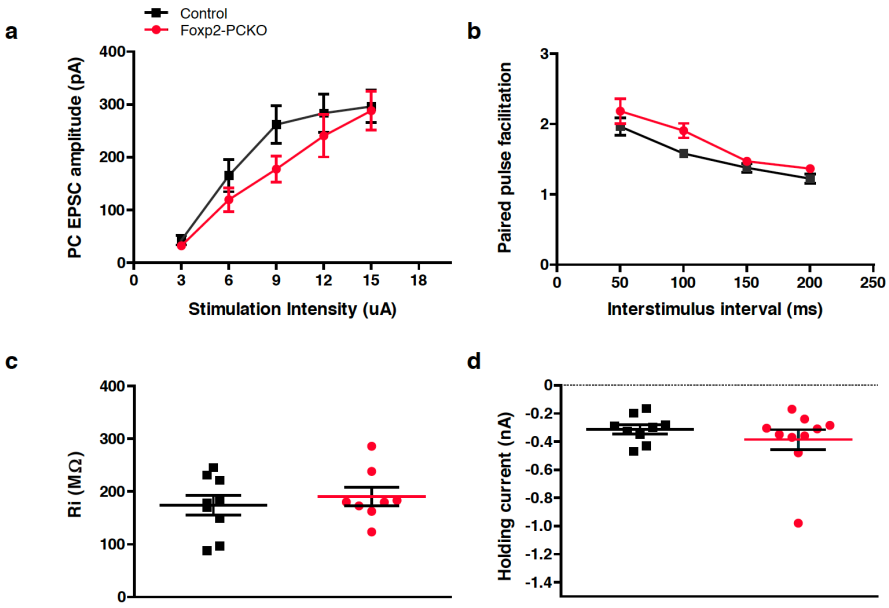

Supplementary Figure 8. PF to PC synaptic baseline input is normal in Foxp2-PCKO mice. (a) No difference in the parallel fibre (PF) to PC input with increasing stimulation intensity was observed in excitatory postsynaptic currents (EPSCs) amplitude (control : n=9 ; 3 mice Foxp2-PCKO ; n=8, 2 mice) and **(b)** paired pulse facilitation (PPF) (control: n=9, 3 mice; Foxp2-PCKO: n=6, 2 mice), where **(c)** input resistance (Ri) (control: n=9, 3 mice; Foxp2-PCKO: n=8, 2 mice) and **(d)** holding current (HC) (control: n=9, 3 mice; Foxp2-PCKO: n=10, 2 mice) were also unaltered. Error bars represent ± s.e.m.

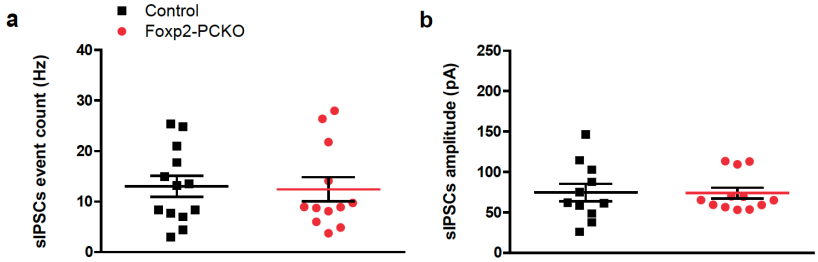

Supplementary Figure 9. Inhibition at the PF to PC synapse is not impaired in Foxp2-PCKO mice. (a) No difference in the inhibitory response of PCs when measuring the frequency of spontaneous inhibitory postsynaptic currents (sIPSCs) (control: n=13; Foxp2-PCKO: n=12, 2 mice) **(b)** and their amplitudes (control: n=11; Foxp2-PCKO: n=12, 2 mice). Error bars represent ± s.e.m.

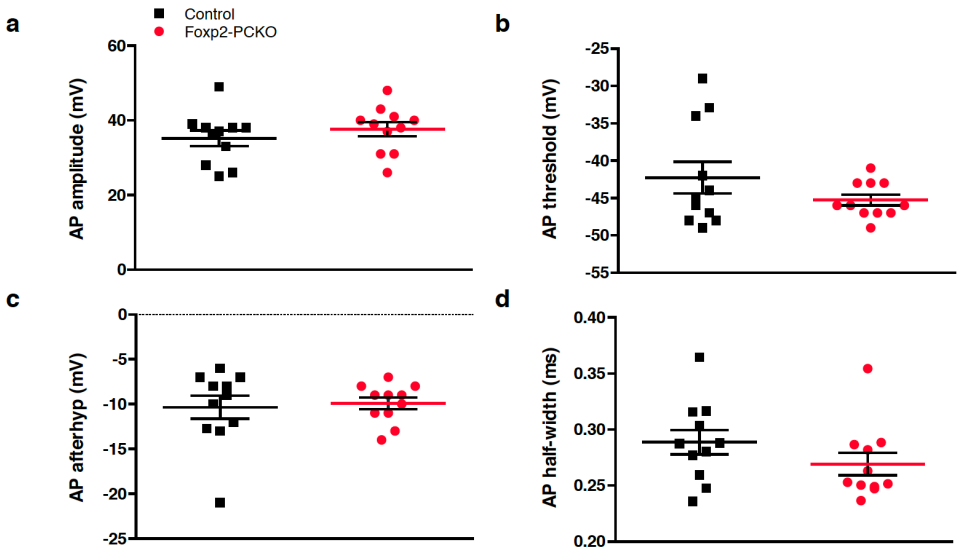

Supplementary Figure 10. Action potentials generated in PCs of Foxp2-PCKO mice appear normal. (a) No difference in the action potential (AP) amplitude **(b)** threshold, **(c)** after hyperpolarization and **(d)** AP half-width of control and Foxp2-PCKO mice. (control: n=11, 3 mice; Foxp2-PCKO: n=11, 2 mice). Error bars represent ± s.e.m.

Chapter 3.1

AMPA-receptor auxiliary protein Shisa6 is essential for Purkinje cell synaptic potentiation and motor learning

Saša Peter *, Bastiaan H.A. Urbanus *, Remco V. Klaassen *, Bin Wu, Henk-Jan Boele, Sameha Azizi, Johan A. Slotman, Adriaan B. Houtsmuller, Martijn Schonewille, Freek E. Hoebeek, Sabine Spijker, August B. Smit ¶ & Chris I. De Zeeuw ¶

* First-Co-author(s)

¶ Corresponding author(s)

Submitted

Abstract

The majority of fast excitatory postsynaptic currents in the brain are gated through AMPA-type glutamate receptors, the kinetics and trafficking of which can be modulated by auxiliary proteins. It is unclear whether and how such proteins can modulate synaptic function to contribute to procedural memory formation. Here, we report that cerebellar Purkinje cells express the auxiliary protein Shisa6 (CKAMP52). Shisa6 co-localizes with GluA2 and interacts with the non-AMPA-receptor GluD2. Absence of *Shisa6* affects basal excitatory transmission, deactivation of AMPA-receptors, as well as induction of long-term potentiation (LTP). Moreover, mice harbouring a Purkinje cell-specific knockout of *Shisa6*, i.e., *Shisa6*$^{L7\ KO}$, show a reduction in their simple spike activity *in vivo*, as well as severe impairments in motor learning tasks including ErasmusLadder, phase reversal learning of the vestibulo-ocular reflex, and eyeblink conditioning. These results indicate that Shisa6 is crucial for Purkinje cell AMPA-receptor function, synaptic plasticity, and cerebellar motor learning.

Introduction

Repetitive postsynaptic depolarization through activation of AMPA-type glutamate receptors (AMPARs) is one of the main mechanisms by which synapses can be potentiated in the brain. AMPAR-driven depolarization can trigger a range of voltage-dependent processes, including Ca^{2+}-influx through voltage-dependent channels and activated NMDA-receptors, which in turn induces modulation of AMPAR currents [245]. This form of synaptic plasticity has garnered great interest in the last decades as it is considered a fundamental cellular mechanism underlying memory formation [246, 247]. Different types of auxiliary proteins have been shown to modulate trafficking, mobility and gating properties of AMPARs, each of which may shape cell and/or brain region specific types of plasticity and AMPAR-modifying molecular pathways [248]. We have shown previously that Shisa proteins can affect mobility (Shisa6) and gating properties of AMPARs (Shisa6, -7 and -9), such as affecting receptor deactivation and desensitization in the hippocampus [248-254]. Also, Shisa9 (CKAMP44) has been shown to be responsible for the distinctive short-term depression in dorsal lateral geniculate nucleus synapses by reducing the rate of recovery from desensitization [255].

In this study, we investigated whether the formation of procedural memories also requires Shisa-dependent modification of AMPARs. The cerebellum is crucial in procedural memory formation and is equipped with a wide spectrum of plasticity forms that are hypothesized to work in a synergistic fashion [24]. Cerebellar plasticity can be studied in well-defined behavioural learning paradigms, such as VOR adaptation and Pavlovian eyeblink conditioning. Various cell-specific promoters allow precise genetic manipulations, through which this unique brain structure has provided important insights into the cellular mechanisms of motor learning in general. For example, experiments using the granule cell-specific $GABA_A$-receptor subunit α6 promoter [179] or the Purkinje cell (PC)-specific L7 promoter [22, 30] have confirmed that synaptic plasticity at the parallel fibre (PF) to PC synapse is essential for cerebellum-dependent motor learning. Since many of these cerebellar forms of plasticity also included potentiation or depression of AMPAR currents [22, 29, 30], we here aim to uncover how the uniquely cerebellum expressed Shisa6 affects synaptic transmission in the cerebellar cortex, and consequently cerebellar motor learning. We found that Shisa6 is prominently expressed by PCs and that PC-specific ablation of *Shisa6* (*Shisa6*$^{L7\,KO}$) affects the function of the PF to PC synapse in that they have increased deactivation of AMPAR-mediated excitatory postsynaptic currents (EPSCs), impaired PF to PC baseline excitatory input as well as LTP. These impairments are

supported by our findings that Shisa6 interacts strongly with AMPAR subunits and that these are downregulated in the absence of Shisa6. Moreover, *Shisa6*$^{L7\ KO}$ mice show both lower simple spike (SS) firing of their PCs and impaired motor learning, highlighting a critical role of AMPAR auxiliary proteins in procedural memory formation.

Results

Increased AMPAR deactivation rate and lower evoked and spontaneous EPSC amplitudes and frequency in PCs of *Shisa6*$^{L7\ KO}$ mice.

In situ hybridization mRNA expression levels (Allen Mouse Brain Atlas) indicate that of the major brain-expressed Shisa family members, only *Shisa6* is expressed in cerebellar PCs. Using immunohistochemistry, we showed that the Shisa6 protein is expressed in PCs of control mice and is absent in the PCs of *Shisa6*$^{L7\ KO}$ mice (Figure 1A and S1A), confirming our PC-specific KO model. Using 3D structural illumination microscopy (3D-SIM), we investigated the previously reported co-localization of GluA2 with Shisa6 in the hippocampus [251]. Similarly, in the cerebellum GluA2 subunits co-localize with Shisa6 in the molecular layer (ML) (Figure 1B). Since Shisa6 is involved in the deactivation and desensitization of AMPARs in the hippocampus [251], we investigated the role of Shisa6 in PCs. For this purpose, we recorded spontaneous excitatory postsynaptic currents (sEPSCs) (Figure 1C). The sEPSCs in *Shisa6*$^{L7\ KO}$ PCs had a similar rise time (Figure 1D, $p = 0.56$), but a decreased decay time (Figure 1E, $p = 0.005$) compared to the control, indicating that Shisa6 has a role in the deactivation rate of AMPARs, in line with what was shown in hippocampal mEPSCs [251]. Examination of the cumulative frequency distribution of the sEPSCs revealed that events with smaller amplitudes dominated the distribution in the *Shisa6*$^{L7\ KO}$ PCs versus those of controls (Figure 1F), an observation that is cerebellum-specific [251]. This phenotype was confirmed when comparing the median amplitude of sEPSCs in the *Shisa6*$^{L7\ KO}$ PCs and the controls, the former group presenting with significantly lower amplitudes (Figure 1G, $p = 0.002$). Additionally, the frequency of sEPSCs was lower in the *Shisa6*$^{L7\ KO}$ (Figure 1H, $p = 0.005$). Together, these results indicate that there is less excitatory postsynaptic current at the PF to PC synapse in the absence of Shisa6. When exploring the possibility of impaired postsynaptic inhibitory responses in the PC, we found that spontaneous inhibitory postsynaptic currents (sIPSCs) did not differ in their rise time (Figure S1B, $p = 0.50$), decay time (Figure S1C, $p = 0.23$,), frequency (Figure S1D, $p = 0.32$) or amplitude (Figure S1E, $p = 0.63$). To explore the reduced excitatory postsynaptic currents as revealed by sEPSCs, we evoked excitatory synaptic input by stimulating PFs with varying stimulation intensities (Figure 1I). The excitatory postsynaptic

response at the PF to PC synapse was highly reduced in *Shisa6*$^{L7\ KO}$ (Figure 1J, $p < 0.001$ for each stimulation amplitude). In contrast, PF paired-pulse facilitation was normal (Figure 1K, p=0.86). From these results, we conclude that Shisa6 is important for excitatory conductance and AMPAR deactivation at the PF to PC synapse.

Cerebellar Shisa6 interacts with both AMPA and Delta-2 type glutamate receptors.

Whereas deletion of *Shisa6* resulted in a reduced sEPSC amplitude and frequency at PC synapses, no such effect was previously observed at hippocampal CA1 pyramidal cells [251]. As such, we next investigated whether the cerebellar interaction profile of Shisa6 might be distinct from that found in the hippocampus. First, we immunoprecipitated cerebellar Shisa6 protein complexes from the n-Dodecyl-beta-D-Maltoside-extracted crude synaptic membrane fraction and subjected these to mass spectrometric (MS) analysis (Figure 2A, Supplementary File 1). As anticipated, AMPAR subunits GluA1-3 (*Gria1-3*) were highly enriched in cerebellar Shisa6 complexes, yet more surprisingly, so was the cerebellum-specific glutamate receptor Delta2 (GluD2; *Grid2*). GluD2 has been reported to have a profound effect on postsynaptic AMPAR levels at PC synapses [256] and to play an essential role in coordinating PF to PC LTD [257, 258]. Next, we confirmed the interaction between Shisa6 (Flag-Shisa6) and GluD2 by co-expression in recombinant HEK293 cells, followed by immunoprecipitation using a Flag-specific antibody (Figure 2B). Immunoblot analysis confirmed that GluD2 can directly bind Shisa6, and interaction as such does not depend on co-association with AMPAR subunits. Finally, we investigated whether GluA2 and GluD2 co-associate within the same native Shisa6 subcomplexes by means of immuno-depletion IP (Figure 2C).

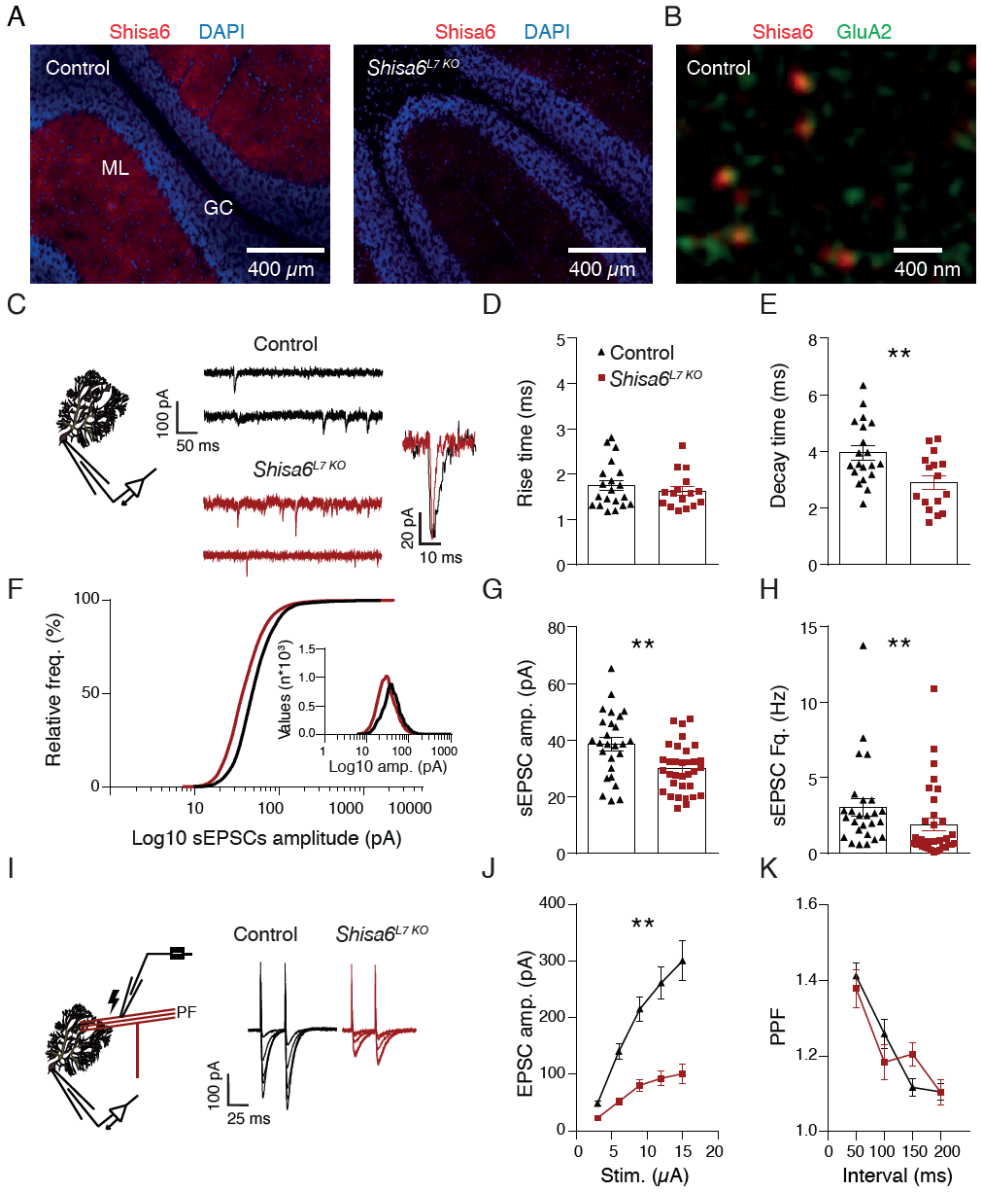

Figure 1. Purkinje cell-specific KO of *Shisa6* has lowered PF to PC excitatory input. (A) Representative confocal images of control and *Shisa6*$^{L7\ KO}$ mice shows Shisa6 expression in the ML of PCs. For split-channel images, see Figure S1A. (B) SIM imaging in control mice shows colocalization of Shisa6 (red) and GluA2 (green) in the PC ML. (C) Whole-cell patch clamp recording configuration of sEPSCs and representative control and *Shisa6*$^{L7\ KO}$ sEPSCs. (D, E) sEPSC rise times are unaffected whereas sEPSC decay times are significantly faster in the *Shisa6*$^{L7\ KO}$ in comparison to controls (control: 20 cells/4 animals; *Shisa*$^{L7\ KO}$: 16 cells; 5 animals). (F) sEPSCs in *Shisa6*$^{L7\ KO}$ PCs show consistently lower amplitudes, as evidenced by the cumulative relative frequency. Inset: histogram of all sEPSCs, similarly showing a leftward shift in sEPSC amplitude. (G, H) *Shisa6*$^{L7\ KO}$ PCs exhibit significantly lower

median sEPSC amplitudes. Additionally, comparison of the sEPSC frequency in the control and the *Shisa6*$^{L7\ KO}$ animals indicates a significant reduction in the mutants' sEPSC number (control: 26 cells/4 animals; KO: 33 cells/7 animals). (I) Sample traces of evoked EPSCs generated by stimulating afferent PFs with increasing stimulation strengths. (J, K) Evoked EPSCs were consistently of a lower amplitude in the *Shisa6*$^{L7\ KO}$ whereas the paired pulse facilitation ratio was unaffected (control: 21 – 25 cells/6 animals; *Shisa6*$^{L7\ KO}$: 25 – 27 cells/7 animals). Data are represented as mean ± SEM, significance indicated by * = $p < 0.05$, ** = $p < 0.01$.

Native cerebellar GluA2 complexes were removed from the crude synaptic lysate by means of immunoprecipitation (depletion with empty beads as control), yielding the "input after depletion" fraction. Subsequently, Shisa6 complexes were immunoprecipitated from this depleted input and analysed for their GluA2 and GluD2 content. Near full depletion of GluA2 was confirmed (beads-depleted: set to 100%, Anti-GluA2-depleted, $p < 0.001$), yet little reduction was observed in the level of Shisa6-associated GluD2 (beads-depleted: set to 100%, anti-GluA2-depleted, $p = 0.31$). We therefore conclude that native Shisa6-GluD2 binding does not depend on co-association with GluA2 and predominantly constitutes a separate protein subcomplex. In conclusion, Shisa6 has a distinct cerebellar interaction profile that includes the independent association with both AMPA- and Delta-2 type glutamate receptors.

Shisa6 deletion results in AMPAR downregulation and GluD2 upregulation

Since Shisa6 associates with both AMPA- and GluD2-type glutamate receptors, and given that sEPSC amplitude and frequency at PC synapses was reduced upon deletion of *Shisa6*, we next investigated how the absence of *Shisa6* affected synaptic protein levels. To this end we first extracted all proteins from the crude synaptic membrane fraction of eight WT and *Shisa6*^{null} mice and subjected these to sequential window acquisition of all theoretical fragment ion spectra (SWATH) MS analysis (Figure 3A, B, S2A and Supplementary File 2). The resulting proteome encompassed 3,043 proteins with highly reproducible quantification (Figure S2C, CV = 0.064). In line with the reduced sEPSC amplitude we observed a significant downregulation of both synaptic GluA3 (*Gria3*) ($p < 0.001$) and GluA2 (*Gria2*) ($p < 0.001$) within *Shisa6*^{null} mice, whereas GluA1 (*Gria1*) levels did not change ($p = 0.026$). Interestingly, the opposite effect was observed for the GluD2 receptor (*Grid2*), which was upregulated under *Shisa6* KO conditions ($p < 0.001$).

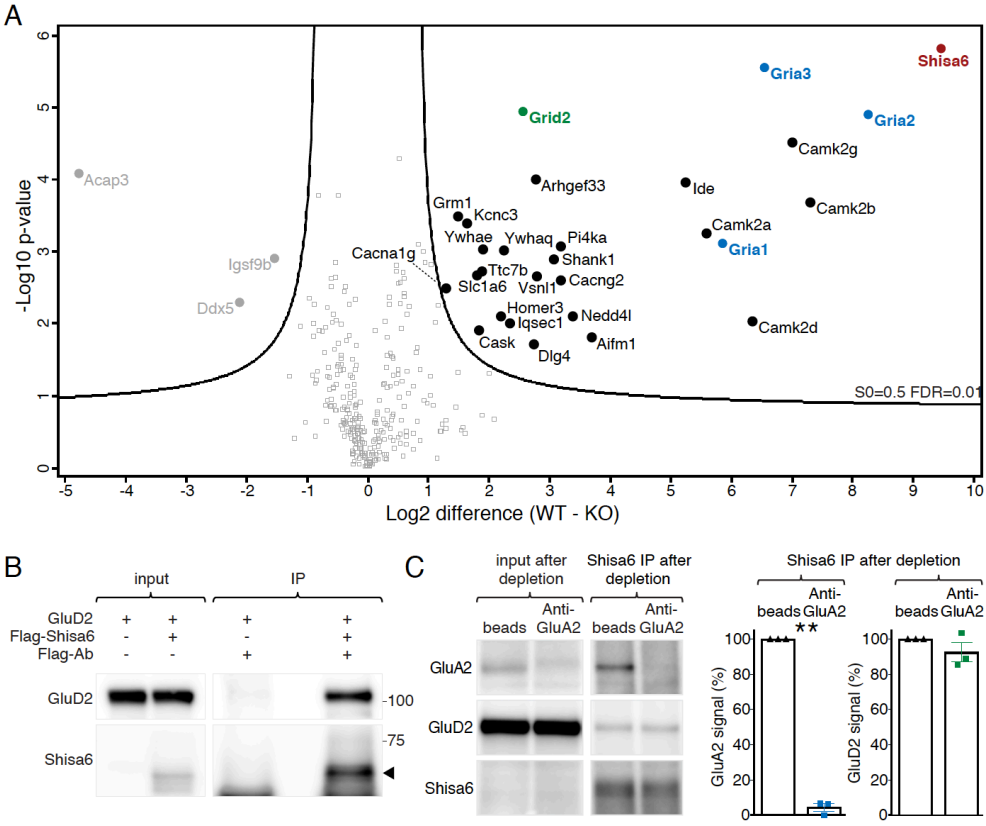

Figure 2. Cerebellar Shisa6 interacts with both AMPA- and Delta-2-type glutamate receptors. (A) Native Shisa6 complexes were immunoprecipitated from the cerebellum of Shisa6 WT and *Shisa6*^{nul} mice (DDM-extracted crude synaptic membranes; n = 3 IPs per genotype) and subjected to mass spectrometric analysis. Significantly enriched proteins are represented by closed circle symbols and labelled by gene name (Student's t-test with permutation-based FDR analysis; S0 = 0.5, FDR = 0.01). Additional information, including protein identification and quantification, statistical analysis, data distribution, and the full list of proteins is provided in Supplementary File 1. (B) GluD2 directly binds to flag-Shisa6 as shown by co-precipitation from HEK293 cells using a Flag-specific antibody. (C) Native Shisa6-GluD2 association is independent of GluA2, as revealed by immuno-depletion IP. GluA2 complexes were removed from the DDM-extracted crude synaptic membrane lysate by immunoprecipitation using an anti-GluA2 antibody (empty beads as control), yielding the "input after depletion" fraction. Shisa6 complexes were immunoprecipitated from this depleted input and their GluA2 and GluD2 content quantified. Shown on the left is an example experiment, with the averaged results of three replicates on the right. Data is represented as mean ± SEM, where significance is indicated by ** = $p < 0.01$.

The function of GluD2 is crucial for the formation, maintenance and even regenerative properties of the PF to PC synapse [259]. Because Shisa6 strongly interacts with GluD2, and the GluD2 levels are upregulated in the absence of Shisa6 in the *Shisa6*$^{L7\ KO}$, we investigated

the impact on synapse number and synaptic morphology in PCs using electron microscopy (Figure 3C).

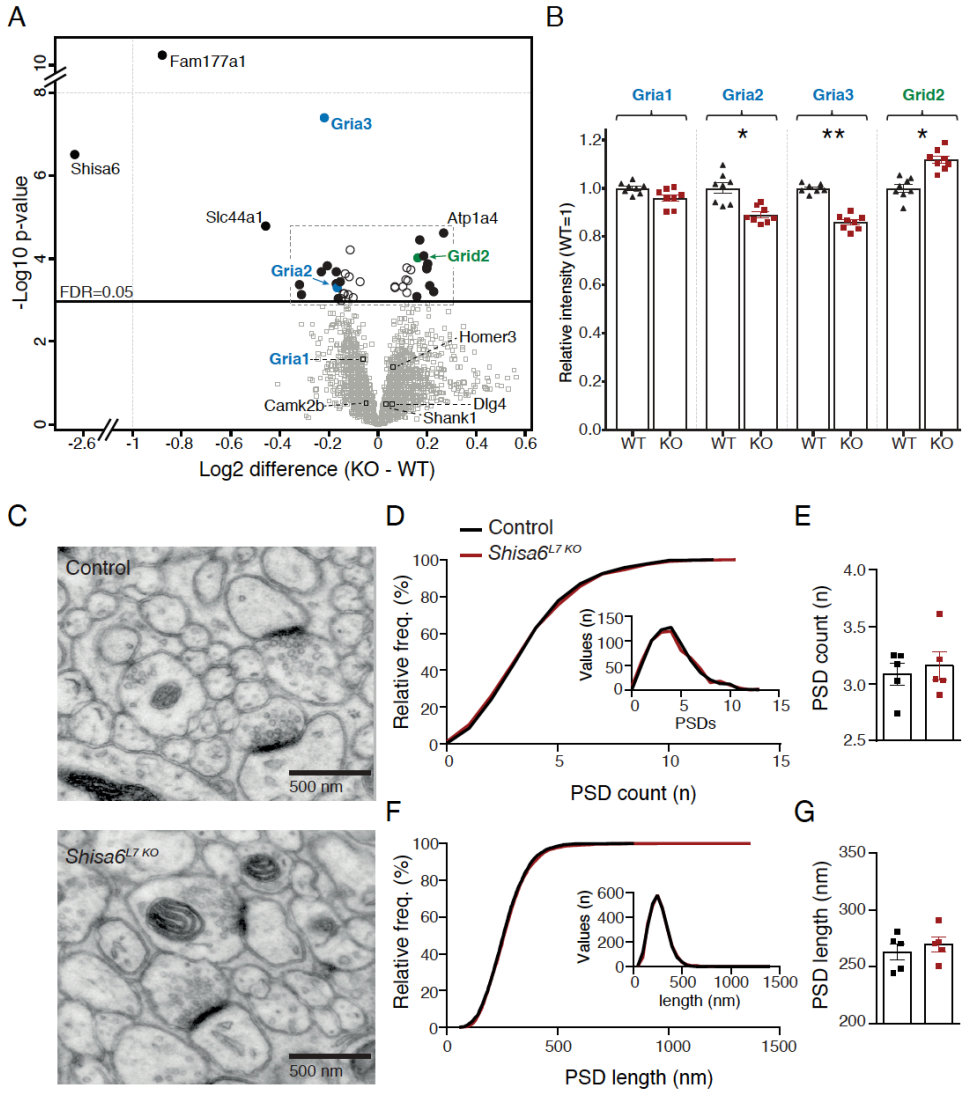

Figure 3. *Shisa6* deletion alters synaptic glutamate receptor levels without affecting PSD length or count. (A) Comparison of the cerebellar synaptic proteome of WT and *Shisa6*^{null} mice, as acquired by label free SWATH-MS measurement. Proteins with a significant difference between the mice are represented by circle symbols and labelled by gene name (Student t-test with permutation-based FDR correction, FDR ≤ 0.05); filled circles indicate proteins with a fold-change greater than 10%. AMPAR subunits GluA2 (*Gria2*) and GluA3 (*Gria3*) are significantly downregulated upon Shisa6 deletion, whereas GluD2 (*Grid2*) reveals an increased expression in the absence of Shisa6. See Supplementary Fig. 2a for a more detailed overview of the proteins at the centre of the

volcano plot, and Supplementary File 2 for a full list of proteins. (B) Detailed comparison of GluA and GluD2 regulation after setting the mean WT intensity to 1. (C) Examples of EM pictures including PF to PC synapses and their PSDs. (D) Cumulative frequency plot (histogram inset) of all sampled EM pictures indicating no population difference in PSD count (control: 640 images/5 mice; *Shisa6*$^{L7\ KO}$: 640 images/5 mice). (E) Average PSD count per animal did not differ between the groups. (F) Cumulative frequency plot (histogram inset) of all sampled PSDs indicating no population difference in PSD length (control: 2629 PSDs/5 mice; *Shisa6*$^{L7\ KO}$: 2629 PSDs/5 mice). (G) Average PSD length per animal did not differ between the groups. Data is represented as individual replicates and by the mean ± SEM; significance is indicated by * = q < 0.05, ** = q < 0.01.

The number of PSDs was unaffected in *Shisa6*$^{L7\ KO}$ (Figure 3D, E, p = 0.65). Similarly, the length of the PSD was not affected (Figure 3F, G, p = 0.51). Finally, we did not observe changes in the protein composition of the postsynaptic density (PSD), as indicated by the unmodified expression of PSD marker proteins, e.g., Shank1, PSD95 (*Dlg4*), Homer3 and CamK2B (Figure S2B). In summary, the absence of *Shisa6* does not affect the composition, length or number of PSDs in PCs. However, the removal of Shisa6 enhances synaptic GluD2 levels, while reducing the number of GluA2- and GluA3-containing AMPAR receptors.

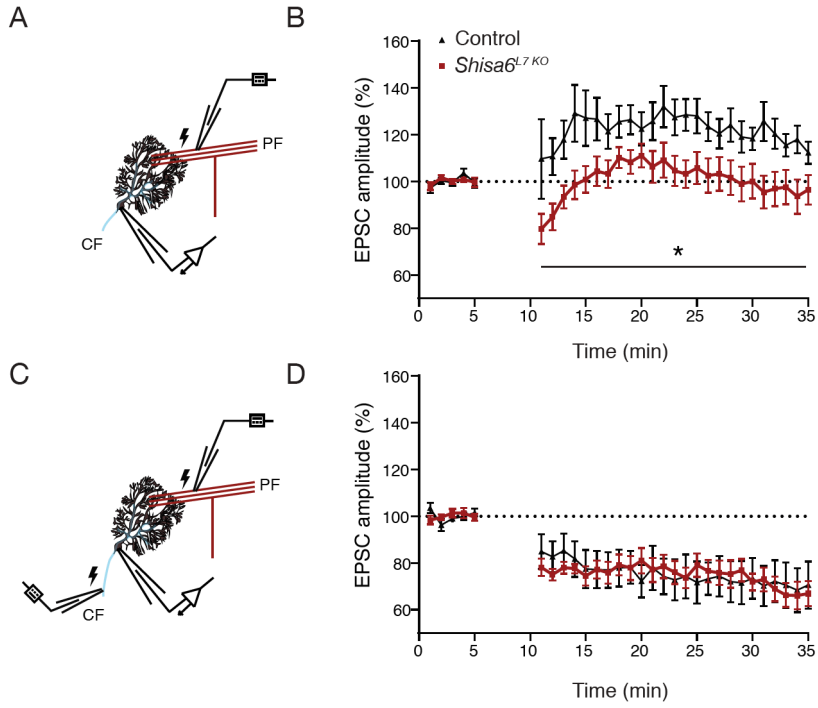

Figure 4. Shisa6 affects LTP, but not LTD at the PF-PC synapse. (A) Recording configuration for PF-PC stimulation and PC voltage clamp in LTP experiments. (B) LTP at the PF-PC synapse was induced in control animals after a 5-minute induction protocol, whereas LTP was absent in the *Shisa6*$^{L7\ KO}$ (control 7 cells/4 mice;

Shisa6$^{L7\ KO}$: 9 cells/5 mice). (c) Recording configuration for PF-PC LTD. PF are stimulated in the distal ML, whereas the CF is stimulated close to the soma. (d) LTD was successfully induced in both control and *Shisa6*$^{L7\ KO}$ animals after a 5-minute induction of conjunctive CF and PF stimulation (control: 7 cells/5 mice; *Shisa6*$^{L7\ KO}$: 7 cells/5 mice). For both LTP and LTD, the pre-induction data is based on the mean of the last 5 minutes of the baseline recording. Post-induction data is the mean of minutes 20-25 of the post-induction recording. Data are represented as mean ± SEM; significance is indicated by * = $p < 0.05$, ** = $p < 0.01$.

Impaired LTP, but not LTD, in PCs of Shisa6$^{L7\ KO}$ mice

Given that auxiliary subunits of AMPARs, of which Shisa6 is one, have previously been shown to affect excitatory current potentiation, we hypothesized that PC synaptic plasticity could be affected in the *Shisa6*$^{L7\ KO}$. Using high frequency stimulation (Figure 4A) we were able to induce LTP in PCs of control mice (Figure 4B, $p = 0.027$), but not of *Shisa6*$^{L7\ KO}$ (Figure 4B, $p = 0.54$). We also evaluated long-term depression (LTD) using the classical 1 Hz protocol of CF activation together with PF stimulation (Figure 4C) and found that LTD could be induced in PCs of both control (Figure 4D, $p = 0.025$) and *Shisa6*$^{L7\ KO}$ mice (Figure 4D, $p = 0.008$). In addition, we explored CFs *ex vivo* during development and found no evidence for impaired CF elimination in the *Shisa6*$^{L7\ KO}$, reducing the possibility of abnormal CF innervation due to a developmental phenotype (Figure S1, $p = 0.57$). Together, these results indicate that a lack of *Shisa6* impairs LTP, whereas LTD and CF development appear unaffected.

Shisa6$^{L7\ KO}$ mice show impaired motor performance and learning

To explore behavioural phenotypes in the *Shisa6*$^{L7\ KO}$, we assessed a number of basic cerebellum-dependent motor behaviours. The baseline motor performance evaluated with rotarod indicated that *Shisa6*$^{L7\ KO}$ mice tend to fall earlier from the rotating wheel (Figure 5A, B, day 1-4, 40 rpm. $p = 0.044$; day 5, 80 rpm., $p = 0.008$). This was not due to altered grip force, because this ability was unaffected (Figure S3A, $p = 0.28$). On the Balance Beam, used to evaluate gross movement coordination on a small diameter rod, we found no significant impairment in the *Shisa6*$^{L7\ KO}$ (Figure S3B, 6 mm rod, $p = 0.24$; 12 mm rod: $p = 0.22$). However, when we evaluated the walking patterns on the pressure-sensitive rungs of the ErasmusLadder we observed significantly impaired motor coordination as indicated by an increased number of missteps in the *Shisa6*$^{L7\ KO}$ (Figure 5A, C, $p = 0.004$) [213].

Next, we analysed compensatory eye movements, commonly used to assess the cerebellar contribution to motor performance and procedural learning [179, 260]. Examination of the visual-input-driven optokinetic reflex (OKR) indicated that both the OKR gain (Figure 5D,

p = 0.012) and OKR phase (Figure 5E, p = 0.008) with respect to the stimulus were reduced in *Shisa6*$^{L7\ KO}$ mice. When testing the vestibulo-ocular reflex (VOR) we found that VOR gain (Figure 5F, p = 0.044) was higher in the KO, whereas VOR phase (Figure 5G, p = 0.15) was not affected. In the visually guided VOR (VVOR) paradigm we found no differences in gain (Figure 5H, p = 0.36) or phase (Figure 5I, p = 0.69), indicating that the increase in VOR gain allowed the *Shisa6*$^{L7\ KO}$ mice to compensate for their impairments in optokinetic control. These data are in line with previous recordings in *Lurcher* mice [261], highlighting that cerebellar cortical deficits generally result in an impaired OKR performance, which is being compensated by increased VOR performance.

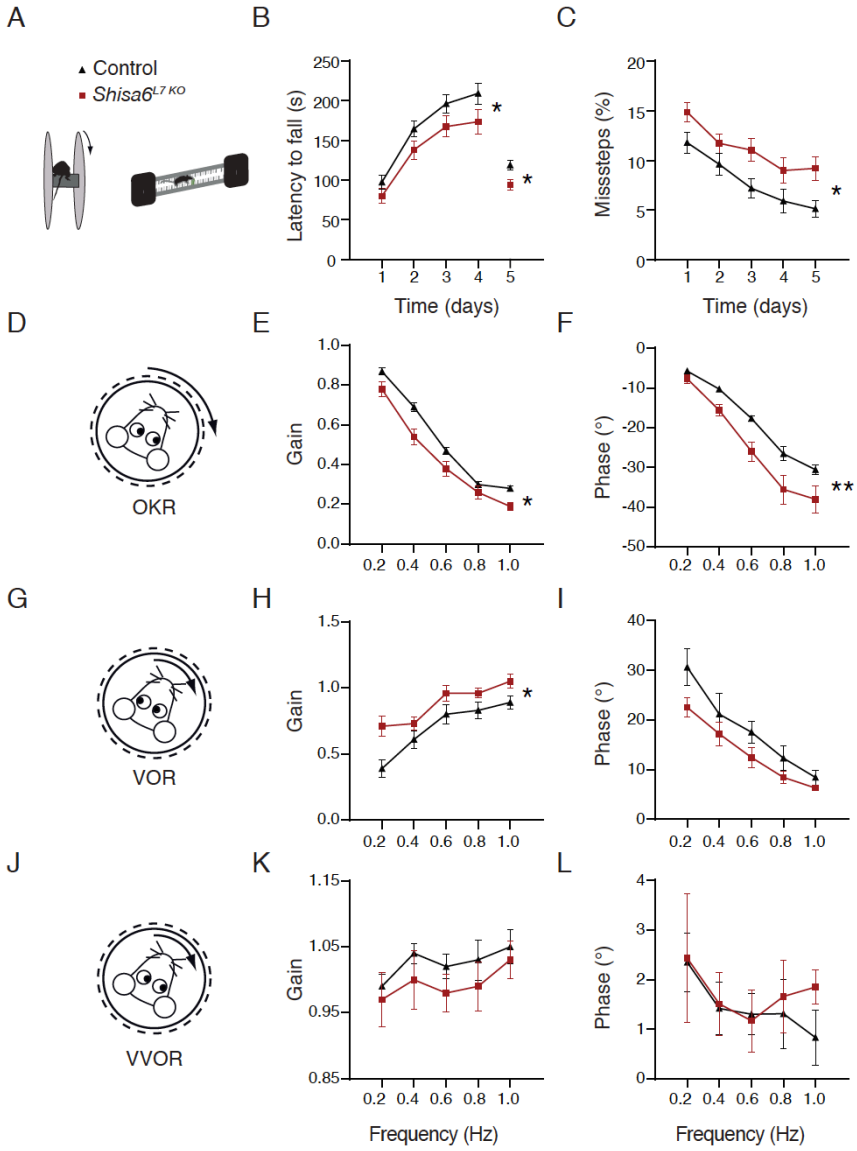

Figure 5. *Shisa6*$^{L7\ KO}$ mice show impaired motor performance. (A, B) The baseline motor performance investigated on the rotarod indicated that *Shisa6*$^{L7\ KO}$ mice tend to fall faster from the rotating wheel (control: 17 mice; *Shisa6*$^{L7\ KO}$: 16 mice). (A, C) Walking patterns on the the ErasmusLadder indicate impaired motor coordination as revealed by an increased number of missteps in the *Shisa6*$^{L7\ KO}$ (control: 10 mice; *Shisa6*$^{L7\ KO}$: 9 mice). (D, E) Motor performance of the optokinetic reflex (OKR), evaluated with a drum that moves in the horizontal plane around the mouse at increasing frequencies, was impaired in both the gain- and phase-measurements for the *Shisa6*$^{L7\ KO}$ mice (control: 7 mice; *Shisa6*$^{L7\ KO}$: 6 mice). (F, G) Vestibulo-ocular reflex (VOR) performance, where vestibular input in the dark induces compensatory eye movements, was significantly higher

for VOR gain in the *Shisa6*$^{L7\ KO}$ (control: 7 mice; *Shisa6*$^{L7\ KO}$: 6 mice). (H, I) Baseline visual VOR (VVOR) performance, utilizing both the vestibular and optokinetic modalities, was unaffected in the *Shisa6*$^{L7\ KO}$ mice (control: 7 mice; *Shisa6*$^{L7\ KO}$: 6 mice). Data are represented as mean ± SEM; significance is indicated by * = $p < 0.05$, ** = $p < 0.01$.

Given that excitatory input and plasticity at the PF to PC synapse is dysfunctional in *Shisa6*$^{L7\ KO}$ mice, we hypothesized that cerebellum-dependent motor learning might also be affected. To test this hypothesis, we first subjected the *Shisa6*$^{L7\ KO}$ and control mice to visuo-vestibular mismatch training (Figure 6A). This sensitive five-day training paradigm first aims to decrease the gain and then to reverse the phase of the VOR from the direction opposite to the vestibular input (indicated as 0°) to an eye movement that is in the same direction as the vestibular input (>90°). Mice were trained with the mismatching visual stimulus in the light, and tested in the dark for learned responses. Analysis of the first day alone indicates that *Shisa6*$^{L7\ KO}$ mice have impaired VOR gain-decrease learning, a sign of severe motor learning impairment (Figure 6B, $p < 0.001$) [109]. Indeed, whereas control mice demonstrated the ability to adapt (stats versus baseline), phase reversal adaptation was severely impaired in mutant mice (Figure 6C, $p = 0.002$). This interpretation was further confirmed when we analysed the eye movements made by the *Shisa6*$^{L7\ KO}$ mice during the training in the light condition. *Shisa6*$^{L7\ KO}$ mice were unable to adapt their VOR, and also impaired in tracking the visual training stimulus during the training (Figure S5B, $p < 0.001$). We next subjected the mice to a Pavlovian eyeblink conditioning paradigm, using a light pulse as a conditioning stimulus (CS) and a corneal air puff as an unconditioned stimulus (US) (Figure 6D). *Shisa6*$^{L7\ KO}$ mice had significantly lower CR amplitudes resulting in a lower CR percentage (Figure 6D-F, CR amplitude, $p = 0.006$; CR percentage, $p = 0.004$). Together, the compensatory eye movement and eye-blink conditioning paradigms reveals that Shisa6 is relevant for both baseline motor performance as well as cerebellum-dependent motor learning.

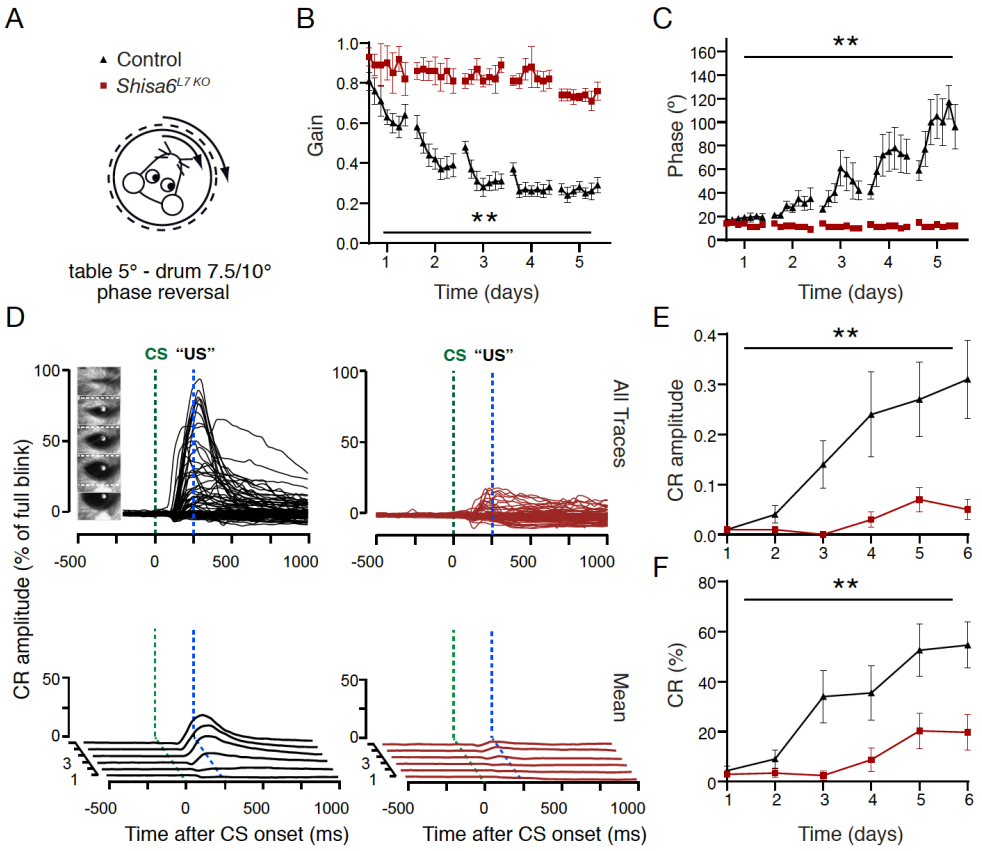

Figure 6. *Shisa6*$^{L7\ KO}$ mice show impaired motor learning. (A) After phase reversal training, in which visual and vestibular input was mismatched, mice were tested in the dark for learned responses. (B, C) The *Shisa6*$^{L7\ KO}$ mice showed severe impairments in phase reversal adaptation, evidenced by a lack of gain and phase modulation over days, whereas control mice showed a reduction in gain and an increase in phase (control: 7 mice; *Shisa6*$^{L7\ KO}$: 6 mice). (D) Experimental setup for the eyeblink conditioning where a 260 ms LED light was used as the conditioned stimulus (CS), and a corneal air puff as the unconditioned stimulus (US). Post-training testing was done using only the CS. Top: the eyelid responses for all individual trials. Bottom: the average eyeblink amplitude for each of the six sessions. (E) The average CR amplitude (threshold: eyelid movement at least 10% of a full blink) for eyelid movements in the 500 ms centred around the US was significantly lower in the *Shisa6*$^{L7\ KO}$ mice compared to the controls (control: 16 mice; *Shisa6*$^{L7\ KO}$: 16 mice). (F) The percentage of CR responses over sessions. The *Shisa6*$^{L7\ KO}$ mice showed significantly fewer responses than the control over time, indicative of impaired learning (control: 16 mice; *Shisa6*$^{L7\ KO}$: 16 mice). Data are represented as mean ± SEM; significance is indicated by * = $p < 0.05$, ** = $p < 0.01$.

Lower spike output and enhanced regularity of PC firing in Shisa6L7 KO mice.

The phenotypes in excitatory synaptic transmission and motor coordination impairments induced by PC-specific ablation of *Shisa6* have relatively strong effect sizes. However, the connection between *ex vivo* physiological abnormalities and behaviour is not directly apparent. To bridge this gap we analysed simple spike (SS) and complex spike (CS) firing frequencies and firing regularity (CV2) of PCs *in vivo*. To align our results with VOR adaptation and eyeblink conditioning while taking the baseline specifics of the mediating cerebellar zones into consideration (Zhou et al., 2014; De Zeeuw and Ten Brinke, 2015), we recorded Purkinje cell activity from both anterior (Figure 7A) and posterior (Figure 7D) lobules in awake mice. The SS firing rate of PCs was significantly lower in *Shisa6*$^{L7\ KO}$ mice in both the anterior (Figure 7B, $p = 0.009$) and posterior lobules (Figure 7E, $p = 0.003$). In addition, there was an increase in the regularity of SS firing in PCs of the anterior lobe (Figure 7C, $p < 0.001$), while the regularity of SS firing in the posterior lobe was not significantly different (Figure 7F, $p = 0.14$). The anterior rate (Figure S5A, $p = 0.40$) and regularity of CSs (Figure S5B, $p = 0.10$) were not affected. Neither was the rate (Figure S5C, $p = 0.16$) and regularity of CSs (Figure S5D, $p = 0.16$) in the posterior lobes. To exclude the possibility that the loss of *Shisa6* impairs firing rates *in vivo* through effects on intrinsic mechanisms for the generation of SSs in PCs, we injected currents of varying strengths into the PC soma *ex vivo* (Figure S6A). We found no change in the number of spikes generated in the *Shisa6*$^{L7\ KO}$ (Figure S6B, $p = 0.79$). In fact, blocking all afferent input and measuring the pacemaker activity of PCs in the anterior lobe with cell-attached recordings *ex vivo* obscured all the differences in firing frequency (Figure S6C, D, $p = 0.29$) or CV2 (Figure S6C, E, $p = 0.60$). For the posterior lobes, there was also no apparent difference in SS firing frequency (Figure S6F, G, $p = 0.64$) and CV2 value *ex vivo* (Figure S6F, H, $p = 0.33$). We conclude that there are no major deficiencies in the ability of PCs to generate SSs or CSs in *Shisa6*$^{L7\ KO}$ *ex vivo*, suggesting that Shisa6 has an important role in the proper integration of synaptic excitatory inputs *in vivo* that is required to control the frequency and regularity of SS firing of PCs in awake behaving animals.

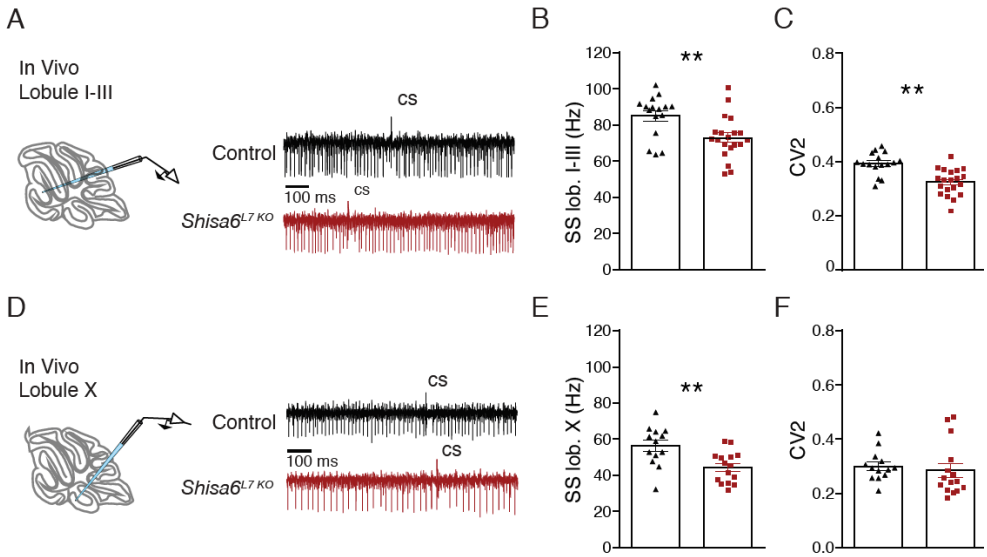

Figure 7. *Shisa6*$^{L7\ KO}$ mice show reduced simple-spike (SS) frequencies, and increased SS regularity *in vivo*. (A) Left: Recording configuration for anterior (lobule I-III) *in vivo* recordings. Right: example excitatory recordings from the anterior cerebellum. Note the complex spikes (CS), and subsequent SS pause. (B, C) SS frequency in lobules I-III was significantly lower in the *Shisa6*$^{L7\ KO}$. Moreover, a significant difference in the CV2 was found between the two groups, indicating that the SS regularity was increased in the *Shisa6*$^{L7\ KO}$ (control: 16 cells/3 mice; *Shisa6*$^{L7\ KO}$: 20 cells/3 mice). (D) Recording configuration for posterior (lobule X) *in* vivo recordings, as in A. (E, F) SS frequency was lowered in the *Shisa6*$^{L7\ KO}$ mice, whereas spike regularity was unaffected (control: 13 cells/3 mice; *Shisa6*$^{L7\ KO}$: 15 cells/3 mice). Data are represented as mean ± SEM; significance is indicated by * = $p < 0.05$, ** = $p < 0.01$.

Discussion

Here, we provide the first evidence for a role of Shisa auxiliary AMPAR subunits in cerebellar PF to PC synaptic function. We report the co-localization of the auxiliary AMPAR subunit Shisa6 with GluA2 in PCs, and a direct interaction with the AMPAR subunits GluA1–3 and non-AMPAR glutamate receptor subunit GluD2. Mice with PC-specific deletion of *Shisa6* showed strongly reduced PF to PC basal excitatory postsynaptic transmission, impaired LTP and reduced SS activity *in vivo*. Moreover, ablation of *Shisa6* in PCs resulted in impaired motor performance as well as severely affected procedural learning. Together, these findings indicate a crucial role for Shisa6 in the physiology of PF to PC synapses and cerebellum-dependent motor behaviour.

Several auxiliary subunits have thus far been shown to affect AMPAR conductance, kinetics and localization [248]. The first mouse line to spur interest in auxiliary subunits was the severely ataxic stargazin mouse mutant, in which a lack of the AMPAR-auxiliary subunit stargazin (TARPγ-2) resulted in absence of excitatory transmission at the mossy fibre to granule cell synapse [262, 263]. Subsequently, TARPγ-2 and other family members of the transmembrane AMPAR regulatory proteins (TARPs) have been shown to control both trafficking and kinetic profiles of AMPARs [248, 264, 265]. Specific and partially overlapping modulating effects have also been found to occur in the Shisa family of auxiliary AMPAR subunits. For instance, the first identified member of the Shisa family, Shisa9 (CKAMP44), was shown to cause stronger and faster desensitization of AMPARs currents in the hippocampus [253, 255], whereas Shisa6 was recently reported to decrease the rates of deactivation and desensitization of AMPARs, while enhancing the steady-state current and providing slow recovery from desensitization [251].

We report that Shisa6 co-localizes with GluA2 in PCs and that its absence from PCs results in decreased decay times of their sEPSCs, in line with previously reported data on Shisa6 at AMPARs in the hippocampus [251]. In addition, we find that the amplitude and frequency of spontaneous EPSCs in PCs are both lower in *Shisa6*$^{L7\ KO}$ mice and that the amplitude of their EPSCs evoked by PF stimulation is also reduced. The latter findings stand in marked contrast to what was observed in the hippocampus, as deletion of *Shisa6* in hippocampal pyramidal neurons did not affect their baseline EPSC amplitudes at CA3/CA1 synapses [251]. To elucidate the mechanism involved in the reduction of excitation at the PF to PC synapse, we first set out to identify Shisa6 interacting proteins in PC synaptosomes. Here, in addition to AMPAR subunits GluA1–3 we identified a strong cerebellum-specific GluD2 interaction with Shisa6. Previously, the absence of GluD2 in different KO models has revealed its function in PF to PC AMPAR composition, morphology as well as LTD [256-259, 266]. We further explored the abundancy of synaptic proteins and found that levels of GluA2 and GluA3 were decreased in the absence of *Shisa6*, whereas GluD2 was increased. The changes in level of GluD2 could signal morphological or pre-synaptic changes, as GluD2 is involved in presynaptic function and glutamate release, as shown from *GluD2* null mice [267]. However, we found no evidence for morphological abnormalities at the PF to PC synapse in both PSD count and length under the condition of increased GluD2 levels. In addition, no pre-synaptic abnormalities were detected in the paired pulse facilitation paradigms, a phenotype that has also previously been detected in the absence of *GluD2* [267]. In the absence of any major morphological PF to PC abnormalities at least two main postsynaptic factors may contribute to the reduced spontaneous and evoked EPSC

amplitudes observed in our study. First, there is a decrease of active postsynaptic AMPARs, as indicated by the down regulation of AMPAR subunits GluA2 and GluA3. Secondly, considering that Shisa6 traps AMPARs by interacting with PSD-95 in the hippocampus, abnormal localization of AMPARs in the PSD could contribute to synaptic potentiation at different time scales, which has been shown to directly impact desensitization of the AMPARs [268]. In contrast to the hippocampal studies, Shisa6 has an additional mode of function in PCs through the mediation of GluD2 receptor function. The upregulation of GluD2 could further restrict the number of active AMPARs at the PF to PC synapse while not affecting CF to PC synapses, as deletion of *GluD2* is known to lead to higher expression of AMPARs at PC synapses [256].

Dynamic changes in the number and sensitivity of AMPARs are thought to be part of the central mechanism that facilitates different types of learning [30, 246, 269]. Work on molecular targets involved in plasticity mechanisms at the PF to PC synapse has revealed different molecules involved in AMPAR modulation, including TARPγ–2, GluD2, phosphatases, kinases, scaffolding proteins, and the GluA3 subunit [22, 29, 30, 270-272]. When assessing the role of Shisa6 in long-term synaptic plasticity we found an impaired induction of LTP in PCs of *Shisa6*$^{L7\ KO}$ mice, whereas LTD can still be induced. Interestingly, recent findings indicate that induction of LTP at the PF to PC synapse can be facilitated through increases in AMPAR open-channel probability [30]. Even though Shisa6 has not been shown to regulate the amplitude of AMPAR-mediated current directly, in the absence of *Shisa6* the total AMPAR depolarizing current over time is reduced because of faster deactivation. Because PF to PC synapses are typically activated by sensory learning-mediated bursts of granule cell activity [273], which in turn can drive Ca^{2+} T-type channel-dependent LTP [274], it is plausible that impaired LTP induction in *Shisa6*$^{L7\ KO}$ is a direct result of faster AMPAR deactivation and thus less postsynaptic depolarization than would be needed for Ca^{2+}-dependent LTP induction. In contrast, LTD is dependent on large climbing fibre depolarization-induced influx of Ca^{2+} and consequently the removal of AMPARs from the membrane. This form of synaptic plasticity appears not directly affected by Shisa6's absence. We find that the CF to PC response leads to normal CS spike frequency and regularity *in vivo,* in addition to normal CF elimination during developmental stages. In short, Shisa6 appears to both affect basal neurotransmission as well as LTP at the PF to PC synapse.

Shisa6$^{L7\ KO}$ mice have strong impairments in behaviour as indicated by the deficiencies identified in OKR and VOR, as well as on the Rotarod and ErasmusLadder. In addition to

the motor performance impairments we found strong motor learning deficits as shown by VOR phase reversal and the classical eye blink conditioning paradigm. Physiological abnormalities, in addition to synaptic LTP, are further revealed using *in vivo* single unit recordings of PCs where we show that the firing frequency, as well as regularity, of simple spikes (SS) is lower. In a similar way that excitatory input at the PF to PC synapse can affect SS regularity, changes in the inhibitory input from molecular layer interneurons could also affect regularity of SS [29, 275]. However, we think this is unlikely as we find no change in the sIPSC frequency or amplitude in the absence of *Shisa6*.

It has become apparent that cerebellar mutant mouse models in which synaptic plasticity is impaired, result in impaired motor learning but not motor performance impairments per se [24, 29, 30]. Here, we show that the absence of *Shisa6* results in both motor impairments and motor learning deficits and that these behavioural abnormalities coincide with basal synaptic excitatory transmission, LTP as well as *in vivo* spike output and regularity of firing deficiencies in PCs. By now, plenty of studies have reported that regularity of SS firing and its modulation through synaptic input plays crucial roles in motor learning [29, 275-279]. One obvious way by which the reduced frequency and regularity of SS firing in PCs of the *Shisa6*$^{L7\ KO}$ mice contributes to the behavioural phenotypes is by impaired spatiotemporal coding of sensory information [13]. To our knowledge, this is the first report on the effects of auxiliary subunit-mediated AMPAR deactivation on LTP and spike frequency modulation in the cerebellum, coupled to strong baseline performance and learning phenotypes. Together, these results provide novel insight into the roles that auxiliary AMPAR subunits can play in the long-term modulation of synaptic currents, neuronal excitability and consequentially behaviour.

AUTHOR CONTRIBUTIONS

Conceptualization, S.P., B.H.A.U., R.V.K., S.S., A.B.S., C.I.D.Z.; Methodology, S.P., B.H.A.U., R.V.K., B.W., J.A.S., H.J.B.; Validation, S.P., B.H.A.U., R.V.K.; Formal Analysis, S.P., B.H.A.U., R.V.K.; Investigation, S.P., B.H.A.U., R.V.K., B.W., J.A.S., H.J.B., S.A.; Resources, S.S., A.B.S., C.I.D.Z.; Data Curation, S.P., B.H.A.U., R.V.K.; Writing-Original Draft, S.P. B.H.A.U.; Writing-review & Editing, S.P., B.H.A.U., R.V.K., M.S., F.E.H., S.S., A.B.S., C.I.D.Z; Supervision, S.S., A.B.S., C.I.D.Z.

ACKNOWLEDGMENTS

We would like to express our gratitude for excellent technical assistance by Elize Haasdijk, Mandy Rutteman and Laura Post.

R.V.K. was funded by NWO-ALW grant (#ALW2PJ/12048), SS by an NWO VICI grant (ALW-Vici 016.150.673/865.14.002).

DECLARATION OF INTEREST

The authors declare no competing interests.

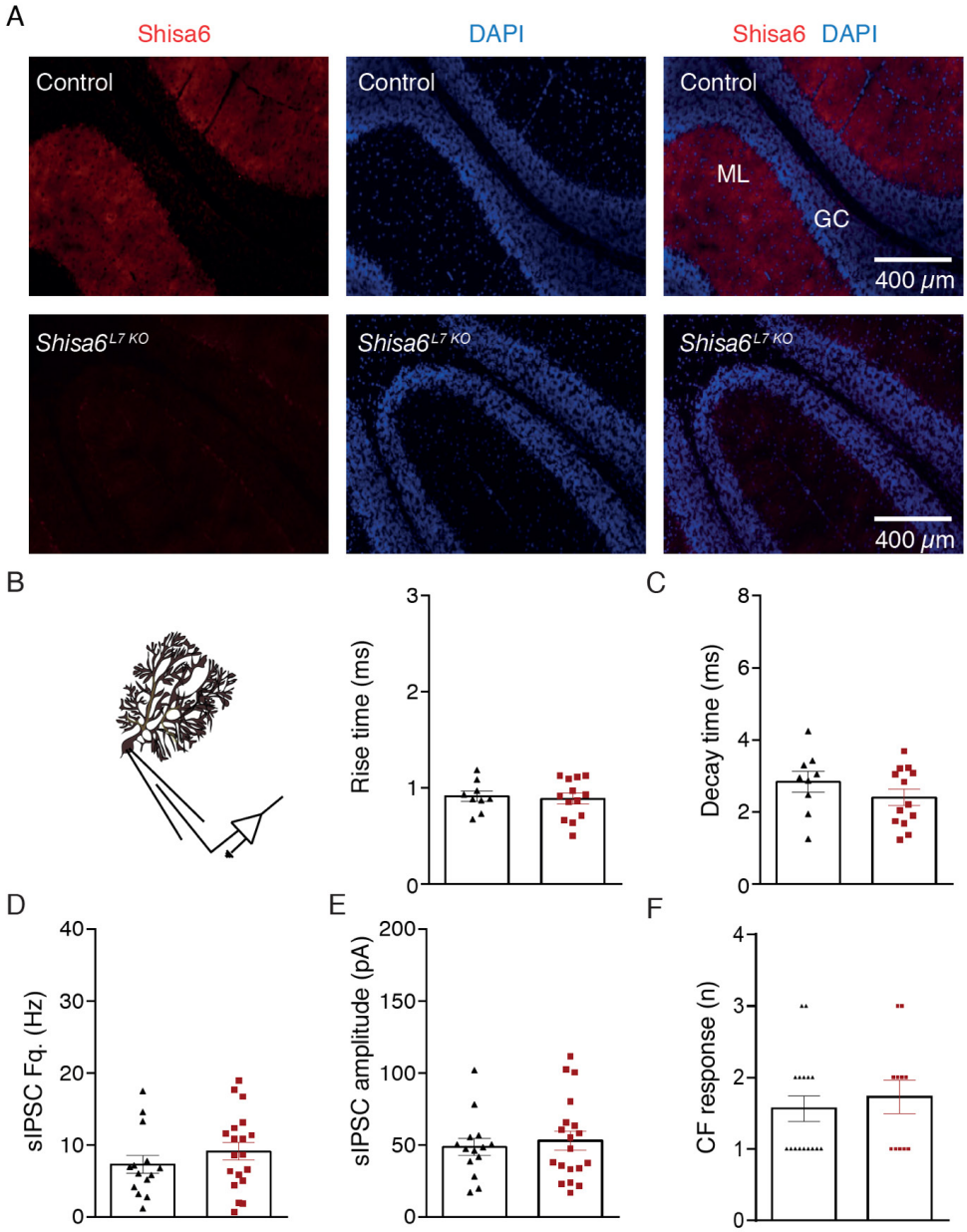

Figure S1. Related to Figure 1, Shisa6 expression is absent in the ML of *Shisa6*$^{L7\ KO}$ mice. The absence of Shisa6 has no impact on either sIPSCs or CF elimination. (A) Representative confocal images of the cerebellar cortex of both control and *Shisa6*$^{L7\ KO}$ littermates, showing strong expression of Shisa6 predominantly in the ML, and absence of Shisa6 in the *Shisa6*$^{L7\ KO}$ mice. (B, C) Left: recording configuration for sIPSC acquisition. Right: The absence of *Shisa6* does not affect sIPSC kinetics, evidenced by the equivalent rise and decay times for both groups (control: 10 cells/3 mice; *Shisa6*$^{L7\ KO}$: 13 cells/3 mice). (D, E) sIPSC frequency and median amplitude are similarly

unaffected by the absence of Shisa6 (control: 14 cells/3 mice; *Shisa6*$^{L7\ KO}$: 19 cells/5 mice). (F) Climbing fibre elimination in young mice was not different in the *Shisa6*$^{L7\ KO}$ mice compared to controls (control: 16 cells/3 mice; *Shisa6*$^{L7\ KO}$: 11 cells/3 mice). Data are represented as mean ± SEM; significance is indicated by * = p < 0.05, ** = p < 0.01.

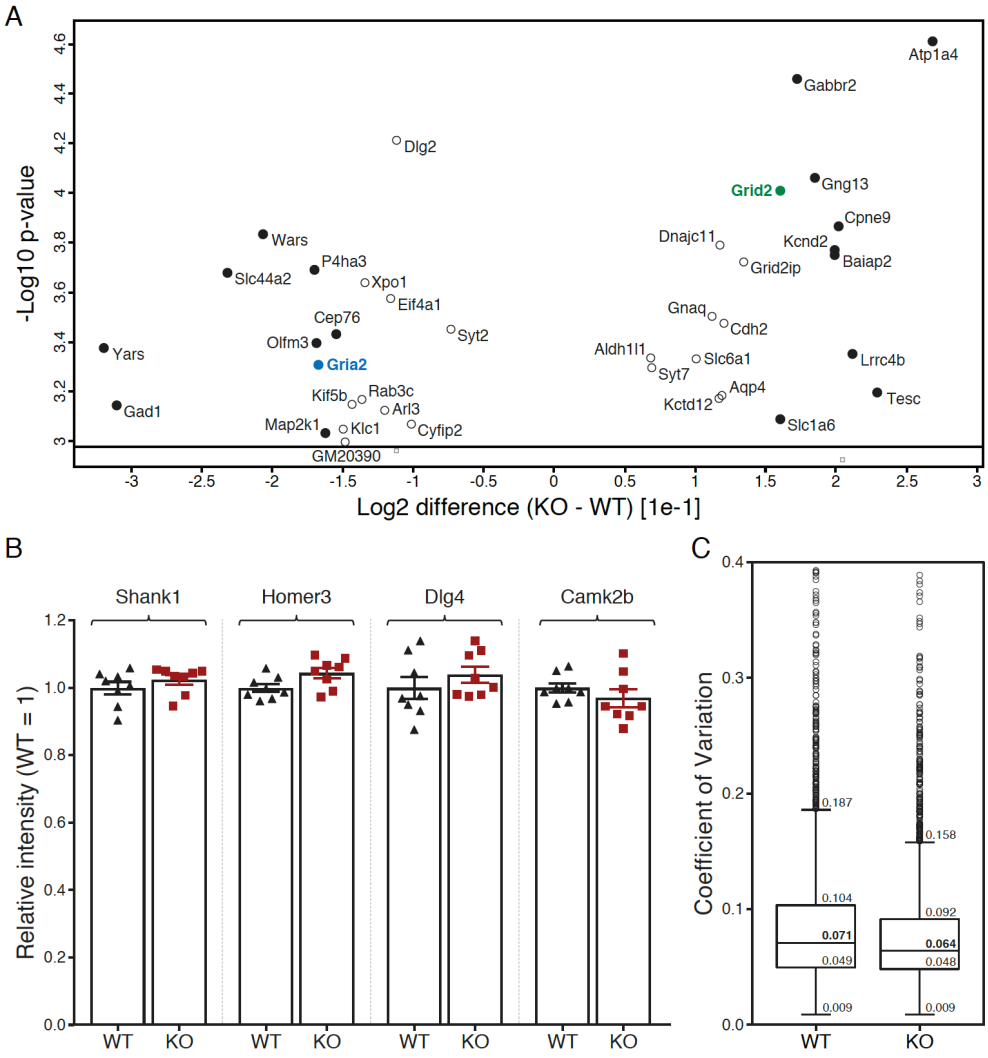

Figure S2. Related to Figure 3, proteins showing increased and decreased expression in the absence of *Shisa6*. A group of core PSD proteins is unaffected. (A) A more detailed view of the significantly differentially expressed proteins in the *Shisa6*^{null} as described in Figure 3a. Open circles are proteins with a fold-change below 10%; filled circles are proteins with a fold-change above 10%. (B) Four PSD-localized proteins, as identified by SWATH MS analysis, are unaffected by the absence of *Shisa6*. (C) The median Coefficient of Variation (CoV) of 3142

quantified protein groups for the Shisa6 WT and Shisa6^{null} replicas was 7.1% and 6.4%, respectively. Thereby demonstrating excellent reproducibility (data presented as Tukey boxed plot).

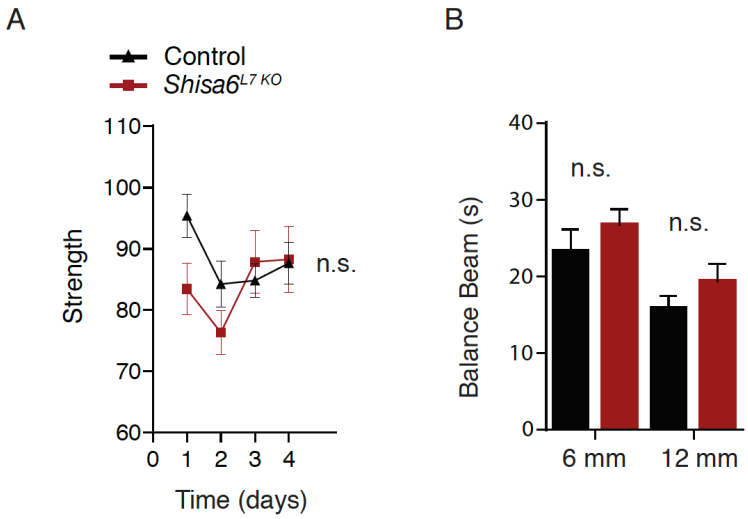

Figure S3. Related to Figure 5, no difference was found in the grip force and balance beam paradigms for the *Shisa6$^{L7\ KO}$* mice. (A) The grip force was not significantly different across 5 days of testing between the two groups (control: 17 mice; *Shisa6$^{L7\ KO}$*: 14 mice). (B) The balance beam test did not show any significant performance difference between the two groups (control: 17 mice; *Shisa6$^{L7\ KO}$*: 16 mice). Data are represented as mean ± SEM; significance is indicated by * = $p < 0.05$, ** = $p < 0.01$.

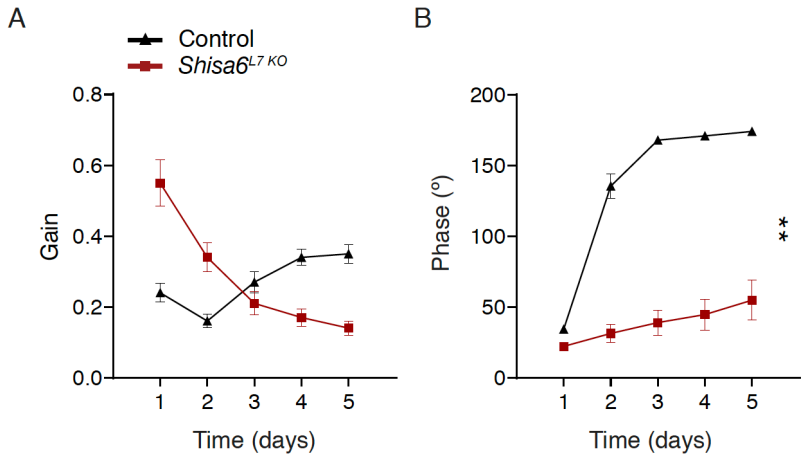

Figure S4. Related to Figure 6, averages of eye movements per day during training (in the light). (A, B) The *Shisa6*$^{L7\ KO}$ mice have extreme difficulties in the tracking of the visual stimulus during phase reversal training, which is clear from both the amplitude (gain) as well as the timing (phase) of the eye movements. (control: 7 mice; *Shisa6*$^{L7\ KO}$: 6 mice). Data are represented as mean ± SEM; significance is indicated by * = $p < 0.05$, ** = $p < 0.01$.

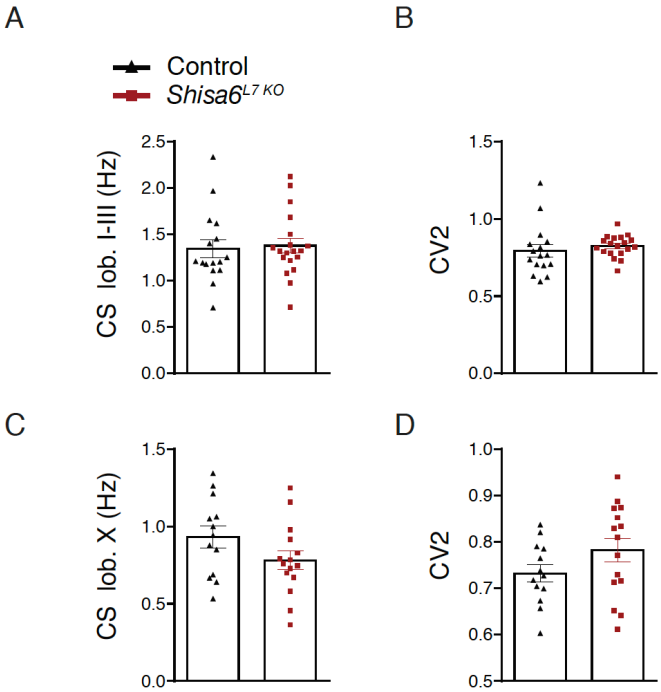

Figure S5. Related to Figure 7, complex spike (CS) parameters *in vivo* were unaffected in *Shisa6*$^{L7\ KO}$ mice. (A, B) CS frequency and regularity in the anterior lobules were unaltered in *Shisa6*$^{L7\ KO}$ *mice* (control: 16 cells/3 mice; *Shisa6*$^{L7\ KO}$: 20 cells/3 mice). (C, D) Similarly, the CS frequency and regularity are unaffected in the posterior lobule X in the *Shisa6*$^{L7\ KO}$ mice (control: 13 cells/3 mice; *Shisa6*$^{L7\ KO}$: 15 cells/3 mice). Data are represented as mean ± SEM.

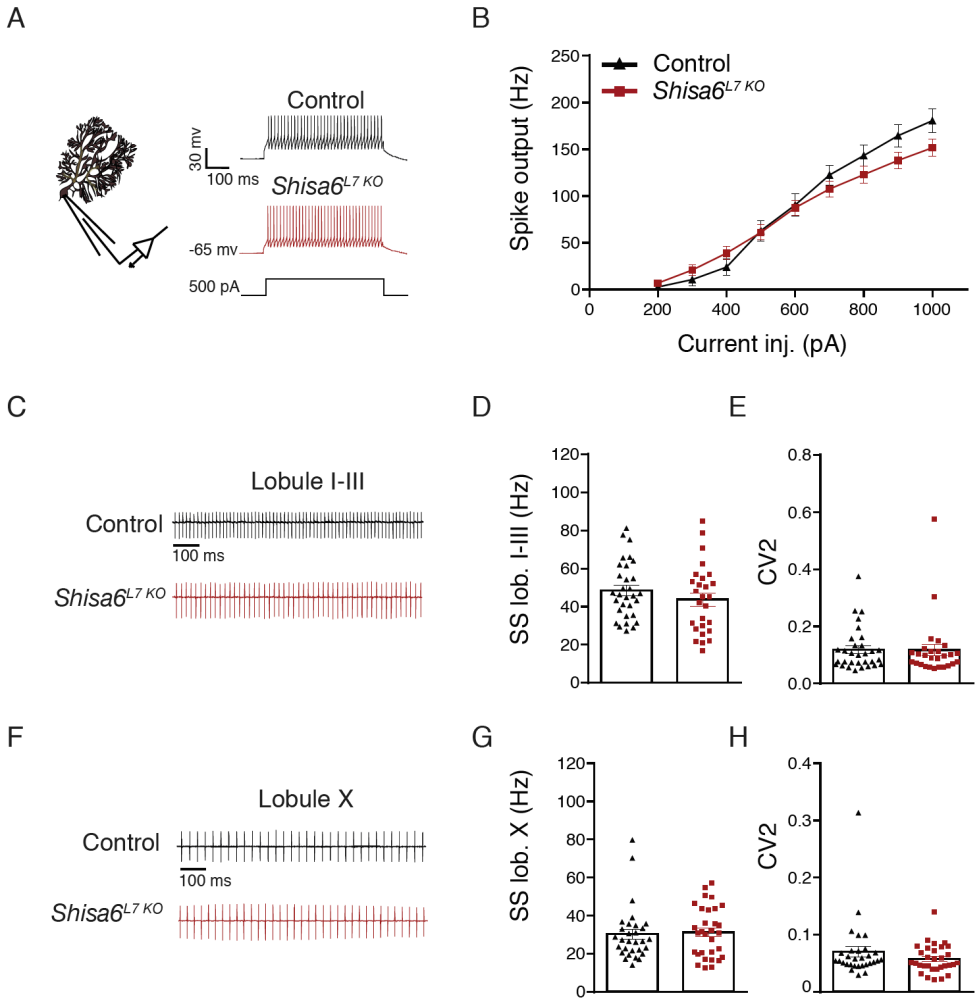

Figure S6. Related to Figure 7, intrinsic excitability as measured by current injections in current clamp recordings and *ex vivo* cell-attached recordings of spontaneous simple-spikes (SS), was unaffected in the *Shisa6*$^{L7\ KO}$ mice. (A) Recording configuration for whole cell patch clamp recording of PCs. Right: sample spike train after a 500 ms, 500 pA current injection in current clamp. (B) Spiking frequency as a measure of intrinsic excitability, evoked by current injections from 200 to 1000 pA, in 100 pA increments. No difference was observed between the control and *Shisa6*$^{L7\ KO}$ mice (control: 26 cells/4 mice; *Shisa6*$^{L7\ KO}$: 31 cells/3 mice). (C) Example traces of *ex vivo* cell-attached recordings in PC in the anterior lobules. (D, E) Neither the SS frequency, nor the SS regularity were not affected in the *Shisa6*$^{L7\ KO}$ animals (control: 31 cells/4 mice; *Shisa6*$^{L7\ KO}$: 27 cells/4 animals). (F) Example traces from *ex vivo* cell-attached recordings in lobule X. (G, H). As in the anterior lobules, SS frequency and regularity were unaffected in the *Shisa6*$^{L7\ KO}$ animals (control: 30 cells/4 mice; *Shisa6*$^{L7\ KO}$: 31 cells/4 mice). Data are represented as mean ± SEM.

Fig.	Exp.	Test	Variable	Group	Mean ± SD	Test statistic	P
1D	sEPSCs	Brown-Forsythe	Rise			W = 1.298	0.262
		Mann-Whitney U		Ctrl	1.75 ± 0.51 ms	U = 141.5	0.556
				Shisa6$^{L7\ KO}$	1.63 ± 0.40 ms		
1E	sEPSCs	Brown-Forsythe	Decay			W = 0.009	0.924
		Ind. t-test		Ctrl	3.95 ± 1.09 ms	t(34) = 2.972	0.005
				Shisa6$^{L7\ KO}$	2.91 ± 0.98 ms		
1G	sEPSCs	Brown-Forsythe	Amplitude			W = 1.829	0.182
		Ind. t-test		Ctrl	38.52 ± 11.72 pA	t(57) = 3.296	0.002
				Shisa6$^{L7\ KO}$	29.84 ± 8.51 pA		
1H	sEPSCs	Brown-Forsythe	Frequency			W = 0.155	0.695
		Mann-Whitney U		Ctrl	3.05 ± 2.86 Hz	U = 243	0.005
				Shisa6$^{L7\ KO}$	1.89 ± 2.41 Hz		
1J	PF-PC	Brown-Forsythe	3μA stim			W = 7.235	0.010
		Mann-Whitney U		Ctrl	48.35 ± 25.70 pA	U = 123	<0.001
				Shisa6$^{L7\ KO}$	22.67 ± 13.98 pA		
1J	PF-PC	Brown-Forsythe	6μA stim			W = 10.982	0.002
		Mann-Whitney U		Ctrl	140.35 ± 69.78 pA	U = 62	<0.001
				Shisa6$^{L7\ KO}$	51.66 ± 34.62 pA		
1J	PF-PC	Brown-Forsythe	9μA stim			W = 11.409	0.001
		Mann-Whitney U		Ctrl	215.41 ± 110.17 pA	U = 82	<0.001
				Shisa6$^{L7\ KO}$	80.43 ± 52.98 pA		
1J	PF-PC	Brown-Forsythe	12μA stim			W = 7.867	0.007
		Mann-Whitney U		Ctrl	261.40 ± 140.09 pA	U = 70	<0.001
				Shisa6$^{L7\ KO}$	92.89 ± 67.80 pA		
1J	PF-PC	Brown-Forsythe	15μA stim			W = 9.512	0.004
		Mann-Whitney U		Ctrl	300.48 ± 174.45 pA	U = 74.5	<0.001
				Shisa6$^{L7\ KO}$	101.14 ± 89.75 pA		
1K	PF-PC	Mixed-model ANOVA	ISI x geno	Between-subjects		F(1, 37) = 0.030	0.863
				Within-subjects		F(2.37, 87.97) = 33.615	<0.001
				Interaction		F(2.37, 87.97) = 2.535	0.075
1K	PF-PC	Brown-Forsythe	50 ms ISI			W = 0.323	0.573
		Descriptives		Ctrl	1.41 ± 0.17		
				Shisa6$^{L7\ KO}$	1.38 ± 0.20		
1K	PF-PC	Brown-Forsythe	100 ms ISI			W = 0.003	0.960
		Descriptives		Ctrl	1.26 ± 0.18		
				Shisa6$^{L7\ KO}$	1.18 ± 0.19		
1K	PF-PC	Brown-Forsythe	150 ms ISI			W = 0.196	0.661
		Descriptives		Ctrl	1.12 ± 0.10		
				Shisa6$^{L7\ KO}$	1.21 ± 0.12		
1K	PF-PC	Brown-Forsythe	200 ms ISI			W = 0.812	0.737
		Descriptives		Ctrl	1.10 ± 0.10		
				Shisa6$^{L7\ KO}$	1.10 ± 0.14		
S1B	sIPSCs	Brown-Forsythe	Rise			W = 0.420	0.524
		Ind. t-test		Ctrl	0.94 ± 0.17 ms	t(21) = 0.685	0.501
				Shisa6$^{L7\ KO}$	0.88 ± 0.21 ms		
S1C	sIPSCs	Brown-Forsythe	Decay			W = 0.453	0.508
		Ind. t-test		Ctrl	2.83 ± 0.82 ms	t(21) = 1.239	0.229
				Shisa6$^{L7\ KO}$	2.40 ± 0.81 ms		
S1D	sIPSCs	Brown-Forsythe	Frequency			W = 0.899	0.350
		Ind. t-test		Ctrl	7.33 ± 4.69 Hz	t(31) = -1.014	0.318
				Shisa6$^{L7\ KO}$	9.14 ± 5.33 Hz		
S1E	sIPSCs	Brown-Forsythe	Amplitude			W = 2.024	0.165

		Ind. t-test		Ctrl	48.64 ± 21.87 pA	t(31) = -0.491	0.627
				$Shisa6^{L7\ KO}$	53.14 ± 28.73 pA		
S1F	CF elim.	Brown-Forsythe	CF count			W = 0.058	0.733
		Mann-Whitney		Ctrl	1.56 ± 0.73	U = 77.5	0.568
				$Shisa6^{L7\ KO}$	1.73 ± 0.79		

Table S1. Related to Figure 1 and Figure S1

Italicized items indicate use of Greenhouse-Geisser correction

Table S2. Related to Figure 2. Additional information can be found in Supplementary File 1.

Fig.	Exp.	Test	Variable	Group	Mean ± SD	Test statistic	P
2C	Shisa6 IP after GluA2 depletion	One sample t-test	GluA2 intensity	Ctrl	4.37 ± 3.78	t(2) = 43.8	0.001
	Tests vs. intensity = 100	One sample t-test	GluD2 intensity	Ctrl	92.53 ± 9.56	t(2) = 1.352	0.309

Table S3. Related to Figure 3. Additional information concerning Figure 3A and 3B can be found in Supplementary File 2.

Fig.	Exp.	Test	Variable	Group	Mean ± SD	Test statistic	P
3D, E	EM	Brown-Forsythe	PSD Count			W = 0.067	0.803
		Ind. t-test		Ctrl	3.09 ± 0.21	t(8) = -0.466	0.654
				$Shisa6^{L7\ KO}$	3.16 ± 0.28		
3F, G	EM	Brown-Forsythe	PSD Length			W = 0.148	0.710
		Ind. t-test		Ctrl	263.18 ± 15.93 nm	t(8) = -0.685	0.512
				$Shisa6^{L7\ KO}$	269.75 ± 14.36 nm		

Table S4. Related to Figure 4.

Fig.	Exp.	Test	Variable	Group	Mean ± SD	Test statistic	P
4B	PF-PC LTP	Brown-Forsythe	Pre-induction			W = 0.266	0.614
			Post-induction			W = 0.005	0.946
4B	PF-PC LTP	Univariate ANCOVA	Effect pre-induction			F(1, 13) = 43.446	<0.001
			Effect genotype			F(1, 13) = 5.086	0.042
		Descriptives	Post-induction	Ctrl	-209.57 ± 72.87 pA		
			Post-induction	$Shisa6^{L7\ KO}$	-145.31 ± 69.62 pA		
4B	PF-PC LTP	Paired-samples t-test	Pre- vs. Post-induction	Ctrl		t(6) = 2.919	0.027

		Descriptives	Pre-induction	Ctrl	-176.33 ± 51.29 pA		
			Post-induction	Ctrl	-209.57 ± 72.87 pA		
4B	PF-PC LTP	Paired-samples t-test	Pre- vs. Post-induction	Shisa6$^{L7\ KO}$		t(8) = 0.633	0.544
			Pre-induction	Shisa6$^{L7\ KO}$	-153.07 ± 69.37 pA		
			Post-induction	Shisa6$^{L7\ KO}$	-145.31 ± 69.62 pA		
4D	PF-PC LTD	Brown-Forsythe	Pre-induction			W = 0.075	0.789
			Post-induction			W = 6.840	0.023
4D	PF-PC LTD	Univariate ANCOVA	Effect pre-induction			F(1, 11) = 9.694	0.010
			Effect genotype			F(1,11) = 0.457	0.513
		Descriptives	Post-induction	Ctrl	-141.12 ± 71.74 pA		
			Post-induction	Shisa6$^{L7\ KO}$	-103.82 ± 21.43 pA		
4D	PF-PC LTD	Paired-samples t-test	Pre- vs. Post-induction	Ctrl		t(6) = -2.980	0.025
		Descriptives	Pre-induction	Ctrl	-194.63 ± 58.04 pA		
			Post-induction	Ctrl	-141.12 ± 71.74 pA		
4D	PF-PC LTD	Paired-samples t-test	Pre- vs. Post-induction	Shisa6$^{L7\ KO}$		t(6) = -3.847	0.008
			Pre-induction	Shisa6$^{L7\ KO}$	-160.53 ± 54.31 pA		
			Post-induction	Shisa6$^{L7\ KO}$	-103.82 ± 21.43 pA		

Table S5. Related to Figure 5 and Figure S3.

Fig.	Exp.	Test	Variable	Group	Mean ± SD	Test statistic	P
5B	Rotarod	Brown-Forsythe	Fall latency day 1			W = 0.012	0.914
		Brown-Forsythe	Fall latency day 2			W = 0.682	0.415
		Brown-Forsythe	Fall latency day 3			W = 0.344	0.562
		Brown-Forsythe	Fall latency day 4			W = 0.254	0.618
		Brown-Forsythe	Fall latency day 5			W = 0.124	0.727
5B	Rotarod	Mixed-model ANOVA	Day (1-4) x geno	Between-subjects		F(1, 31) = 4.425	0.044
				Within-subjects		F(2.31, 71.48) = 58.277	<0.001
				Interaction		F(2.31, 71.48) = 0.375	0.718
		Descriptives	Day 1	Ctrl	97.56 ± 35.41 s		
				Shisa6$^{L7\ KO}$	79.83 ± 37.29 s		
		Descriptives	Day 2	Ctrl	164.53 ± 40.66 s		
				Shisa6$^{L7\ KO}$	137.91 ± 46.76 s		
		Descriptives	Day 3	Ctrl	196.18 ± 48.98 s		
				Shisa6$^{L7\ KO}$	167.47 ± 53.40 s		
		Descriptives	Day 4	Ctrl	209.13 ± 54.81 s		
				Shisa6$^{L7\ KO}$	173.38 ± 60.20 s		
5B	Rotarod	Paired-samples t-test	Day 5			t(31) = 2.833	0.008
		Descriptives		Ctrl	118.87 ± 24.43 s		
				Shisa6$^{L7\ KO}$	94.20 ± 25.61 s		
S3A	Griptest	Brown-Forsythe	Day 1			W = 0.128	0.723
		Brown-Forsythe	Day 2			W = 0.089	0.768
		Brown-Forsythe	Day 3			W = 3.300	0.080
		Brown-Forsythe	Day 4			W = 0.875	0.357
S3A	Griptest	Mixed-model ANOVA	Day x geno	Between-subjects		F(1, 29) = 1.229	0.277
				Within-subjects		F(3, 87) = 2.664	0.053
				Interaction		F(3, 87) = 2.066	0.111
		Descriptives	Day 1	Ctrl	95.41 ± 14.37		
				Shisa6$^{L7\ KO}$	83.46 ± 15.88		

		Descriptives	Day 2	Ctrl	84.26 ± 15.42		
				Shisa6$^{L7\ KO}$	76.36 ± 13.34		
		Descriptives	Day 3	Ctrl	84.82 ± 11.46		
				Shisa6$^{L7\ KO}$	87.86 ± 19.03		
		Descriptives	Day 4	Ctrl	87.65 ± 14.02		
				Shisa6$^{L7\ KO}$	88.29 ± 20.20		
S3B	Balance beam	Brown-Forsythe	6 mm			W = 1.456	0.237
	Balance beam	Ind. t-test	6 mm	Ctrl	21.54 ± 12.05 s	t(30) = -0.967	0.341
				Shisa6$^{L7\ KO}$	24.97 ± 8.32 s		
S3B	Balance beam	Brown-Forsythe	12 mm			W = 0.086	0.771
	Balance beam	Ind. t-test	12 mm	Ctrl	13.23 ± 5.44 s	t(31) = -1.260	0.217
				Shisa6$^{L7\ KO}$	19.19 ± 10.91 s		
5C	Erasmus-ladder	Brown-Forsythe	Missteps day 1			W = 0.088	0.769
		Brown-Forsythe	Missteps day 2			W = 0.535	0.470
		Brown-Forsythe	Missteps day 3			W = 0.961	0.335
		Brown-Forsythe	Missteps day 4			W = 0.699	0.409
		Brown-Forsythe	Missteps day 5			W = 1.783	0.192
5C	Erasmus-ladder	Mixed-model ANOVA	Day x geno	Between-subjects		F(1, 31) = 9.966	0.004
				Within-subjects		F(2.67, 82.74) = 67.779	<0.001
				Interaction		F(2.67, 82.74) = 1.577	0.205
		Descriptives	Day 1	Ctrl	11.8 ± 3.32		
				Shisa6$^{L7\ KO}$	14.87 ± 2.93		
		Descriptives	Day 2	Ctrl	9.6 ± 3.53		
				Shisa6$^{L7\ KO}$	11.72 ± 2.89		
		Descriptives	Day 3	Ctrl	7.19 ± 3.05		
				Shisa6$^{L7\ KO}$	11.05 ± 3.53		
		Descriptives	Day 4	Ctrl	5.91 ± 3.87		
				Shisa6$^{L7\ KO}$	8.97 ± 3.9		
		Descriptives	Day 5	Ctrl	5.12 ± 2.63		
				Shisa6$^{L7\ KO}$	9.21 ± 3.57		
5D	OKR Gain	Brown-Forsythe	Frequency 0.2			W = 2.218	0.165
		Brown-Forsythe	Frequency 0.4			W = 2.741	0.126
		Brown-Forsythe	Frequency 0.6			W = 3.286	0.097
		Brown-Forsythe	Frequency 0.8			W = 1.243	0.289
		Brown-Forsythe	Frequency 1.0			W = 0.241	0.633
5D	OKR Gain	Mixed-model ANOVA	Frequency x geno	Between-subjects		F(1, 11) = 9.145	0.012
				Within-subjects		F(4, 44) = 484.233	<0.001
				Interaction		F(4, 44) = 3.285	0.019
		Descriptives	Frequency 0.2	Ctrl	0.87 ± 0.05		
				Shisa6$^{L7\ KO}$	0.78 ± 0.09		
		Descriptives	Frequency 0.4	Ctrl	0.69 ± 0.06		
				Shisa6$^{L7\ KO}$	0.54 ± 0.10		
		Descriptives	Frequency 0.6	Ctrl	0.47 ± 0.05		

				Shisa6$^{L7\ KO}$	0.38 ± 0.09		
		Descriptives	Frequency 0.8	Ctrl	0.31 ± 0.04		
				Shisa6$^{L7\ KO}$	0.26 ± 0.08		
		Descriptives	Frequency 1.0	Ctrl	0.28 ± 0.04		
				Shisa6$^{L7\ KO}$	0.19 ± 0.05		
5E	OKR Phase	Brown-Forsythe	Frequency 0.2			W = 1.765	0.211
		Brown-Forsythe	Frequency 0.4			W = 3.233	0.100
		Brown-Forsythe	Frequency 0.6			W = 9.713	0.010
		Brown-Forsythe	Frequency 0.8			W = 0.930	0.356
		Brown-Forsythe	Frequency 1.0			W = 3.375	0.093
5E	OKR Phase	Mixed-model ANOVA	Frequency x geno	Between-subjects		F(1, 11) = 10.441	0.008
				Within-subjects		F(2.02, 22.19) = 137.40	<0.001
				Interaction		F(2.02, 22.19) = 2.043	0.153
		Descriptives	Frequency 0.2	Ctrl	-5.71 ± 1.30		
				Shisa6$^{L7\ KO}$	-7.68 ± 2.68		
		Descriptives	Frequency 0.4	Ctrl	-10.30 ± 1.11		
				Shisa6$^{L7\ KO}$	-15.61 ± 3.76		
		Descriptives	Frequency 0.6	Ctrl	-17.65 ± 1.90		
				Shisa6$^{L7\ KO}$	-26.00 ± 5.84		
		Descriptives	Frequency 0.8	Ctrl	-26.55 ± 4.53		
				Shisa6$^{L7\ KO}$	-35.56 ± 8.99		
		Descriptives	Frequency 1.0	Ctrl	-30.60 ± 3.31		
				Shisa6$^{L7\ KO}$	-38.05 ± 8.47		
5F	VOR Gain	Brown-Forsythe	Frequency 0.2			W = 0.044	0.838
		Brown-Forsythe	Frequency 0.4			W = 0.767	0.400
		Brown-Forsythe	Frequency 0.6			W = 1.517	0.244
		Brown-Forsythe	Frequency 0.8			W = 1.113	0.314
		Brown-Forsythe	Frequency 1.0			W = 0.180	0.680
5F	VOR Gain	Mixed-model ANOVA	Frequency x geno	Between-subjects		F(1, 11) = 5.151	0.044
				Within-subjects		F(4, 44) = 74.828	<0.001
				Interaction		F(4, 44) = 4.019	0.007
		Descriptives	Frequency 0.2	Ctrl	0.39 ± 0.17		
				Shisa6$^{L7\ KO}$	0.71 ± 0.19		
		Descriptives	Frequency 0.4	Ctrl	0.61 ± 0.18		
				Shisa6$^{L7\ KO}$	0.73 ± 0.12		
		Descriptives	Frequency 0.6	Ctrl	0.80 ± 0.20		
				Shisa6$^{L7\ KO}$	0.96 ± 0.15		
		Descriptives	Frequency 0.8	Ctrl	0.83 ± 0.16		
				Shisa6$^{L7\ KO}$	0.96 ± 0.09		
		Descriptives	Frequency 1.0	Ctrl	0.89 ± 0.13		
				Shisa6$^{L7\ KO}$	1.05 ± 0.13		
5G	VOR Phase	Brown-Forsythe	Frequency 0.2			W = 1.324	0.274
		Brown-Forsythe	Frequency 0.4			W = 0.841	0.379
		Brown-Forsythe	Frequency 0.6			W = 0.229	0.642
		Brown-Forsythe	Frequency 0.8			W = 0.615	0.450

		Brown-Forsythe	Frequency 1.0			W = 2.743	0.126
5G	VOR Phase	Mixed-model ANOVA	Frequency x geno	Between-subjects		F(1, 11) = 2.393	0.150
				Within-subjects		F(2.33, 25.60) = 43.180	<0.001
				Interaction		F(2.33, 25.60) = 0.914	0.427
		Descriptives	Frequency 0.2	Ctrl	30.63 ± 9.92		
				Shisa6$^{L7\ KO}$	22.52 ± 4.87		
		Descriptives	Frequency 0.4	Ctrl	21.16 ± 11.03		
				Shisa6$^{L7\ KO}$	17.17 ± 5.91		
		Descriptives	Frequency 0.6	Ctrl	17.51 ± 5.98		
				Shisa6$^{L7\ KO}$	12.42 ± 4.80		
		Descriptives	Frequency 0.8	Ctrl	12.31 ± 6.59		
				Shisa6$^{L7\ KO}$	8.39 ± 3.07		
		Descriptives	Frequency 1.0	Ctrl	8.39 ± 4.07		
				Shisa6$^{L7\ KO}$	6.26 ± 1.38		
5H	VVOR Gain	Brown-Forsythe	Frequency 0.2			W = 2.770	0.124
		Brown-Forsythe	Frequency 0.4			W = 6.438	0.028
		Brown-Forsythe	Frequency 0.6			W = 0.743	0.407
		Brown-Forsythe	Frequency 0.8			W = 0.351	0.565
		Brown-Forsythe	Frequency 1.0			W = 0.119	0.737
5H	VVOR Gain	Mixed-model ANOVA	Frequency x geno	Between-subjects		F(1, 11) = 0.933	0.355
				Within-subjects		F(2.43, 26.68) = 3.174	0.049
				Interaction		F(2.43, 26.68) = 0.235	0.832
		Descriptives	Frequency 0.2	Ctrl	0.99 ± 0.05		
				Shisa6$^{L7\ KO}$	0.97 ± 0.10		
		Descriptives	Frequency 0.4	Ctrl	1.05 ± 0.04		
				Shisa6$^{L7\ KO}$	1.00 ± 0.11		
		Descriptives	Frequency 0.6	Ctrl	1.02 ± 0.05		
				Shisa6$^{L7\ KO}$	0.98 ± 0.07		
		Descriptives	Frequency 0.8	Ctrl	1.03 ± 0.08		
				Shisa6$^{L7\ KO}$	0.99 ± 0.09		
		Descriptives	Frequency 1.0	Ctrl	1.05 ± 0.07		
				Shisa6$^{L7\ KO}$	1.03 ± 0.07		
5I	VVOR Phase	Brown-Forsythe	Frequency 0.2			W = 7.080	0.022
		Brown-Forsythe	Frequency 0.4			W = 3.398	0.092
		Brown-Forsythe	Frequency 0.6			W = 0.202	0.662
		Brown-Forsythe	Frequency 0.8			W = 0.173	0.686
		Brown-Forsythe	Frequency 1.0			W = 1.208	0.295
5I	VVOR Phase	Mixed-model ANOVA	Frequency x geno	Between-subjects		F(1, 11) = 0.164	0.693
				Within-subjects		F(2.08, 22.85) = 1.708	0.203
				Interaction		F(2.08, 22.85) = 0.397	0.684
		Descriptives	Frequency 0.2	Ctrl	2.35 ± 1.58		

		Shisa6$^{L7\ KO}$	4.43 ± 3.18
Descriptives	Frequency 0.4	Ctrl	1.42 ± 1.08
		Shisa6$^{L7\ KO}$	1.51 ± 1.54
Descriptives	Frequency 0.6	Ctrl	1.30 ± 1.10
		Shisa6$^{L7\ KO}$	1.17 ± 1.53
Descriptives	Frequency 0.8	Ctrl	1.31 ± 1.84
		Shisa6$^{L7\ KO}$	1.66 ± 1.81
Descriptives	Frequency 1.0	Ctrl	0.83 ± 1.48
		Shisa6$^{L7\ KO}$	1.85 ± 0.84

Italicized items indicate use of Greenhouse-Geisser correction

Table S6. Related to Figure 6 and Figure S4

Fig.	Exp.	Test	Variable	Group	Mean ± SD	Test statistic	P
6B	VOR Reversal	Brown-Forsythe	Day 1			W = 0.829	0.382
	Gain	Brown-Forsythe	Day 2			W = 0.029	0.868
		Brown-Forsythe	Day 3			W = 0.002	0.965
		Brown-Forsythe	Day 4			W = 0.179	0.681
		Brown-Forsythe	Day 5			W = 0.115	0.741
	VOR Reversal	Mixed-model ANOVA	Day x geno	Between-subjects		F(1, 11) = 72.734	<0.001
	Gain			*Within-subjects*		F(1.90, 20.86) = 42.112	<0.001
				Interaction		F(1.90, 20.86) = 15.811	<0.001
		Descriptives	Day 1	Ctrl	0.67 ± 0.13		
				Shisa6$^{L7\ KO}$	0.89 ± 0.16		
		Descriptives	Day 2	Ctrl	0.44 ± 0.13		
				Shisa6$^{L7\ KO}$	0.85 ± 0.11		
		Descriptives	Day 3	Ctrl	0.34 ± 0.10		
				Shisa6$^{L7\ KO}$	0.84 ± 0.09		
		Descriptives	Day 4	Ctrl	0.28 ± 0.07		
				Shisa6$^{L7\ KO}$	0.83 ± 0.09		
		Descriptives	Day 5	Ctrl	0.26 ± 0.06		
				Shisa6$^{L7\ KO}$	0.73 ± 0.05		
6C	VOR Reversal	Brown-Forsythe	Day 1			W = 1.296	0.279
	Phase	Brown-Forsythe	Day 2			W = 2.716	0.128
		Brown-Forsythe	Day 3			W = 7.021	0.023
		Brown-Forsythe	Day 4			W = 5.826	0.034
		Brown-Forsythe	Day 5			W = 5.161	0.044
	VOR Reversal	Mixed-model ANOVA	Day x geno	Between-subjects		F(1, 11) = 17.154	0.002
	Phase			*Within-subjects*		F(1.49, 16.35) = 16.787	<0.001
				Interaction		F(1.49, 16.35) = 16.986	<0.001
		Descriptives	Day 1	Ctrl	18.37 ± 5.31		
				Shisa6$^{L7\ KO}$	12.82 ± 2.99		
		Descriptives	Day 2	Ctrl	28.52 ± 11.50		
				Shisa6$^{L7\ KO}$	11.31 ± 3.22		
		Descriptives	Day 3	Ctrl	44.29 ± 23.89		
				Shisa6$^{L7\ KO}$	11.07 ± 3.78		
		Descriptives	Day 4	Ctrl	66.74 ± 35.30		
				Shisa6$^{L7\ KO}$	11.53 ± 4.32		
		Descriptives	Day 5	Ctrl	91.76 ± 41.48		
				Shisa6$^{L7\ KO}$	12.08 ± 3.40		
S4A	VOR Reversal	Brown-Forsythe	Day 1			W = 2.792	0.123
	Training Gain	Brown-Forsythe	Day 2			W = 1.056	0.326
		Brown-Forsythe	Day 3			W = 0.361	0.560

		Brown-Forsythe	Day 4			W = 0.195	0.667
		Brown-Forsythe	Day 5			W = 0.429	0.526
	VOR Reversal	Mixed-model ANOVA	Day x geno	Between-subjects		F(1, 11) = 0.128	0.727
	Training Gain			*Within-subjects*		F(1.47, 15.474	16.19) = <0.001
				Interaction		F(1.47, 45.816	16.19) = <0.001
		Descriptives	Day 1	Ctrl	0.24 ± 0.07		
				Shisa6$^{L7\ KO}$	0.55 ± 0.16		
		Descriptives	Day 2	Ctrl	0.16 ± 0.05		
				Shisa6$^{L7\ KO}$	0.34 ± 0.10		
		Descriptives	Day 3	Ctrl	0.27 ± 0.08		
				Shisa6$^{L7\ KO}$	0.21 ± 0.08		
		Descriptives	Day 4	Ctrl	0.34 ± 0.06		
				Shisa6$^{L7\ KO}$	0.17 ± 0.06		
		Descriptives	Day 5	Ctrl	0.35 ± 0.07		
				Shisa6$^{L7\ KO}$	0.14 ± 0.05		
S4B	VOR Reversal Training Phase	Brown-Forsythe	Day 1			W = 0.105	0.752
		Brown-Forsythe	Day 2			W = 0.356	0.563
		Brown-Forsythe	Day 3			W = 7.019	0.023
		Brown-Forsythe	Day 4			W = 4.792	0.051
		Brown-Forsythe	Day 5			W = 4.779	0.051
	VOR Reversal Training Phase	Mixed-model ANOVA	Day x geno	Between-subjects		F(1, 11) = 141.86	<0.001
				Within-subjects		F(1.79, 138.36	19.64) = <0.001
				Interaction		F(1.79, 67.789	19.64) = <0.001
		Descriptives	Day 1	Ctrl	34.38 ± 6.32		
				Shisa6$^{L7\ KO}$	22.31 ± 7.05		
		Descriptives	Day 2	Ctrl	135.51 ± 23.45		
				Shisa6$^{L7\ KO}$	31.47 ± 15.18		
		Descriptives	Day 3	Ctrl	167.91 ± 4.19		
				Shisa6$^{L7\ KO}$	39.06 ± 21.75		
		Descriptives	Day 4	Ctrl	170.97 ± 3.19		
				Shisa6$^{L7\ KO}$	44.65 ± 26.77		
		Descriptives	Day 5	Ctrl	174.15 ± 2.71		
				Shisa6$^{L7\ KO}$	54.89 ± 34.66		
6E	Eyeblink CR Amplitude	Brown-Forsythe	Day 1			W = 0.264	0.611
		Brown-Forsythe	Day 2			W = 2.160	0.152
		Brown-Forsythe	Day 3			W = 8.728	0.006
		Brown-Forsythe	Day 4			W = 5.622	0.024
		Brown-Forsythe	Day 5			W = 7.270	0.011
		Brown-Forsythe	Day 6			W = 8.420	0.007
		Mixed-model	Day x	Between-		F(1, 30) = 8.697	0.006

		ANOVA	geno	subjects			
				Within-subjects		F(1.95, 58.34) = 11.494	<0.001
				Interaction		F(1.95, 58.34) = 5.295	0.008
		Descriptives	Day 1	Ctrl	0.01 ± 0.02		
				Shisa6$^{L7\ KO}$	0.01 ± 0.02		
		Descriptives	Day 2	Ctrl	0.04 ± 0.07		
				Shisa6$^{L7\ KO}$	0.01 ± 0.02		
		Descriptives	Day 3	Ctrl	0.14 ± 0.19		
				Shisa6$^{L7\ KO}$	0.0 ± 0.01		
		Descriptives	Day 4	Ctrl	0.24 ± 0.34		
				Shisa6$^{L7\ KO}$	0.03 ± 0.06		
		Descriptives	Day 5	Ctrl	0.27 ± 0.3		
				Shisa6$^{L7\ KO}$	0.07 ± 0.10		
		Descriptives	Day 6	Ctrl	0.31 ± 0.31		
				Shisa6$^{L7\ KO}$	0.05 ± 0.08		
6F	Eyeblink CR Percentage	Brown-Forsythe	Day 1			W = 0.372	0.546
		Brown-Forsythe	Day 2			W = 2.011	0.167
		Brown-Forsythe	Day 3			W = 10.326	0.003
		Brown-Forsythe	Day 4			W = 6.656	0.015
		Brown-Forsythe	Day 5			W = 3.386	0.076
		Brown-Forsythe	Day 6			W = 1.803	0.189
		Mixed-model ANOVA	Day x geno	Between-subjects		F(1, 30) = 9.760	0.004
				Within-subjects		F(2.91, 87.39) = 15.395	<0.001
				Interaction		F(2.91, 87.39) = 4.046	0.010
		Descriptives	Day 1	Ctrl	4.39 ± 7.59		
				Shisa6$^{L7\ KO}$	3.0 ± 5.11		
		Descriptives	Day 2	Ctrl	9.09 ± 14.44		
				Shisa6$^{L7\ KO}$	3.45 ± 6.67		
		Descriptives	Day 3	Ctrl	34.01 ± 41.67		
				Shisa6$^{L7\ KO}$	2.5 ± 7.22		
		Descriptives	Day 4	Ctrl	35.47 ± 43.1		
				Shisa6$^{L7\ KO}$	8.81 ± 18.75		
		Descriptives	Day 5	Ctrl	52.5 ± 41.7		
				Shisa6$^{L7\ KO}$	20.27 ± 28.35		
		Descriptives	Day 6	Ctrl	54.5 ± 36.84		
				Shisa6$^{L7\ KO}$	19.7 ± 28.03		

Italicized items indicate use of Greenhouse-Geisser correction

Table S7. Relates to Figure 7 and Figure S6

Fig.	Exp.	Test	Variable	Group	Mean ± SD	Test statistic	P
7B	*In Vivo* SS	Brown-Forsythe	Anterior			W = 0.003	0.957
		Mann-Whitney U	SS freq			U = 78	0.009
		Descriptives		Ctrl	85.02 ± 11.69		
				Shisa6$^{L7\ KO}$	72.90 ± 11.88		
7C	*In Vivo* SS	Brown-Forsythe	Anterior			W = 0.831	0.369
		Mann-Whitney U	CV2			U = 42	<0.001
		Descriptives		Ctrl	0.39 ± 0.04		
				Shisa6$^{L7\ KO}$	0.32 ± 0.05		
7E	*In Vivo* SS	Brown-Forsythe	Posterior			W = 0.351	0.559
		Mann-Whitney U	SS freq			U = 35	0.003
		Descriptives		Ctrl	56.21 ± 11.04		
				Shisa6$^{L7\ KO}$	44.41 ± 8.58		
7F	*In Vivo* SS	Brown-Forsythe	Posterior			W = 1.453	0.239
		Mann-Whitney U	CV2			U = 65.5	0.142
		Descriptives		Ctrl	0.30 ± 0.06		
				Shisa6$^{L7\ KO}$	0.28 ± 0.10		
S6B	Intrinsic Excitability	Brown-Forsythe	100 pA			W = 0.698	0.407
		Brown-Forsythe	200 pA			W = 0.341	0.562
		Brown-Forsythe	300 pA			W = 1.721	0.195
		Brown-Forsythe	400 pA			W = 2.136	0.150
		Brown-Forsythe	500 pA			W = 2.054	0.157
		Brown-Forsythe	600 pA			W = 1.401	0.242
		Brown-Forsythe	700 pA			W = 1.039	0.313
		Brown-Forsythe	800 pA			W = 1.081	0.303
		Brown-Forsythe	900 pA			W = 0.350	0.557
		Brown-Forsythe	1000 pA			W = 0.006	0.941
		Mixed-model ANOVA		Between-subjects		F(1, 55) = 0.073	0.788
				Within-subjects		F(2.28, 125.43) = 407.26	<0.001
				Interaction		F(2.28, 125.43) = 0.098	0.928
		Descriptives	100 pA	Ctrl	10.40 ± 24.50		
				Shisa6$^{L7\ KO}$	6.23 ± 12.08		
			200 pA	Ctrl	25.45 ± 45.02		
				Shisa6$^{L7\ KO}$	20.47 ± 26.97		
			300 pA	Ctrl	44.61 ± 59.24		
				Shisa6$^{L7\ KO}$	42.27 ± 36.86		
			400 pA	Ctrl	63.63 ± 69.20		
				Shisa6$^{L7\ KO}$	62.43 ± 44.15		
			500 pA	Ctrl	85.59 ± 75.73		
				Shisa6$^{L7\ KO}$	84.71 ± 47.36		
			600 pA	Ctrl	109.23 ± 76.20		
				Shisa6$^{L7\ KO}$	106.78 ±		

					48.95		
			700 pA	Ctrl	130.73	±	
					77.05		
				Shisa6$^{L7\ KO}$	125.66	±	
					49.91		
			800 pA	Ctrl	151.09	±	
					76.07		
				Shisa6$^{L7\ KO}$	144.70	±	
					48.23		
			900 pA	Ctrl	164.64	±	
					67.00		
				Shisa6$^{L7\ KO}$	159.80	±	
					49.27		
			100 pA	Ctrl	174.41	±	
					56.51		
				Shisa6$^{L7\ KO}$	170.77	±	
					54.45		
S6D	*In Vivo* CS	Brown-Forsythe	Anterior			W = 0.108	0.744
		Mann-Whitney U	CS freq			U = 126.5	0.403
		Descriptives		Ctrl	1.35 ± 0.40		
				Shisa6$^{L7\ KO}$	1.38 ± 0.35		
S6E	*In Vivo* CS	Brown-Forsythe	Anterior			W = 4.023	0.053
		Mann-Whitney U	CV2			U = 102	0.102
		Descriptives		Ctrl	0.79 ± 0.16		
				Shisa6$^{L7\ KO}$	0.82 ± 0.07		
S6G	*In Vivo* CS	Brown-Forsythe	Posterior			W = 0.530	0.473
		Mann-Whitney U	CS freq			U = 66	0.156
		Descriptives		Ctrl	0.93 ± 0.25		
				Shisa6$^{L7\ KO}$	0.78 ± 0.23		
S6H	*In Vivo* CS	Brown-Forsythe	Posterior			W = 2.679	0.114
		Mann-Whitney U	SS freq			U = 66	0.156
		Descriptives		Ctrl	0.73 ± 0.07		
				Shisa6$^{L7\ KO}$	0.78 ± 0.10		

Italicized items indicate use of Greenhouse-Geisser correction

EXPERIMENTAL MODELS AND SUBJECT DETAILS

Experiments and analyses were performed with the experimenters blinded to the genotype. Both males and females were used for all experiments and all mice were randomly allocated to an experimental group. All mice were individually housed from the age of P21 with food and water available *ad libitum* and in 12:12 h light/dark cycles. All experiments were approved by local (DEC) and national ethical committees. Adult mice aged 4 to 24 weeks old were used for the behavioural assays, *in vivo* physiology and immunoprecipitation and SWATH protocol. Mice used were *Shisa6*$^{L7\ KO}$ and their littermate controls all bred on a mixed C57BL6/Nhsd and C57BL6/J background. The *Shisa6*$^{L7\ KO}$ model was generated by crossing Purkinje specific L7(Pcp2)-Cre mice [280] with *Shisa6*$^{tm1a2(Caliper)CNCR\text{-}VUA}$ [251]. Genotyping was performed on postnatal day (P)7–10 using primers Rz742, Rz804 and Rz803. Using a previously described PCR method [251], we found that the *Shisa6*$^{L7\ KO}$ littermates contained a relatively large number of germline deletions always affecting one allele. For the immunoprecipitation and SWATH protocols we used *Shisa6*^{null} mice and their WT litter mates. In the current manuscript, all mice denoted as control are *Shisa6*$^{L7\ HET}$ (i.e., heterozygous whole-body deletion), whereas the *Shisa6*$^{L7\ KO}$ is a full KO for PCs and has heterozygous whole-body deletion.

METHOD DETAILS

DNA expression constructs

The full-length coding DNA for mouse GluD2 (*Grid2*) was obtained from Genecopoeia (Mm02855; Rockville, MD, USA) as shuttle-clone and subsequently Gateway-cloned (Invitrogen; Waltham, MA, USA) into the pTRCGw-IRES2-EGFP vector (Klaassen et al., 2016)). FLAG-Shisa6-pTRCGw-IRES2-EGFP as described previously (Klaassen et al., 2016).

Immunoprecipitation and mass spectrometry of mouse cerebellar Shisa6 protein-complexes

Immunoprecipitation using anti-Shisa6 antibody was performed on the n-Dodecyl-beta-Maltoside (DDM) extracted crude synaptic membrane fraction, prepared from the cerebellar tissue of WT and Shisa6^{null} mice, as described previously for the hippocampus (Klaassen et al., 2016). Eluted proteins were fractionated by SDS-PAGE, subjected to in-gel tryptic digestion, and analysed on a TripleTOF 5600+ mass spectrometer (Sciex,

Framingham, MA, USA) operating in information-dependent acquisition (IDA) mode, as decribed previously (Klaassen et al., 2016).

TripleTOF 5600+ data was imported into MaxQuant (version 1.6.1.0) (Cox and Mann, 2008) and searched against the Uniprot mouse reference proteome (April 2018 release; including canonical and additional sequences). Methionine oxidation and N-terminal acetylation were selected as variable modifications, and proprionamide set as fixed cysteine modification. For both peptide and protein identification the false discovery rate was set to 0.01. Match between runs was enabled with a match time window of 0.7 min and alignment time window of 20 min. MaxLFQ normalization was enabled with a LFQ minimal ratio count of 1. Remaining parameters were left to default, with proteingroup identification requiring a minimum of 1 razor + unique peptide. The filtering and statistical analysis of the Maxquant results was performed in Perseus (version 1.6.2.1)(Tyanova et al., 2016) in the following order: (1) Importing the Maxquant *proteinGroups.txt* file into Perseus; (2) Removal of "Reverse", "Potential contaminant", and "Only identified by site" proteingroups; (3) Log2 transformation of all LFQ intensity values; 4) Removal of proteingroups in which any WT value was derived “By matching”, (5) Removal of proteingroups with less then three valid Log2 LFQ intensity values in the WT group; (6) Imputation of missing values (7.7% of the KO population) from a normal distribution (width 0.3, down shift 1.8, whole matrix) (7) Performing a Student's T-test (S0=0.5) followed by permutation-based FDR analysis on the Log2 LFQ intensity values (FDR=0.01, 2500 permutations).

Immunoprecipitation of mouse cerebellar Shisa6 protein-complexes after immuno-depletion of GluA2

All extraction, binding and washing steps were performed at 4 ˚C with ice-cold buffers. GluA2 antibody was added to DDM-extracted crude synaptic membranes and incubated O/N. The antibody-GluA2 complexes were subsequently cleared from the lysate by addition of protein A/G agarose beads (Santa Cruz, sc-2003; Dallas, TX, USA). Shisa6 antibody was added to the “GluA2-depleted” lysate, incubated O/N and immobilized on protein A/G agarose beads. The beads were washed four times with wash buffer (0.1% DDM, 150 mM NaCl, 25 mM HEPES pH7.4) and eluted with Laemmli sample buffer.

HEK293 cell culture and transfection

HEK293 cells (ATCC; Manassas, VA, USA) were cultured for a maximum of 20 passages in DMEM medium (Gibco, Life Technologies; Waltham, MA, USA) supplemented with 10%

FBS (Invitrogen; Waltham, MA, USA) and 1% Penicillin-Streptomycin (Gibco, Life Technologies; Waltham, MA, USA). Cells were plated in 10 cm dishes 16-24 hours prior to transfection, and 50-60% confluent at the time of transfection. HEK293 cells were transfected with plasmid DNA (5ug) encoding GluD2 alone or in combination with flag-Shisa6 using Polyethylenimine (PEI) (25 kDa linear, Polysciences; Hirschberg an der Bergstrasse, Germany) and incubated for 42-48 hr.

Co-precipitation from HEK293 cells

All lysis, washing and centrigation steps were performed at 4 ˚C with ice-cold buffers. HEK293 cells were washed once with PBS, resuspended in lysis buffer (1% Triton X-100, 150 mM NaCl, 25 mM HEPES (pH 7.4), supplemented with EDTA-free Complete protease inhibitor (Roche, Basel, Switzerland)), and incubated for 1 hr with 10 RPM end-over-end mixing. The supernatant was cleared of debris by two consecutive 20 minute centrifugation steps at 20,000x g. Anti-flag antibody was added to the supernatant, incubated O/N, and immobilized on Protein A/G agarose beads. The beads were washed four times with lysis buffer and eluted with Laemmli sample buffer.

Immunoblot analysis

Protein samples were dissolved in Laemmli sample-buffer, heated to 96 ˚C for 5 minutes, and loaded onto a 4–15% Criterion TGX Stain-Free gel (Bio-Rad, Temse, Belgium) along with Precision Plus protein standard (Bio-Rad, Temse, Belgium). The gel-separated proteins were imaged with the Gel-Doc EZ system (Bio-Rad, Temse, Belgium), transferred O/N onto PVDF membrane (Bio-Rad; Temse, Belgium) and probed with various antibodies (see 'Antibodies' section). Scans were acquired with the Odyssey Fc system (Li-Cor, Lincoln, NE, USA), and adjusted and quantified using Image Studio Lite 5.2.5 software (Li-Cor, Lincoln, NE, USA).

Sample preparation for SWATH MS analysis

Crude synaptic membranes were prepared from the cerebellum of Shisa6 WT and Shisa6^{null} mice as described previous (Klaassen et al., 2016), with the addition of PhosSTOP phosphatase inhibitors (Roche, Basel, Switzerland) to the homogenisation buffer. Proteins were extracted and digested according to the filter-aided sample preparation (FASP) protocol (Wisniewski et al., 2009) with some adaptations. Proteins were extracted and reduced by incubation with SDS-lysis buffer (final concentration of 1 ug protein / ul, 2%

SDS, 100 mM Tris-HCl (pH 8.5) and 2.5 mM Tris(2-carboxyethyl)phosphine-HCl (TCEP)) for 1 hr at 56 ˚C with 1100 RPM mixing. Next, proteins were alkylated by addition of methyl methanethiosulfonate (MMTS; final concentration of 5mM) for 10 minutes at RT. The protein lysate was diluted to 0.5% SDS with Urea buffer (8M Urea, 100mM Tris-HCL (pH8.5)), centrifuged at 20000g for 2 minutes at 20 ˚C, and 100 ul was loaded onto a Microcon Ultracel PL-30 filter (Merck Millipore, Darmstadt, Germany). The filters were centrifuged at 12000g for 10 minutes at 20 ˚C and subsequently washed five times with 100 ul Urea buffer and four times with 100 ul 50 mM NH4HCO3 (identical centrifugation settings). After washing, Trypsin/LysC Mix (Promega, Leiden, The Netherlands) was added to the filters at an enzym to protein ratio of 1 to 25, and incubated O/N at 37 °C within a humidified chamber. Digested peptides were collected from the filter by elution with 50 mM NH4HCO3 and acidified to a final concentration of 0.5% trifluoroacetic acid (TFA). Finally, the eluted peptides were desalted using an Oasis HLB 96-well μelution plate (Waters, Milford, MA, USA) following the manufacturer's guidelines and using 0.1% TFA and 80% acetonitril + 0.1% TFA as binding and elution buffers, respectively.

In order to prepare an experiment-specific spectral library, an additional four FASP preparations were performed on lysate pooled equally from all Shisa6 WT mice. Two samples were purified directly by Oasis HLB desalting, with the remaining two samples pooled and fractionated using the high pH reversed-phase peptide practionation kit (Pierce, Thermo Scientific, Waltham, MA, USA) according to the manufacturer's instructions.

Micro-LC and information-dependent acquisition MS of spectral library fractions

Peptides were analyzed by micro LC MS/MS using an Ultimate 3000 LC system (Dionex, Thermo Scientific, Waltham, MA, USA) coupled to the TripleTOF 5600+ mass spectrometer. Dried peptide samples were redissolved in 5% acetonitril + 0.1% formic acid (FA), supplemented with iRT calibration peptides (Biognosys, Zurich, Switzerland) and loaded onto a 5 mm PepMap100 C18 precolumn (300 μm i.d., 5 μm particle size (Dionex, Thermo Scientific, Waltham, MA, USA). Separation was achieved on a 150 mm ChromXP C18 column (300 μm i.d., 3 μm particle size (Sciex)) using a linear aquous-organic gradient of 5%-18% acetonitrile (+0.1% FA) in 88 minutes, 25% at 98 minutes, 40% at 108 minutes and 90% at 110 minutes, using a flow rate of 5 μL / minute. Eluting peptides were electrosprayed directly into the TripleTOF MS operated in IDA mode. One full scan consisted of a single full profile MS scan (150 ms, m/z 350 to 1250 and charge state +2 to +5), followed by MS/MS analysis of the top 25 most intense precursor ions (150ms, m/z 200 to 1800, charge state +2 to +5, high sensitivity mode and precursor ion count/s > 150).

Dynamic exclusion was set to 16 seconds. Ions were fragmented using rolling collision energy with an energy spread of 5eV.

Micro-LC and SWATH MS

The LC setup and settings were identical to those described for the IDA MS of spectral library fractions. SWATH measurement consisted of a full precursor ion scan (150 ms, m/z 350–1250) followed by sequential precursor isolation windows of 8 Da across the mass range of m/z 450-770 with 1 Da overlap (80 ms). Total cycle time was around 3.2 seconds, providing 8-9 data points across a typical peptide. The collision energy for each window was determined by the appropriate collision energy for a 2+ ion, centered upon the window with a spread of 15 eV.

Analysis of spectral library IDA MS results

The spectral library files were imported into MaxQuant (version 1.6.1.0) (Cox and Mann, 2008) and searched against the Uniprot mouse reference proteome (April 2018 release; including canonical and additional sequences) supplemented with the Biognosys iRT FASTA database. Methionine oxidation and N-terminal acetylation were selected as variable modifications, and MMTS modification of cysteine set as fixed modification. For both peptide and protein identification the false discovery rate was set to 0.01. Remaining parameters were left to default. The spectral library was made from the MaxQuant *msms.txt* file using Spectronaut (version 11.0.15038.23) (Bruderer et al., 2015). Imported peptides were filtered for a Q-value threshold of <0.01 with all other settings left to default.

SWATH data processing and statistical analysis

The peptide abundances were extracted from the raw SWATH data by Spectronaut (version 11.0.15038.23), using default BGS factory settings. Next, Spectronaut performed across-run normalization based on total peak areas. Peptide abundances were exported from Spectronaut as a report and further processed using the R language for statistical computation (R Core Team, 2014). Each unique precursor was considered a peptide (e.g., the same peptide sequence observed with distinct modifications or charge was considered a distinct peptide). The Spectronaut fragment group Q-values were used to select for high confidence peptides, with the following filter settings: Peptides must have a Q-value smaller than, or equal to, 10^{-4} in at least seven out of eight replicas within at least one group. Protein abundances were calculated at the gene level by summation of the normalized peak area of

their respective peptides. Peptides that matched to multiple genes in the spectral library were compiled into separate groups with unique sets of genes. Next, the protein abundance matrix was Loess normalized using the *normalizeCyclicLoess* function from the limma R package (Smyth et al., 2005), which was set to 'fast' and iterations were set to 10. Finally, the normalized protein abundances were imported into Perseus (version 1.6.2.1) for statistical analysis. All data was Log2 transformed and differential expression between the groups was assessed by Student's T-test (S0=0) followed by permutation-based FDR analysis (FDR=0.05, 2500 permutations).

Electron microscopy

Adult mice were transcardially perfused with fixative 4 % PFA (EM grade) 1 % Glutaaraldehyde (EM grade) In 0.12 M Natrium Cacodylaat (NaCac). The brains were removed and put in 4 % PFA at 4 °C overnight. The following day 100 µm sagittal slices were cut using a Vibratome (VT1000S, Leica, The Netherlands) The slices were then washed, in order: 3 times 10 min in 0.1 M NaCac, 2 h 4 °C in 2 % Osmium Tetroxide + 0.1 M NaCac + 1.5 % K3Fe(CN)6, then 3 times 10 min in 0.1 M NaCac. Finally, 3 times 10 min MilliQ wash. The slices were then bathed in ISO 3696 Type 1 ultrapure water (MilliQ) overnight. The next day, slices were washed again, and dehydrated in order: 10 min MilliQ, 10 min 50 % EtOH, 60 min 1 % Uranyl Acetate/50 % EtOH, 10 min 70 % EtOH, 5 min 80 % EtOH, 5 min 90 % EtOH, 5 min 96 % EtOH, 5 min 100 % EtOH, 2 times 8 min Dimethoxypropane (DMP), 2 h DMP: Durcupan 1 (Fluka) (1:1), 2 h DMP: Durcupan 1 (1:3). The following day this was continued: 2 h D1 (50 °C), 2 h Durcupan 2 (Fluka) (50 °C) and then polymerized 3 nights at 60 °C. Ultrathin sections (60 nm) were cut using an ultramicrotome (Ultracut UCT, Leica) and contrasted with 6 % uranyl acetate in MilliQ and lead citrate staining, sections from controls and *Shisa6*$^{L7\ KO}$ mice were examined using an electron microscope (Philips CM100). For ultrastructural PSD analysis, spine synapses have been selected from proximal and distal molecular layer from lobule 3 and lobule 10. PSDs were manually counted and their length was quantified using Fiji software.

Immunohistochemistry

Mouse brains were snap-frozen after removal without perfusion. Tissue was sectioned at 10 µm using a cryostat at −20 °C and a knife temperature of −14 °C. Sections were air-dried on superfrost glass and stored at −80 °C. For staining, sections were defrosted at room temperature (RT) for 60 min and subsequently washed with −20 °C Clarks liquid (75 mL EtOH + 25 mL HAc) for 10 min followed by 3 times 10 min of PBS wash. Sections were

incubated for 120 min in blocking solution (PBS + 0.3 % Triton X-100 + 4 % NGS) at RT and washed 3 times in PBS for 10 min. Following a 60-min incubation in 5 % BSA (in PBS) at RT and subsequent PBS washing, sections were incubated in SA5193 antibody (1:1000, dissolved in 2 % bovine-serum albumin) and anti-GluA2 antibody (1:200) overnight at 4 °C. The sections were then washed for 3 times 10 min in PBS followed by 120 min of fluorescent antibody staining (1:200, Streptavidin-Cy3) in 2 % BSA at RT. After the fluorescent antibody staining, a wash of 3 times 10 min of PBS was followed by 2 times 10 min wash with PB. The sections were then put in DAPI (200 µL in 50 mL 0.1 M PB) for 10 min. This was concluded by 2 times 10 min PB wash. Following PBS washing, the sections were thionin-stained and permount-covered using standard protocols. Images were taken using an upright confocal microscope (LSM 700, Zeiss, Oberkochen, Germany).

3D-SIM imaging and analysis

3D-SIM images were acquired using a Zeiss Elyra ps.1 microscope, fitted with bp 420-480, bp 495 – 575, bp 570 – 650 and lp 655 emission filters. Five rotations and five shifts of the illumination pattern were used to acquire raw images. A 3D volume was imaged using a z-stack with an interval of 110 nm. Raw images were reconstructed into high resolution images using the Zeiss ZEN software on the default settings (segmentation of zeroth, first and second order were set on 100,100 and 83 respectively, where 100 is maximum filtering, the generalised Wiener filter with a regularization of 10^{-6} was used to filter noise, images were baseline cut to remove negative values).

Images were analysed using ImageJ in the FIJI framework [281]. The number of distinct synapses in which co-localization was observed were determined using the maxima of individual Shisa6 and GluA2 spots in a single field of view at the centre of the 3D imaged volume. If Shisa6 spots were at a distance closer than 120 nm, they were defined as co-localizing.

***Ex vivo* electrophysiology**

Following decapitation of mice under isoflurane anaesthesia, the cerebellum was removed, and moved into an ice-cold 'slicing medium'. The slicing medium contained (in mM) 240 sucrose, 2.5 KCL, 1.25 Na_2HPO_4, 2 $MgSO_4$, 1 $CaCl_2$, 26 $NaHCO_3$ and 10 D-Glucose and was carbogenated continuously (95 % O2 and 5 % CO2). Sagittal slices, 250 µm thick, of the cerebellar vermis were cut using a vibrotome (VT1200S, Leica) and put in carbogenated artificial cerebrospinal fluid (ACSF) containing (in mM): 124 NaCl, 5 KCL, 1.25 Na_2HPO_4,

2 $MgSO_4$, 2 $CaCl_2$, 26 $NaHCO_3$ and 15 D-Glucose. Slices were incubated for at least 1 h at 34 ± 1 °C before the start of the experiment. Slice physiology was done at 34 ± 1 °C unless otherwise specified in the methods section. Recordings were done in the presence of 100 µM picrotoxin, except for the spontaneous inhibitory postsynaptic current (sIPSC) recordings. Whole-cell patch clamp recordings and cell-attached recordings were performed with EPC9 and EPC10-USB amplifiers (HEKA Electronics, Lambrecht, Germany) using Pulse and Patchmaster software (HEKA Electronics). Recordings were excluded if the series (R_s) or input resistances (R_i) changed by >15 % during the experiment, which was determined using a hyperpolarizing voltage step relative to the −65 mV holding potential. Analysis of the spontaneous inhibitory postsynaptic currents (sIPSC) and sEPSC event frequencies, amplitudes, 10 – 90 % rise times, and decay times (τ) was done using Mini-analysis software (Synaptosoft). Analysis of the AP threshold (defined by a slope of >20 mV/ms), AHP amplitude, decay time (τ), spike count, and seal tests in intrinsic excitability experiments was performed exclusively on the first AP elicited by a depolarizing current injection. All electrophysiological recordings were analysed using Clampfit (Molecular Devices). Spontaneous spiking rates in cell-attached experiments were analysed using Clampfit, after filtering the data with a 1.5 kHz low-pass filter and calculating the derivative of the original signal.

For whole-cell recordings PCs were visualized using upright microscopes (Axioskop 2 FS and Axio Examiner.D1, Carl Zeiss Microscopy GmbH, Jena, Germany) equipped with a 40x objective. Recording electrodes (3–5 MΩ, 1.65 mm outside diameter (OD) and 1.11 mm interior diameter (ID), World Precision Instruments, Sarasota, FL, USA) were prepared using a P-97 micropipette puller (Sutter Instruments, Novato, CA, USA), and filled with an intracellular solution containing (mM): 120 K-Gluconate, 9 KCL, 10 KOH, 4 NaCl, 10 HEPES, 28.5 Sucrose, 4 Na_2ATP, 0.4 Na_3GTP (pH 7.25 – 7.35 with an osmolarity of 295±5). Note that we adjusted the osmolarity using sucrose. sIPSCs were recorded in the presence of NBQX disodium salt hydrate and APV (Sigma-Aldrich, Missouri, United States), using an intracellular solution containing (mM): 150 CsCl, 1.5 $MgCl_2$, 0.5 EGTA, 4 Na_2ATP, 0.4 Na_3GTP, 10 HEPES, 5 QX-314 (pH 7.25 – 7.35 with an osmolarity of 295±5). sEPSCs were recorded at -75 mV using an intracellular solution containing (in mM): 130 $CsMeSO_4$, 4 $MgCl_2$*$6H_2O$, 0.2 EGTA, 10 HEPES, 4 Na_2ATP, 0.4 Na_3GTP, 10 phosphocreatine-disodium, 1 QX-314 (pH 7.25-7.35, osmolarity 295±5). The same internal solution was used for the climbing fiber elimination experiments. Cslow and Rseries compensation were used for both sIPSC and sEPSC recordings, in order to improve the accuracy of measurements of the event kinetics For extracellular stimulation of PFs, patch

electrodes were filled with ACSF and positioned in the upper third of the molecular layer lateral to the soma of the patched PC. For afferent PF stimulation protocols intensities were varied between 3 – 15 μA, with 3 μA increments for the experiments involving evaluation of stimulation strength to PC EPSC amplitude. For PF–PC transmission, we used various inter-stimulus intervals (50 – 200 ms).

For CF stimulation, similar electrodes (filled with ACSF) were positioned near the patched PC soma in the surrounding granule layer. We selected those recordings in which CF stimuli elicited clear all-or-none responses and lacked the co-activation of PC axons (identifiable by antidromic APs) for further analysis. For CF elimination, experimental tissue was prepared in a similar way. We systematically scanned the granule cell layer to elicit CF responses and recorded PC responses at −20 mV holding potential to prevent voltage escape during the CF-evoked EPSCs.

The synaptic plasticity protocols for inducing LTP and long-term depression (LTD) were applied to lobules 5/6 and conducted as described previously [29]. In short, for synaptic plasticity all recordings were done in voltage-clamp, except for the tetanus, which consisted of 8 pulses of PF-stimulation at 100 Hz for 5 min (21 ± 1 °C, LTP) or single-pulsed PF + CF stimulation (5 ms interval) at 1 Hz for 5 min (34 ± 1 °C, LTD). We evaluated the synaptic plasticity by the change in PF-EPSC (baseline at 0.05 Hz) relative to the mean value calculated during the last 5 min pre-tetanus.

Cell-attached (CA) recordings were made using similar patch pipettes as in the previously described experiments, and using ACSF as an internal solution. Recordings were made in voltage clamp mode in lobules I-III and lobule X of the vermal cerebellum to allow a comparison between anterior and posterior activity, respectively. Spontaneous spiking rates were recorded in the presence of PTX, NBQX and APV, in order to eliminate synaptic input. Intrinsic excitability was measured using sequential current injections in current clamp mode. Cells were held at a holding current equivalent to a -65 mV holding potential, and injected with 500 ms long current pulses ranging from -100 pA to +1000 pA, relative to the holding current, in 100 pA increments (5 s inter-sweep interval).

In vivo electrophysiology

In vivo recordings were performed as recently described [282]. In short, an immobilizing pedestal was fixed on the skull (see for details the section on “compensatory eye movements” below) and a craniotomy (Ø 1 mm) was performed on the occipital bone

under general anesthesia with an isoflurane/O2 mixture (5 % induction, 1.5 – 2.0 % maintenance). The craniotomy was protected by a recording chamber made with Charisma (Heraeus Kulzer, Germany) and closed with bone wax. After 3 days of recovery mice were head-fixed to a head bar and the body was restrained in a custom-made tube for electrophysiological recordings. PCs were recorded from vermal lobules I–III (pitch angle: -40°) and X (pitch angle: -65°) using borosilicate glass pipettes (OD 1.5 mm, ID 0.86 mm, Sutter Instruments, USA) mounted on a digital 3-axis drive (SM-5, Luigs & Neumann, Germany). PCs were identified by the presence of simple and complex spikes, and determined to be from a single unit by confirming that each complex spike was followed by a climbing fiber pause. All in vivo recordings were recorded amplified, filtered and digitized (Axon Multiclamp 700B, CED Power1401) and were analysed offline using Spiketrain (Neurasmus BV, Rotterdam, The Netherlands, www.neurasmus.com), running under MatLab (Mathworks, MA, USA). For each cell the firing rate, CV and mean CV2 were determined for simple and complex spikes, as well as the climbing fiber pause. The CV is calculated by dividing the s.d. by the mean of the interspike intervals, whereas CV2 is calculated as $2 \times |ISI_{n+1} - ISI_n| / (ISI_{n+1} + ISI_n)$. Both are measures for the regularity of the firing, with CV reflecting that of the entire recording and mean CV2 that of adjacent intervals, making the latter a measure of regularity on small timescales. The climbing fiber pause is determined as the duration between a complex spike and the first following simple spike.

Compensatory eye movements

Mice between 6 and 8 weeks of age were prepared for head-restrained recordings of compensatory eye movements. These types of recordings have been described in detail previously [22]. In order to head restrain the mice during the eye movement task a small pedestal was attached using optibond primer and adhesive (Kerr, Bioggio, Switzerland) under isoflurane anaesthesia (induction with 4 % and maintained at 1.5 % concentration). After a recovery period of two to three days the mouse head was restrained by fixation with screws on the pedestal at the experimental setup. A round screen with a random dotted pattern (the drum) surrounded the mouse during the experiment. The optokinetic reflex (OKR), vestibulo-ocular reflex (VOR) and the light guided vestibulo-ocular reflex (VVOR) were induced using a sinusoidal rotation of the drum (OKR) in light, rotation of the table in the dark (VOR) or the rotation of the table and drum (VVOR) in the light. The motor behaviour was assessed by rotating the table and/or drum at 0.1 to 1 Hz with a fixed 5° amplitude. In order to evaluate motor learning, a mismatch between visual and vestibular input was created. Rotating both the visual and vestibular stimuli in phase (at the same

amplitude) induced a decrease of gain; rotating the drum at greater amplitude relative to the table induced the so-called phase reversal of the VOR (day 1, 5°; day 2, 7.5°; day 3 – 4, 10°). Both training protocols were induced at 0.6 Hz with table rotation amplitude of 5°. For eye illumination during the experiments two table fixed infrared emitters (output 600 mW, dispersion angle 7°, peak wavelength 880 nm) and a third emitter, which produced the tracked corneal reflection (CR), were mounted to the camera and aligned horizontally with the optical axis of the camera. The movements of the eyes were recorded with eye-tracking software (ETL-200, ISCAN systems, Burlington, NA, USA). Gain and phase values of eye movements were calculated using Matlab (MathWorksInc, City, Country).

Eyeblink conditioning

L7-Shisa6 mice and control L7-Shisa6 were anesthetized with an isoflurane/oxygen mixture (5% for induction, 1.5 – 2 % for maintenance). After a local scalp injection of bupivacaine hydrochloride (2.5 mg/ml, Bupivacaine Actavis) we made a sagittal scalp incision of 2 – 3 cm length. Next, we carefully removed the exposed periosteum and further scratched the skull using an etchant gel (Kerr, Bioggio, Switzerland). After this, we placed a construct allowing head-fixation using Optibond primer and adhesive (Kerr, Bioggio, Switzerland) and Charisma (Heraeus Kulzer, Armonk, NY, USA). After surgery, mice had 3 – 5 days to recover.

All behavioural experiments were conducted using head-fixed mice that were placed on top of a cylindrical treadmill on which they were allowed to walk freely. The treadmill consisted of a foam roller (diameter 15 cm, width 12 cm; Exervo, TeraNova EVA) with a horizontal metal rod through the axis that was connected with a ball bearing construction to two solid vertical metal poles. A horizontal messing bar was fixated to the same vertical poles at 3-5 cm above the treadmill. Mice were head-fixed to this bar using 1 screw and 2 pins, thereby ensuring perfect head-fixation. This entire setup was placed in a sound- and light-isolating chamber. National Instruments (NI-PXI) processors were used to control experimental parameters and to acquire the eyelid position signal. Eyelid movements were recorded with the magnetic distance measurement technique (MDMT), which makes use of an NVE GMR magnetometer, positioned above the upper left eyelid, that measures movements of a minuscule magnet (1.5 x 0.7 x 0.5 mm) that is placed on the lower eyelid of the animal with superglue (cyanoacrylate). This way, MDMT allows high spatio-temporal detection of eyeblink kinematics (For details: Koekkoek et al., 2002). The unconditioned stimulus (US) consisted of a weak air-puff applied to the eye (30 psi, 10 ms duration), which was

controlled by an API MPPI-3 pressure injector, and delivered via a 27.5 gauge needle that was perpendicularly positioned at 0.5 – 1 cm from the centre of the left cornea. Prior to training the experimenter always carefully inspected whether the needle opening was positioned exactly perpendicular to the center of the mouse's cornea so that the air puff would hit the cornea and not too much the surrounding areas and would thus elicit reliable reflexive eyeblinks. The conditional stimulus (CS) was a green LED light (CS duration 260 ms, LED diameter 5 mm) placed 10 cm in front of the mouse's head. Because we performed our experiments in almost complete darkness this small LED light was a salient stimulus, which could be easily detected by both eyes. The training consisted of 2 daily habituation sessions, 1 baseline measurement and 6 daily acquisition sessions. During the habituation sessions, mice were placed in the setup for 30 – 45 min, during which the air puff needle (for US delivery) and green LED (for CS delivery) were positioned properly but no stimuli were presented. On the day of acquisition session 1, each animal first received 20 CS-only trials as a baseline measure, to establish that the CS did not elicit any reflexive eyelid closure. During each daily acquisition session, animals received 200 paired CS-US trials and 20 CS only trials. The interval between the onset of CS and that of US was set at 250 ms. Because of the inherent delay in the delivery of air puff of 14 ms, we triggered the air puff at 236 ms after CS onset so that it would hit the cornea exactly at 250 ms after CS onset. The inter-trial interval was set according to the following constraints: at least 10 seconds had to elapse, the eyelid had to be open below a predetermined threshold, and eyelid position had to be stable for at least 1 s for a trial to begin. During all training sessions, the experimenter carefully inspected threshold and stability parameters and adjusted them if necessary. All experiments were performed at approximately the same time of day by the same experimenter.

Individual eyeblink traces were analysed automatically with custom computer software (LabVIEW or MATLAB) in a five-step process. First, trials with significant activity in the 500 ms pre-CS period were regarded as invalid for further analysis. Second, trials were normalized by aligning the 500 ms pre-CS baselines and calculating the averaged UR amplitude in Volts per session. The voltage corresponding with a full closure was further used in the analysis of the eyeblink traces as the 100 % value reflecting full eyelid closure (± 1 mm movement), and other values like CR amplitude were expressed relative to this 100 % value. Third, in valid normalized CS-only trials, eyelid movements larger than 5 % of the 500 ms pre-CS period and with a latency to CR onset between 10 – 250 ms and a latency to CR peak of 25 – 500 ms (both relative to CS onset) were considered as conditioned responses (CRs). Fourth, based on this trial-by-trial analysis we calculated for each session

per mouse (1) the percentage of eyeblink CRs, (2) the averaged amplitude in the CS-US interval (based on all valid trials and not thus only for trials in which a CR was present), and (3) timing parameters such as latency to CR onset and latency to CR peak time relative to CS onset (based on only these trials wherein a CR is present). Fifth, we calculated group averages (*Shisa6*$^{L7\ KO}$ *vs.* controls) for the same parameters (1 – 3) and determined statistically significant differences using Repeated Measures ANOVA. Data was considered statistically significant if $p < 0.05$.

Griptest

The strength of the mice was determined using a grip test. By placing the forepaws of a grid attached to a force gauge (BIOSEB, Chaville, France) and steadily pulling the mice by the tail. The grip strength was defined as the maximum strength produced before releasing the grid. The test was performed over the course of four consecutive days.

Rotarod

Mice were trained to walk on the accelerating Rotarod (Ugo Basile, Comerio Varese, Italy). The Rotarod consisted of a cylinder with a diameter of 3 cm. The starting speed of the Rotarod was 3 rotations per minute (rpm) and was set to a maximum of 40 r.p.m. in 270 s. The maximum walking time on the rotarod was 300 s. Latency to fall was recorded on the moment the mouse fell down or clang to the rod for three turns. This experiment consisted of four days with four daily turns on the Rotarod. On the fifth day there was an additional trial set to 80 r.p.m. The interval between each turn was 1 h.

Balance Beam

The Balance Beam is a small rod with a diameter of 12 or 6 mm. The Balance Beam was elevated for 43 cm with two steel rods at both ends. The home cage of the animal was placed at the end of the rod. Mice were placed on the beam and had to walk from one end of the beam to the other end where their home cage was located. The length of this trajectory was 80 cm. We measured the time it took for the mice to cross the beam. In addition, we analysed video material to inspect if the mice presented with misstep behaviour.

ErasmusLadder

Mice were tested on ErasmusLadder (Noldus, Wageningen, NL). The ErasmusLadder is a fully automated system consisting of a horizontal ladder between two shelter boxes. It has 37 rungs on each side of the ladder and all the rungs are attached to custom-made pressure sensors that are continuously monitored [213] In the current study, mice were tested in 5 daily sessions, during which mice were trained to walk between two shelter boxes for 50 trials each day. Step length and step time were defined as the distance and time between two consecutive touches from the right front limb, respectively.

QUANTIFICATION AND STATISTICAL ANALYSIS

All statistical analysis was performed using SPSS, Python or Graphpad Prism. Data in the figures is presented as mean ± SEM. Sample sizes (n) are present in all Figure legends. The p-values are indicated in the results section. Mean ± SD, Brown-Forsythe tests for homogeneity of variances, type of statistical analysis, test-statistics and exact p-values are reported in Table S1-S7, Supplementary File 1 and Supplementary File 2. All statistical analyses of the SWATH data were performed on Log2-transformed data (see Supplementary File 2).

DATA AND CODE AVAILABLITY

Further information and requests for data and code should be directed to and will be fulfilled by the Lead Contact, Chris I. De Zeeuw (c.dezeeuw@erasmusmc.nl).

SUPPLEMENTAL TABLES NOT INCLUDED IN MAIN SUPPLEMENTARY FILE

Extensive statistics related to Figure 2 and Figure 3 are reported in Supplementary Files 1 and 2.

Chapter 3.2

Impact of NMDA receptor overexpression on cerebellar Purkinje cell activity and motor learning

Elisa Galliano ¶, *, Martijn Schonewille *, **Saša Peter**, Mandy Rutteman, Simone Houtman, Dick Jaarsma, Freek E. Hoebeek and Chris I. De Zeeuw

* First-Co-author(s)

¶ Corresponding author(s)

E-neuro (2018)

Abstract

In many brain regions involved in learning *N*-methyl-D-aspartate glutamate receptors (NMDARs) act as coincidence detectors of pre- and post-synaptic activity, mediating Hebbian plasticity. Intriguingly, the parallel fiber (PF) to Purkinje cell (PC) input, which is critical for procedural learning, shows virtually no postsynaptic NMDARs. Why is this? Here, we address this question by generating and testing independent transgenic lines that over-express NMDA-NR2B specifically in PCs. PCs of the mice that show larger NMDA-mediated currents than controls at their parallel fiber (PF) input, suffer from a blockage of long-term potentiation (LTP) at their PF-PC synapses, while long-term depression (LTD) and baseline transmission are unaffected. Moreover, introducing NMDA-mediated currents affects cerebellar learning in that phase-reversal of the vestibulo-ocular reflex is impaired. Our results suggest that under physiological circumstances PC spines lack NMDARs postsynaptically at their PF input so as to allow LTP to contribute to motor learning.

Introduction

A basic property of chemical synapses is their ability to be permanently modified in response to stimulus patterns. This property, which is known as long-term synaptic plasticity, can result in potentiation or depression of transmission, and is thought to serve as a cellular basis for memory formation [247]. The existence of long-term synaptic plasticity was predicted by Donald Hebb, who postulated that the synaptic connection between two neurons would be strengthened when pre- and postsynaptic elements are active simultaneously [18]. Such a process implies the existence of a coincidence detector able to sense at the same time the pre- and postsynaptic activity. The *N*-methyl-D-aspartate receptor (NMDAR), which is a cationic channel sensitive for glutamate released at the presynaptic site and voltage changes at the postsynaptic site, is a well-known coincidence detector, the activity of which appears to be key to the induction of various types of synaptic plasticity in the CNS [283]. However, in the cerebellar Purkinje cell (PC), a neuron with great capacity for synaptic plasticity [284, 285], things are peculiar. First, NMDARs in PCs are expressed relatively late, after the second postnatal week; second, their NMDARs are expressed at a relatively low level; and finally, NMDAR currents in PCs can only be measured at just one of their inputs, *i.e.* the climbing fiber (CF) synapse [286, 287], where they are required for the induction of long-term depression at the parallel fiber to Purkinje cell synapse (PF-PC LTD) (Piochon et al., 2010). So why are there virtually no functional NMDARs postsynaptically at the other glutamatergic afferent to PCs, *i.e.* the PF synapse? This is an intriguing question, especially given the facts that PF to PC synapses are abundant (between 100,000 and 200,000 for each PC), that these synapses show multiple forms of plasticity, and that they even express NMDARs presynaptically [288, 289]. One could speculate that since the opening of NMDARs will induce a calcium influx [290], and the level of calcium influx in turn will determine to what extent a PF-PC synapse will be potentiated or depressed at its postsynaptic site [25], it is possible that the virtual absence of NMDARs at this synapse is necessary to keep the local calcium transients at PC spines relatively low and thereby allow long-term potentiation (LTP) to occur. Here, we set out to test the hypothesis that the lack of NMDARs at the PF-PC synapse is permissive for LTP induction by generating novel Purkinje cell specific transgenic mouse lines that over-express the NR2B subunit of NMDARs under the L7-promotor (L7-NR2B+/Tg1 and L7-NR2B+/Tg2; hereafter referred to as Tg1 and Tg2) and by subsequently investigating their cellular and behavioral consequences. We selected the form B of the NR2 subunit, because this is the most permeable subunit for Ca^{2+}, it has been shown to enhance synaptic plasticity, it is not expressed by any other neuron in the cerebellar cortex, and it has

previously been inserted successfully in neuronal cultures, forming functional units with NR1 [291-293]. To minimize the possibility that all new overexpressed NMDARs would be directed to the climbing fiber synapse as occurs under physiological circumstances [286, 287], we overexpressed NR2B subunits with truncated UTR sites, which might serve as regulatory elements for subcellular trafficking [294, 295]. Our data show that such overexpression of NR2B subunits in PCs *in vivo* results in functional NMDARs and that many of the genetically induced, additional NMDA-mediated currents are located at the PF to PC synapse. Moreover, overexpression of NR2B impaired induction of LTP, but not LTD, at the PF to PC synapse, and affected adaptation of the vestibulo-ocular reflex (VOR), which is known to depend on LTP [22, 30, 296, 297]. Together, these findings highlight the quintessence of regulating the low and site-specific expression of NMDAR subunits in PCs, setting it apart from that in other neurons involved in memory formation [298, 299].

Results

Transgenic overexpression of NR2B in PCs increases CF-PC NMDA responses and introduces functional NMDA receptors in PF to PC synapses

NMDA receptors are complex, heterotetrameric channels formed by two NR1 subunits and two NR2 subunits [300]. Under normal developmental and physiological circumstances NR1 is expressed by PCs directly after birth, while NR2 subunits, required to form functional receptors at the climbing fiber to PC synapses, are not expressed until 2 to 3 weeks after birth, reaching a plateau at approximately 2 months [286] (Figure 1A). To introduce functional NR1/NR2 NMDA currents at the parallel fiber to PC synapse, we generated transgenic mouse lines over-expressing the NR2B subunit by inserting the linearized NR2B transgene without its 5'-UTR and most of its 3'-UTR (leaving only 470 bases) under control of the Pcp-2/L7 promoter in an expression vector [270, 280], which was pronuclearly injected into a C57BL/6 inbred zygote (see methods for detailed procedures). Western blot analysis at six weeks of age confirmed the over-expression of NR2B protein in the cerebellum of two lines of L7-NR2B+ transgenic animals, Tg1 and Tg2 (Figure 1B). In accord with increased expression of NR2B in Purkinje cells, immuno-fluorescence showed increased NR2B staining in the cerebellar molecular layer of both transgenic lines (Figure 1C). Western blot and immunohistology also indicated that in both transgenic lines labeling in the cerebellum was still considerably lower than that in hippocampus and cortex, which are known for very high levels of NR2B expression [291]. The ratio of NR-labeling to loading control actin labeling indicated a relatively high

amount of the actual protein present in Tg2, but the generally low expression levels and suboptimal antibody quality, commonly seen with channel receptors, prohibited an accurate evaluation of the sub-cellular localization or quantification of the expression. We therefore took these results as qualitative evidence for the presence of NR2B, while the functional consequences and related quantifications were tested with cell physiological approaches (see Figure 2).

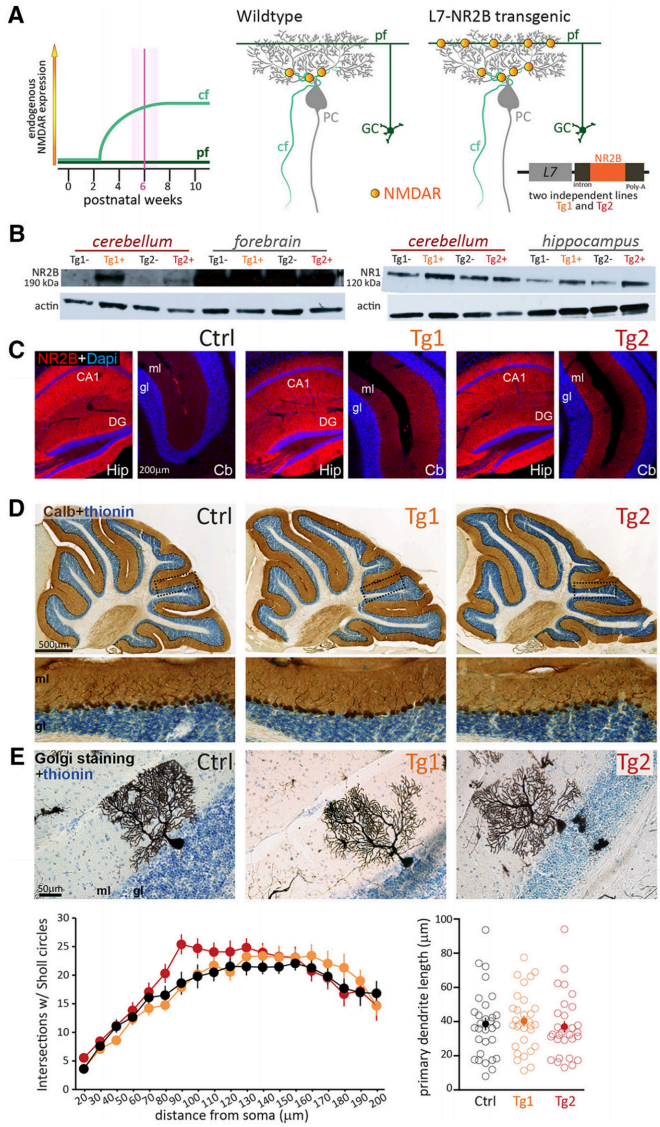

Figure 1. Generation of NR2B transgenic mice. **A**, Schematic representation of the expression of endogenous NMDARs at CF-PC and PF-synapses over the wild-type mouse lifetime. All experiments performed in the following figures are performed at 6 ± 1 weeks of age (for details, see Materials and Methods). Middle, Scheme depicting the expression of NMDAR (dots) in a wild-type mouse at the synapses formed on the PC dendritic tree by CFs. Synapses formed by PFs (the axons of granule cells, GC) do not have NMDARs. Right, Same schematic representation of synapses onto PCs in the L7-NR2B Tg transgenic mouse. Note that NMDARs are present also at the PF-PC synapse. Inset, Details of the vector used to generate the two independent lines used in the study. **B**, Western blotting gels containing homogenates of adult cerebella, forebrains, and hippocampi of two transgenic mice (Tg1 and Tg2) and their control littermates (Tg1- and Tg2-). The left blot was processed with an anti-NR2B antibody, which visualizes a band at 190 kDa, the right one with an anti-NR1 antibody (120 kDa). Actin was used as loading control; note that

the ratio of NR labeling to actin labelling should be taken into account for assessing the amounts of protein present. **C**, Confocal immunofluorescent images of NR2Bimmunoreactivityin dorsal hippocampus (Hip) and cerebellar cortex (Cb) in control (left), Tg1 (middle), and Tg2 (right) mice. Note in control mice, the low level of NR2B labeling (blue) in the cerebellum as compared to hippocampal CA1 and dentate gyrus (DG). In addition, note moderate increased labeling in cerebellar molecular layer (ml) of transgenic mice. **D**, Low- and high-magnification images of calbindin immunoreactivity in sagittal cerebellar sections illustrating the normal appearance of cerebellar gross morphology and PCs of adult transgenic (Tg1 and Tg2) mice. **E**, top, High magnification of individual Golgi-stained PCs (black) of control (left) as well as Tg1 (middle) and Tg2 (right) NR2B mice, counterstained with thionin (blue). Bottom, Sholl analysis of the dendritic arborization of PCs (left) and length of their primary dendrites (right) for control (black, n = 30, N = 4), Tg1 (orange, n = 30, N = 3), and Tg2 (red, n = 30, N = 4) NR2B mice. Empty circles indicate individual data points, full circles indicate mean ± SEM.

Both Tg1 and Tg2 mice showed normal growth, body weights and breeding ratios compared to control littermates. The cyto-architecture of the cerebellum of both lines was normal and their foliation was well preserved (Figure 1D). Immunohistochemistry for calbindin-D28K and Sholl analysis of Golgi material of the mice indicated that morphology of Purkinje cells was unaltered (Figure 1E). Immunohistochemistry for calbindin-D28K and Sholl analysis of Golgi stained tissue indicated that morphology of PCs was unaltered (Sholl analysis: $p = 0.90$ and $p = 0.32$ for Tg1 and Tg2 vs Ctrls, respectively, Rep. measures ANOVA; Primary dendrite length: Tg1 40.3 ± 3.1 μm, Tg2 37.0 ± 3.3 μm, Ctrl 38.6 ± 3.6 μm; $p = 0.93$ and $p = 0.94$ for Tg1 and Tg2 vs Ctrls, respectively) (Fig. 1E). Furthermore, behaviour of both Tg1 and Tg2 in the home cage was indistinguishable from that of wild-type littermates.

To determine whether ectopic NR2B subunits assemble and result in altered synaptic NMDA currents in PCs, we performed patch-clamp recordings of PCs in acute cerebellar slices bathed in Mg^{2+}-free solution with subsequent application of AMPAR and NMDAR blockers (NBQX and D-AP5, respectively). In line with previous studies [286, 287], PCs from 6-week old controls showed a NMDA-mediated current (*i.e.* NBQX-insensitive and AP5-sensitive) at the CF to PC synapse (77 ± 21 pA). In both Tg1 and Tg2 mutant mice the NMDAR-mediated currents at CF-PC synapses were significantly larger than those in controls (262 ± 52 and 365 ± 41 pA; $p = 0.025$ and $p = 0.001$ vs. Ctrl, respectively) (Figure 2A). Next, we determined whether NMDA-mediated currents also occurred at the PF to PC synapse; *i.e.* we quantified the percentage of a 200-300 pA PF to PC excitatory postsynaptic current (EPSC) that was NMDA-mediated. These percentages were negligible in controls (4 ± 1 %), modestly present in Tg1 (18 ± 5 %), but more prominently present in Tg2 PCs (38 ± 11 %); the percentage of Tg2, but not that of Tg1,

was significantly higher than that in controls (p = 0.001 and p = 0.10, respectively) (Figure 2B).

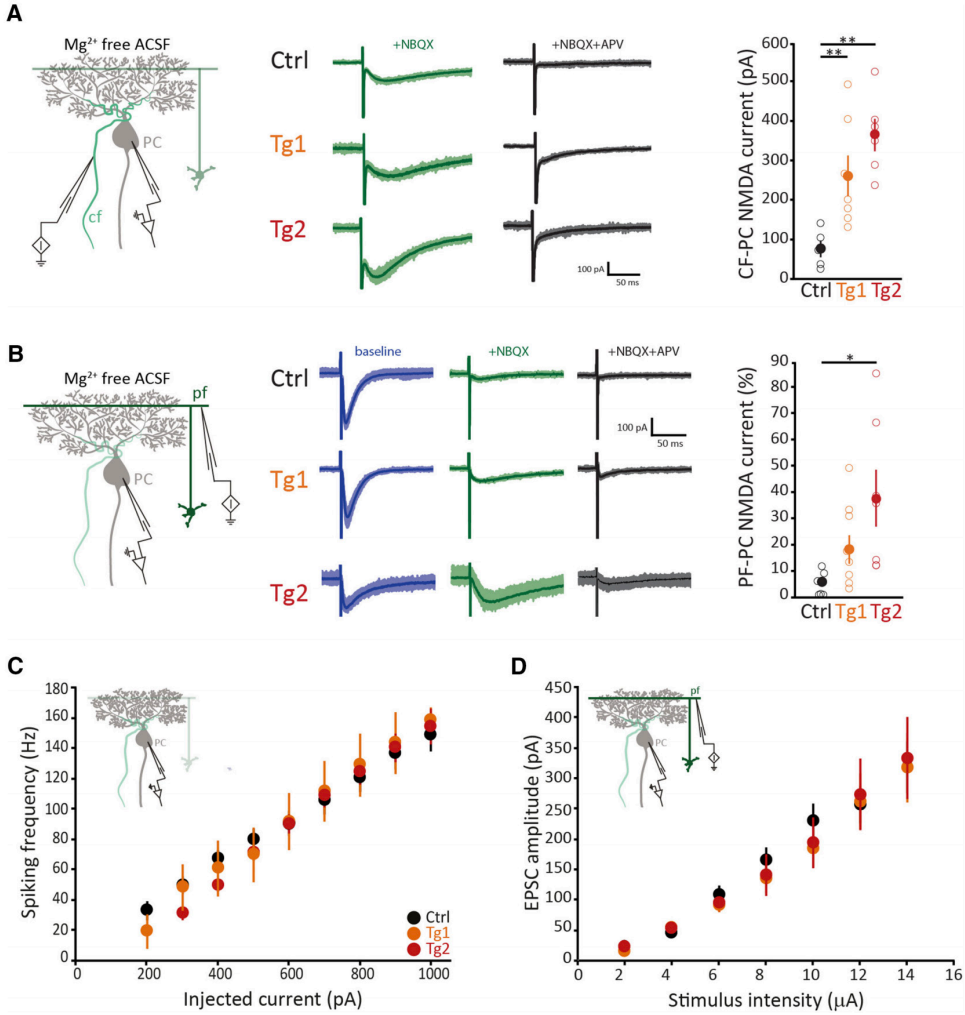

Figure 2. Functional NMDARs are present at six weeks of age and do not compromise PCs' basic electrophysiological properties. **A**, left, Schematic representation of the recording configuration. Middle, Example traces of CF currents recorded in the presence of the AMPA antagonist NBQX (green) and subsequently of blockers of both AMPA and NMDARs (D-AP5, black) in PCs of both transgenic lines and control littermates. Bold lines are average values; shading indicates individual cell variability. Right, Quantification of NMDA current at the CF-PC synapse in control (Ctrl, black, n = 5) and transgenic animals (Tg1, orange, n = 7; Tg2, red, n = 6). **B**, Similar to A, with additional example traces of baseline PF-evoked EPSCs before the addition of glutamatergic receptors blockers (blue), and normalized PF-PC NMDA current quantification (Ctrl, n = 9; Tg1, n = 9; Tg2, n = 7). Note that NMDA-mediated currents are only significantly different from controls in Tg2. **C**, Average firing frequency elicited by somatic current injections from -65 mV in PCs of transgenic (Tg1, orange, n =5; Tg2, red, n

= 12) and control (Ctrl, black, n = 15) mice. The inset illustrates the recording configuration. **D**, Average amplitude of the EPSCs at the PF-PC synapse to stimuli of increasing intensity for transgenic (Tg1, orange, n = 5; Tg2, red, n = 8) and control (Ctrl, black, n = 18) mice. The inset illustrates the recording configuration. Empty circles represent individual data points, full circles are mean ± SEM; p 0.05, p 0.01, and absolute p values are indicated in the main text.

Next to study the effect of ectopic NR2B expression on basic PC electrophysiological properties we first performed whole cell current-clamp recordings at physiologically relevant temperatures to investigate intrinsic excitability (Figure 2C). PCs of all genotypes showed increasing action potential firing frequencies upon somatic current injections of increasing amplitude comparable to the ones of their control littermates. The slope of the linear input-output relationship in transgenic mice did not differ from that in control animals (Tg1 17.4 ± 1.5 Hz/pA, Tg2 18.1 ± 1.9 Hz/pA, Ctrls 15.0 ± 0.9 Hz/pA; $p = 0.47$ and $p = 0.45$ for Tg1 and Tg2 vs. Ctrls, respectively), indicating a normal level of excitability. In addition, for each cell we analyzed the action potential properties and again we found no significant differences in terms of spike baseline, peak amplitude, after-hyperpolarization amplitude or half-width among genotypes (all p values > 0.13). Finally, the presence of NMDARs in PCs prompted us to investigate the post-synaptic amplitude evoked by PF stimulation (*i.e.* in a recording solution with Mg^{2+} and holding at -65 mV) at increasing stimulus intensities (Figure 2D). No obvious differences were found in the EPSC kinetics (all p-values > 0.9), nor in the input/output ratio of PF-EPSCs between transgenic animals and controls ($p = 0.83$, repeated measures ANOVA).

Taken together, our data show that we generated transgenic mice over-expressing NR2B subunits without affecting baseline transmission, but that only Tg2 showed significantly more NMDAR-mediated currents at their PF to PC synaptic inputs compared to Ctrls.

NMDA currents at the PF-PC synapse selectively prevent the induction of long-term potentiation

While induction of PF to PC LTD depends on CF activation for its high Ca^{2+} influx, LTP is achieved through repetitive stimulation of only PFs and requires a low Ca^{2+} concentration [25] and has been shown to be independent of postsynaptic NMDARs [301] [302]. We therefore hypothesized that insertion of Ca^{2+}-permeable NMDARs at the PF-PC synapse would affect LTP induction (Figure 3A). Given that only Tg2 showed significantly more NMDA-mediated currents at their PF-PC synapses than controls, we focused our plasticity

experiments on Tg2 and their wild type littermates. Indeed, whereas the controls showed normal potentiation (pre- vs. post-tetanus: $p < 0.001$, Linear Mixed Model, see Methods), the amplitude of the EPSCs of the Tg2 mice after LTP induction was significantly lower from the ones recorded in control cells (Tg2 vs. Ctrls $p = 0.034$, repeated measures ANOVA). In contrast, LTD at the PF to PC synapse (Ctrls, pre- vs. post-tetanus: $p < 0.05$, Linear Mixed Model, see Methods) was not affected (Tg2 vs. Ctrls, $p = 0.63$, repeated measures ANOVA) (Figure 3B). To unequivocally link the phenotype in LTP induction to the activation of NMDARs we repeated the experiment in presence of NMDAR antagonist D-AP5 (Figure 3C). Blocking NMDA currents minimized the effects on the induction of LTP (pre- vs. post-tetanus for Ctrls, $p < 0.001$; Linear Mixed Model, see Methods), ablating the difference between genotypes ($p = 0.80$, repeated measures ANOVA).

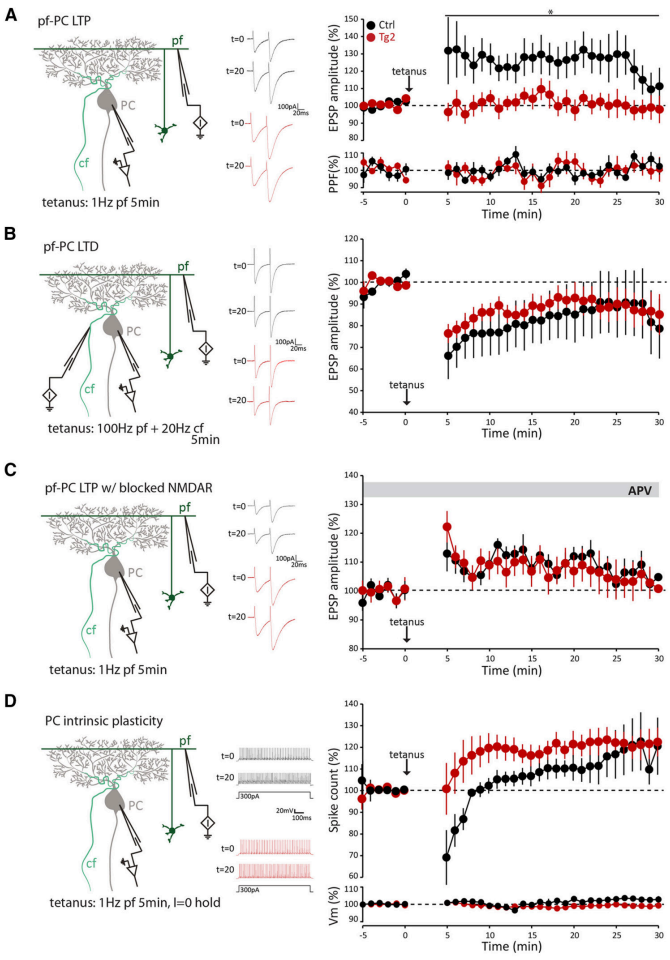

Figure 3. PF-PC LTP is selectively affected in transgenic mice. **A**, LTP was induced by PF stimulation at 1 Hz for 5 min in six-week-old transgenic (Tg2, red, n = 8) and control (Ctrl, black, n = 7) mice. The normalized paired-pulse ratio (50-ms interstimulus interval) of the recordings of the same cells is plotted below. **B**, LTD was induced as described in A, but with concomitant CF activation (Ctrl, n = 8; Tg2, n = 8). **C**, Similar to A, but with the NMDAR blocker D-AP5 present in the extracellular solution (Ctrl, n = 7; Tg2, n = 8). **D**, Induction of IP by 5 min of PF stimulation at 1 Hz did not result in significant differences between transgenic and control mice (both n = 6). The normalized membrane potentials of the same cells are represented below. The scheme at the left of each panel depicts the

respective recording configuration, while the middle example traces of Ctrl (black) and Tg2 (red) EPSCs (A–C) or action potentials (D) recorded before (t = 0 min) and after (t = 20 min) the tetanic stimuli show the plastic changes. Values are mean ± SEM; p 0.05; p 0.01; absolute p values are indicated in the main text.

Impairment in PF to PC LTP induction often co-occurs with long-term deficits in intrinsic plasticity [22, 29, 303]. Instead, in PCs of Tg2 mice the overall intrinsic plasticity was enhanced shortly after induction (p = 0.036 for the first 10 min after induction, 0.095 for the entire period, repeated measures ANOVA) (Figure 3D). We conclude that over-expression of NMDAR's in PCs selectively prevents the induction of LTP at the PF-PC synapse, and that this deficit might be partly compensated for by a modest early increase in intrinsic plasticity.

Normal motor behavior but impairment in motor learning

LTP at the PF-PC synapse probably does not affect baseline motor performance, but it may well contribute to vestibulo-cerebellar motor learning [13, 284, 304]. At the same time, it should be noted that short-lasting enhanced intrinsic plasticity, as observed in the Tg2 mutant, might partly compensate for a deficit in LTP induction [13, 284].

To evaluate the behavioral consequences of overexpression of NR2B in the Purkinje cells of the Tg2 mice we subjected them to both motor performance and learning tests. First, we confirmed that the general motor behavior of Tg2 animals was comparable to that of their control littermates in an open field test; neither path length nor average speed was affected (p = 0.28 and p = 0.29, respectively; Figure 4A). In addition, we evaluated oculomotor activity, which is particularly sensitive to cerebellar deficits [22, 304, 305].

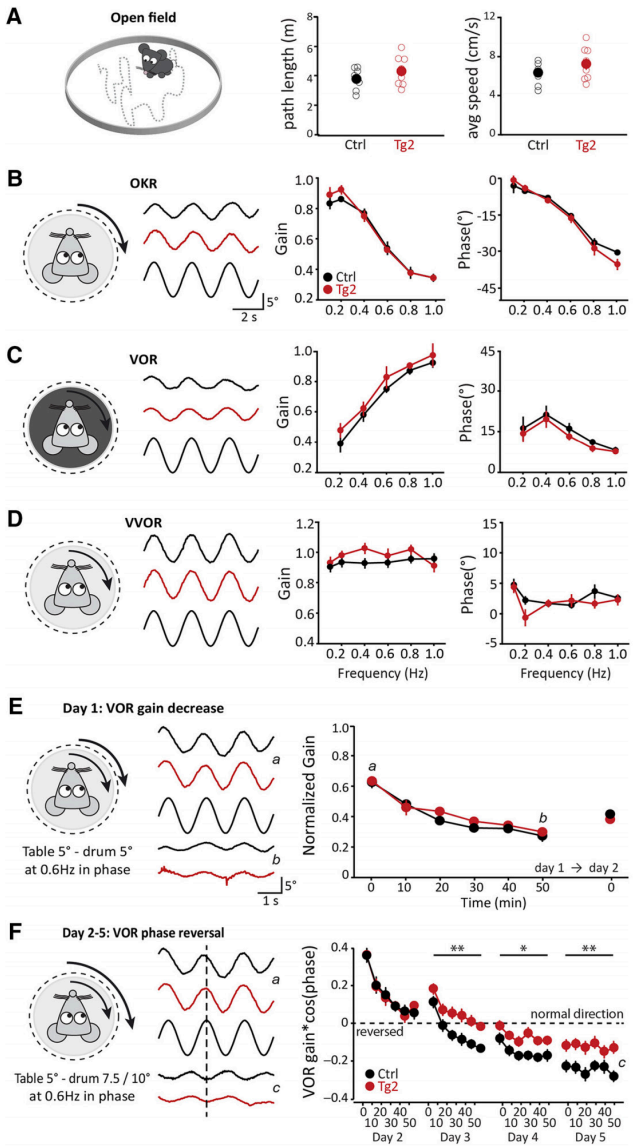

Figure 4. Motor performance is normal, but motor learning is impaired in transgenic mice. **A**, Distance traveled and average speed in the open field for transgenic (Tg2, red, n = 8) and control (Ctrl, black, n = 7) mice. **B–D**, Baseline compensatory eye movements (examples traces for 0.4 Hz, middle left) quantified by gain (middle right) and phase (right) for Tg2 mice (red, n = 9) and control (Ctrl, black, n = 10) mice: (B) OKR; (C) VOR (in the dark); and (D) VVOR (in the light), schematized on the left of each respective panel. **E**, left, Representation of gain-decrease training paradigm (day 1: 5 = 10 min sinusoidal, in-phase drum and table rotation at 0.6 Hz, both with an amplitude of 5°; day 2: VOR gain measurement at 0.6 Hz). Middle, Example traces of before (time point, t = 0, indicated by a) and after (t = 50 min, b) adaptation. Right, Normalized gain for VOR recorded with 10-min intervals during 50-min training session for six-week-old Tg2 mice (red, n 8) and control (Ctrl, black, n 11) mice on day 1 and a single measurement at day 2. F, Similar to E; following the gain-decrease protocol, for four consecutive days the six-week old transgenic and control mice were subjected to the phase reversal protocol (5 10 min sinusoidal in-phase drum and table rotation at 0.6 Hz, but with drum amplitudes of 7.5° on day 2 and 10° on days 3–5, while the table amplitude was 5°). VOR responses (middle: example traces, a same as E, c: t 50 min on day 4) are depicted as gain of eye movement multiplied by the cosine of its phase, gaincos(phase). Negative values here indicate a phase larger than 90° and the (theoretical) goal of the training is a value of -1. Empty circles represent individual data points, full circles are mean

SEM; p values are indicated in the main text; asterisks indicate significant difference.

Both gain and phase values during the optokinetic reflex (OKR) as well as during the vestibulo-ocular reflex in the dark (VOR) and the light (VVOR) elicited by sinusoidal stimulation at different frequencies (0.1 – 1.0 Hz) with a fixed amplitude (5°) did not differ significantly between genotypes (all p values > 0.13, repeated measures ANOVA; Figures 4B-D).

Next, we subjected the Tg2 animals to the type of VOR training that is most sensitive, *i.e.* phase reversal learning, which is aimed at gradually converting the direction of the eye movements over several days of in-phase vestibular and visual stimulation [306]. During the first session, which entails standard

gain-decrease training evoked by rotating drum and table in-phase at 5° at 0.6 Hz, the amplitude of the VOR in Tg2 mice decreased to similar levels as that in control mice (p = 0.33, repeated measures ANOVA; Figure 4E). Moreover, when the animals were tested again after spending 23 hours in the dark, the consolidation of the change in VOR gain was not different among genotypes (p = 0.21). However, when we subjected animals to phase reversal training for four consecutive days, the Tg2 mice performed worse than controls in that their adaptation was delayed. The training aims to reverse the direction of the VOR, resulting in a negative gain*cos(phase) value (Figure 4F) and this adaptation is impaired in Tg2 mouse from day 3 onwards (day 3, 4 and 5, p = 0.005, p = 0.026 and p = 0.001, respectively, repeated measures ANOVA). Together, these data show that NR2B transgenic mice have an unaffected baseline motor performance and that their learning capabilities are slightly, but significantly, affected.

Discussion

To shed light on the surprisingly low expression level of the main coincidence detector in the brain, the NMDAR, we generated a transgenic mouse line that over-expresses NMDARs at one of the most studied and phylogenetically oldest sites of plasticity in the brain, the parallel fiber to Purkinje cell synapse. The L7-NR2B+ Tg2 mice, which expresses functional NMDAR-mediated currents not only at the CF-PC synapse, but also at the PF-PC synapse, develop normally and have no morphological abnormalities or impaired motor performance. Interestingly, the NMDAR-mediated currents diminish the ability for LTP induction at the PF-PC synapse and affects a demanding form of cerebellar-dependent motor learning, VOR phase-reversal learning.

As previously shown in an *in vitro* essay [293], our data imply that NR1 subunits are sufficiently expressed in PCs to aggregate with the exogenously expressed NR2 subunits to form functional heterotetramers. As low expression levels and suboptimal antibody quality prohibit determining the sub-cellular localization of the NR2B subunit in our experiments, we cannot exclude the possibility of extra-synaptic receptors. The normal absence of NMDARs at PF input sites under physiological circumstances is therefore not caused by the scarceness of NR1 subunits, but by the limited and finely regulated NR2 expression and selective intracellular transport machinery [286, 287], which may in part depend on the UTR sites of the subunits [294, 295]. Moreover, it also appears that NMDARs are not absent from the PF-PC synapse in controls to prevent excitotoxicity [307], as we found no sign of PC death in our transgenic mouse lines. Still, the amount of NMDAR-mediated current was not massive, and we cannot exclude the possibility that higher expression levels could potentially trigger PC apoptosis.

The main consequence of the genetically induced presence of NMDARs at the PF-PC synapse is that it renders the synapse incapable of potentiation. In contrast to other well-studied excitatory synapses, *e.g.* the well-characterized hippocampal CA3 to CA1 synapse or the synapses formed by the cerebellar mossy fibers with granule cells and cerebellar nuclei neurons [247, 308, 309], NMDARs at the PF-PC synapse are not only dispensable for LTP induction, they are in fact effectively blocking it if present at the postsynaptic site. The plasticity induction rule in PCs is, in terms of calcium dependence, reversed compared to the traditional BCM-rule in pyramidal cells [25, 310]; hence, LTP induction is only possible when Ca^{2+} concentrations are relatively low. In fact, in normal mice the presence or absence of CF-triggered Ca2+-level increase determines the occurrence of LTD or LTP, respectively, and this effect is independent of the change in Ca2+-level evoked by the PF stimulation [311]. It is therefore tempting to hypothesize that in our transgenic mice the presence of Ca^{2+}-permeable NMDARs increases the Ca^{2+} concentration to a level that is too high to allow LTP, while leaving LTD induction unaffected. Conversely, but in line with this concept, blocking Ca^{2+}-permeable NMDARs in mature mice reduces the dendritic Ca^{2+} influx during a complex spike to a level that is too low for LTD, while leaving LTP unaffected [301]. Such a mechanism, which will have to be looked at in future studies, may also explain why intrinsic plasticity was slightly increased in the Tg2 mice, as this form of plasticity is largely regulated by the activity of SK2 channels, which is also Ca^{2+}-dependent [27, 312]. In this regard, the L7-NR2B+ Tg2 mice diverge from other LTP-deficient mutants in which the calcium dynamics are not directly affected. PC-specific mutants, such as the L7-PP2B-, L7-Shank2-, and L7-GluR3-mutants [22, 29, 30], all do not only show a

blockage of LTP induction, but they also show a profound reduction in intrinsic plasticity, rather than an enhancement as found here in the Tg2 mice. The combination of deficits in both LTP-induction and intrinsic plasticity leads to a more severe behavioral phenotype in that the VOR phase reversal adaptation is, unlike that of the Tg2 mice, virtually completely abolished [22, 29, 30]. Thus, the relatively mild behavioral phenotype of the Tg2 mice may be explained by an intact, if not elevated, level of intrinsic plasticity, which might also at least partly result from an elevated Ca^{2+}.

Our results fit with the interpretation that different types of plasticity in PCs – and in other cerebellar neurons – synergistically interact to ensure optimal learning [284]. According to this theory, mutations that impair several plasticity mechanisms or network elements simultaneously typically affect more basic types of cerebellar-dependent learning and, if they do so, they affect them more severely [22, 275, 313, 314]. In contrast, when a single mechanism at a single type of synapse in the circuit is impaired, other mechanisms may compensate (Gao et al., 2012) and the ability to perform and learn motor tasks may be maintained to a larger extent (this manuscript; [23].

Methods

Generation of transgenic mice

The NR2B transgene (Mouse Grin2b-001; ENSMUST00000053880.12) including 470 bases of the 3' UTR, was cloned into expression vector pGEM-L7containing the L7-promoter [280], by fusing the ATG initiation codon of the NR2B transgene with the initiation codon of the L7 gene. The resulting pGEM-L7NR2B was digested with with SalI/ClaI and the insert was used to generate the transgenic founders by pronuclear injection into C57BL/6NHsd inbred zygotes. The inbred founders were crossed into C57BL/6NHsd to produce F1 generation, two of which were selected for F2 offspring (Tg1 and Tg2) against a C57BL/6NHsd background. The genotypes of all offspring were analyzed by preparing tail DNAs. The 5' and 3' primers for detecting NR2B transgene were L7 S (CAC TTC TGA CTT GCA CTT TCC TTG G), L7 AS (TTC TTC AAG CTG CCC AGC AGA GCT C) and 165 (GCC AAA CTG GAA GAA CAT GGA GGA C); wild-type 450 bp, transgenic 557 bp. Mouse tail DNAs (about 1 mg) were amplified (94°C 3'//94°C 1'; 58°C 45"; 72°C 1':30cycles//72°C 10'// 4°C) on a Robo cycler. For all experiments the researchers were blind to the genotype of the animals. Unless stated otherwise we used 6 ± 1 weeks old male and female littermates, gender-matched across groups. All experiments were performed in

accordance with the guidelines for animal experiments of Erasmus MC, Netherlands Institute for Neuroscience (KNAW), and the Dutch National Legislation.

Western Blot

Lysates for Western Blot were prepared by quick dissection of the brain and by homogenization of the brain tissue in lysis buffer (10 mM TRISHCl 6.8, 2.5% SDS, 2 mM EDTA) and protease and phosphatase inhibitor cocktails (Sigma). The concentration of the lysates was adjusted to 1 mg/ml and a 10 µg volume was used for Western blot analysis. Western blots were probed with antibodies directed against the N-terminal NR2B (anti-mouse, 1:1000; Cell Signaling) and NR1 (anti-rabbit, 1:1000; Cell Signaling). Bands were visualized using Enhanced Chemo Luminescence (Pierce). Loading controls were performed with anti-actin antibodies (1:20000, Cell Signaling).

Histology

Mice were anesthetized with an overdose of Nembutal (i.p.) and transcardially perfused with saline followed by 4% paraformaldehyde (in 0.12 M phosphate buffer; PB). Sagittal sections (40-µm thick) were processed free-floating for calbindin immunohistochemisty or NR2B-immunofluoresence. For NR2B-immunofluoresence sections were exposed to limited proteolytic digestion to expose synaptic receptors (Watanabe et al., 1998): Sections were incubated in 0.2 M HCl containing 0.4 mg / mL pepsin (Sigma) for 20 min with continuous agitation. After rinsing in PBS and pre-incubation with PBS with 0.1% Triton X-100 (PBST) and 10% normal horse serum, the sections were incubated in PBST/1% normal horse serum with Ms anti-NR2B (NeuroMab clone N59/36; dilution 1:1000) for 48 h at 4 °C. NR2B antibody was visualized with Cy3-Donkey anti-mouse secondary antibody (1:400), and analyzed with (Zeiss Jena, Germany) LSM 700 upright confocal laser scanning microscope. For calbindin immunohistochemistry, after preincubation in PBST sections were incubated with Rabbit anti-Calbindin (Swant; dilution 1:15000) in PBST/1% normal horse serum for 48 h at 4 °C, followed by incubation with biotinylated goat-anti-rabbit secondary antibody (1:200; Vector), incubation with avidin-biotin-peroxidase complex (ABC) (Vector Laboratories, Burlingame, CA, USA), and reaction with diaminobenzidine (DAB, 0.05%). Calbindin-immunoperoxidase-stained sections were analyzed using a Leica (Nussloch, Germany) DM-RB microscope, or scanned with a Hamamatsu NanoZoomer 2 whole slide imager and analyzed with NDP.view (Hamamatsu city, Japan) software. For Golgi staining, which was used for Sholl analysis, Tg1-, Tg2- and control mice were perfused with saline, followed by a buffered aldehyde fixative and a mordant consisting of

6% potassium dichromate, 6% chloral hydrate, and 4% formaldehyde. After postfixation in the same mordant for 3 days, blocks of the cerebellar cortex were treated with 0.75% silver nitrate for an additional 3 days, embedded in a soft Epon mixture and sectioned with a heated steel knife [315].

***In vitro* electrophysiology**

Mice (6±1 weeks old) were decapitated under isoflurane anaesthesia. Subsequently, the cerebellum was removed and transferred into ice-cold slicing medium containing (in mM): 240 Sucrose, 5 KCl, 1.25 Na_2HPO_4, 2 $MgSO_4$, 1 $CaCl_2$, 26 $NaHCO_3$ and 10 D-Glucose, bubbled with 95% O_2 and 5% CO_2. Parasagittal slices (200- or 250-µm thick) of the cerebellar vermis were cut using a vibratome (VT1000S, Leica) and afterwards kept in ACSF containing (in mM): 124 NaCl, 5 KCl, 1.25 Na_2HPO4, 2 $MgSO_4$, 2 $CaCl_2$, 26 $NaHCO_3$ and 20 D-Glucose, bubbled with 95% O_2 and 5% CO_2 for > 1 h before the experiments started. *In vitro* experiments were performed in slices at room temperature (20-22 °C), which were continuously perfused with ACSF that was supplemented with picrotoxin (100µM) or bicuculline methiodide (20µM) to block $GABA_A$ receptors. All drugs were purchased from Sigma (St. Louis, MO). Whole-cell patch-clamp recordings were performed using either an EPC-10 amplifier (HEKA Electronics, Lambrecht, Germany) or an Axopatch amplifier 700B (Molecular Devices, Union City, CA, USA). PCs were visualized using an upright microscope (Axioskop 2 FS plus, Carl Zeiss, Jena, Germany) equipped with a 40X water immersed objective. If not stated otherwise, recording electrodes were filled with an intracellular solution containing (in mM): 124 K-Gluconate, 9 KCl, 10 KOH, 4 NaCl, 10 HEPES, 28.5 Sucrose, 4 Na_2ATP, 0.4 Na_3GTP (pH 7.25-7.35; osmolarity ~290). For extracellular stimulation, patch electrodes filled with ACSF were positioned to touch the surface of the slice at the most distal 1/3 of the molecular layer lateral to the recorded PCs for PF stimulation and in the granular layer close to the recorded PC for CF stimulation. Recordings were excluded if series or input resistances (R_S and R_I, respectively) (assessed by -10 mV voltage steps following each test pulse) varied by > 15% over the course of the experiment. The liquid junction potential was not corrected for. Quantification of NMDA currents was performed in magnesium-free ACSF supplemented with glycine (10 µM, Sigma) by subsequent application of the AMPA antagonist NBQX (12.5 µM, Tocris) and the NMDA antagonist D-AP5 (10 µM, Tocris). All-or-none climbing fibers responses were first identified in current clamp by the typical complex spike shape and the absolute NMDA contribution was calculated in voltage clamp (holding potential -65 mV) by subtracting the NBQX+AP5 insensitive residual component

to the NBQX sensitive. PF responses of approximately -200 pA were taken as a baseline in voltage clamp (holding potential -65 mV) and the NMDA contribution was calculated as described for CF-responses but normalized to the baseline response. Rs was compensated online to obtain a residual value > 10 MΩ. PC intrinsic excitability was recorded in current-clamp mode at 34 ± 1 °C. PCs were discarded when >800 pA hyperpolarizing current was required to maintain the holding potential at -65 mV or when action potential firing occurred at this holding potential. We injected 800 ms current steps ranging from -100 to +1000 pA with 100 pA increments. The average spiking frequency measured over the entire current pulse was used to construct current-frequency plots. Action potential properties (peak amplitude, after-hyperpolarization amplitude and half-width) were evaluated using the first action potential generated by each PC. To assess the stimulus intensity - EPSC amplitude (input-output) ratio consistently, only PCs were selected in regions with comparable width of the molecular layer. For these recordings electrodes contained (in mM): 130 $CsMeSO_4$, 4 $MgCl_2$, 0.2 EGTA, 10 HEPES, 10 Na-Phosphocreatine, 1 QX-314, 4 Na_2ATP, 0.4 Na_3GTP (pH 7.25-7.35). LTP at the PF-PC synapse was assessed by PF stimulation at 1 Hz for 5 min (PF-LTP protocol; Coesmans et al., 2004), while long-term depression (LTD) was induced by PF activation (10 stimuli at 100 Hz) and CF activation (2 stimuli at 20 Hz), repeated 30 times every 10 s at 34 ± 1°C (PF-LTD protocol; [316]. Test responses were evoked at a frequency of 0.05 Hz (2 stimuli of 0.5-6 μA pulses; 50 ms inter-stimulus interval). PCs were clamped at -65 to -70 mV to prevent spontaneous action potential firing. Plasticity of PC's intrinsic excitability was recorded in current-clamp mode at 34 ± 1°C. PCs were discarded when >800 pA hyperpolarizing current was required to maintain the holding potential at -65 mV or when action potential firing occurred at this holding potential. We induced intrinsic plasticity by 1 Hz PF stimulation for 5 min (PF-LTP protocol, comparable to Belmeneguai et al, 2010, but with short ramping current injections to probe the response; see Fig. 3D) at I=0. Four current steps (800 ms), ranging from 100 to 800 pA in 100 pA increments were injected to evoke action potential firing during steps 2-4. The spike count at the third current step was taken as a measure of excitability. RI was calculated from the first hyperpolarizing current injection. To determine if plasticity was induced a linear mixed model was used based on dividing the post-tetanus period into two 15 min periods (post1 and post2) and comparing these to pre-tetanus values (pre). For LTP, LTD, and intrinsic plasticity (IP) the estimates of fixed effects (of tetanus stimulus) on EPSCs in control mice were: LTP, post1 vs pre, estimated +25.9 ± 4.9 %, $p < 0.001$; post2 vs. pre, estimated +21.3 ± 5.0 %, $p < 0.001$; LTD, post1 vs pre, estimated –21.7 ± 5.5 %, $p < 0.001$; post2 vs. pre, estimated –12.8 ± 5.6 %, $p = 0.022$; LTP with D-AP5, post1 vs pre, estimated +10.2 ± 1.9 %, $p < 0.001$; post2 vs. pre, estimated +6.9

± 1.9 %, $p < 0.001$; and IP, post1 vs pre, estimated –4.3 ± 4.5 %, p =0.34; and post2 vs. pre, estimated +16.1 ± 4.6 %, $p = 0.001$. To compare genotypes a repeated measures ANOVA was used on the 20 min recording period post tetanus (the minimal recording duration).

Open field

To test locomotor activity and anxiety, individual mice were placed in a circular, dimly–lit open field (120 cm diameter), and the total distance traveled, together with the average speed of each mouse, was recorded for 10 min (SMART software, Panlab, Barcelona, Spain).

Compensatory eye movements

During their fifth postnatal week mice were prepared for chronic, head-restrained recordings of compensatory eye movements. Mice were 37 ± 3 days at the beginning of the 5 days of compensatory eye movement testing. In short, under isoflurane anaesthesia (initiation at 4%, maintenance at ~1.5% with O_2) a pedestal was constructed using Optibond primer and adhesive (Kerr, Bioggio, Switzerland) and Charisma (Haeraeus Kulzer, Armonk, NY, USA). After a recovery period (2-3 days) mice were head-fixed by means of a magnet (Neodymium, 4x4x2 mm, MTG Europe, Weilbach, Germany) embedded in a custom-made U-shaped pedestal and a securing screw. A cylindrical screen (diameter 63 cm) with a random-dotted pattern (each element 2°) surrounded the turntable (diameter 60 cm) on which the mouse was placed. The optokinetic reflex (OKR) and the vestibulo-ocular reflex in dark (VOR) and light (VVOR) were elicited by sinusoidal rotation of either drum (OKR) or table (VOR and VVOR). Motor performance was tested by rotating at 0.1-1.0 Hz with 5° amplitude (fixed). Each frequency – amplitude combination was tested twice with 8 (for 0.1 Hz) to 20 (for 1.0 Hz) repeated cycles and results were averaged. Motor learning was tested by mismatching visual and vestibular input: 'gain decrease' was evoked by rotating drum and table in phase at the same amplitude (5°) at 0.6 Hz and 'phase reversal' by subsequent rotation in phase with increased amplitude of the drum (day 2, 7.5°; day 3, 10°) at the same frequency. Animals were kept in the dark in between training sessions. Phase reversal results are depicted as gain multiplied by the cosine of the phase to capture the change in timing and amplitude of movement in a single value (gain*cos(phase). Phase values larger than 90° result in a negative gain*cos(phase) value. Consolidation was calculated as the learned response on the second day as a percentage of the learning during the first day; for example, gain decrease consolidation = 100% · (gmax-day1 - gmax-day2 / (gmax-day1 – gmin-day1), with gmin-

day1 being the minimum gain on day 1 and gmax-day2 the maximum gain on day 2. To illuminate the eye during the recordings we used two table-fixed infrared emitters (OD-50L, max. output 600 mW, dispersion angle 7°, peak wavelength 880 nm; Opto-Diode, Camarillo, CA, USA), and a third emitter mounted to the camera aligned horizontally with the camera's optical axis. This third emitter produced the tracked corneal reflection. The pupil position, after subtraction of the corneal reflecting position, was recorded using the eye-tracking device (ETL-200, ISCAN systems, Burlington, NA, USA). Calibrations were performed as described previously [317]. Gain and phase values of the eye movements were calculated using a custom-made Matlab routine (Matlab, MathWorks Inc, Natick, Massachusetts, USA). Gain and phase results plotted against frequency or time were statistically analyzed using repeated-measures ANOVA.

Data analysis

All values are represented as mean ± SEM, p-values of < 0.05 were considered significant. Data distributions were evaluated using either Levene's test of equality of variance for independent data or Mauchly's test of sphericity for repeated measures. Unless stated otherwise, statistical analysis was done using one-way ANOVA test with Tukey's post-hoc correction where three groups were compared (see Table for details per test).

Chapter 3.3

Impact of parallel fiber to Purkinje cell long-term depression is unmasked in absence of inhibitory input

Henk-Jan Boele *, **Saša Peter** *, Michiel M. Ten Brinke *, L. Verdonschot, A.H.C. Ypelaar, D. Rizopoulos, Z. Gao, S.K.E. Koekkoek & Chris .I. De Zeeuw ¶

* First-Co-author(s)

¶ Corresponding author(s)

Science Advances (2018)

Abstract

Pavlovian eyeblink conditioning has been used extensively to study the neural mechanisms underlying associative and motor learning. During this simple learning task, memory formation takes place at Purkinje cells in defined areas of the cerebellar cortex, which acquire a strong temporary suppression of their activity during conditioning. Yet, it is unknown which neuronal plasticity mechanisms mediate this suppression. Two potential mechanisms include long-term depression of parallel fiber to Purkinje cell synapses and feed-forward inhibition by molecular layer interneurons. We show, using a triple transgenic approach, that only concurrent disruption of both these suppression mechanisms can severely impair conditioning, highlighting that both processes can compensate for each other's deficits.

During eyeblink conditioning, subjects typically will hear a short beep or see a light (conditional stimulus, CS) followed several hundred milliseconds later by an air-puff on the eye (unconditional stimulus, US). As a result of repeated CS-US pairings, subjects will eventually learn to close their eye in response to the CS, which is called the conditioned response (CR). The CR is not simply a static reflex, but instead an acquired, precisely timed eyelid movement, the kinetic profile of which is determined by the temporal interval between CS and US (**Fig. 1a**), [for review: 34, 318]. During Pavlovian eyeblink conditioning, memory formation takes place in Purkinje cells (PCs) of defined areas of the cerebellar cortex [32, 109, 319-322]. These PCs receive inputs from the mossy fiber - parallel fiber (PF) system, which conveys sensory CS signals and input from only one climbing fiber (CF), which transmits the instructive US signal (**Fig. 1b**). During the conditioning process, these PCs acquire a well-timed suppression of their simple spike firing in response to the CS [109, 279, 323], thereby temporarily disinhibiting the cerebellar nuclei, which elicits the eyeblink CR.

But how can PCs time their simple spike suppression with such millisecond precision? Most models on eyeblink conditioning assume a critical role for long-term depression (LTD) of the PF-PC synapse [324, 325]. However, PCs show high firing frequencies that are intrinsically generated, even when the PF input is silenced [31, 326, 327], and animal models lacking PF-PC LTD can have completely normal eyeblink conditioning [23, 328]. A second contribution, which in principle may actively suppress the intrinsic PC simple spike activity, could be provided by molecular layer interneurons (MLIs), since they provide the PC with a powerful feed forward inhibition (FFI) [320, 329]. However, removal of MLI-PC FFI induces compensation at the PF-PC synapse [275] and only mildly impairs eyeblink conditioning [109, 330].

Here, we asked the question to what extent a concurrent disruption of PF-PC LTD *ánd* MLI-PC FFI affects cerebellar learning using a Pavlovian eyeblink conditioning task. To this end, we developed a mouse line in which we aimed to block both synaptic processes simultaneously (**Fig. 1c**); we generated *GluR2Δ7-L7-Δγ2* mice by crossing *GluR2Δ7* KI mice with *L7-Δγ2* KO mice. *GluR2Δ7* KI mice have impaired PF-PC LTD, because they lack the last seven amino acids at the intracellular C-terminus tail, which hampers the interaction of GluR2 with PICK1 and GRIP1/2 and thereby its internalization [331]. *L7-Δγ2* KO mice have impaired MLI-PC FFI, as they have a PC-specific ablation of the γ2-subunit of $GABA_a$ receptors [109, 275].

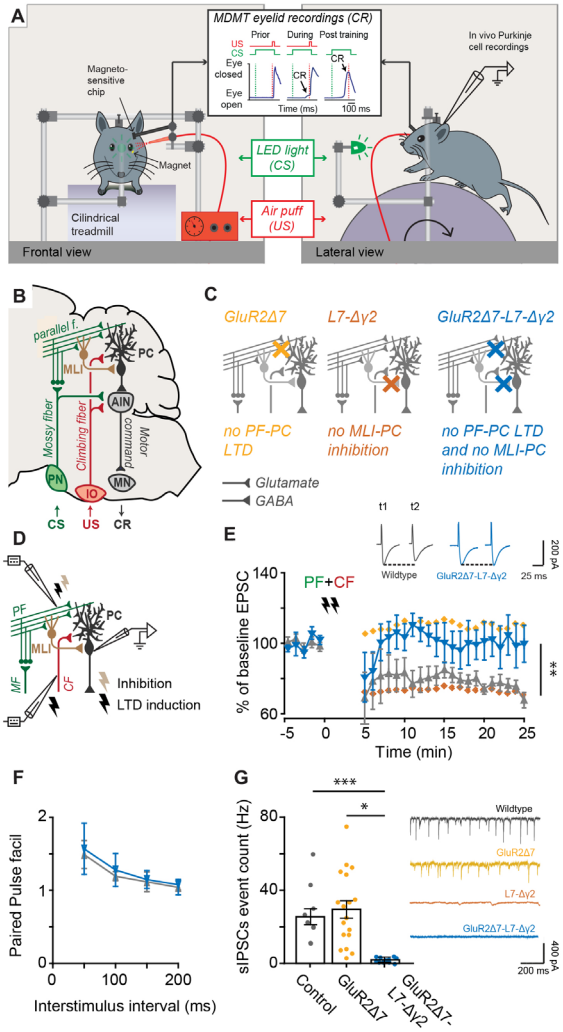

Figure 1 | Eyeblink conditioning setup and confirmation that *GluR2Δ7-L7-Δγ2* mice lack both pf-PC LTD and MLI-PC FFI. (a) Mice are placed in a light and sound- and light isolating chamber with their head fixed on a freely moving foam treadmill. Unconditional stimulus (US) consisted of a weak air puff and conditional stimulus (CS) was a green LED light. Eyelid movements were recorded with magnetic distance measurement technique (MDMT). *In vivo* PC recording were performed on the same treadmill system. **(b)** Neural circuits essential and sufficient for eyeblink conditioning. See main text for explanation. **(c)** Schematic representation of the different mutations: *GluR2Δ7* lack PF-PC LTD, *L7-Δγ2* lack MLI-PC inhibition, *GluR2Δ7-L7-Δγ2* have both disrupted PF-PC LTD and MLI-PC inhibition. **(d)** Schematic overview of MLI-PC inhibition and PF-PC LTD induction experiments. **(e)** In contrast to controls, *GluR2Δ7-L7-Δγ2* show no PF-PC LTD using an induction protocol which consisted of a 100 Hz PF stimulation in 8 pulses followed by a 110 ms delay of single CF activation at 1 Hz for 5 minutes (Controls: t (5) = -4.28, p = 0.008; *GluR2Δ7-L7-Δγ2*: t (5) = 0.052, p = 0.96; Paired t-test). **(f)** Applying inter-stimulus intervals varying from 50 to 200 ms evoked similar levels of paired-pulse facilitation indicating that baseline PF–PC synaptic transmission is unaltered in *GluR2Δ7-L7-Δγ2* mice (F (1,16) = 0.81, p = 0.38, RM ANOVA). **(g)** *GluR2Δ7-L7-Δγ2* mice show significantly less sIPSCs than controls, indicating that they indeed lack MLI-PC inhibition (F (2, 32) = 11.39, p=0.0001, ANOVA, Bonferroni post-hoc). For PF-PC LTD and sIPSCs, data of *GluR2Δ7* and *L7-Δγ2* mice is used with permission from (Schonewille et al., 2011) and (Wulff et al., 2009), respectively. For all comparisons see **Supplementary Table 1**; * $p < 0.05$, ** $p < 0.001$, *** $p < 0.0001$

We first established that *GluR2Δ7-L7-Δγ2* mice lack both PF-PC LTD and MLI-PC FFI. For PF-PC LTD induction, we used a high frequency stimulation of PF in conjunction with CF stimulation (**Fig. 1d**) [332]. Indeed, we were unable to induce postsynaptic PF-PC LTD in *GluR2Δ7-L7-Δγ2* mice just like in the *GluR2Δ7* mice (**Fig. 1e**; **Supplementary Table 1**; see also [23]), whereas LTD could be readily induced in controls

and *L7-Δγ2* mice (**Fig. 1e**; **Supplementary Table 1**; see also [275]). In contrast, there were no signs of presynaptic neurotransmitter release abnormalities at the PF-PC synapse in *GluR2Δ7-L7-Δγ2* mice in that paired-pulse facilitation was unaffected following PF stimulation at intervals varying from 50 to 200 ms (**Fig. 1f**; **Supplementary Table 1**). For evaluation of the inhibitory MLI to PC input, we measured the spontaneous inhibitory post synaptic currents (sIPSCs) of PCs. We found that these sIPSCs were virtually absent in *GluR2Δ7-L7-Δγ2* mice (**Fig. 1g**; **Supplementary Table 1**), similar to what has been reported for *L7-Δγ2* mice [275].

Next, we evaluated the level of eyeblink conditioning. The *GluR2Δ7-L7-Δγ2, GluR2Δ7*, *L7-Δγ2* and control mice all showed a significant increase in CR percentage and CR amplitude over the course of 10 acquisition sessions (**Fig. 2a, Supplementary Table 2**). However, *GluR2Δ7-L7-Δγ2* mice, where PF-PC LTD and MLI-PC inhibition are impaired, this acquisition is severely affected, both in terms of CR percentage and CR amplitude (**Fig. 2a-c, Supplementary Table 2)** compared to the other three groups. Interestingly, latency to CR onset was also significantly longer compared to controls, whereas latency to CR peak time was not. In line with previous findings [23], *GluR2Δ7* mice, lacking only PF-PC LTD, showed normal acquisition of eyelid CRs over the course of 10 days of training. Neither the percentage, nor amplitude, nor timing of eyeblink CRs showed any abnormalities compared to control litters (**Fig. 2a-c, Supplementary Table 2).** The *L7-Δγ2* mice had a virtually normal acquisition in terms of CR percentage, (**Supplementary Table 2),** but their CRs did not reach the amplitude values of control mice at the end of training (**Fig. 2a-c, S Table 2)**. CRs timing was not significantly different from controls (**Fig. 2b, Supplementary Table 2**). For none of the groups we could establish any significant difference between the latency to onset and peak time of the unconditioned response to the US **(Fig. 2d, Supplementary Table 2)**, showing that the performance of the blink response is intact and thus the observed learning deficits are not a result of impairments in the eyelid closure. Thus, over the course of ten training sessions *GluR2Δ7-L7-Δγ2* mice acquired only a few CRs, and if present, these CRs had a relatively small amplitude and delayed onset.

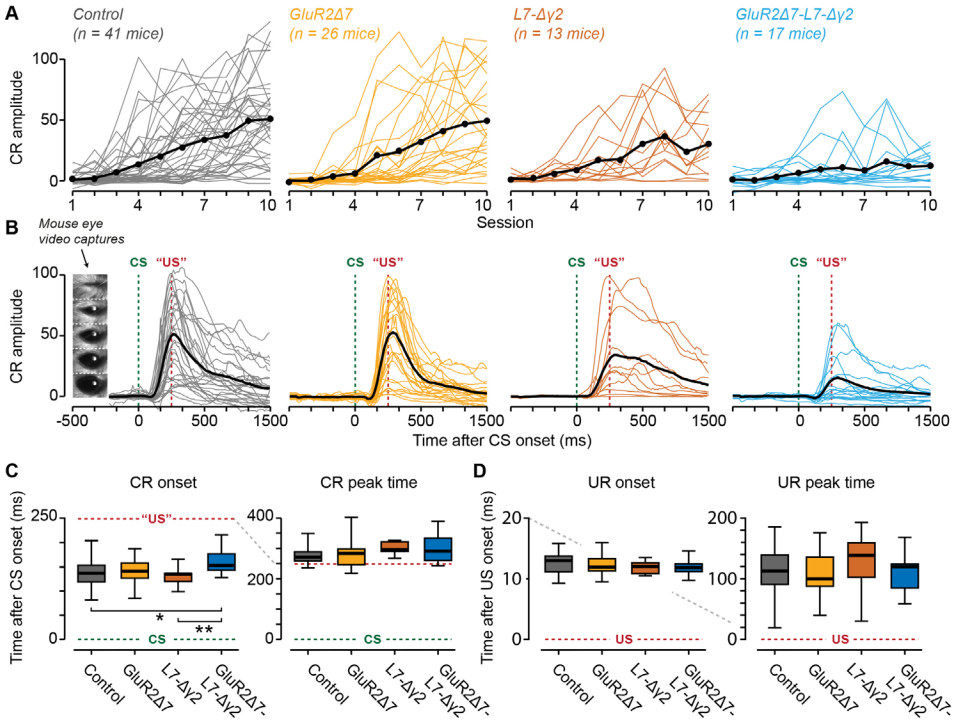

Figure 2 | Pavlovian eyeblink conditioning is severely impaired in *GluR2Δ7-L7-Δγ2* mice whereas the mutants that carry the mutations individually show normal or only mildly impaired conditioning. (a) Mouse individual (colored) and average (black) learning curves per group showing the development of CR amplitudes over the ten consecutive training sessions. Compared to controls, *GluR2Δ7-L7-Δγ2* mice have significantly lower CR amplitudes than *GluR2Δ7* and *L7-Δγ2* mice ($F(3,97) = 3.482$, $p < 0.0001$ RM ANOVA; Tukey HSD post-hoc Control vs. *GluR2Δ7* $p = 0.989$; Control vs. *L7-Δγ2* $p = 0.623$ Session 9 $p = 0.02$, Session 10 $p = 0.03$; Control vs. *GluR2Δ7-L7-Δγ2* $p = 0.007$). **(b)** Mouse individual average (colored) and total average (black) eyeblink traces of CS only trials in the probe session following acquisition. Mouse eye video captures show eyelid closure at 0, 25, 50, 75, and 100% values of a full blink. Compared to controls, *GluR2Δ7-L7-Δγ2* mice have much smaller eyeblink CRs than *GluR2Δ7* and *L7-Δγ2* mice (Control vs. *GluR2Δ7* $t(82.3) = -0.335$, $p = 0.738$; Control vs. *L7-Δγ2* $t(80.0) = -2.44$, $p = 0.017$; Control vs. *GluR2Δ7-L7-Δγ2* $t(80.1) = -3.928$, $p = 0.0002$; All Linear Mixed Effect Model) CR amplitude value is based on *all* 100 paired CS-US trials (a panel) or 30 CS only trials (b panel) per session and represents the highest point in the CS-US interval. Note that, although eyeblink conditioning is severely disrupted, in *GluR2Δ7-L7-Δγ2* mice they still do show properly timed eyeblink CRs, i.e. CRs that peak around the US. **(c)** *GluR2Δ7-L7-Δγ2* mice have a significantly longer latency to CR onset ($t(69.7) = 2.31$, $p = 0.024$, Linear Mixed Effect Model). No differences were found between groups for CR peak time. Both CR onset and CR peak time are based only on trial in which a CR was present (i.e. > 10% eyelid closure in CS-US interval). **(d)** Reflexive eyelid

closures (unconditioned response, UR) show similar latencies to onset and peak time for all groups. For all comparisons see **Supplementary Table 2**; * $p < 0.05$, ** $p < 0.001$

The level of eyeblink conditioning in the *GluR2Δ7-L7-Δγ2* mice was much more affected than what could be expected based on the individual phenotypes observed in the LTD-deficient *GluR2Δ7* mice or the FFI-deficient *L7-Δγ2* mice. These data are in line with our hypothesis that the two mechanisms may both contribute to the simple spike suppression required for eyeblink conditioning [109] and that each of them may compensate for the absent or mild behavioral phenotype in the mutant with the other isolated cellular deficit [284]. However, the exceptionally strong behavioral phenotype in the *GluR2Δ7-L7-Δγ2* mice could potentially also result from deficits in their spontaneous complex spike and simple spike firing levels [13], which appear relatively normal in the *GluR2Δ7* and *L7-Δγ2* mice [23, 275]. We therefore recorded PC activity in the anterior lobe of awake *GluR2Δ7-L7-Δγ2* mice, which should have the characteristic firing patterns of zebrin-negative modules, including that of the eyeblink microzone [109, 320, 327]) (**Fig. 3a**).

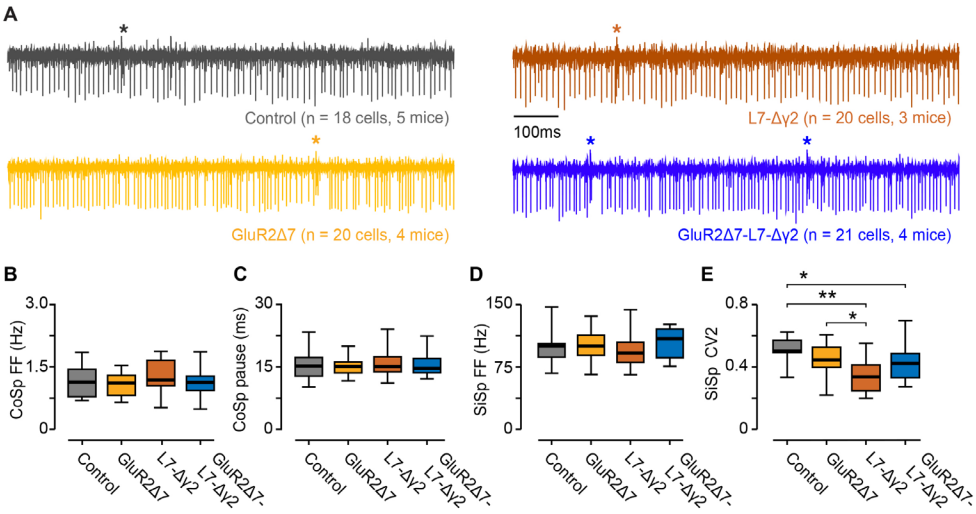

Figure 3 | *GluR2Δ7-L7-Δγ2* have no gross abnormalities in spontaneous firing behavior *in vivo*. **(a)** Raw examples of *in vivo* PC recordings from lobule I-V for all four groups. For **(b)** complex spike firing frequencies, **(c)** simple spike pauses following complex spikes, and **(d)** simple spike firing frequencies, no differences were found between controls and any of the mutant groups. **(e)** As for *L7-Δγ2* mice, *GluR2Δ7-L7-Δγ2* mice have a higher simple spike regularity, as shown by the lower CV^2 value (Control vs. *GluR2Δ7* t (10.25) = -1.48, p = 0.168; Control vs. *L7-Δγ2* t (8.26) = -4.71, p = 0.001; Control vs. *GluR2Δ7-L7-Δγ2* t (10.99) = -2.64, p = 0.023; All Linear Mixed Effect Model). For all comparisons see **Supplementary Table 3**; * $p < 0.05$, ** $p < 0.001$

The complex spike activity of *GluR2Δ7-L7-Δγ2* mice showed an average firing frequency of 1.13 Hz (± 0.32 SD) and the simple spike pause following the complex spike was on average 15.55 ms (± 2.63 SD), which were both indistinguishable from that of *GluR2Δ7* mice, *L7-Δγ2* mice or controls (**Fig. 3b**, **Supplementary Table 3**). Likewise, the firing frequency of their simple spikes, which was, as expected for the anterior lobe [327]), relatively high 104.49 Hz (± 18.28 SD), was not significantly different from that of the other mutant lines or controls (**Fig. 3c**, **Supplementary Table 3**). Moreover, the regularity (i.e. coefficient of variation for adjacent intervals CV^2) of simple spike activity of PCs in the anterior lobe of *GluR2Δ7-L7-Δγ2* mice was, albeit slightly different from controls, not significantly different from that in *GluR2Δ7* mice or *L7-Δγ2* mice (**Fig. 3d**, **Supplementary Table 3**).

Together, these data indicate that the strong phenotype in eyeblink conditioning in the *GluR2Δ7-L7-Δγ2* mice cannot be explained by the abnormal baseline firing patterns of its PCs. Instead, the most parsimonious explanation is that the simple spike suppression required for eyeblink conditioning is facilitated by both PF-PC LTD and MLI-PC FFI, and that ablating only one of these mechanisms will elicit processes that can at least partly compensate for the deficit induced. Indeed, it has been shown that deleting $GABA_a$ receptors from PCs, as occurs in the *L7-Δγ2* mice, will reduce the efficacy of the excitatory PF to PC synapse [275]. Such presumptively homeostatic mechanisms may well keep the excitatory - inhibitory inputs in balance, and still permit simple spike suppression to be induced. This notion is further supported by the observation that PF stimulation followed by CF stimulation may lead to concurrent long-term potentiation (LTP) of the PF-MLI synapse and LTD of the PF-PC synapse *in vivo* [333].

Whether induction of PF-PC LTD is completely blocked in the *GluR2Δ7-L7-Δγ2* mice under physiological circumstances is unclear. Recently, it was shown that some PF-PC LTD can still be induced in *GluR2Δ7* mice when the PF stimulus conditions are intensified, the CF stimulus is replaced by a strong somatic depolarization of the PC, and their stimulus interval is shortened [334]. In the current study, we used conditions that more closely matched those of the eyeblink paradigm in that we used a more subtle PF stimulation followed by a single CF activation after a 110 ms delay. This paradigm appears to be physiological, as it allowed concomitant phenotypical differentiation at both the cell physiological and behavioral level.

Although eyeblink conditioning in *GluR2Δ7-L7-Δγ2* mice is severely affected, they do undeniably show some CRs at the end of the training. Importantly, these eyeblink CRs

are properly timed, that is, they peak around the onset of the expected US. This finding suggests additional neural mechanisms that contribute to PC simple spike suppression. In fact, it is unclear at this point whether PF-PC LTD and MLI-PC inhibition are indeed the only factors driving the PC simple spike suppression or only facilitating it by optimizing the PC's inputs that transmit the CS information. In line with recent findings supporting a more neurocentric instead of exclusively circuit-synaptocentric view on learning, such a mechanism might well involve a temporal memory that is partly formed *in* the Purkinje cell itself [330, 335]. Such a cell intrinsic learning mechanism, however, may still depend on optimized synaptic inputs provided by PFs and MLIs. Our finding that only a concurrent disruption of PF-PC LTD *and* MLI-PC inhibition could severely impair eyeblink conditioning, but not completely block learning, rejects the idea that a single form of neural plasticity is essential and sufficient, and it supports the notion that synaptic and intrinsic plasticity synergistically contribute to form a temporal memory in the cerebellum [284].

Table S1 In vitro electrophysiology: LTD induction, sIPSC analysis, and Paired Pulse Facilitation

LTD analysis (non normalized data)	**Control (n = 6 cells, 4 mice)**	**GluR2Δ-L7-Δγ2 (n = 6 cells, 4 mice)**	**Statistics Base**		
			Control baseline vs. Control post induction	GluR2Δ- L7-Δγ2 baseline vs. GluR2Δ7-L7-Δγ2 post induction	Statistical test
LTD baseline (pA)	192.77 (± 57.05 sd)	180.81 (± 46.08 sd)			
LTD post induction last 5 minutes (pA)	146.60 (± 41.93 sd)	181.70 (± 52.99 sd)	t(5)=-4.28, p=0.008	t(5)=0.052, p=0.96	Paired t-test
sIPSCs analysis	**Control (n = 6 cells, 2 mice)**	**GluR2Δ7 (n = 18 cells, 3 mice)**	**GluR2Δ7-L7-Δγ2 (n = 11 cells, 2 mice)**	**Statistics Base**	
					Statistical test
sIPCSs (Hz)	25.38 (± 10.71 sd)	29.44 (± 20.27 sd)	1.87 (± 1.42 sd)	F(2, 32)=11.39, p = 0.0001 post-hoc Bonferroni: Control vs. GluR2Δ7, p=1.00 Control vs. GluR2Δ- L7-Δγ2, p = 0.015 GluR2Δ7 vs. GluR2Δ- L7-Δγ2 , p = 0.005	ANOVA, post-hoc Bonferroni
Paired Pulse facilitation (PPF)	**Control (n = 8 cells, 3 mice)**	**GluR2Δ7-L7-Δγ2 (n = 10 cells, 3 mice)**	**Statistics Base**		
					Statistical test
Paired Pulse facilitation (PPF)				F (1,16) = 0.81, p = 0.38	ANOVA, Repeated measures
Inter stimulus interval 50ms	1.49 (± 0.19 sd)	1.57 (± 0.35 sd)			
Inter stimulus interval 100ms	1.20 (± 0.06 sd)	1.28 (± 0.23 sd)			
Inter stimulus interval 150ms	1.12 (± 0.13 sd)	1.15 (± 0.12 sd)			
Inter stimulus interval 200ms	1.04 (± 0.10 sd)	1.08 (± 0.07 sd)			

Table S2 Pavlovian eyeblink conditioning: %CR, CR amplitude, CR timing, UR performance

	Control (n = 41 mice)	GluR2Δ7 (n = 26 mice)	L7-Δγ2 (n = 13 mice)	GluR2Δ7-L7-Δγ2 (n = 17 mice)	Group comparisons						
						Control vs. GluR2Δ7	Control vs. L7-Δγ2	Control vs. GluR2Δ7-L7-Δγ2	GluR2Δ7-L7-Δγ2 vs. GluR2Δ7	GluR2Δ7-L7-Δγ2 vs. L7-Δγ2	GluR2Δ7 vs. L7-Δγ2	Statistical test
CR percentage session 1-10 (based on 10% threshold)	9.7 (± 12.5 sd) - 73 (± 28.5 sd) F = 58.9, p < 0.00001, one-way ANOVA	7.2 (± 6.3 sd) - 67 (± 26.6 sd) F = 46.4, p <0.00001, one-way ANOVA	4.2 (± 3.6 sd) - 58.4 (± 36.0 sd) F = 12.2, p <0.00001, one-way ANOVA	9.3 (± 6.8 sd) - 34.9 (± 25.9 sd) F = 5.8, p = 0.0001, one-way ANOVA	F (3,97) = 3.092, p < 0.00001	p = 0.518	p = 0.704	p = 0.002	p = 0.101	p = 0.208	p = 1.0	RM ANOVA, Tukey HSD post hoc, all acquisition sessions
CR amplitude session 1-10 (% of full blink)	1.7 (± 4.2 sd) - 58.1 (± 41.1 sd) F = 37.3, p < 0.00001, one-way ANOVA	0.4 (± 2.0 sd) - 60.8 (± 47.7) F = 22.8, p < 0.00001, one-way ANOVA	1.6 (± 2.2 sd) - 36.1 (± 29.4 sd) F = 9.4, p < 0.00001, one-way ANOVA	0.7 (± 5.5 sd) - 13.9 (± 14.3 sd) F = 3.7, p = 0.018, one-way ANOVA	F (3,97) = 3.482, p < 0.0001	p = 0.989	p = 0.623, Ses9 p = 0.02, Ses10 p = 0.03	p = 0.007	p = 0.031	p = 0.414	p = 0.806	RM ANOVA, Tukey HSD post hoc, all acquisition sessions
CR timing: latency to onset (ms)	137.8 (± 36.6 sd)	142.9 (± 25.5 sd)	118.9 (± 22.6 sd)	160.1 (± 26 sd)		t (73.3) = 0.97, p = 0.33	t (67.8) = -1.72, p = 0.89	t (69.7) = 2.31, p = 0.024	t (72.8) = -1.48, p = 0.142	t (68.8) = -3.31, p = 0.001	t (70.4) = -2.38, p = 0.02	LLM - CS only trials in probe session
CR timing: latency to peak (ms)	285.6 (± 42.9 sd)	282.0 (± 44.3 sd)	303.3 (± 20.2 sd)	279.0 (± 85.3 sd)		t (53.2) = -0.05, p = 0.963	t (49.1) = 1.64, p = 0.107	t (52.14) = 0.89, p = 0.377	t (55.3) = -0.90, p = 0.374	t (51.3) = 0.73, p = 0.471	t (51.6) = 1.63, p = 0.110	LLM - CS only trials in probe session
CR amplitude (% of full blink)	64.1 (± 40.0 sd)	61.6 (± 49.8 sd)	30.7 (± 32.9 sd)	17.5 (± 21.4 sd)		t (82.3) = -0.34, p = 0.738	t (80.0) = -2.44, p = 0.017	t (80.1) = -3.93, p = 0.0002	t (80.4) = 3.57, p = 0.001	t (79.1) = 0.88, p = 0.382	t (80.3) = -2.16, p = 0.034	LLM - CS only trials in probe session
UR performance: latency to onset (ms)	12.5 (± 1.8 sd)	12.4 ms (± 1.8 sd)	11.9 (± 0.9 sd)	11.9 (± 1.2 sd)		t (77.7) = 0.14, p = 0.890	t (74.6) = -0.51, p = 0.610	t (73.9) = 1.14, p = 0.258	t (71.7) = -1.04, p = 0.303	t (71.3) = - - 1.40, p = 0.165	t (72.5) = -0.62, p = 0.535	LLM - US only trials in baseline session
UR performance: latency to peak (ms)	62.0 (± 17.6 sd)	61.3 (± 16.7 sd)	69.6 (± 25.8 sd)	61.2 (± 16.1 sd)		t (91.4) = -0.77, p = 0.446	t (88.1) = 0.85, p = 0.396	t (87.3) = -0.69, p = 0.494	t (85.0) = 0.08, p = 0.935	t (84.6) = 1.31, p = 0.193	t (85.9) = 1.45, p = 0.151	LLM - US only trials in baseline session

Table S3 In vivo Purkinje cell recordings from anterior cerebellar cortex.

	Control (n = 18 cells, 5 mice)	GluR2Δ7 (n = 20 cells, 4 mice)	L7-Δγ2 (20 cells, 3 mice)	GluR2Δ7-L7-Δγ2 (21 cells, 4 mice)	Group comparisons						
					Control vs. GluR2Δ7	Control vs. L7-Δγ2	Control vs. GluR2Δ7-L7-Δγ2	GluR2Δ7 L7-Δγ2 vs. GluR2Δ7	GluR2Δ7-L7-Δγ2 vs. L7-Δγ2	GluR2Δ7 vs. L7-Δγ2	Statistical test
Complex spike firing frequency (Hz)	1.16 (± 0.38 sd)	1.08 (± 0.27 sd)	1.28 (± 0.39 sd)	1.13 (± 0.32 sd)	t (10.27) = -0.81, p = 0.439	t (8.30) = 1.2, p = 0.262	t (10.85) = -0.23, p = 0.826	t (10.07) = -0.61, p = 0.556	t (8.01) = 1.48, p = 0.176	t (7.70) = 2.05, p = 0.08	Linear mixed effect model
Complex spike pause duration (ms)	15.25 (± 3.62 sd)	15.22 (± 2.29 sd)	15.84 (± 3.07 sd)	15.55 (± 2.63 sd)	t (79) = -0.04, p = 0.971	t (79) = 0.64, p = 0.523	t (79) = 0.33, p = 0.745	t (79) = -0.37, p = 0.710	t (79) = 0.33, p = 0.741	t (79) = 0.70, p = 0.488	Linear mixed effect model
Simple spike firing frequency (Hz)	97.88 (± 19.36 sd)	101.23 (± 17.41 sd)	94.92 (± 18.73 sd)	104.49 (± 18.28 sd)	t (9.79) = 0.62, p = 0.549	t (7.84) = -0.46, p = 0.657	t (11.06) = 1.17, p = 0.27	t (8.33) = -1.68, p = 0.130 t (10.29) = 1.17, p = 0.270	t (10.69) = -0.56, p = 0.587	t (7.49) = -1.11, p = 0.302	Linear mixed effect model
CV2 simple spike	0.51 (± 0.07 sd)	0.46 (± 0.10 sd)	0.46 (± 0.10 sd)	0.42 (± 0.12 sd)	t (10.25) = -1.48, p = 0.168	t (8.26) = -4.71, p = 0.001	t (10.99) = -2.64, p = 0.023		t (8.15) = -2.23, p = 0.056	t (7.72) = -3.32, p = 0.011	Linear mixed effect model

Methods and Materials

Subjects and generation of mice

For all experiments, we used male and female mice with a C57Bl/6 background, individually housed, food ab libitum, 12:12 light/dark cycles. For in vitro electrophysiology experiments we used mice aged 5-20 weeks old mice; for in vivo electrophysiology and eyeblink conditioning, mice were 15-25 weeks old. We made use of three different transgenic mouse lines. First, GluR2Δ7 knock-in mice lack the last seven amino acids at the intracellular C-terminus tail, thereby disrupting the interaction of GluR2 with PICK1 and GRIP1/2, in turn disrupting the internalization of AMPA receptors, which impairs PF-PC LTD (n = 26 mice) [331, 336]. Second, L7-Δγ2 mice have a Purkinje cell specific (L7) ablation of the γ2 subunit of the $GABA_a$ receptors resulting in impaired feed-forward inhibition provided by MLIs [109, 275] (n = 13 mice). For the L7-Δγ2 mice we first generated γ2I77lox mice by flanking exon 4 of the Gabrg2 gene with loxP sites and

changing the codon encoding F77 in exon 4 to I, which resulted in a neutral amino acid substitution. Next, homozygous γ2I77lox were crossed with mice hemizygous for the PC specific L7-cre transgene and heterozygous for γ2I77lox [280, 337]. For experiments L7-cre γ2I77lox/ γ2I77lox mice (L7-Δγ2) and γ2I77lox/ γ2I77lox mice (controls) were used. Third, GluR2Δ7 L7-Δγ2 mice (n = 17 mice), which both lack both pf-PC LTD and MLI feed-forward inhibition were generated by crossbreeding female mice hemizygous for L7-cre and homozygous for γ2I77lox/ γ2I77lox with male homozygous GluR2Δ7 knock-in mice (= F0). Next, F1 female mice hemizygous for L7-cre and heterozygous for both γ2I77lox/ γ2I77lox and GluR2Δ7 were crossed with F1 male mice heterozygous for both γ2I77lox/ γ2I77lox and GluR2Δ7. This F1 breeding generated F2 mice, which were hemizygous for L7-cre and homozygous for both γ2I77lox/ γ2I77lox and GluR2Δ7 and F2 mice homozygous for both γ2I77lox/ γ2I77lox and GluR2Δ7. F2 mice were used in experiments. F2 mice homozygous for both γ2I77lox/ γ2I77lox and GluR2Δ7 were pooled with GluR2Δ7 knock-in mice. As controls (n = 41) we used pooled data from littermate GluR2Δ7 wildtypes and γ2I77lox/ γ2I77lox mice. All mice were genotyped by performing PCR analyses of genomic DNA at 2-3 weeks postnatal and once again post mortem. All experiments were approved by the Dutch Ethical Committee for animal experiments and were in accordance with the Institutional (Erasmus MC) Animal Care and Use Committee guidelines.

Eyeblink conditioning

Surgery: Mice were anesthetized with an isoflurane/oxygen mixture (5% for induction, 1.5-2% for maintenance) and body temperature was kept constant at 37° Celsius. Eyes were protected against drying using an eye lubricant (Duratears). After a local scalp injection of bupivacaine hydrochloride (2.5mg/ml, Bupivacaine Actavis) we made a sagittal scalp incision of 2-3 cm length. Next, we carefully removed the exposed periosteum and roughened the surface of the skull using an etchant gel (Kerr, Bioggio, Switzerland). After this, a small messing block (1.0 x 0.4 x 0.3 mm) with 1 screw thread and 2 additional pinholes was placed on the skull using Optibond primer and adhesive (Kerr, Bioggio, Switzerland) and Charisma (Heraeus Kulzer, Armonk, NY, USA). The surgical placement of this so-called pedestal and allowed for head-fixation during the eyeblink conditioning experiments.

Behavioral training: All behavioral experiments were conducted using head-fixed mice that were placed on top of a cylindrical treadmill on which they were allowed to walk freely (Fig 1a) The treadmill consisted of a foam roller (diameter ±15cm, width ±12cm; Exervo,

TeraNova EVA) with a horizontal metal rod through the axis that was connected with a ball bearing construction to two solid vertical metal poles. A horizontal messing bar was fixated to the same vertical poles at 3-5 cm above the treadmill. Mice were head-fixed to this bar using 1 screw and 2 pins, thereby ensuring perfect head-fixation (further details [338]). National Instruments (NI-PXI) equipment was used to control experimental parameters and to acquire the eyelid position signal. Eyelid movements were recorded with the magnetic distance measurement technique (MDMT), which makes use of an NVE GMR magnetometer, positioned above the left upper eyelid, that measures movements of a minuscule magnet (1.5x0.7x0.5mm) that is placed on the left lower eyelid of the animal with superglue (cyanoacrylate). This way, MDMT allows high spatio-temporal detection of eyelid kinematics (further details [339]). The conditional stimulus (CS) was a green LED light (CS duration 280 ms, LED diameter 5 mm) placed 10 cm in front of the mouse's head. Because we performed our experiments in almost complete darkness, this small LED light was a salient stimulus, which could be easily detected by both eyes. The unconditional stimulus (US) consisted of a weak air-puff applied to the eye (30 psi, 30 ms duration), which was controlled by an API MPPI-3 pressure injector, and delivered via a 27.5-gauge needle that was perpendicularly positioned at 0.5 - 1 cm from the center of the left cornea. The training consisted of 3 daily habituation sessions, 1 baseline measurement, 5 or 10 daily acquisition sessions, and 1 probe session immediately after the last training session. During the habituation sessions, mice were placed in the setup for 30-45 minutes, during which the air puff needle (for US delivery) and green LED (for CS delivery) were positioned properly but no stimuli were presented. On the day of acquisition session 1, each animal first received 20 CS-only trials as a baseline measure, to establish that the CS did not elicit any reflexive eyelid closure. During each daily acquisition session, animals received either 100 or 200 paired CS-US trials, separated over 10 or 5 daily acquisition sessions, respectively. The interval between the onset of CS and that of US was set at 250 ms. Because of an inherent 14 ms delay in the delivery of the air puff, we triggered the air puff at 236 ms after CS onset so that it would hit the cornea exactly at 250 ms after CS onset. The inter-trial interval was set according to the following constraints: at least 10 seconds had to elapse, the eyelid had to be open below a predetermined threshold of 50% of a full eyelid closure, and eyelid position had to be stable for at least 2 seconds for a trial to begin. Immediately after acquisition session 10, we started a probe session during which we presented another 100 paired CS-US trials, but now intermingled with 30 CS-only trials. During all training sessions, the experimenter carefully inspected threshold and stability parameters and

adjusted them if necessary. All experiments were performed at approximately the same time of day by the same experimenter.

Data analysis: Individual eyeblink traces were analyzed automatically with custom computer software (LabVIEW or MATLAB) in a five-step process. First, trials with significant activity in the 500 ms pre-CS period (> 6 SD) were regarded as invalid for further analysis. Second, trials were normalized by aligning the 500 ms pre-CS baselines and calculating the averaged UR amplitude in Volts per session. The voltage corresponding with a full closure was further used in the analysis of the eyeblink traces as the 100% value reflecting full eyelid closure (± 1 mm movement), and other values like CR amplitude were expressed relative to this 100% value. Third, in the valid normalized trials, all eyelid movements larger than 10% of a full eyelid closure and with a latency to CR onset between 50-250 ms and a latency to CR peak of 100-250 ms (both relative to CS onset) were considered as conditioned responses (CRs). For CS only trials in the probe session we used the exact same criteria except that the latency to CR peak time was set at 100-500 ms after CS onset. Additionally, we determined for each individual trial the following parameters: (1) maximum/average eyelid closure (= amplitude) in the full CS-US interval; (2) eyelid closure specifically at US onset (i.e. 250 ms after CS onset); (3) latency to CR onset; (4) latency to CR peak. For 1 and 2 we used all valid trials, for 3 and 4 we only used the trials in which a CR was present. Fourth, based on this trial-by-trial analysis we calculated for each session per mouse the percentage of eyeblink CRs. Statistical effects of session and genotype on CR percentage were established in SPSS 24 using a repeated measures ANOVA and LSD post hoc testing. Fifth, linear mixed effect models were used in SPSS 24 to determine statistically significant effects of genotype and session on parameters 1-4. Data was considered statistically significant if $p < 0.05$.

In vitro electrophysiology

Decapitation and preparation: Following isoflurane anaesthesia, mouse were decapitated, and the cerebellum was obtained and put in an ice-cold 'slicing medium', containing (in mM) 3 NMDG, 93 HCl, 2.5 KCl, 1.2 NaHPO4, 30 NaHCO3, 25 Glucose, 20 HEPES, 5 Na-ascorbate, 3 Na-pyruvate, 2 Thiourea, 10 MgSO4, 0.5 CaCl2, 5 N-acetyl-L-Cysteine that was carbogenated continuously (95% O2 and 5% CO2). Sagittal slices, 250 mm thick, of the cerebellar vermis were cut using a vibrotome (VT1200S, Leica) and put in carbogenated artificial cerebrospinal fluid (ACSF) containing (in mM): 124 NaCl, 5 KCL, 1.25 Na2HPO4, 2 MgSO4, 2 CaCl2, 26 NaHCO3 and 20 D-Glucose, for at least 1 h at 34±1 °C before the start of the experiment. All slice physiology was done at 34±1 °C in the presence of 100 mM

picrotoxin except for the sIPSCs recordings. Whole-cell patch clamp recording were performed with an EPC9 amplifier (HEKA Electronics, Lambrecht, Germany). Recordings were excluded if the series (Rs) or input resistances (Ri) changed by 20% during the experiment, which was determined using a hyperpolarizing voltage step relative to the -65 mV holding potential. For whole-cell recordings PCs were visualized using an upright microscope (Axioskop 2 FS, Carl Zeiss) equipped with a 40x objective. Recording electrodes (3–5 MO, 1.65 mm outside diameter (OD) and 1.11 mm interior diameter (ID), World Precision Instruments, Sarasota, FL, USA) were filled with an intracellular solution containing (mM): 120 K-Gluconate, 9 KCL, 10 KOH, 4 NaCL, 10 HEPES, 28.5 Sucrose, 4 Na2ATP, 0.4 Na3GTP (pH 7.25–7.35 with an osmolarity of 295±5).

PF-PC transmission: For PF–PC transmission, we used various inter-stimulus intervals (50–200 ms). For recordings of spontaneously occurring IPSCs (sIPSCs), we used the previously mentioned K-based internal and recorded their occurrence during 120 s. For CF stimulation, similar electrodes (filled with ACSF) were positioned near the patched PC soma in the surrounding granule layer.

sIPSC: For the recording of spontaneous inhibitory post synaptic currents (sIPSCs), we used an intracellular solution containing (mM): 150 CsCl, 1.5 MgCl2, 0.5 EGTA, 4 Na2ATP, 0.4 Na3GTP, 10 HEPES, 5 QX314 (pH 7.25–7.35 with an osmolarity of 295±5). For extracellular stimulation of PFs, similar patch electrodes were filled with ACSF and positioned in the upper third of the molecular layer lateral to the patched PC. The stimulation intensity was set to evoke an excitatory post synaptic current (EPSC) of 200±50 pA (typically 3–5 μA stimulation intensity).

PF-PC induction: For PF-PC LTD induction we recorded from lobules 5/6. Recordings were done in voltage-clamp, except for the tetanus, which consisted of 100 Hz PF stimulation in 8 pulses followed by a 110 ms delay of single CF activation at 1 Hz for 5 minutes. We evaluated the synaptic plasticity by the change in PF-EPSC (baseline at 0.05 Hz) relative to the mean value calculated during the 5min long baseline pre-tetanus [332].

Data analysis: Data analysis was performed using Clampfit software (Molecular Devices).

In vivo PC recordings

Surgery: Mice were surgically prepared following the same procedure as described for eyeblink conditioning. Additionally, a craniotomy (Ø 2-3 mm) was performed on the

occipital bone in order to perform extracellular PC recordings from both the anterior and posterior cerebellum. A small rim of Charisma was made around the craniotomy and anti-inflammatory (Dexamethasone 4 mg/ml) solution was applied inside, after which the chamber was closed with a very low viscosity silicone elastomer sealant (Kwik-cast, World Precision Instruments). After surgery mice had 5 days to recover.

Recordings: Extracellular PC recordings were conducted using head-fixed mice that were placed on top of a cylindrical treadmill system as described above. Mice were first habituated for 3 days to the treadmill. PCs were recorded from vermal lobules I–V and lobules VI-X using glass micropipettes (2.0 mm OD, 1.16 mm ID, Harvard Apparatus, MA, USA, tip 2-5 um, impedance 2-5 mOhm. Single unit Purkinje cells were recorded for 2–5 minutes. Single-unit recording was identified online by the presence of a short SS pause (20-50 ms) after each complex spike. To verify recording locations, we made small alcian blue injections after recording sessions.

Analysis: In vivo recordings were analyzed offline using custom scripts in MatLab (Mathworks, Natick, MA, USA) and SPSS 24. Average simple spike and complex spike firing were calculated. Simple spike firing regularity was investigated using the CV^2 value, which was calculated as $2 * | ISI_{n+1} - ISI_n | / (ISI_{n+1} - ISI_n)$.

Chapter 4.1

Chloride Homeostasis in Neurons with Special Emphasis on the Olivocerebellar System: Differential Roles for Transporters and Channels

Negah Rahmati ¶, Freek E. Hoebeek, **Saša Peter**, Chris .I. De Zeeuw

¶ Corresponding author(s)

Frontiers in Cellular Neuroscience (2018)

Abstract

The intraneuronal ionic composition is an important determinant of brain functioning. There is growing evidence that aberrant homeostasis of the intracellular concentration of Cl^- ($[Cl^-]_i$) evokes, in addition to that of Na^+ and Ca^{2+}, robust impairments of neuronal excitability and neurotransmission and thereby neurological conditions. More specifically, understanding the mechanisms underlying regulation of $[Cl^-]_i$ is crucial for deciphering the variability in GABAergic and glycinergic signalling of neurons, in both health and disease. The homeostatic level of $[Cl^-]_i$ is determined by various regulatory mechanisms, including those mediated by plasma membrane Cl^- channels and transporters. This review focuses on the latest advances in identification, regulation and characterization of Cl^- channels and transporters that modulate neuronal excitability and cell volume. By putting special emphasis on neurons of the olivocerebellar system, we establish that Cl^- channels and transporters play an indispensable role in determining their $[Cl^-]_i$ and thereby their function in sensorimotor coordination.

Chloride regulation in brain cells

Chloride (Cl^-) is the most abundant transportable anion in all cells of the body and it performs fundamental biological functions in all tissues. The intracellular concentration of chloride ($[Cl^-]_i$) is regulated and maintained by a delicate functional balance between the operations of plasma membrane Cl^- channels and those of transporters, as well as those of local impermeant anions [340, 341]. In the central nervous system, Cl^- channels and transporters play key roles in neuronal growth and development, neurotransmitter uptake, intracellular pH modulation, cell volume regulation and, perhaps most importantly, setting $[Cl^-]_i$ either above or below its equilibrium potential [342-346]. In addition, $[Cl^-]_i$ plays a crucial role in moderating neuronal excitability by determining the postsynaptic responses to the neurotransmitters GABA and glycine [347-349]. One of the most studied roles of $[Cl^-]_i$ in neurons is its modulatory function in postsynaptic responses evoked by activation of ligand-gated Cl^- channels, such as $GABA_A$ receptors ($GABA_ARs$) [350]. The direction of the Cl^- flow depends on the difference between the reversal potential of Cl^- (E_{Cl}) and the resting membrane potential (RMP) (**Figure 1B**). If E_{Cl} is negative compared to the RMP of the neuron, Cl^- flows inside the neuron. $GABA_ARs$ in these types of cells mediate inward (hyperpolarizing) Cl^- currents, which in turn lead to inhibition of the postsynaptic neuronal activity (**Figure 1B**, panel a). In contrast, if E_{Cl} becomes more positive compared to the RMP, outward (depolarizing) Cl^- flow through $GABA_ARs$ leads to excitation of the postsynaptic neuron (**Figure 1B**, panel c). Therefore, the activities of Cl^- channels and

transporters that regulate $[Cl^-]_i$ are critical for determining the polarity of the impact of $GABA_A$Rs on the neuronal membrane potential.

Mutations or deletions of Cl^- channels and transporters in the brain have been linked to genetic disorders, such as particular forms of neonatal seizures and epilepsy, ataxia, hyperekplexia (startle disease) and autism spectrum disorders [344, 351-353]. In addition, impaired Cl^- homeostasis has been associated with pathology of the brain following acute injuries, such as hypoxic-ischemic encephalopathy, brain edema and post-traumatic seizures [354-357]. Therefore, targeting Cl^- channels/transporters has been investigated as a therapeutic tool for re-balancing neuronal $[Cl^-]_i$ and rescuing the consequential neurological symptoms. One example of such a Cl^- based intervention is dampening the elevation of $[Cl^-]_i$ following traumatic brain injury (TBI), so as to prevent further neuronal swelling, excitatory GABA signaling and risk of seizure [358, 359]. Developing drugs that specifically target Cl^- channels or transporters may thereby not only ameliorate the short-term pathological processes induced by TBI, but also the long-term behavioral consequences [360, 361].

Chloride channels and transporters may become activated in response to membrane potential changes (such as ClC-channels), intracellular Ca^{2+} signaling (such as anoctamin-channels) and changes in intracellular pH (SLC4 and SLC26). In addition, Cl^- is transported across the membrane by cation-chloride co-transporters (CCCs), like the Na^+-K^+-Cl^- cotransporter (NKCC1) and K^+-Cl^- cotransporters (KCCs). Investigating the impact of such a rich set of widely expressed ion channels/transporters on neuronal functioning is a complex matter, not in the least because of the heterogeneity of the neuronal populations and the diverse functional interactions of Cl^- channels/transporters with each other and other ion carriers.

To allow an in-depth review of the functionality of neuronal Cl^- channels and transporters, we focus here on their impact on the olivocerebellar system. This interconnected brain network has been investigated in detail over the past decades and the extensive anatomical, electrophysiological and behavioral datasets provide a remarkably detailed view of the properties of olivocerebellar circuitry, rendering it a suitable model for studying the consequences of abnormalities in Cl^- homeostasis at the cellular and network level. In order to set the stage, we will first provide a synopsis on the anatomical blueprint of the olivocerebellar system and highlight several hotspots where Cl^- homeostasis has been shown to be crucial for proper functioning. Thereafter we will discuss in detail several families of Cl^- channels and transporters and provide a concise view of the *status quo* in

experimental studies. Hereby we hope to guide future translational investigations that aim to improve therapeutic strategies of Cl^- based treatments.

Significance of chloride in the olivocerebellar network

The olivocerebellar system consists of 3 key regions: cerebellar cortex (CX), cerebellar nuclei (CN) and inferior olive (IO). A large part of the neuronal interactions in this network depends on GABAergic signaling (**Figure 1A**) [12, 362-365]. The output of the cerebellar cortex is exclusively mediated by GABAergic Purkinje cells. Several of the PC's downstream target neurons in the CN are also GABAergic who in turn inhibit neurons in the IO and cerebellar cortex [366, 367]. Another source of inhibition in the cerebellar cortex comes from molecular layer interneurons, which are not only activated by synaptic excitation from granule cells, but also by non-synaptic glutamate-spillover from IO axons, i.e. climbing fibers (CFs). MLIs synapse on either the somatic or dendritic membrane of PCs and thereby control PC action potential firing patterns (**Figure 1A**) [368]. Aberrant GABAergic signaling at any of these synapses has been shown to evoke abnormalities in acquisition, correction and timing of movements and thereby disrupt motor behavior [166, 369-371]. To the same extent, impairments of PC activity have been recently linked to autistic traits and other non-motor behaviors [99, 372] .

It is particularly well documented that the MLI to PC input determines the regularity and frequency of PC action potential firing [166, 167] and that the MLI-mediated inhibition depends on the $[Cl^-]_i$ of PCs [370, 371]. Therefore, malfunction or deletion of GABAergic inhibitory input from MLIs to PCs leads to altered temporal firing patterns of PCs and causes various behavioral phenotypes in animal models [166, 370, 371, 373]. Likewise, in the olivary neurons the $[Cl^-]_i$ modulates their excitability and thereby the excitation of PCs, CNs, and MLIs as mediated by their CFs [368, 374]. Altered neuronal excitability in IO evokes long-term changes in the activity of cerebellar neurons and the spatiotemporal firing pattern of the olivocerebellar network [375]. The impact of $[Cl^-]_i$ on GABAergic signaling in the olivocerebellar circuitry is also remarkable for its role in controlling the electrical coupling among olivary neurons. It has been proposed that activation of the GABAergic input from the CN to the IO leads to a reduction of coupling, whereas blocking this input increases IO coupling [366, 375, 376]. Thus, various cellular components of the olivocerebellar system appear highly sensitive to $[Cl^-]_i$ disruptions by mutations in plasma membrane Cl^- transporters and channels. Below we review the studies that investigated the effects of mutations and functional deletions of some of these proteins on $[Cl^-]_i$, which in many cases altered neuronal excitability, action potential firing patterns and motor coordination.

1. Voltage-gated chloride channels (ClC family)

ClC isoforms exhibit unique cellular expression patterns, with certain members (ClC-1 and ClC-2) primarily detected in plasma membrane, whereas some other members (ClC3-7) predominantly distributed in intracellular organelles and vesicles. Functional studies indicate that plasma membrane-bound ClCs operate in Cl^- channel mode and play a role in stabilizing membrane potential and/or Cl^- concentration across the membrane, while the intracellular organelles' ClCs function as electrogenic Cl^-/H^+ exchangers and facilitate endosomal and vesicular acidification [377-380]. Many ClCs have not been studied in great detail for their function in the brain, but rather in other organs, including kidney where their malfunctions or deletions have been linked to various diseases in human (See **Table 1** for further references and information regarding the members of the ClC-family). Below, we focus on the roles of ClC-1, ClC-2 and ClC-3 in the olivocerebellar system.

ClC-1, which is a plasma membrane-bound chloride channel encoded by the *CLCN-1* gene, is particularly known for its high Cl^- conductance, its expression in skeletal muscles, and its genetic mutations causing myotonia congenita [380]. Recent studies have also identified mRNA and protein expression of ClC-1 in neuronal tissue, including pyramidal and dentate granule cells of the hippocampus, brain stem nuclei, thalamic nuclei, frontal neocortex, as well as cerebellar PCs [381, 382]. The presence of polymorphic alleles in *CLCN-1* gene in patients with idiopathic epilepsy underscores an important role for this Cl^- channel in neurological diseases [381]. Although the precise pathophysiological mechanisms of ClC-1 channel mutations in epilepsy remain unknown, overexpression of ClC-1 in the inhibitory PCs has been found to hyperpolarize their resting membrane potential and reduce their excitability [383], which in turn may well lead to disinhibition of the cerebellar nuclei and thereby influence epileptogenesis [384]. Given that overexpression of ClC-1 even enhances inwardly rectifying Cl^- currents during depolarization in Xenopus oocytes, the impact on the membrane potential observed in PCs may also hold for other neurons [377, 385]. One more unique impact of ClC-1 overexpression appears to be on synapse elimination. PCs overexpressing ClC-1 show a delayed elimination of their supernumerary CF inputs during development [386-388]; in normal wild type animals this process is finalized by the end of the third postnatal week, whereas in ClC-overexpressing transgenic mice it lasts at least three months [383]. Thus, these studies provide supportive evidence for a contribution of voltage-gated Cl^- channels to the maturation of neuronal networks and neuronal excitability, and they suggest that their function is critical to prevent neurological disorders such as epilepsy [382].

ClC-2, which is a plasma membrane-bound chloride channel encoded by the *CLCN-2* gene, is broadly expressed in the body with a wide range of functions, including regulation of cell volume and extracellular pH. In the brain, ClC-2 is expressed in numerous types of neurons, including pyramidal cells of the hippocampus and cerebral cortex and PCs of the cerebellum [389, 390], as well as in glia cells, like Bergmann glia in the cerebellar cortex [391-393]. In olivocerebellar system, ClC-2 knockout mice show the typical progressive spongiform vacuolation of their white matter tracts, which in the rest of the brain is manifested as leuko-encephalopathy [393]. Although no study has yet specifically examined the cell physiological role of ClC-2 in cerebellar neurons, several studies have evaluated its function in mediating the inwardly rectifying Cl^- current in hippocampal pyramidal cells [394, 395]. Under conditions of high $[Cl^-]_i$, i.e., those found in dorsal root ganglion cells and hippocampal neurons of rats with temporal lobe epilepsy, ClC-2 channels have been shown to extrude Cl^- [396, 397]. Endogenously, neuronal ClC-2 is open at resting membrane potentials and it does not inactivate or close at a given time upon activation [396]. Thereby, it also has a profound effect on the membrane resistance, action potential threshold, and neuronal excitability [394, 398, 399]. However, ClC-2 knockout mice do not show lowered seizure susceptibility levels in their temporal lobe compared to their wild type littermates [394]. One possible explanation may be that the hyperexcitability of part of their neurons was balanced out by increased excitability of their local inhibitory interneurons [394]. Similar compensatory mechanisms may also occur in the olivocerebellar network, as ClC-2 KO mice do not show obvious abnormalities in movement performance [393]. Alternatively, it is also plausible that up and/or downregulation of other Cl^- channels (for instance ClC-1) can compensate for deletion of ClC-2.

ClC-3, which is a Cl^-/H^+ exchanger encoded by the *CLCN-3* gene, is broadly expressed in many tissues, including brain, kidney, skeletal muscles, heart and liver [377, 400, 401]. It shows ubiquitous expression throughout the brain with some of the highest levels of expression in hippocampus and cerebellum (2004 Allen Institute for Brain Science; Allen Human Brain Atlas. Available from: mouse.brain-map.org). With regard to the cellular distribution of ClC-3, the existing literature points to predominant expression in endosomal compartments and synaptic vesicles where it contributes to acidification by mediating the exchange of Cl^- against protons [402]. However, its expression in plasma membrane has been the subject of conflicting reports [377, 403]. Recent studies by Nelson and colleagues showed that ClC-3 is expressed on the plasma membrane of postsynaptic hippocampal neurons, where it is functionally linked to NMDA receptors and activated by CaMKII [404, 405]. In addition, ClC-3 may participate in controlling Ca^{2+} influx and

plasticity in hippocampal neurons [405]. ClC-3 knock-out mice show postnatal degeneration of the retina and hippocampus [402]. In the cerebellum, expression is high in PCs (2004 Allen Institute for Brain Science; Allen Human Brain Atlas. Available from: mouse.brain-map.org). According to the studies by Farmer and colleagues, it is tempting to hypothesize that ClC-3 may also play a role in controlling plasticity at the PF to PC synapse by reducing Ca^{2+} influx. However, it has not been established yet whether ClC-3 is also expressed at the plasma membrane of PCs.

2. Ca^{2+}-activated Cl^- channels (anoctamins)

The intracellular Ca^{2+} concentration ($[Ca^{2+}]_i$) plays a vital role in cellular signal transduction pathways, neurotransmitter release, as well as cellular excitability [406, 407]. Voltage-gated Ca^{2+} channels, which open upon membrane depolarization, form the main source of Ca^{2+} influx, but intracellular Ca^{2+}-stores also contribute to elevating $[Ca^{2+}]_i$. The increase of $[Ca^{2+}]_i$ is the prime activator for Ca^{2+}-activated ion channels, including the large- (K_{Ca}, BK) and small-conductance (K_{Ca}, SK) Ca^{2+}-activated K^+ channels. BK and SK channels are well-known for their predominant effects on the repolarization of the membrane following an action potential, influencing intrinsic excitability and shaping the postsynaptic currents, such as those of dendritic Ca^{2+} spikes [407]. In addition to the K_{Ca} channels, several *in vitro* electrophysiological studies have shown the existence of a range of Ca^{2+}-activated Cl^- currents (Cl_{Ca}), which can, depending on the $[Cl^-]_i$, depolarize or repolarize the membrane potential. One of the main families of Ca^{2+}-activated Cl^- channels is the TMEM16 family (also referred to as anoctamins), which contains 10 members (Ano1-10), most of which are present in many different cell types in the body. In addition to their ion channel activity, anoctamins have been implicated in a wide range of physiological tasks, such as phospholipid scrambling or regulation of specific K^+ channels [408-411]. As a consequence, anoctamins have been attributed to various functionalities, such as smooth muscle contraction, olfactory and sensory signal transduction, and neuronal excitability [408]. Not surprisingly, the clinical implications of impaired TMEM16 activity is equally diverse in that patients with mutated anoctamins are associated with cancer [412-415], muscular dystrophy [416], Scott syndrome [409] and autosomal recessive cerebellar ataxia [353].

In line with their de- or repolarizing impact on the membrane potential, opening of anoctamins leads to Cl^- efflux or influx depending on the gradient of Cl^- across the cell membrane. For instance, in olfactory and dorsal root ganglion (DRG) neurons with high $[Cl^-]_i$, Cl^- efflux through anoctamins amplifies the sensory signal transduction by

depolarizing the cell [417, 418]. In contrast, in hippocampal pyramidal cells and IO neurons, which typically have relatively low $[Cl^-]_i$, anoctamins cause hyperpolarization by mediating Cl^- influx [374, 419]. It should be noted that not all anoctamins have yet been characterized as a Cl_{Ca} channel. So far Ano1, Ano2 and Ano6 have been shown to gate Cl^- dependent on Ca^{2+}-activation, albeit with variable affinities for Ca^{2+}. For example, Ano1 exhibits a higher affinity for Ca^{2+} and a longer de-activation time than Ano2, while Ano6 appears to have a very low affinity for Ca^{2+} [417, 420, 421].

Anoctamins start gating Cl^- fluxes upon a rise in $[Ca^{2+}]_i$ evoked by the opening of voltage-gated Ca^{2+} channels and release from internal Ca^{2+}-stores. Both Ano1 and Ano2 have been shown to interact with Ca^{2+} driven calmodulin complexes [422-424]. Additional layers of complexity are added by the observations that Ano1 does not have to be activated by a postsynaptic Ca^{2+} influx per se, but can also be activated locally by interacting with Ca^{2+} dependent G protein-coupled receptor signaling and compartmentalized Ca^{2+} [425, 426]. Not surprisingly, also this affinity for the modulation by compartmentalized Ca^{2+} signals from internal stores is likely differentially modulated between anoctamin family members. The diverse functionalities, together with the differentially distributed expression among cell types (**Table 2**), reveal a picture where it seems likely that anoctamin members are expressed as a function of cell-specific Ca^{2+} dynamics.

Neurons are characterized by continuously changing local $[Ca^{2+}]_i$. Therefore, it is important to understand how these changes in intracellular milieu influence the responses of anoctamins. In hippocampal neurons, TMEM16B (Ano2) has been shown to affect action potential generation through a Ca^{2+} induced suppression of excitatory postsynaptic potentials in dendrites, which in turn lowers probability of action potential generation [419]. In support of these data, a recent study performed in thalamic neurons demonstrated that Ano2 contributes to spike-frequency adaptation in thalamic neurons [427]. In this study, knockdown of Ano2 reduces inter-spike interval lengths, resulting in a higher firing rate. The authors conclude that in the thalamus the main function of Ano2 is to drive hyperpolarizing currents as a consequence of depolarization induced $[Ca^{2+}]_i$ increase. The difference between SK K_{Ca} and Ano2 Cl_{Ca} mediated hyperpolarization in thalamic cells was hypothesized to be due to different decay time kinetics between these channels, in that Ano2 has a longer decay time duration and thus stronger influence on spike-frequency adaptation. In addition, a behavioral relevance for the Ano2 mediated spike-frequency adaptation was revealed in thalamic neurons, as the mice that have Ano2 knockdown in the thalamus experience an increase in pain responses. From these data, the authors proposed that the Ano2-driven modulation of spike frequency adaptation may provide thalamic cells

with the ability to suppress excessive thalamo-cortical transmission, which tunes the network sensitivity to sensory inputs that reach the thalamic complex.

In contrast to the previously discussed increase of excitability in thalamic neurons, a recent study on the role of Ano2 in IO cells reported that functional deletion of Ano2-channels resulted in decreased excitability of IO neurons [374]. In light of the typical IO activity pattern, which is dominated by oscillatory fluctuations of membrane potentials partially driven by Ca^{2+}-currents, the impact of Ano2-mutations can be substantial. The so-called high threshold spikes are formed when high threshold Ca^{2+} channels are activated that allow for a large after-depolarization potential (ADP) upon which additional spikes (spikelets) can be detected [428, 429]. In a study by Zhang and colleagues (2017) this ADP was shown to be prolonged in mouse mutants lacking Ano2. In addition, the IO cells showed prolonged AHP duration, which coincided with less spiking upon current injection. They hypothesized that the loss of the hyperpolarizing Cl_{Ca} current in the Ano2 deficient mice leads to prolonged activation of K_{Ca} SK channels and therefore to prolonged AHP duration, which in turn reduces the likelihood for action potential firing. The authors conclude that the role for Ano2 in IO cells seems to primarily function as a repolarizing current of the voltage gated Ca^{2+} currents and as such determines the ADP length to a rather large degree.

Other mechanisms by which anoctamins could potentially regulate neuronal excitability in the cerebellar system has been touched upon by recent studies in PCs, where Cl_{Ca} channels were found to be involved in depolarization-induced depression of inhibition [430, 431]. Here, the authors reported Ano2-induced reduction of GABAergic transmission through an increase of postsynaptic $[Cl^-]_i$ that reduces the driving force for Cl^- influx. As the IO is an integrated part of the olivo-cerebellar circuit, which has been shown to be critical for motor coordination and learning, Zhang and colleagues (2017) hypothesized that a less excitable IO due to the absence of Ano2 would lead to less input to PCs and as a consequence impaired motor learning. Zhang et al (2017) investigated the behavioral consequences of Ano2 absence and found that Ano2 knockout mice had significant deficits in their motor learning performance during classical eyeblink conditioning, a cerebellar dependent task where a conditioned stimulus (light/sound) predicts the arrival of an unconditioned stimulus (air puff). However, the idea that a cerebellar related dysfunction in behavior can solely be due to IO expression of Ano2 has recently been put to question [432]. In this study, Neureither and colleagues (2017) proposed the previously mentioned depolarization-induced depression of inhibition in PCs to be the main cause for the motor deficits found in their Ano2 knockout model. In this respect, it is important to emphasize

that even though the Ano2 protein is abundantly expressed in the IO, there is also evidence for its expression in other brain areas involved in motor function, including the thalamus (**Table 2**). Further research will have to be conducted to determine whether the dysfunctional cerebellar related motor behaviors described in these studies can be reproduced in the conditional removal of Ano2 in the IO and/or PCs.

3. pH-sensitive Cl^- channels and transporters

Acid-base regulation is a homeostatic mechanism, which is crucial for cell survival and function in all tissues. All vertebrates generate significant amount of acid via metabolism. To buffer the metabolic acid load, increasing the concentration of systemic bicarbonate (HCO_3^-) aids the cell's capacity to extrude acid (H^+). The transmembrane transport mechanisms for pH regulation include Cl^-/HCO_3^- exchangers, Na^+/H^+ exchangers and Na^+/HCO_3^- cotransporters. These transporters are expressed in all cell types, including neurons and glia and are localized at the plasma membrane and membranes of the intracellular organelles [433]. Studies on hippocampal neurons have reported an association between intracellular pH changes with neuronal excitability, in a way that a rise in the intracellular pH leads to increased neuronal excitability, while a fall in pH has the opposite effect [434, 435]. It has been suggested that pH-induced neuronal activity may be related to the activation of NMDA receptors, which are highly pH sensitive and show increased open probability at alkaline pH [436-438]. Here, we emphasize the expression, localization and functional significance of Cl^-/HCO_3^- exchangers of the SLC4 and SLC26 families, which are involved in regulation of both intracellular pH and $[Cl^-]_i$.

3.1. SLC4 family

One of the well-known families of HCO_3^- transporters is the SLC4 family of Cl^-/HCO_3^- exchangers, which is widely expressed in the body. This family contains 10 members (SLC4A1-5 and A7-11), with some mediating Na^+-independent Cl^-/HCO_3^- exchange (Anion Exchanger 1-3 or AE1-AE3) and some isoforms facilitating Na^+-dependent Cl^-/HCO_3^- exchange (NCBE and NDCBE). AE transporters mediate HCO_3^- extrusion while transporting Cl^- inside the cell. In contrast, NCBE and NDCBE transport HCO_3^- inside and Cl^- outside of the cell (**Figure 2**). The Cl^-/HCO_3^- exchangers have been shown to be important for baseline intracellular pH regulation, as well as facilitation of recovery after pH modifications [439, 440]. Three members of the SLC4 family are expressed in the cerebellum, including SLC4A3 (AE3), SLC4A8 (NDCBE) and SLC4A10 (NCBE) [441, 442]. Here we review the literature on AE3 and NCBE, which have been studied for their functional roles.

SLC4A3 (AE3)

AE3 is an anion exchanger expressed by a wide variety of cells, which include for example particular types of excitable cells in the retina, heart and brain [433]. Alike NKCC1, AE3 is considered as one of the main Cl^- accumulators in neurons by mediating the electroneutral exchange of one Cl^- while extruding one HCO_3^- (**Figure 2**). In mammals, there are two variants of the *SLC4A3* gene product: bAE3, which is abundant in the brain and retina, and cAE3, which is highly expressed in the cardiac tissue [439, 443]. bAE3 protein has been found in the hippocampus, cerebral cortex, cerebellum and brainstem [443]. In hippocampal pyramidal cells elevated pH levels activate bAE3, which leads to HCO_3^- extrusion, a function essential for recovery of intracellular alkalosis [439]. There are reports on single nucleotide polymorphisms that occur in SLC4A3 gene and are predicted to impact the protein sequence of bAE3 at the extracellular loop and that may promote a higher sensitivity to idiopathic generalized epilepsy [444]. While AE3 knockout mice appeared to be normal, they were affected by a lower seizure threshold and higher mortality rates after exposure to bicuculline, pentylenetetrazole or pilocarpine [439]. It is hypothesized that the increased seizure susceptibility of AE3 knockout mice is due to increased $[HCO_3^-]_i$ in hippocampal pyramidal neurons [439]. Considering that $GABA_A$Rs are also permeable to HCO_3^-, Henstsche and colleagues (2006) proposed that the observed phenotype of AE3 knockout mice can be due to reduced GABAergic inhibition as a result of increased $[HCO_3^-]_i$ [439]. However, lack of AE3 exchanger should also result in decreased $[Cl^-]_i$ and enhanced GABAergic inhibition. To identify the cellular mechanisms underlying the involvement of AE3 in neuronal excitability in future studies, one may have to combine Cl^- and pH measurements in neurons lacking AE3, as well as perform RNA-seq and DNA microarray to study the possibility of genetic compensations.

SLC4A10 (NCBE)

NCBE functions as a Na^+-dependent Cl^-/HCO_3^- exchanger. It is expressed in the olfactory bulb, cerebral cortex, brain stem, spinal cord and cerebellum [440]. In the cerebellum, it is densely expressed in PCs [443, 445]. Similar to SLC4A8 (NDCBE), NCBE may mediate the inward transport of Na^+ and HCO_3^- in exchange for intracellular Cl^- (**Figure 2**). Various studies have proposed that modest levels of intracellular acidification can lead to termination of seizure-related activities [440, 446-448]. Using a global NCBE knockout mouse, Jacob and colleagues found a significant increase in seizure threshold, supporting the impact of reduced HCO_3^- uptake and prolonged intracellular acidosis on seizure generating processes [440]. NCBE knockout mice showed normal locomotor activity, as

well as motor and spatial learning [440]. MRI analysis of knockout mice indicated a significant reduction in the volume of brain ventricles compared to littermate controls. One of the reasons for collapsed ventricles could be an increase in intracranial pressure due to water accumulation in the brain parenchyma [440]. However, NCBE knockout mice did not show any other anatomical signs of increased intracranial pressure [440]. Jacob and colleagues concluded that NCBE can be considered as a new target for treatment of epilepsy.

How the $[Cl^-]_i$ and the pH regulation by Cl^-/HCO_3^- transporters interact in the olivocerebellar system remains to be investigated. However, studies on other channels and transporters sensitive to pH levels (e.g. Acid-Sensing Ion Channels or ASICs) have indicated a modulatory role for pH in neurotransmission and neuronal plasticity via influencing the activity of ionotropic and metabotropic glutamate receptors in both cerebellar and extracerebellar neurons [449, 450]. Tissue distributions and functions of SLC4 isoforms with Cl^-/HCO_3^- activity are summarized in **Table 3**.

3.2 SLC26 family

The SLC26 family of anion exchangers consists of 10 members (SLC26A1-A11). Each SLC26 isoform has different modes of ion transport activities, including the exchange of Cl^- for various other molecules (bicarbonate, hydroxyl, sulfate, formate, iodide, or oxalate) and the formation of Cl^- channels [451, 452]. Mutations in human SLC26 genes can cause several autosomal recessive diseases, such as chondrodysplasias (by mutations in A2), chloride diarrhea (A3) and deafness and enlargement of the vestibular aqueduct in the Pendred syndrome (A4) [453, 454]. Several mouse models of SLC26-family members have confirmed the wide range of tissue specific deficits (**Table 4**). Although studies have demonstrated the important roles of SLC26 family in different tissues, there are only few reports describing their expression patterns and functions in the brain. Here, we review the most recent findings for SLC26A7 and SLC26A11, which have been studied by utilizing knock-out mouse models.

SLC26A7

SLC26A7 functions as a Cl^- channel, which is regulated by intracellular pH [455]. It can also operate as Cl^-/HCO_3^- exchanger, which plays a role in cell volume regulation during hypertonicity [452, 456, 457]. SLC26A7-null mice show deficits in acid secretion in both kidney and stomach [452]. In the brain, SLC26A7 is expressed in several regions including hippocampus and cerebellum, with the highest expression level in cerebellar PCs [458]. In PCs SLC26A7 is densely expressed in both soma and dendrites. At the subcellular level, it is

expressed both in cell membrane and intracellular compartments, but the function of SLC26A7 in cerebellar neurons remains to be elucidated. The locomotor activity of global SLC26A7 knockout mice is altered (smaller step size) compared to their wild type controls [458]. One potential cause for this behavioral abnormality could be that the lack of SLC26A7 disrupts $[Cl^-]_i$ and/or intracellular pH, which in principle could disrupt cerebellar activity patterns. Future experiments should address this hypothetical cascade.

SLC26A11 (KBAT)

SLC26A11, also referred to as the 'kidney brain anion transporter' (KBAT) due to its high expression levels in the kidney and brain, has been identified to operate as a Cl^-/HCO_3^- exchanger, Cl^-/SO_4^{2-} exchanger or Cl^- channel [451, 452, 459]. KBAT is expressed in different parts of the brain with various intensities, including cerebral cortex, hippocampus, olfactory bulb and cerebellum. Cerebellar PCs show prominent expression of KBAT [451]. At the subcellular level, KBAT was identified both in the cytoplasm and at the plasma membrane of PCs. Studies on HEK293 cells showed that KBAT can operate as a Cl^- channel that functionally interacts with H^+-ATPase. Transfection of cells with KBAT stimulated acid transport via H^+-ATPase and the cells with KBAT expression showed a more robust recovery from intracellular acidosis relative to mock transfected cells [451].

Studies on hippocampal and cortical pyramidal cells have reported the direct involvement of KBAT in cell death after cytotoxic edema [360]. Cytotoxic edema is one of the hallmark features of TBI and starts with an excessive Na^+ entry that depolarizes the membrane [360]. These processes activate the Cl^- influx through KBAT channels that eventually causes cell swelling and cell death [360]. Inhibition of KBAT by utilizing siRNA-mediated knockdown of KBAT significantly prevents Cl^- influx and cell death after cytotoxic edema [360]. Rungta and colleagues showed that in their mouse model of TBI the recovery mechanism after increased cell volume was independent of NKCC1 and KCC2 activity as 100 μM bumetanide did not significantly affect the volume of swollen neurons.

In the cerebellum, recent data support the role of KBAT in intracellular Cl^- accumulation. Selective deletion of KBAT from PCs causes a significant reduction in $[Cl^-]_i$ and a more negative E_{Cl}. At the behavioral level, lack of KBAT in PCs causes deficits in locomotor activity [371]. Considering the role of KBAT in neuronal Cl^- transport, as well as its involvement in cell swelling after cytotoxic edema, KBAT may provide a novel target for designing new therapeutic strategies for neurological conditions such as TBI.

4. Cation-chloride co-transporters (SLC12 family)

The SLC12 family has been studied in greater detail compared to other Cl^- transporters. It is known as the cation-chloride-coupled cotransporter gene family (CCC), which contains 9 members (SLC12A1- SLC12A9). SLC12 isoforms (except A8 and A9) transport Cl^-, together with Na^+ and/or K^+ in an electroneutral manner [460]. In neurons, studies have mostly focused on the roles of SLC12A2 (NKCC1) and SLC12A5 (KCC2) in regulation of inhibition through $GABA_AR$ activity [370, 461, 462]. Earlier studies reported differential expression patterns for NKCC1 and KCC2 during development with higher NKCC1 expressions in immature brain and increased KCC2 levels in the adult brain [340, 463-466]. According to these studies, the protein expression ratio of NKCC1 to KCC2 can explain the differences in $[Cl^-]_i$ and GABAergic signaling during development. However, recent findings suggest that NKCC1 and KCC2 cannot always explain the levels of $[Cl^-]_i$ [341, 345, 467], because their activities as ion transporters are controlled by post-translational modifications, such as protein phosphorylation [468, 469]. SLC12 isoforms in the brain are also involved in cell volume regulation. Transport of Cl^- and cations through some CCCs is accompanied by the movement of water which can lead to neuronal swelling or shrinkage, unless other volume-regulated Cl^- transporters and channels are activated [345, 470-472]. Mutations in genes encoding for CCC isoforms result in various brain pathologies, like seizures, cerebral edema, neurodevelopmental deficits and neuropathic pain. Pharmacological inhibitors of CCC functioning, like bumetanide and furosemide, which are well-known as loop diuretics, inhibit the CCCs both *in vitro* and *in vivo* [464, 473]. In low concentrations (2-10 μM) bumetanide specifically inhibits NKCC1 and exerts antiepileptic effects in human neonates [474]. In the cerebellum, four members of SLC12 family are expressed; these include SLC12A2 (NKCC1), SLC12A4 (KCC1), SLC12A5 (KCC2) and SLC12A6 (KCC3) [475, 476]. Here, we review the literature on NKCC1, KCC2 and KCC3, which all have been studied in the brain in more detail.

SLC12A2 (NKCC1)

NKCC1, which is an electroneutral Na^+-K^+-$2Cl^-$ cotransporter, is one of the main Cl^- accumulator in neurons [477]. Genetically modified animal models lacking NKCC1 show severe phenotypes, including: deafness due to inner ear dysfunction, deficits of spermatocyte production that lead to complete infertility, hypotension, reduction in saliva production and sensory perception impairment due to abnormal responses of the dorsal root ganglion neurons to GABA release [478-482]. Studies have shown that NKCC1 is heavily expressed in brain cells, including cerebellar neurons and glia. These studies reported that the expression of NKCC1 gradually decreases in cerebellar neurons except for

granule cells (GrCs), which show robust expression in both neonatal and adult stages of the brain [475, 476, 483, 484]. It has been suggested that strong expression of NKCC1 in mature GrCs causes higher $[Cl^-]_i$ compared to other cerebellar neurons [370]. NKCC1 is also repeatedly reported to be involved in cell volume control [485, 486]. Lowering $[Cl^-]_i$ and cell shrinkage stimulate NKCC1 ion transport activity, which is associated with increased levels of NKCC1 protein phosphorylation [487, 488].

SLC12A5 (KCC2)

KCC2 plays a crucial role in regulating cell volume as well as neuronal excitability [489, 490]. Under normal physiological conditions the electrochemical balance dictates K^+-efflux, which supports exchange of one K^+ with one Cl^- by KCC2 and leads to the reduction of $[Cl^-]_i$ (**Figure 2**). Although KCC2-mediated ion transport occurs in normal isotonic conditions, cell swelling causes a 20-fold increase in its activity [491]. In the cerebellum, KCC2 is expressed in PCs, GrCs, MLIs and CN [475, 487, 492]. At the subcellular level, KCC2 is detected at the plasma membrane and it is localized at both cell body and dendrites of PCs [370]. Gramicidin-perforated patch-clamp recordings of PCs from PC-specific KCC2 knockout mice revealed that KCC2 is the major Cl^- extruder of PCs [370]. Studies on PC-specific and GrC-specific knockouts of KCC2 indicated that their $[Cl^-]_i$ was doubled in both PCs and GrCs. This significant increase in $[Cl^-]_i$ almost eliminated GABA-induced hyperpolarization in PCs without affecting their resting membrane potential. In GrCs, which have been shown to have a more positive E_{GABA} compared to RMP in normal physiological conditions [370], elevated $[Cl^-]_i$ caused higher excitability by increasing the resting membrane potential by ~15 mV [370]. Utilizing cerebellar specific behavioral tests, such as compensatory eye movements, Seja and colleagues (2012) showed that KCC2 deletion in PCs resulted in impairments in baseline motor performance, as well as motor learning. GrC-specific KCC2 knockout mice did not show prominent deficits in their baseline motor performance, while they were significantly impaired in motor learning (for details see Seja et al. 2012).

SLC12A6 (KCC3)

KCC3 is a widespread K^+-Cl^- cotransporter, which particularly shows significant expression in brain and spinal cord [493]. In the cerebellum, KCC3 is expressed in cerebellar PCs [493, 494]. Conventional KCC3 knockout mice revealed important roles at cellular and behavioral levels. Deletion of KCC3 increased the $[Cl^-]_i$ in PCs and resulted in severe motor abnormalities. The knockout mice also showed hypertension, progressive

neurodegeneration and deafness, as well as reduced seizure threshold [494]. However, later studies on PC-specific KCC3-KO mutant mice could not detect any difference with control mice neither at the cellular nor behavioral level [370]. It has been proposed that KCC3 mostly functions as a volume regulator in mature neurons, while in immature neurons it may participate in modulation of $[Cl^-]_i$ and network development [370].

5. Ligand-gated Cl^- channels

Hyperpolarizing inhibition was discovered in 1951 by John C. Eccles and his colleagues [495]. Their work on identification of ionic mechanisms underlying the generation of inhibitory postsynaptic potentials (IPSPs) and the activity of ligand-gated Cl^- channels questioned the "passive distribution dogma" of Cl^-. Ever since, researchers have been investigating the underlying mechanisms of $[Cl^-]_i$ regulation and neuronal inhibition in various parts of the brain.

5.1 GABA-activated chloride channels

Gamma-aminobutyric acid (GABA) is the main inhibitory neurotransmitter in the brain and plays vital roles in the development, migration and assembly of neurons to create functional networks [496-498]. In the CNS, GABA receptors appear as ionotropic $GABA_A$ receptors ($GABA_ARs$) and metabotropic $GABA_B$ receptors; the latter do not directly gate anions and therefore are not considered in this review. $GABA_ARs$ are anion selective channels that are gated upon binding of GABA, permeable to Cl^- and HCO_3^- and mediate a fast postsynaptic current. Due to $GABA_ARs$' five times higher permeability to Cl^- than HCO_3^- and four times higher concentration of extracellular Cl^- compared to HCO_3^-, $[Cl^-]_i$ is considered to be the main determinant of the direction of current through $GABA_ARs$ [499]. In other words, $[Cl^-]_i$ dictates the GABAergic reversal potential (E_{GABA}). However, the permeability to HCO_3^- functions as a depolarizing current through $GABA_ARs$. Therefore, the E_{GABA} differs from E_{Cl} to more positive values [500].

$GABA_A$ receptors are pentameric proteins composed of different subunits [501]. It is known that in human there are six α subunits, three β subunits, three γ subunits, three ρ subunits and one ε, δ, θ and π subunit [502]. This reflects the large diversity of subunit assembly, which is further increased by alternative splicing. The subunit composition, which is shown to be important for the kinetics and pharmacological properties of the receptor, changes during development [503]. Whereas immature GABAergic synapses contain high expression levels of α3 subunit, the adult isoform of $GABA_A$ receptor mainly contains α1, β2 and γ2 subunits [504]. In the adult cerebellum, whole-cell recordings of spontaneous inhibitory postsynaptic currents (sIPSCs) of PCs and GrCs revealed

differences between the shapes and decay times of the recorded currents. Purkinje cells typically express a combination of α1-, β2 or 3- and γ2-subunits, which mediates sIPSCs with a single, fast exponential decay time constant, whereas GrCs, which specifically express α6 subunit, show sIPSCs with the sum of fast and slow exponential curves, indicating that GrCs express both fast- and slow-mediated receptor compositions [505]. The variation in the expression of subunits does not only differ depending on the cell type, but also on subcellular location (e.g. soma vs. dendrites) [505]. To estimate the impact of local $GABA_ARs$ on the membrane potential and $[Cl^-]_i$, one should consider the location together with the composition of subunits, which also determines the conductance level of the $GABA_ARs$ [506, 507]. Studies on HEK293 cells showed that α1β2γ2-containing $GABA_ARs$, which is the composition expressed in mature cerebellar PCs, have the highest conductance of 30 pS [508].

Throughout the olivocerebellar system all cell-types appear to express $GABA_ARs$ where they not only gate phasic inhibition, which is fast and lasts for milliseconds, but also gate tonic inhibition. The former type of synaptic inhibition is gated by synaptic $GABA_ARs$ and the latter mostly by extrasynaptic $GABA_ARs$ [502, 505, 509]. The targeting of $GABA_ARs$ to synaptic or extrasynaptic compartment is determined by the presence of specific subunits [510]. For instance, γ2 subunit is primarily expressed at synaptic sites, whereas δ subunit is mostly present at extrasynaptic locations [511-513]. In addition to phasic and tonic inhibition, spillover inhibition also occurs in cerebellar cortex, a phenomenon that is moderated by GABA spilling out of the synaptic cleft. For example, high affinity $GABA_ARs$ expressed on GrCs can sense low concentrations of GABA spilling out of their synapses with GoCs [514]. The impact of GABA spillover in cerebellar cortex has also been demonstrated at excitatory terminals within the cerebellar glomerulus [515]. In olivocerebellar system, some of the subunits of $GABA_ARs$ show ubiquitous expression, whereas others represent a restricted expression pattern, such as the α6 subunit, which is only expressed in cerebellar granule cells [501, 516]. Inferior olive neurons abundantly express α2, α4 and γ1-subunits, while α1, α3, β2, β3 and γ2 are detected at lower levels [517]. Expression of the α3 subunit appears to be restricted to the soma of olivary neurons and mediate a slow postsynaptic response to GABA [369].

$GABA_ARs$ are involved in various brain disorders, including epilepsy, movement disabilities, cognitive disorders, anxiety disorders, mood disorders, schizophrenia, autism and sleep disorders [518]. Various synaptic connections in the olivocerebellar network are GABAergic and through the inhibition of postsynaptic neurons can not only dampen action potential firing, but also drive timed action potential firing in groups of neurons

with strong pace-making activity, such as PCs and CNs and thereby promote synchronous activity [166, 519-521]. In addition, the direct projection from the cerebellum to the IO is GABAergic, which is crucial for modulating activity patterns in the olivo-cerebellar-olivary loop [369]. Several studies have utilized the Cre-loxP system to create mouse models with specific deletion of GABAergic synapses in subsets of cells. For instance, deletion of γ2 subunit in PCs (PC-γ2 KO) leads to disruption of the receptor targeting to the postsynaptic membrane and selective removal of synaptic $GABA_A$Rs from PCs [166]. These studies have shown that deletion of GABAergic input to PCs by removing $GABA_A$Rs alters the temporal pattern of PC activity by affecting the regularity of both spontaneous and parallel fiber-evoked simple spike firing. *In vivo* extracellular recordings of PCs from PC-γ2 mice also showed higher simple spike firing regularity in the flocculus during compensatory eye movement and spontaneous behavior [166], indicating that GABAergic inputs from MLIs to PCs may form the main source of irregularity in PC firing pattern [167]. Compensatory eye movement experiments on PC-γ2 mice revealed severe motor learning deficits and supported the importance of GABAergic signaling and feed-forward inhibition in cerebellar learning [166]. Surprisingly, PC-γ2 did not show ataxia, but only mild gait abnormalities [522]. In order to understand whether genetic compensatory mechanisms were involved in saving these mice from strong baseline motor deficits, Wisden and colleagues performed a series of studies in 2009 where they manipulated $GABA_A$Rs by intraperitoneal injection of zolpidem [373]. To specifically study the MLI-PC synapse, they developed genetically modified mouse models, which were selectively sensitive to rapid manipulation of $GABA_A$R modulator zolpidem only at MLI-PC synapse (PC-γ2-swap mice). PC-γ2-swap mice showed severe motor abnormalities, highlighting the crucial role of MLI-PC synapse-mediated inhibition in motor control [373]. Studies have also examined the importance of GABAergic input to GrCs by eliminating Golgi cells; this manipulation caused overexcitation of GrCs and resulted in sever ataxia [523].

In the IO $GABA_A$Rs modulate the strength of the inhibitory response to the afferent input from the cerebellar nuclei (CN). Apart from classical hyperpolarizing effects, the CN-IO GABAergic synapses are suggested to be important for regulation of neuronal coupling in the olive [375]. Thereby GABA-mediated inputs to the IO are not only affecting the excitability of olivary neurons, but also the local oscillations [524, 525]. Both these mechanisms have profound effects on cerebellar PC and CN firing by means of CF innervation [375]. For instance, it is shown that CFs regulate the synaptic plasticity at the level of PF-PC, as well as MLI-PC synapses by inducing long-term depression (LTD) and rebound potentiation (RP), respectively [526]. Therefore, the activity level of olivary neurons can induce long-term changes at different cerebellar synapses [526-529].

5.2. Glycine-activated chloride channels

The glycine receptors (GlyRs) function as ligand-gated Cl^- channels. Similar to $GABA_A$Rs, GlyRs mediate excitatory or inhibitory responses by promoting the efflux or influx of Cl^-, respectively [530, 531] – the polarity is determined by the membrane potential and E_{Cl}. GlyRs are found throughout the central nervous system, with noticeable densities in the spinal cord, cerebellum, hippocampus, amygdala, hypothalamus, substantia nigra, cochlear nuclei, superior olivary complex and trapezoid body [391, 532-539]. GlyRs undergo developmental changes in their subunit composition. They mostly contain α2 subunit at early stages of development, whereas the adult receptor contains 2α1/3β subunits [540-542]. These subunits have different localizations and expression intensities. In the cerebellar cortex, GlyRs are labeled on the dendrites of Golgi cells where they receive inhibitory input from Lugaro cells [543]. In the CN, there is a small group of glycinergic, or mixed glycinergic/GABAergic interneurons, which locally innervate principal CN neurons [544, 545]. Studies by Husson and colleagues identified predominant expression of GlyRs on principal output CN neurons, where they receive inhibitory inputs from local CN interneurons [546]. They showed that at these synapses GlyRs mediate Cl^- currents and participate in inhibition of CN principal neurons, alike the GABAergic input from PCs. In addition, there is a subgroup of glycinergic projection neurons in the CN that adjusts the impact of glutamatergic inputs and facilitates vestibulocerebellar function [547].

Mutations in GlyRs have been identified in humans and cause autosomal dominant and recessive hyperekplexia or startle disease, which is characterized by pronounced and exaggerated responses to tactile or acoustic stimuli and hypertonia [548]. Natural occurring murine startle disease has been reported and shows similar phenotypes, such as reduced glycine sensitivity or reduced membrane expression of GlyRs. The specific impact of GlyRs in cerebellar activity has not been studied in detail yet. Most GlyRs seem to operate only during a limited developmental window and may contribute to the establishment of synaptic connections. In the developing cerebellum, *in vitro* whole-cell patch-clamp recordings of PCs from rats on postnatal days 3-10 (P3-P10) showed a significant increase in frequencies of both excitatory and inhibitory postsynaptic currents (EPSCs and IPSCs) upon application of 100 μM glycine [533, 549]. These glycine-evoked synaptic events were abolished by application of strychnine (1 μM), a specific blocker of the GlyRs [549]. Thus, ionotropic GlyRs may be transiently expressed in the developing cerebellum and play important roles in maturation and organization of cerebellar circuits [533, 549].

5.3. Glutamate-activated chloride channel (EAAT4)

Excitatory amino acid transporters (EAATs) are known to play a crucial role in terminating glutamatergic transmission by uptake of glutamate from the synaptic cleft. This function is necessary to prevent glutamate receptor overstimulation [550, 551]. In addition, EAATs can function as glutamate-activated, Na^+ dependent Cl^- channels [552-554]. They belong to the solute carrier family 1 (SLC1), which contains five members: (EAAT1-EAAT5). EAAT4 is highly expressed in the cerebellum with an uneven parasagittal zonal distribution, which is very similar to that of Zebrin II (aldolase C) [550, 555]. *In situ* hybridization, immunohistological studies and electron microscopy have revealed that EAAT4 is a postsynaptic transporter with predominant expression on PC spines where they receive inputs from PFs and CFs [554, 556, 557]. Other studies have reported the extrasynaptic expression of EAAT4 on PC spines, where it restricts glutamate spillover to neighboring synapses [558]. Electrophysiological studies of PCs indicate that after glutamate release and high frequency action potential firing, EAAT4 increases its Cl^- transport, which may serve as an extra force for limiting excessive PC firing [550]. Given the preponderance of EAAT4 in the zebrin-positive zones, which probably all require a low baseline firing frequency of simple spikes so as to allow ample enhancement during motor learning [559], this prevention fits in perfectly with ongoing hypotheses on the roles of zonally distributed forms of long-term postsynaptic potentiation and depression [170].

Concluding remarks and future perspectives

While the roles of Cl^- channels and transporters are established and proven to be vital in various organs of the body, their impact on neuronal activity requires further investigations. Neurons express a rich set of plasma membrane Cl^- channels and transporters, which belong to various protein families and have different modes of activation. The roles and regulations of many of these transporters and channels in the brain remain to be elucidated. As we have discussed here, Cl^- transporting proteins show distinct expression patterns in the brain and are activated through different intra-and extracellular signaling pathways to establish and maintain the $[Cl^-]_i$. Investigating how Cl^- channels and transporters function and how they interact with each other to set the $[Cl^-]_i$ will help to develop new strategies for treatment of various neurological conditions linked to aberrant Cl^- homeostasis. The recent advancements in fluorescent Cl^- indicators have considerably helped to understand the variability in $[Cl^-]_i$ and GABAergic signaling in different brain regions. Utilizing these Cl^- indicators, the impact of Cl^- transporting proteins and other Cl^- regulatory mechanisms on $[Cl^-]_i$ can be simultaneously visualized for

hundreds of cells. However, the interpretation of the physiological and pathophysiological modifications in $[Cl^-]_i$ is not easy, because the intracellular Cl^- dynamics are tightly intermingled with multiple cellular mechanisms, such as pH modifications and membrane potential regulation. Therefore, Cl^- dynamics need to be investigated by combining Cl^- measurements with pH imaging and electrophysiological recordings. In addition, the significance of deletions or mutations of Cl^- transporters and channels on regulating $[Cl^-]_i$ and neuronal activity needs to be analyzed while taking developmental compensations into account. Recent advances of genetic sequencing techniques such as RNA sequencing analysis have now made it possible to take a further step in investigating the impacts of genetic compensations. Together, these approaches will ultimately shed light on the complex interactions of various ionic channels and transporters and their up and/or down regulations during development and adulthood. In this manuscript, we reviewed the main Cl^- channels and transporters currently known for the olivocerebellar system, which is implicated in various movement disorders and probably also in neurological diseases like epilepsy.

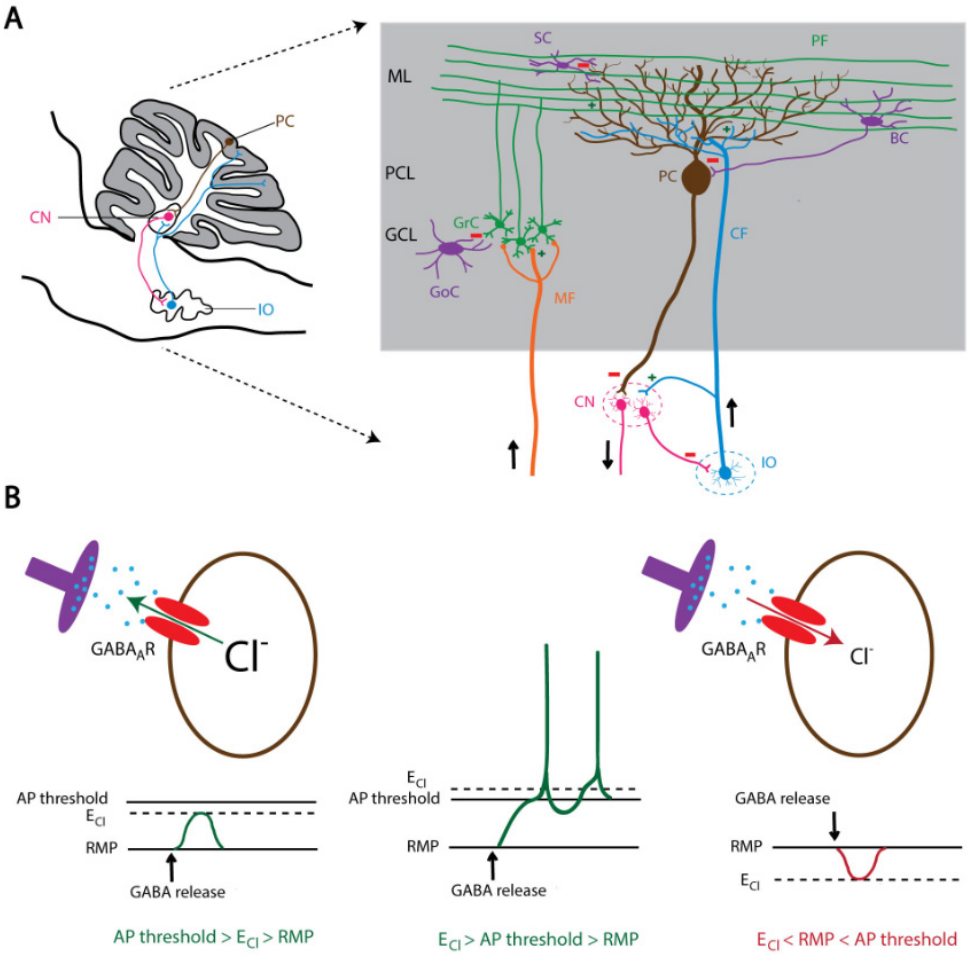

Figure 1: GABAergic signaling in olivo-cerebellar circuit. A. Schematic representation of a sagittal section of the mouse olivo-cerebellar system **(left)**. Inferior olivary neurons (shown in blue) project to the cerebellar cortex (gray) and excite Purkinje cells (brown), as well as the deeply located cerebellar nuclei (CN) neurons (pink). A particular subset of CN neurons projects back to the inferior olive (IO), forming the olivo-nucleo-olivary loop. The **right** panel demonstrates the anatomical circuit of the cerebellar cortical neurons and their connectivity with CN and the IO. ML: molecular layer, PCL: Purkinje cell layer, GCL: granule cell layer, PC: Purkinje cell, GrC: granule cell, SC: stellate cell, BC: basket cell, GoC: Golgi cell, PF: parallel fiber, CF: climbing fiber, MF: mossy fiber, CN: cerebellar nuclei, IO: inferior olive. **B.** The level of intracellular chloride concentration ($[Cl^-]_i$) dictates the polarity of the current through $GABA_A$ receptors ($GABA_AR$s). If $[Cl^-]_i$ is high, the reversal potential of Cl^- (E_{Cl}) becomes more positive compared to the resting membrane potential (RMP). In this condition $GABA_AR$s mediate an outward Cl^- current that results in depolarization of the cell membrane **(left)** that potentially induces action potential firing. In contrast, low $[Cl^-]_i$ results in a negative shift of E_{Cl} and leads to an inward Cl^- current through $GABA_AR$ and hyperpolarization of the cell membrane **(right)**.

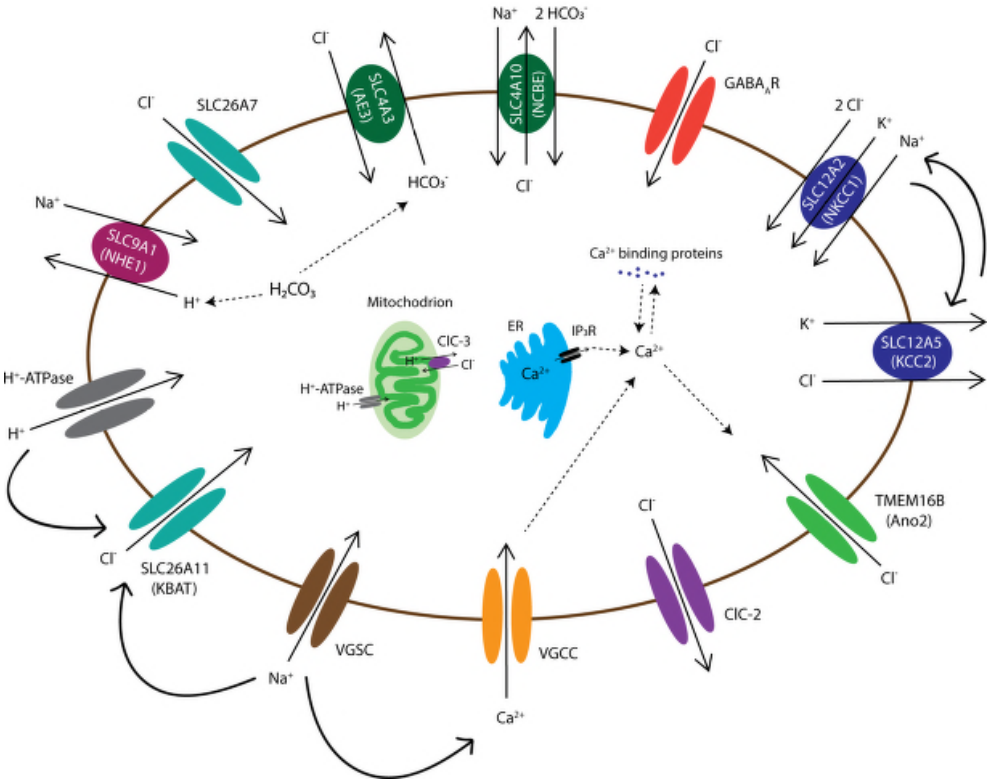

Figure 2: Diagram of chloride channels and transporters that are expressed in the olivocerebellar neurons. The intracellular Cl^- concentration in all neurons, including the neurons of cerebellum and inferior olive, is maintained by activation of various transmembrane anion channels and transporters. These anion transporters/channels also interact with H^+ exchangers/channels, such as NHE1 and H^+-ATPase, and thereby are involved in intracellular pH regulation. Cell membrane depolarization, through voltage-gated Na^+ channels (VGSCs), activates several Cl^- channels/transporters, such as SLC26A11 (KBAT), to repolarize the cell by mediating inward Cl^- currents. In addition, depolarizations activate voltage-gated Ca^{2+} channels (VGCCs) and the resulting rise in intracellular Ca^{2+} levels, which may be aided by internal Ca^{2+} stores, may lead to activation of Ca^{2+} sensitive Cl^- channels, such as anoctamin-2 (Ano2). Transmembrane movements of Cl^- together with cations such as K^+ and Na^+ also control cell volume through transport of water molecules. Channels and transporters which belong to the same family of proteins are shown with a similar color.

Tables:

Table 1: ClC family of voltage-gated Cl^- channels.

ClCs	Expression	Function	Human disease	KO mouse	Pharmacology	Ref.
ClC-1	skeletal muscle, smooth muscle, heart, brain?	stabilizing membrane potential in muscle	myotonia congenita	myotonia congenita, altered neuronal excitability	inhibitors: Zn^{2+} and Cd^{2+}, 9-AC, DPC and niflumic acid	Lorenzetto et al. 2009 Chen et al. 2013, Imbrici et al. 2015
ClC-2	broad (brain, heart, muscle, kidney,...)	transepithelial transport, cell volume control, neuronal excitability	cardiovascular disease, epilepsy?	leukoencephalopathy, degeneration of retina and testis, altered neuronal excitability	inhibitors: Zn^{2+} and Cd^{2+} DIDS, SITS	Smith et al. 1995, Clayton et al. 1998, Rinke et al. 2010, Ratte and Prescott 2011
ClC-3	broad (brain, heart, muscle, kidney,...)	vesicular and endosomal acidification	?	hippocsampal neuronal degeneration, degeneration of retina		Kawasaki et al. 1994, Borsani et al. 1995
ClC-5	kidney, intestine	endosomal acidification	Dent's disease	defects in renal endocytosis, proteinuria, hyperphosphaturia		Günther et al. 1998, Vandewalle et al. 2001, Schwake et al. 2001
ClC-6	brain	endosomal acidification	?	lysosomal storage disease		Brandt et al. 1995, Poet et al. 2006
ClC-7	broad (brain, bone, kidney,...)	lysosomal Cl^- regulation, acidification of osteoclast, resorption lacuna	osteopetrosis, neuronal ceroid lipofuscinosis, retinal degeneration, lysosomal storage disease	lysosomal storage disease, retinal degeneration, osteopetrosis		Brandt and Jentsch 1995, Kornak et al. 2002, Kasper et al. 2005
ClC-Kb	kidney, inner ear	transepithelial transport, salt reabsorbtion	Bartter syndrome type III	salt loss, deafness	Inhibited by phenylbenzofuran carboxylic acids	Kobayashi et al. 2002, Jeck et al 2004, Frey et al. 2006

Table 2: TMEM16 (Anoctamin) family

Anoctamins	Expression	Function	Human disease	KO mouse	Pharmacology	Ref.
TMEM16A (Ano1)	epithelial tissue, smooth muscle, interstitial cells of Cajal, dorsal root ganglion neurons	Cl_{Ca} channel, involved in fluid secretion, muscle contraction, gastrointestinal contractility, pain processing	tumor growth, cystic fibrosis, asthma	low blood pressure	inhibitors: CaCCinh-A01, CaCCinh-B01, Niflumic acid (NFA), and NPPB, agonists: INS37217	Yang et al.2008, Stohr et al. 2009, Jin et al. 2013, Neureither et al. 2017, Huang et al. 2009, Chen et al. 2007, Namkung et al. 2011
TMEM16B (Ano2)	brain (hippocampal and thalamocortical neurons, olfactory bulb, inferior olive, Purkinje cells), retina, muscle	Cl_{Ca} channel, involved in neuronal excitability, olfactory and sensory signal transduction and smooth muscle contraction	?	impaired motor behavior, partial reduction of electrical response to odorants, normal olfaction	inhibitors: CaCCinh-A01, CaCCinh-B01, Niflumic acid (NFA) agonists: INS37217	Stohr et al. 2009 Zhang et al. 2017 Huang et al. 2012 Ha GE et al. 2016 Zhang et al. 2015 Billig et al. 2011 Dauner et al. 2013
TMEM16C (Ano3)	brain (dorsal root ganglion cells), blood vessles, lung	phospholipid scrambeling, K_{Na} channel regulator	craniocervical dystonia, tremor, athma	impaired endoplasmic reticulum-dependent Ca^{2+} signaling		Huang et al. 2013 Charlesworth et al. 2012, Miltgen et al. 2016, Suzuki et al. 2013
TMEM16E (Ano5)	muscle, bone, sperm	phospholipid scrambeling	muscular dystrophy, gnathodisphy seal dysplasia			Tsutsumi et al. 2004, Katoh et al. 2004, Gyobu et al. 2015
TMEM16F (Ano6)	blood vessels, endosomes, brain?	phospholipid scrambeling, blood coagulation, $SCAN_{Ca}$ channel, Cl_{Ca} channel, involved in membrane excitabilty	Scott syndrome			Yang et al. 2012 Suzuki et al. 2010 Grubb et al. 2013 Suzuki et al. 2013 Shimizu et al. 2013, Yu K et al. 2015
TMEM16J (Ano9)	epithelial cells, colonic tissue	phospholipid scrambeling	colorectal carcinoma			Suzuki et al. 2013 Li C et al. 2015
TMEM16K (Ano10)	epithelial cells, cerebellum?	intracellular protein involved in intracellular Ca^{2+} signaling, essential for apoptosis	autosomal recessive cerebellar ataxia			Vermeer et al. 2010, Miskovic et al. 2016, Chamard et al. 2016, Wanitchakool et al. 2017, Renaud et al. 2014

Table 3: SLC4 family of anion transporters.

SLC4	Expression	Function	Human disease	KO mouse	Pharmacology	Ref.
SLC4A1 (AE1)	erythrocytes, kidney, heart, colon	Cl^-/HCO_3^- exchanger	hemolytic anemia, distal renal tubular acidosis		inhibitor: DIDS	Bruce et al. 1997, Jarolim et al. 1998, Karet et al. 1998, Shayakul, Alper 2004, Stehberger et al 2007, Romero et al. 2013
SLC4A2 (AE2)	most epithelial cells	Cl^-/HCO_3^- exchanger,	osteopetrosis		inhibitor: DIDS	Gawenis et al. 2004, Romero et al. 2013
SLC4A3 (AE3)	brain, kidney, GI tract, smooth muscle and heart	Cl^-/HCO_3^- exchanger,	epilepsy, blindness	lower seizure threshold	inhibitor: DIDS	Sander et al. 2002, Hentschke et al. 2006, Romero et al. 2013, Ruffin et al. 2014
SLC4A8 (NDCBE)	brain, kidney, testes and ovary	Na^+ - dependent Cl^-/HCO_3^- exchanger, acid extruder	?		inhibitor: DIDS	Chen et al. 2008, Burette et al. 2012
SLC4A10 (NCBE)	brain	pH regulation (acid extrusion)	?	higher seizure threshold, volume reduction of brain ventricles	inhibitor: DIDS	Jacobs et al. 2008, Chen et al. 2008, Liu et al. 2011, Romero et al. 2013

Table 4: SLC26 family of anion transporters.

SLC26	Expression	Function	Human disease	KO mouse	Pharmacology	Ref.
SLC26A1 (SAT1)	kidney, GI tract, liver, lung	SO_4^{2-}/Ox^{2-} exchanger, SO_4^{2-}/HCO_3^- exchanger		oxalate urithiasis, nephroclacinosis, urinary sulfate wasting, hepatotoxicity		Xie et al. 2002, Soleimani, Xu, 2006, Soleimani 2013
SLC26A2 (DTDST)	kidney, GI tract, chondrocytes	Cl^-/SO_4^{2-} transporter, SO_4^{2-}/Ox^{2-} exchanger	diastrophic dysplasia	diastrophic dysplasia		Hastabacka et al. 2002, Soleimani, Xu, 2006, Soleimani 2013
SLC26A3 (DRA)	GI tract, epididymis, entrocytes	Cl^-/HCO_3^- exchanger	congenital chloride diarrhea	congenital chloride diarrhea		Airola et al. 1996, Soleimani 2013
SLC26A4 (pendrin)	kidney, inner ear, thyrocytes, lung	Cl^-/HCO_3^- exchanger	pendred syndrome	deafness, enlargment of the vestibular aqueduct		Everett et al. 1994, Reardon, Trembath 1996, Kopp 2000, Soleimani 2013
SLC26A5 (prestin)	cochlear hair cells	Cl^-/HCO_3^- exchanger	deafness	deafness		Liberman et al. 2002, Liu et al. 2003, Cheatham et al. 2004, Alper and Sharma 2013
SLC26A6 (PAT1)	GI tract, kidney, cardiac myocytes	Cl^-/HCO_3^- exchanger, Cl^-/Ox^{2-} exchanger, Cl^-/formate exchanger	?			Aronson 1989, Soleimani 2001, Mount et al. 2004, Alper 2006
SLC26A7	brain, kidney, GI tract, lung	Cl^-/HCO_3^- exchanger, Cl^- channel	?	locomotor impairment,gastric hypochlorhydria, distal renal tubular acidosis	inhibitor: DIDS	Kim et al. 2005, Xu et al. 2006, Soleimani 2013, Rahmati et al. 2015
SLC26A8	male germ cells, kidney	Cl^-/Ox^{2-} exchanger, Cl^-/SO_4^{2-} exchanger	?	male infertility		Lohi et al. 2000, Tourne et al. 2001, Soleimani 2006
SLC26A9	stomach, lung, lower levels in kidney	Cl^-/HCO_3^- exchanger, Cl^- channel, Na^+/Cl^- cotransporter	?	hypertention		Xu et al. 2005, Amlal et al. 2012, Soleimani 2013
SLC26A11 (KBAT)	brain, kidney, GI tract	Cl^- channel, Cl^-/HCO_3^- exchanger, volume control, pH regulation	?	locomotor impairement	inhibitor: GlyH-101, CFTRinh, DIDS (partial inhibition)	Rahmati et al. 2016, Rahmati et al. 2013, Rungta et al. 2015, Vincourt, Jullien 2003

Table 5: SLC12 family of cation-chloride cotransporters.

SLC12	Expression	Function	Human disease	KO mouse	Pharmacology	Ref.
SLC12A1 (NKCC2)	kidney	$Na^+/K^+/Cl^-$ cotransporter involved in sult reabsorption	Bartter's syndrom type I	sever hypotention, hypokalemia, hypercalcinuria, metabolic alkalosis	inhibitors: bumetanide (10 µM), furosemide	Rocha, Kokko 1973, Simon, Karet 1996, Castrop, Schießl 2014
SLC12A2 (NKCC1)	broad	$Na^+/K^+/Cl^-$ cotransporter involved in regulation of $[Cl^-]_i$ and cell volume, regulation of E_{GABA} in neurons	?	impaired sensory perception, deafness, infertility, hypotension, reduction of saliva production	inhibitors: bumetanide (10 µM), furosemide	Cherubini et al. 1991, Ben-Ari et al. 1997, Delpire et al. 1999, Dixon et al.1999, Evans et al. 2000, Pace et al. 2000, Sung et al. 2000
SLC12A3 (NCC)	kidney	Na^+/Cl^- cotransoporter, invloved in sult reabsorption	Gitelman's syndrom	hypotension, hypokalemia, hypercalcinuria, hypomagnesemia	inhibitor: thiazide	Costanzo 1985, Ellison et al. 1987, Arroyo et al. 2013
SLC12A4 (KCC1)	broad	K^+/Cl^- cotransporter, involved in cell volume regulation	?	no phenotype is reported	inhibitor: furosemide	Kanaka et al. 2001 Mikawa et al. 2002 Arroyo et al. 2013
SLC12A5 (KCC2)	brain (neuron sepcific)	K^+/Cl^- cotransporter, involved in regulation of $[Cl^-]_i$, E_{GABA}, neuronal excitability and cell volume	?	comolete KO: death conditional KO: increased $[Cl^-]_i$, positive shift of E_{GABA}, neuronal hyperexcitability, impaired motor performance and motor learning	inhibitors: bumetanide (100 µM), furosemide, VU0463271 (selective for KCC2)	Williams et al. 2001, Song et al. 2002, Ben-Ari et al. 2002, Seja et al. 2012, Arroyo et al. 2013
SLC12A6 (KCC3)	broad	K^+/Cl^- cotransporter, involved in cell volume regulation	Andeermann syndrom (ACCPN), epilepsy?	hypertension, progressive neurodegeneration, reduced seizure threshold, deafness	inhibitor: furosemide	Pearson et al. 2001 Hebert et al. 2004 Seja et al. 2012

Table 6: Ligand-gated chloride channels.

channel	Expression	Function	Human disease	KO mouse	Pharmacology	Ref.
$GABA_AR$	nervous system	inhibitory synaptic transmission in the brain, neuronal excitability and development	epilepsy, movement disorders, cognitive disorders, autism, anxiety disorders, schizophrenia, sleep disorders, mood disorders	epilepsy, movement disorders, impaired motor learning and cognition	agonists: benzodiazepins, barbiturates, zolpidam, muscimol antagonists: bicuculline, picrotoxin, Cu^{2+} (blocks tonic inhibition)	Gonzalez-Burgos 2011, Kaila 2010, Wisden et al. 2009, Braat and Kooy 2015, Möhler 2006
GlyR	nervous system	inhibitory synaptic transmission in the central nervous system, neuronal excitability and development	startle disease, autism	natural occuring mutation: startle disease	agonists: Taurine, α-L-alanine, L-serine, low concentration of Zn^{2+}, antagonists: strychnine, high concentration of Zn^{2+}	Curtis et al. 1968, Werman et al. 1968, Lynch 2004, Burgos et al. 2016, Ito 2016
SLC1A4 (EAAT4)	nervous system	glutamate/Na^+/Cl^- transport, involved in neuronal excitability and development	neurodegenerative disorders, stroke	down-regulation of EAAT4 leads to PC hyperexcitability	agonists: TBOA, L-α-aminoadipate, T3MG, Zn^{2+} (selective blocker of Cl^- conductance)	Robinson, Dowd, 1997, Fairman et al. 1995, Nagao et al. 1997, Fairman, Amara 1999

Chapter 4.2

Anoctamin2/TMEM16B is important for Inferior Olive cell physiology and motor performance

Saša Peter *, Leonoor Schonebaum *, Vincenzo Romano, Maria Fernanda Vinueza Veloz, Negah Rahmati, Maurizio Cundari, Marcel de Jeu, Laurens W.J. Bosman, Thomas J. Jentsch, Freek E. Hoebeek and Chris I. De Zeeuw ¶

* First-Co-author(s)

¶ Corresponding author(s)

In preparation

Abstract

Ca^{2+} -activated ion channels play important roles in the excitability of cells. Here, we report the robust expression of TMEM16B (Ano2), a Ca^{2+} -activated chloride channel, in inferior olivary neurons. We show that there is a large Ca^{2+}-activated Cl^- current present in olivary neurons and confirm that this current is absent in inferior olive cells of Ano2 KO mice. The absence of Ano2 results in impaired motor coordination and walking patterns as evaluated on the ErasmusLadder. A possible physiological impairment is revealed in vitro, where we identify lower duration of the after-depolarization plateau of high threshold spikes in Ano2 KO mice.

Introduction

Neurons of the inferior olive (IO) receive GABAergic projections from the cerebellar nuclei (CN) and in turn provide strong excitatory inputs to cerebellar Purkinje cells (PCs) through climbing fibers (CFs). The connectivity loop of CN-IO-PC gives rise to the olivo-cerebellar modules where the CF to PC synapse innervation is believed to be crucial for correction of errors during movements, as well as timing of motor activities. The modulation of olivary cell excitability is therefore crucial for the CF to PC input.

The role of voltage-gated Ca^{2+} channels and Ca^{2+}-activated K^+ channels in the IO has been extensively studied [560-563]. T- and P/Q type calcium channels together with large (BK) and small conductance (SK) Ca^{2+}-activated K^+ channels shape the characteristic inferior olive cell action potentials, like the high threshold Ca^{2+} spikes (HT spike) with its Ca^{2+} dependent after depolarization plateau (ADP) [560-563]. Even though BK and SK channels are well characterized for their role in the repolarization of the HT spike, relatively little is known about the role of Ca^{2+} activated chloride channels in the inferior olive cells. Recently, a large Ca^{2+} activated chloride current was identified in the inferior olive that was shown to be mediated by Ano2, a Ca^{2+} activated chloride channel [374]. Throughout various brain regions Ano2 has been ascribed various functions in regulating action potential firing: in hippocampal pyramidal cells Ano2-mediated currents have been shown to affect the probability of action potential generation [419]; in thalamic cells Ano2 mediates spike-frequency adaptation [564]; in inferior olive Ano2 currents prolong HT ADP [374]; and in cerebellar Purkinje cells Ano2 has been associated with depolarization-induced depression of synaptic inhibition [430, 431]. In addition, one of the few behavioural studies that have been done on cerebellum related behaviour in Ano2 KO mice both report impaired motor coordination and learning [374, 432].

We confirm that there is a strong expression of the Ano2 channel in the inferior olive and that it functions as a Ca^{2+} activated chloride channel. The absence of Ano2 results in a change in the ADP length of high threshold Ca^{2+} spikes in the Ano2 KO mice, which could result in altered climbing fiber to Purkinje cell transmission. In addition, we find that Ano2-KO mice present with abnormal walking patterns and an increased number of missteps, indicative of motor coordination impairments as evaluated on the Erasmus Ladder paradigm.

Materials and Methods

Ano2-KO mice and the guinea pig-Ano2 antibody were provided by the lab of Dr. Thomas Jentsch in Berlin, Germany. For details of generation of mice see [565].

DAB staining

For DAB staining we used guinea pig-Ano2 antibody provided by the lab of Dr. Thomas Jentsch in Berlin, Germany [565]. Mice were anesthetized with an overdose of Pentobarbital and transcardially perfused with saline followed by 4% paraformaldehyde. Brains were extracted and post-fixed for 2 hours in 4% PFA at room temperature. Subsequently, brains were embedded in 12% gelatine and 10% sucrose and stored overnight in 30% sucrose/0.1 M PB at 4 °C for cryoprotection. Coronal brainstem slices of 40 µm were cut using a freezing microtome and left for 3 hrs in 10 mM Natriumcitrate (pH 6) followed by a block of endogenous peroxidase activity using 10% H_2O_2. Sections were rinsed and left in a block of TBS + 10 % NHS + 0.5 % Triton for an hour. Next, sections were incubated for 48 hrs with TBS + 2% NHS + 0.4% Triton + 1:500 guinea pig-Ano2 primary antibody. Guinea pig-Biotine (Vector BA-7000) diluted at 1:200 in TBS containing 2% NHS and 0.4% Triton was used as a secondary antibody and applied to the sections for 90 min. Additionally sections were processed using the avidin-biotin complex method (ABC, PK-6100, Vector Laboratories, USA) to enhance sensitivity. Sections were visualized using a solution of 1 ml diaminobenzidine (DAB, 75 mg/ml), 150 ml Tris and 50 µL 30% H_2O_2. After a final wash with 3 x 10 min Tris HCl, the slices were put on glass with chroomaluin.

In vitro electrophysiology

Following decapitation of mice under isoflurane anaesthesia, the cerebellum with the brain stem attached was removed, and moved into an ice-cold 'slicing medium'. The slicing medium contained (in mM) 240 sucrose, 2.5 KCL, 1.25 Na_2HPO_4, 2 $MgSO_4$, 1 $CaCl_2$, 26

$NaHCO_3$ and 10 D-Glucose and was carbogenated continuously (95% O2 and 5% CO2). Coronal slices, 200 µm thick were cut using a vibrotome (VT1200S, Leica) and put in carbogenated artificial cerebrospinal fluid (ACSF) containing (in mM): 124 NaCl, 5 KCL, 1.25 Na_2HPO_4, 2 $MgSO_4$, 2 $CaCl_2$, 26 $NaHCO_3$ and 15 D-Glucose. Slices were incubated for at least 1 hr at 34±1 °C before the start of the experiment. Slice physiology was done at 33±1 °C and in the presence of 100 µM picrotoxin. Whole-cell patch clamp recordings were performed with an EPC10-USB amplifier (HEKA Electronics, Lambrecht, Germany) using Patchmaster software (HEKA Electronics). Analysis of the AP threshold (defined by a slope of >20 mV/ms), AP and AHP amplitude, decay time (τ) was performed exclusively on the first HT spike elicited by a depolarizing current injection. All electrophysiological recordings were analysed using Clampfit (Molecular Devices). For whole-cell recordings IO cells were visualized using upright microscopes (Axioskop 2 FS and Axio Examiner.D1, Carl Zeiss Microscopy GmbH, Jena, Germany) equipped with a 40x objective. Recording electrodes (4–5 MΩ, 1.65 mm outside diameter (OD) and 1.11 mm interior diameter (ID), World Precision Instruments, Sarasota, FL, USA) were prepared using a P-97 micropipette puller (Sutter Instruments, Novato, CA, USA). For current clamp experiments we filled the pipets with an intracellular solution containing (mM): 120 K-Gluconate, 15 KCL, 10 KOH, 4 NaCl, 10 HEPES, 28.5 Sucrose, 4 Na_2ATP, 0.4 Na_3GTP (pH 7.25–7.35 with an osmolarity of 295±5). For voltage clamp experiments we filled the pipets with an intracellular solution containing (mM): 110 $CsMeSO_4$, 20 TEACl, 8 KCL, 10 HEPES, 2 MgATP, 0.3 NaGTP, 0.2 EGTA, 5 QX-314 (pH 7.25–7.35 with an osmolarity of 295±5). In addition, we added TTX (1mM) to the ACSF for voltage clamp experiments.

Erasmus ladder

Detailed analysis of gait patterns of Ano2 knockout mice and their littermate controls were performed and compared by utilizing the Erasmus ladder paradigm as described previously [213]. Data collected from the ErasmusLadder were stored in a relational database (MySQL, Oracle, Redwood Shores, CA, USA) and then processed off-line using custom-written software in LabView and Python (Python Software Foundation, Beaverton, OR, USA). Steps were recorded as two consecutive touches on the rungs; to prevent false positives we took into account only touches that lasted 30 ms. To avoid detecting hind limb touches as backward steps, we accepted only sequences of two or more consecutive backward steps as true backward movements. Step lengths were determined by the distance between two consecutive touches. Likewise, step time was defined as the time that elapsed between the onsets of two consecutive touches. The analyses of forward steps revealed that mice usually

step from one elevated rung to the next, skipping the lower rung (i.e., step length = 2 or small steps) or to the consecutive elevated rung skipping three rungs (i.e., step length = 4 or large steps). Although mice completed 45 trials, for the current analysis we considered only those where mice walked constantly (i.e. the computer is able to predict where the mouse is going step). These trials were automatically selected by the computer and as a result, mice had a different number of trials per day. Before running analyses, we calculated the median of all parameters at four points during each session. Variables were grouped by percentiles 0.25, 0.50 and 0.75 of number of trials. Thus, each mouse had four time points during the seven days of training.

For the statistical analysis, we considered seven outcome variables: number of all steps, number of large steps, number of small steps, number of jumps, number of backward steps, slips and step-time in milliseconds (ms). To investigate the relationship between the outcome variables and genotype we implemented regression models for each of the outcomes. We modeled the data as nested, hierarchical data (trials within sessions within mouse). To analyze number of all steps, number of large steps, number of small steps and step-time we fit generalized linear mixed effect models with Poisson distribution.

Results

Ano2 is expressed in the inferior olive and absent in the Ano2-KO mice.

DAB staining of Ano2 in the inferior olive indicated a strong expression in the Ano2 WT (Fig. 1a), but absent of expression in the inferior olive of the Ano2-KO mice (Fig. 1b) confirming the absence of Ano2 in our mutant model.

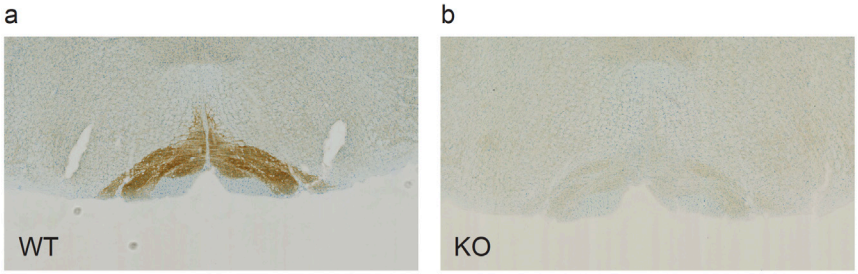

Figure 1: Global deletion of Ano2. a. Ano2 is expressed in the inferior olive of WT mice. **b.** Ano2 is absent in the inferior olive of Ano2-KO mice.

Inferior olive cells present with Ca^{2+} dependent Cl^- currents that are absent in Ano2-KO mice.

We first set out to confirm the existence of Ca^{2+} activated chloride currents in inferior olive cells. Using a voltage clamp step protocol in a whole cell recording mode with an internal solution blocking all but Ca^{2+} and Cl^- receptors, we observed the presence of tail currents (Fig. 2a, black trace). Using pharmacological interventions to separately block Ca^{2+} (Fig. 2a, $Ano2^{WT+Cd2}$ blue trace) and Cl^- (Fig. 2a, $Ano2^{WT+NFA}$ green trace) receptors we observed an absence of tail currents, indicating that the tail currents essentially needed both of these populations of receptors in order to be facilitated. Using the Ano2 KO mice we confirmed that the tail currents were mediated by Ano2 (Fig. 2a, $Ano2^{KO}$ red trace) a Ca^{2+} activated Cl^- channel. Multiple comparisons of quantitative measurements revealed that of the different conditions only the $Ano2^{WT}$ had a strong presence of tail currents (Fig. 2b) ($p < 0.001$, Bonferroni post-hoc).

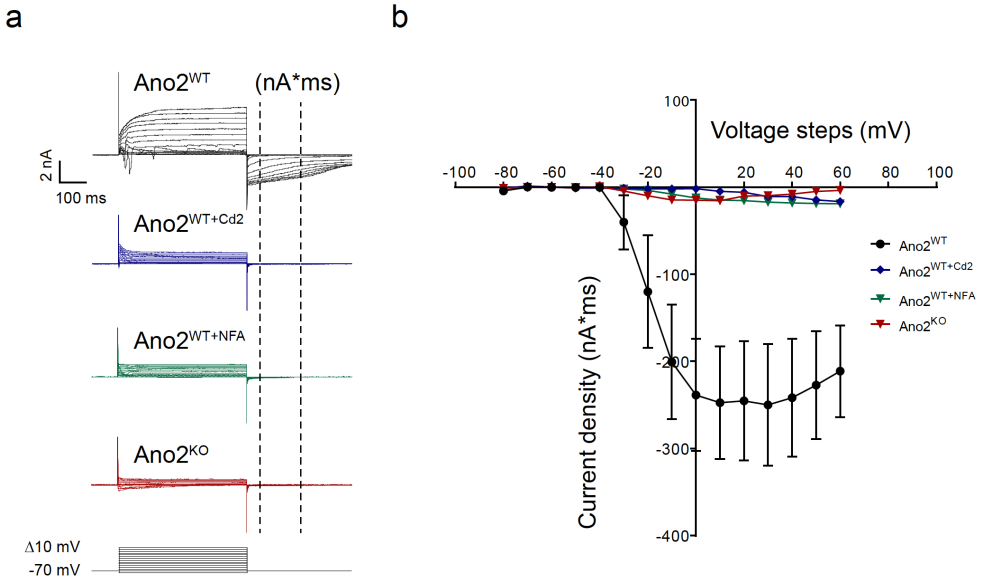

Figure 2: Presence of a Ca^{2+} activated Cl^- current in Inferior Olive cells. a. Samples of traces using pharmacological and Ano2-KO mediated interventions **b.** The charge (nA*ms, during 150 ms) of tail currents was measured as induced by 15 voltage steps for $Ano2^{WT}$ (5 mice, 7 cells), $Ano2^{WT+Cd2}$ (2 mice, 4 cells), $Ano2^{WT+NFA}$ (2 mice, 4 cells) and $Ano2^{KO}$ (2 mice, 6 cells).

Ano2-KO inferior olive cells have lower ADP duration of the HT spike

A few studies have reported on the differential role of Ano2 in the excitability of cells in different brain regions [374, 419, 564]. There is one recent study on Ano2 related inferior olive physiology in a Ano2-KO mouse model that revealed prolonged ADP and AHP duration of HT spikes that also resulted in lower frequencies of spiking upon current injections [374]. We utilized whole cell recordings of inferior olive cells with current injections in current clamp mode to reliably evoke HT spikes (Fig. 3a). Using this procedure for both the $Ano2^{WT}$ and $Ano2^{KO}$ olivary neurons we found that there was no difference in Ri (Fig. 3b) (WT 188 ± 118 MΩ; KO 170 ± 166 MΩ, p = 0.7, t-test), Vm rest (Fig. 3c) (WT -49.4 ± 4.55 mV; KO -45.3 ± 7.21 mV, p = 0.27, t-test), spike amplitude (Fig. 3d) (WT 75.7 ± 12.7 mV; KO -68.1 ± 14.2 mV, p = 0.11, t-test) or spike threshold (Fig. 3e) (WT -27.9 ± 5.57; KO -28.6 ± 6.94, p = 0.39, t-test). We did, however, find a prolonged duration of the ADP of HT spikes in the Ano2-KO (Fig. 3i) (WT 8.33 ± 0.43 ; KO 10.5 ± 0.51, p = 0.17, t-test), which is in agreement with previously reported findings [374]. Considering the study by Zhang et al. (2017) also reported on changes in AHP duration we investigated both AHP decay (Fig. 3f) (WT 61.0 ± 14.6 ms; KO 63.2 ± 18.9 ms, p = 0.71, t-test), AHP amplitude (Fig. 3g) (WT 30.82 ± 6.02 mV; KO 32.3 ± 6.32 mV, p = 0.50, t-test) and the number of ADP spikelets generated (Fig. 3h) (WT 1.59 ± 1.33 n; KO 1.31 ± 1.49, p = 0.57, t-test), yet we found no difference for these parameters.

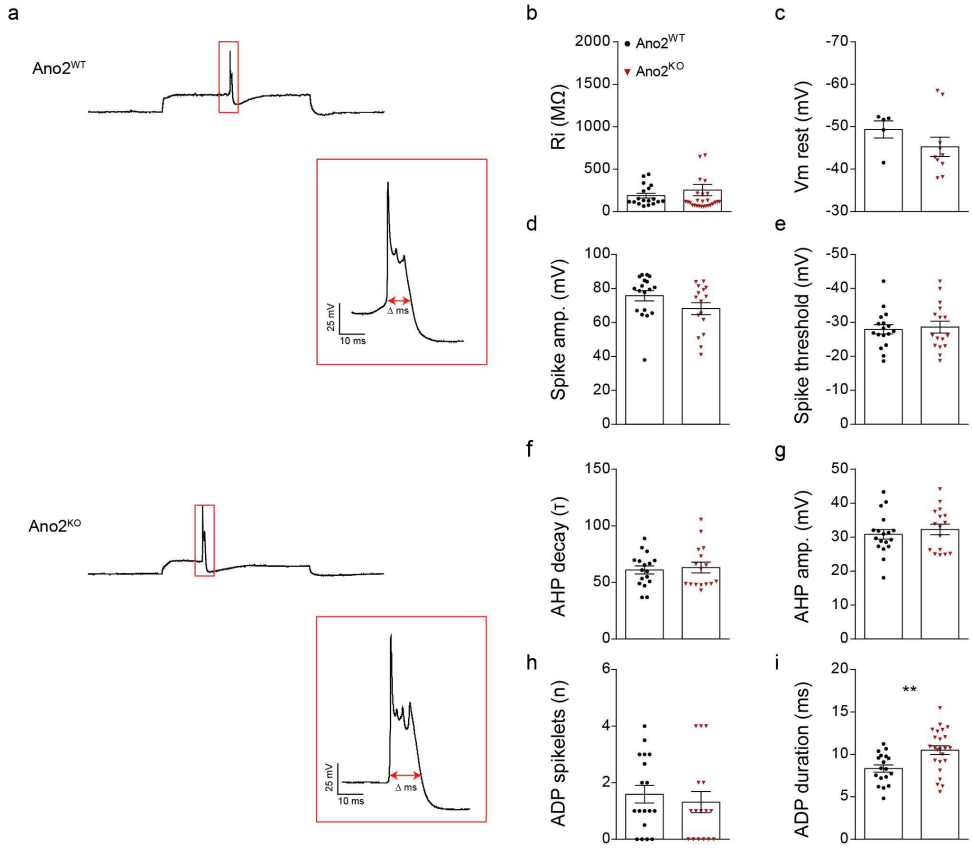

Figure 3: Inferior Olive cells in the Ano2-KO have HT spikes with lower ADP durations a. Samples of traces where current injections evoked HT spikes in IO cells. **b-i.** Quantitative measurements of HT spike parameters.

Mice lacking Ano2 show impaired locomotion on the Erasmus Ladder.

Recent reports indicate impaired motor coordination in Ano2-KO mice [432]. The tests utilized to evaluate motor coordination included rotarod and the horizontal-grid task, both of which are not very precise motor skill tests. To examine the effects of Ano2 deletion on motor coordination and walking patterns in more detail we subjected Ano2-KO mice to the Erasmus ladder (Table 1). Ano2-KO mice presented with significantly lower number of small steps and a higher number of backward steps compared to the control mice (Table 2). In addition, the Ano2-KO mice had significantly higher number of slips compared to controls (Table 2 and Fig. 4) indicative of impairment in motor coordination.

		control (n = 11)			ano2 -/- (9)		
non-perturbed (n = 222 ; SD = 38)		**mean**	**median**	**SD**	**mean**	**median**	**SD**
all steps (n)		16.6	16	4.65	14.9	14	4.2
	small (n)	8.1	6	7.2	4.6	3	4.8
	large (n)	6.3	6	3.2	7.1	7	2.5
	jump (n)	0.1	0	0.3	0.1	0	0.3
	backward (n)	0	0	0.2	0.2	0	0.1
slips (n)		0.5	0	0.8	0.8	1	0.9
step-time (ms)		306.5	279	125.2	260.9	245	96.1

Table 1: Summary of walking parameters.

	β	**Std. Error**	**p-value**
All steps (n)			
Trial	-0.022	0.009	0.023
Day (Day 7)	-0.336	0.050	< 0.001
Genotype (Ano2 -/-)	-0.104	0.072	0.147
Small steps (n)			
Trial	-0.014	0.015	0.358
Day (Day 7)	-0.948	0.148	< 0.001
Genotype (Ano2 -/-)	-0.359	0.176	**0.042**
Large steps (n)			
Trial	0.037	0.015	0.013
Day (Day 7)	0.343	0.069	< 0.001
Genotype (Ano2 -/-)	0.044	0.078	0.570
Jumps (n)			
Trial	0.160	0.130	0.217
Day (Day 7)	-1.032	0.501	0.039
Genotype (Ano2 -/-)	1.068	0.928	0.250
Backward (n)			
Trial	0.076	0.146	0.599
Day (Day 7)	1.7 + 02	9.15 + 04	0.999
Genotype (Ano2 -/-)	2.26	0.885	**0.011**
Slips (n)			
Trial	-0.073	0.047	0.132
Day (Day 7)	-1.027	0.255	< 0.001
Genotype (Ano2 -/-)	0.602	0.224	**0.007**
Step-time (ms)			
Trial	-7.174	2.260	0.002
Day (Day 7)	-61.921	17.482	< 0.001
Genotype (Ano2 -/-)	-27.340	17.100	0.314

Table 2: Association between walking parameters and genotype.

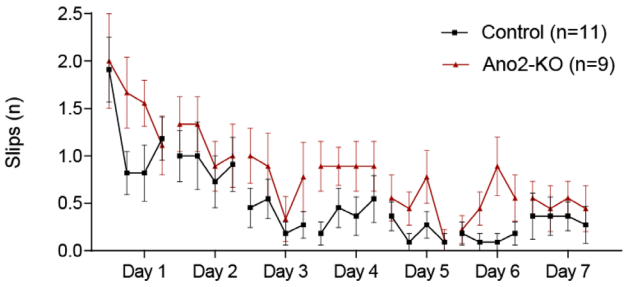

Figure 4: Increased number of slips on the Erasmus Ladder in the Ano2-KO. Ano2-KO mice present with an increase in the number of slips (see table 2 for stats).

Discussion

Here, we confirm the presence of a recently reported Ca^{2+} activated Cl^- current in IO cells [374]. The reported current is mediated by Ano2, a Ca^{2+}-activated Cl^- channel, and can readily be blocked by cadmium and NFA and is absent in IO cells of Ano2-KO mice. On a physiological level ANO2-KO IO cells have longer ADP lengths of HT spikes, indicating prolonged Ca^{2+} influx, which could be a result of absent repolarizing Ca^{2+}-activated Cl^- currents mediated by Ano2 to promote de-activation of voltage gated Ca^{2+} currents. In addition, ANO2-KO mice present a higher number of miss steps on the Erasmus Ladder indicative of dysfunctional motor coordination.

Ancotamins are a family of Ca^{2+}-activated Cl^- channels with a broad expression in tissues of the body. Ano2 is a member of this family and is expressed in the olfactory bulb, hippocampal pyramidal neurons, cerebellar PCs, thalamocortical and IO neurons [374, 419, 430, 432, 564, 565]. Ano2 channels in the olfactory bulb play a role in olfaction by facilitating chloride extrusion and influencing neuronal excitability [565] while in hippocampal pyramidal neurons Ano2 is thought to raise the threshold for action potential generation reducing neuronal excitability [419]. Ano2 channels located in cerebellar PCs facilitate a type of depolarization-induced depression of inhibition [430, 432] whereas in thalamocortical neurons Ano2 can mediate spike-frequency adaptation [564].

In the current study, we confirm the presence of Ano2 in the inferior olive using DAB staining. To study the function of Ano2, we first present evidence that IO cells have Ca^{2+} activated Cl^- currents using Ca^{2+} and Cl^- channel blockers. Patching IO cells in Ano2-KO mice reveals that these Ca^{2+} activated Cl^- currents are mediated by the Ano2 channel. Similar to other cell types, Ano2 could have a strong effect on the excitability of IO cells in

addition to other well-studied Ca^{2+} activated ion conductances, like those mediated by BK and SK channels [560, 561]. In our study, current injection evoked HT spikes reveal that the ADP length of the HT spike is longer in Ano2-KO mice. Zhang et al., (2017) have recently reported a longer ADP duration in the IO of Ano2-KO mice. In this study, the authors propose that Ano2 is coupled to the dendritic high threshold Ca^{2+} channels that generate the long ADP of the HT spike. Because of the prolonged Ca^{2+} influx, in absence of Ano2 Cl^- mediated repolarization, the cells could have stronger BK and SK mediated AHP durations increasing the interval of spike generation and thus reduction of excitability. Indeed, Zhang et al., (2017) report longer AHP duration of HT spikes that in turn coincide with lower frequencies of HT spiking upon current injections. However, we find no difference in AHP or HT spiking frequency parameters between WT and Ano2-KO IO cells. One reason for this discrepancy could be the different ages of experimental mice, Zhang et al., (2017) use young mice (P10-P16) during development, whereas we use young adults (P30-P40). Indeed, it is quite possible that the number of available voltage gated Ca^{2+} channels and how they are coupled to Ano2 channels in developing dendrites is significantly different compared to developed dendrites. To resolve these discrepancies future studies have to utilize *in vivo* single unit recordings to assess complex spike physiology using an Ano2-KO cell specific mutant.

It is of importance to deploy a KO model with cell specificity to study the physiology of the olivo cerebellar network as it is has come to our attention that studies using Ano2 global KO models have contributed the observed motor learning and coordination abnormalities to fundamentally different physiological explanations involving either lowered IO excitability or depolarization induced depression of inhibition in PCs of the cerebellar cortex [374, 430, 432]. It is important to note that by now the expression of Ano2 is found in many different cell types, including extra-cerebellar regions important for motor function. Because of these arguments the behavioural relevance of Ano2 as exposed in Ano2-KO mice on the Erasmus ladder behavioural paradigm indicative of motor coordination impairments has to be re-evaluated as well. We need additional specificity in targeting strategies to come to the correct conclusions regarding the significant involvement of neuro circuits in these behavioural phenotypes.

Chapter 5

General discussion

The studies presented in this dissertation can be divided in two parts. The first explores the role of the cerebellum, and more specifically Purkinje cell physiology, in models for autism and speech disorders. Here, we have studied the function of the cerebellum in the absence of a scaffolding protein (Shank2) and a transcription factor (FoxP2), which have been associated with ASD and speech disorder respectively. The second part involves work that reflects on fundamental questions regarding Purkinje cell physiology through synaptic excitatory and inhibitory transmission. How is PF to PC potentiation affected by various molecular PSD targets? How do these changes contribute to the rate and regularity of spike output that is responsible for the modulation of cerebellum-related behaviour? For this purpose, we evaluate mutants that have modifications of post-synaptic AMPA, NMDA and GABA receptor mediated currents. The last two chapters are devoted to the function of chloride in the olivocerebellar system and ongoing work on Ano2 mediated calcium activated chloride currents in the inferior olive.

The cerebellum is important for non-motor behaviour

The cerebellum has traditionally been viewed as a structure controlling motor function. Anatomically the connections between the cerebellum and cerebrum were mostly thought to reflect the ability of the cerebellum to assemble information from different cortical areas of the cerebral cortex and consequentially help generate movements by processing this cortical information and sending it through the thalamus to M1. However, by now it has become clear that the cerebellar nuclei project to different areas of the thalamus and basal ganglia and indirectly affect a large range of cortical areas that are functionally relevant in non-motor-related tasks. The experimental evidence of cerebellar and striatal contributions to ASD symptoms in different mouse models are reviewed in **chapter 2.1**. Evidence from functional imaging and viral tracing studies [145] indicates strong interaction between both brain regions, which could have significant implications for neuropsychiatric diseases. Importantly in this context, physiologically relevant data have been published that underline a short latency modulation of the basal ganglia through cerebellar nuclei stimulation [146]. Given the evidence of striatal involvement in repetitive behaviours in ASD [117], we hypothesised that the striatum-related phenotypes of repetitive and cognitive behaviours may be modulated by cerebellar output. The ASD mouse models reviewed in **chapter 2.1** provide insights into the pathology that could result from specific ASD related gene mutations.

In **chapter 2.2** a high risk ASD gene expressed in Purkinje cells, SHANK2, and its function in the cerebellum is investigated. Severe loss-of-function mutations in SHANK2 have been

firmly established as conferring a high genetic risk for ASD and intellectual disability [156, 158, 162]. Children with disruptive SHANK2 mutations have in addition been shown to exhibit motor impairments, language delay and cerebellar dysfunction including dysmetria and dysdiadochokinesis [162]. In addition to cerebellum dependant motor learning phenotypes, we report impaired social and task specific repetitive behaviour due to the Purkinje cell-specific deletion of Shank2 in mice. Absence of Shank2 impairs both Purkinje cell intrinsic plasticity and induction of long-term potentiation at the parallel fiber to Purkinje cell synapse. Moreover, inhibitory input onto Purkinje cells is significantly enhanced, which we believe to be the main reason for increased simple spike irregularity of firing. We know by now that cerebellar abnormalities are one of the most consistent findings in persons with ASD [566, 567]. In addition, cerebellar lesions are correlated with higher occurrence of ASD [568, 569]. However, these findings are considered to be strong correlations whereas understanding of the contribution of the cerebellum to the pathophysiology of ASD remains elusive. In a recent study a team, well known for their work on cerebellar function in ASD, explored a specific cerebellar region involved in ASD phenotypes [570]. By experimenting with the right Crus1(RCrus1) area using neuromodulation, neuroimaging and electrophysiology in mice as well as humans Stoodly et al. (2017) established that in ASD the RCrus1 area presents with abnormal functional connections to the left inferior parietal lobule (IPL). The IPL is important for visuospatial and cognitive information [571], including the interpretation of gestures [571]. Interestingly, these functionalities are often found to be impaired in children with ASD [572, 573]. Another important question is how Purkinje cell impairments might lead to abnormal brain function during neurodevelopmental critical periods? Indeed, the cerebellum could also contribute to ASD relevant behaviours by dysfunction during the developmental phase. The idea that disruption of a certain brain area during development could affect the development and consequently the function of other inter-connected areas, also termed developmental diaschisis, has been put forward as a prime mechanism for the cerebellum in its ability to influence other cortical areas in critical developmental periods [57].

In **chapter 2.3** we explore cerebellar involvement related to disruptions of the *FOXP2* gene that causes a speech disorder involving difficulties in sequencing movements. The majority of brain lesions causing verbal apraxia occur in cortical and sub-cortical regions, and most functional FoxP2 studies to date have focused on cortico-striatal circuits. Nevertheless, like we discussed for the previous chapters involving ASD it is becoming increasingly clear that the role of the cerebellum goes beyond that of a coordinator of basic motor function [241]

and extends to regulating purposeful skilled motor actions such as those required for spoken language [242]. In line with the finding that cerebellar lesions can give rise to verbal apraxia by disrupting cerebro-cerebellar connectivity [243], patients suffering from FOXP2 mutations show altered activity in both the cerebral cortex ánd the cerebellum when subjected to verbal tasks under the fMRI [244]. In the current study, we observed differences between knockout and control mice after analyses of the temporal aspects of lever pressing, where the phenotypes emerged depending on the site of Foxp2 deletion. Cerebellar KO mice were much slower in their execution, whereas striatum KO mice were more variable in their execution. In addition, we found more missteps in cerebellar KO mice on the ErasmusLadder compared to the cortical and striatal KO mice. Recordings in behaving mice from PCs revealed increased SS frequency and decreased modulation of firing during limb movements. Using electrophysiology in vitro recordings we revealed that increased intrinsic excitability rather than changes in excitatory or inhibitory inputs are more likely to be the cause for the increased firing in vivo. We argued that in the case of higher intrinsic excitability, the SS frequency may sustain high output in zebrin-negative modules, which might reduce the modulation magnitude of firing preventing the structuring of an internal model [224].

Purkinje cell synaptic potentiation and simple spike frequency and regularity of firing is key for the modulation of motor and non-motor behaviour

In the first three chapters we explore Purkinje cell physiology in mouse mutant models where motor and non-motor behaviour was affected. Foxp2 mutants present with an increase in PC intrinsic firing, while Shank2 mutants show more irregular simple spike firing in addition to dysfunctional synaptic LTP. For Foxp2 and Shank2 it has been rather difficult to reveal the underlying cellular mechanisms responsible for the changes at the PC synapse and intrinsic activity, since both proteins can affect the function of many other proteins. To investigate how potentiation at the level of the synapse can affect PC spiking we could also modify the activity and/or presence of specific ion conducting receptors, like AMPAR, that directly mediate depolarization at the post-synaptic site. The role of AMPAR in PCs becomes more evident in **chapter 3.1** where we provide evidence for a role of the Shisa6 auxiliary AMPAR subunit in parallel fiber to Purkinje potentiation. Mice with PC specific deletion of Shisa6 have strongly reduced PF to PC excitatory postsynaptic transmission, impaired LTP as well as reduced *in vivo* PC SS frequency and regularity of firing. These PC abnormalities result in impaired motor performance and dysfunctional procedural learning behaviours. The results reported in **chapter 3.1** posit an important role

for Shisa6 in synaptic transmission between PFs and PCs as its absence results in the downregulation of AMPAR subunits and upregulation of the GluD2 receptor. In recent studies the absence of GluD2 is associated with PF to PC AMPAR composition, morphology as well as LTD [256-259, 266]. Considering that the changes in GluD2 expression could signal morphological changes [267], we also investigated some of these properties but we found no evidence for significant abnormalities at the PF to PC synapse in the PSD count and length. In addition, we found no impairments in LTD but we did find dysfunctional LTP at the PF to PC synapse. It seems that an increase, in contrast to an absence, of GlurD2 does not immediately lead to impairment in LTD. This leads us to hypothesize that LTP is primarily affected because of the lowered number of available AMPAR subunits and/or their abnormal localization within the PSD post LTP induction. Because the SS intrinsic activity and spontaneous inhibitory input of PCs is normal, the PC lowered spiking output and regularity in vivo is likely to be caused by the lack of afferent excitatory inputs at the PF to PC synapse. This greatly reduced potentiation leads to pronounced difficulties in proper spatiotemporal information processing normally facilitated by the PC to CN projections, thus severely affecting behaviour.

One type of receptor that allows Ca^{2+} influx but is not present at the adult PF to PC synapse is the NMDAR. In **chapter 3.2** we introduce NMDAR at the PF to PC synapse with the main consequence being that it renders the synapse incapable of LTP and results in impaired motor learning. Plasticity in PCs is Ca^{2+} dependent and reversed when compared to pyramidal cells [25, 310], thus, LTP induction is possible only when Ca^{2+} is present in low concentrations. With the results published here we hypothesized that in the presence of NMDARs the Ca^{2+} concentrations might increase such that they do not allow proper LTP to be facilitated, while LTD remains unaffected. In line with these findings it has already been shown that the blocking of NMDARs at the CF to PC synapse leads to low levels of Ca^{2+} that leave LTD impaired while LTP is not affected [301].

So far we have seen that LTP at the PF to PC synapse is important for motor learning. Nevertheless, it is clear from shank2 as well as the additionally aggravated shisa6 KO model that additional PC physiological abnormalities of intrinsic or general baseline excitatory nature result in additionally aggravated behavioural phenotypes. The observation that more than one abnormality of input to PCs can aggravate learning is further explored in **chapter 3.3** where we investigate eyeblink conditioning in the GluR2Δ7-L7-Δγ2 mice that lack LTD and inhibition. The data discussed in this chapter is in support of the hypothesis that more than two mechanisms may both contribute to the simple spike suppression required for

eyeblink conditioning [109] and that each of them may compensate for the absent or mild behavioural phenotype in the mutant with either physiological dysfunctions alone [284]. Interestingly, the data presented here indicates that unlike for Shank2 (**chapter 2.2**) and Shisa6 (**chapter 3.1**), where both eye blink conditioning and PC baseline firing patterns were affected, the strong phenotype in the GluR2Δ7-L7-Δγ2 mice cannot be explained by abnormal PC SS firing. From these observations we hypothesize that SS suppression, which is required for eyeblink conditioning, is brought about by both LTD and inhibition and that dysfunction of LTD or inhibition alone could lead to partial compensation of the phenotype [275]. However, it should be noted that at this point in time it is unclear whether LTD and inhibition are indeed the main effects that drive PC SS suppression or that they only support its facilitation by making the PCs inputs more optimized to transmit the conditioned stimulus information. In addition to the many different plasticity mechanisms that might strengthen or weaken the PC synapse, it is important that we do not exclude the possibility of intrinsic forms of memory in the PC which might affect its spiking output [330, 335].

In **chapter 4.1** we shift the discussion from depolarising to repolarising currents and look at the significance of chloride in the olivocerebellar network. As discussed in the first chapter, a big part of the olivo cerebellar network is in fact GABAergic (Figure 5). Abnormal GABAR function at any of these synapses has been shown to result in dysfunctional motor behaviour [166, 369-371]. As we have discussed in **chapter 3.3,** the presence of proper feed forward inhibition to PCs is important in PC signal processing. Similarly is the case in olivary neurons where the Cl^- concentration influences the excitability of these cells and thus the excitation of key neuronal cells of the cerebellar cortex through CFs [368, 374]. Altered neuronal excitability in IO evokes long-term changes in the activity of cerebellar neurons and the spatiotemporal firing pattern of the olivocerebellar network [375]. This line of reasoning is continued in **chapter 4.2** where we present preliminary findings confirming the presence of a recently reported Ca^{2+} activated Cl^- current in IO cells [374]. We confirm this by showing that the current is gated through Ano2 and can be blocked by cadmium and NFA and is absent in IO cells of Ano2-KO mice. On a physiological level the IO cells of the Ano2-KO mice have longer ADP durations of HT spikes, similar to the results published by Zhang et al., (2017). We hypothesize that this might indicate prolonged Ca^{2+} influx, which could be a result of absent repolarizing Ca^{2+}-activated Cl^- currents through Ano2 to effectively promote the de-activation of VGCCs. However, there are still significant discrepancies with the published study. We found no signs of reduced excitation as measured by the number of occurring high threshold Ca^{2+} spikes. In addition, we found no

strong impairments in several eye blink conditioning paradigms that were performed using the Ano2-KO mice (data not shown here). We did, however, see higher number of miss steps on the Erasmus Ladder for the Ano2-KO mice which could be indicative of impaired motor coordination. However, these results are of a minor effect size and should be interpreted carefully. More experiments are needed to elucidate the effects of the Ano2 on IO cell excitability and how this might affect PC physiology through CF innervation.

Future perspectives

To advance the topics in this dissertation in a significant manner, future research should carefully disentangle the temporal and spatial aspects of information processing. For example, the question of how brain insult during sensitive periods can affect ASD aetiology can only truly be tackled by inducing specific and temporally controlled experimental insults. Current experimental approaches often have many side-effects that blur our understanding of the underlying processes. This includes KO mouse models and their imperfect inducibles. Once techniques, like CRISPR/Cas9 [574] and other non-invasive possibilities for the recording and manipulation of neuron population activities becomes experimentally viable, future research can use improved temporal and spatial resolutions to map brain activity to behaviour.

References

1. Zackowski, K.M., W.T. Thach, Jr., and A.J. Bastian, *Cerebellar subjects show impaired coupling of reach and grasp movements.* Exp Brain Res, 2002. **146**(4): p. 511-22.
2. Wolpert, D.M., R.C. Miall, and M. Kawato, *Internal models in the cerebellum.* Trends Cogn Sci, 1998. **2**(9): p. 338-47.
3. Ito, M., *Control of mental activities by internal models in the cerebellum.* Nat Rev Neurosci, 2008. **9**(4): p. 304-13.
4. Courchesne, E. and G. Allen, *Prediction and preparation, fundamental functions of the cerebellum.* Learn Mem, 1997. **4**(1): p. 1-35.
5. Voogd, J., *Cerebellar zones: a personal history.* Cerebellum, 2011. **10**(3): p. 334-50.
6. Cerminara, N.L., et al., *Redefining the cerebellar cortex as an assembly of non-uniform Purkinje cell microcircuits.* Nat Rev Neurosci, 2015. **16**(2): p. 79-93.
7. Apps, R., et al., *Cerebellar Modules and Their Role as Operational Cerebellar Processing Units.* Cerebellum, 2018.
8. Sugihara, I. and Y. Shinoda, *Molecular, topographic, and functional organization of the cerebellar cortex: a study with combined aldolase C and olivocerebellar labeling.* J Neurosci, 2004. **24**(40): p. 8771-85.
9. Voogd, J. and M. Glickstein, *The anatomy of the cerebellum.* Trends Neurosci, 1998. **21**(9): p. 370-5.
10. Zhou, H., et al., *Cerebellar modules operate at different frequencies.* eLife, 2014: p. e02536-e02536.
11. Xiao, J., et al., *Systematic regional variations in Purkinje cell spiking patterns.* PLoS One, 2014. **9**(8): p. e105633.
12. De Zeeuw, C.I., et al., *Microcircuitry and function of the inferior olive.* Trends in neurosciences, 1998. **21**(9): p. 391-400.
13. De Zeeuw, C.I., et al., *Spatiotemporal firing patterns in the cerebellum.* Nat Rev Neurosci, 2011. **12**(6): p. 327-44.
14. Eccles, J.C., R. Llinas, and K. Sasaki, *The excitatory synaptic action of climbing fibres on the Purkinje cells of the cerebellum.* J Physiol, 1966. **182**(2): p. 268-96.
15. Eccles, J.C., R. Llinas, and K. Sasaki, *The inhibitory interneurones within the cerebellar cortex.* Exp Brain Res, 1966. **1**(1): p. 1-16.
16. Witter, L., et al., *Purkinje Cell Collaterals Enable Output Signals from the Cerebellar Cortex to Feed Back to Purkinje Cells and Interneurons.* Neuron, 2016. **91**(2): p. 312-9.
17. Davie, J.T., B.A. Clark, and M. Hausser, *The origin of the complex spike in cerebellar Purkinje cells.* J Neurosci, 2008. **28**(30): p. 7599-609.
18. Hebb, D.O., *The organization of behavior*. 1949, New York: Wiley & Sons
19. Ito, M., *Experimental verification of Marr-Albus' plasticity assumption for the cerebellum.* Acta Biol Acad Sci Hung, 1982. **33**(2-3): p. 189-99.
20. Marr, D., *A theory of cerebellar cortex.* J Physiol, 1969. **202**(2): p. 437-70.

21. Albus, J.S., *A theory of cerebellar function.* Math Biosci, 1971. **10**: p. 25-61.
22. Schonewille, M., et al., *Purkinje cell-specific knockout of the protein phosphatase PP2B impairs potentiation and cerebellar motor learning.* Neuron, 2010. **67**(4): p. 618-28.
23. Schonewille, M., et al., *Reevaluating the role of LTD in cerebellar motor learning.* Neuron, 2011. **70**(1): p. 43-50.
24. Gao, Z., B.J. van Beugen, and C.I. De Zeeuw, *Distributed synergistic plasticity and cerebellar learning.* Nature reviews. Neuroscience, 2012. **13**: p. 619-35.
25. Coesmans, M., et al., *Bidirectional parallel fiber plasticity in the cerebellum under climbing fiber control.* Neuron, 2004. **44**(4): p. 691-700.
26. Belmeguenai, A., et al., *Intrinsic plasticity complements long-term potentiation in parallel fiber input gain control in cerebellar Purkinje cells.* The Journal of neuroscience, 2010. **30**(41): p. 13630-13643.
27. Hosy, E., et al., *SK2 channel expression and function in cerebellar Purkinje cells.* J Physiol, 2011. **589**(Pt 14): p. 3433-40.
28. De Zeeuw, C.I., et al., *Phase relations of Purkinje cells in the rabbit flocculus during compensatory eye movements.* J Neurophysiol, 1995. **74**(5): p. 2051-64.
29. Peter, S., et al., *Dysfunctional cerebellar Purkinje cells contribute to autism-like behaviour in Shank2-deficient mice.* Nat Commun, 2016. **7**: p. 12627.
30. Gutierrez-Castellanos, N., et al., *Motor Learning Requires Purkinje Cell Synaptic Potentiation through Activation of AMPA-Receptor Subunit GluA3.* Neuron, 2017. **93**(2): p. 409-424.
31. Galliano, E., et al., *Silencing the majority of cerebellar granule cells uncovers their essential role in motor learning and consolidation.* Cell Rep, 2013. **3**(4): p. 1239-51.
32. Hesslow, G., *Correspondence between climbing fibre input and motor output in eyeblink-related areas in cat cerebellar cortex.* J Physiol, 1994. **476**(2): p. 229-44.
33. De Zeeuw, C.I. and M.M. Ten Brinke, *Motor Learning and the Cerebellum.* Cold Spring Harbor Perspectives in Biology, 2015. **7**: p. a021683.
34. Boele, H.J., M.M. Ten Brinke, and C.I. De Zeeuw, *Classical conditioning of timed motor responses: neural coding in cerebellar cortex and cerebellar nuclei*, in *The Neural Codes of the Cerebellum*, D. Heck, Editor. 2015, Academic press. p. 53-96.
35. Witter, L., et al., *Strength and timing of motor responses mediated by rebound firing in the cerebellar nuclei after Purkinje cell activation.* Front Neural Circuits, 2013. **7**: p. 133.
36. Inhoff, A.W., et al., *The role of cerebellar structures in the execution of serial movements.* Brain, 1989. **112 (Pt 3)**: p. 565-81.
37. Middleton, F.A. and P.L. Strick, *Cerebellar projections to the prefrontal cortex of the primate.* J Neurosci, 2001. **21**(2): p. 700-12.
38. Wagner, M.J., et al., *Cerebellar granule cells encode the expectation of reward.* Nature, 2017. **544**(7648): p. 96-100.
39. Sears, L.L., P.R. Finn, and J.E. Steinmetz, *Abnormal classical eye-blink conditioning in autism.* Journal of autism and developmental disorders, 1994. **24**(6): p. 737-751.

40. Oristaglio, J., et al., *Children with autism spectrum disorders show abnormal conditioned response timing on delay, but not trace, eyeblink conditioning.* Neuroscience, 2013. **248**: p. 708-718.
41. Takarae, Y., et al., *Pursuit eye movement deficits in autism.* Brain, 2004. **127**(12): p. 2584-2594.
42. Schmitt, L.M., et al., *Saccadic eye movement abnormalities in autism spectrum disorder indicate dysfunctions in cerebellum and brainstem.* Molecular autism, 2014. **5**(1): p. 47.
43. Marko, M.K., et al., *Behavioural and neural basis of anomalous motor learning in children with autism.* Brain, 2015. **138**(3): p. 784-797.
44. Mostofsky, S.H., et al., *Evidence for a deficit in procedural learning in children and adolescents with autism: implications for cerebellar contribution.* Journal of the International Neuropsychological Society, 2000. **6**(07): p. 752-759.
45. Memari, A.H., et al., *Postural control impairments in individuals with autism spectrum disorder: a critical review of current literature.* Asian journal of sports medicine, 2014. **5**(3).
46. Stins, J.F., et al., *Attentional and sensory contributions to postural sway in children with autism spectrum disorder.* Gait & Posture, 2015.
47. Molloy, C.A., K.N. Dietrich, and A. Bhattacharya, *Postural stability in children with autism spectrum disorder.* Journal of autism and developmental disorders, 2003. **33**(6): p. 643-652.
48. Schmahmann, J.D., *The role of the cerebellum in cognition and emotion: personal reflections since 1982 on the dysmetria of thought hypothesis, and its historical evolution from theory to therapy.* Neuropsychology review, 2010. **20**(3): p. 236-260.
49. Allen, G., *The cerebellum in autism.* Clinical Neuropsychiatry, 2005. **2**(6): p. 321-337.
50. Bailey, A., et al., *A clinicopathological study of autism.* Brain, 1998. **121**(5): p. 889-905.
51. Silvestri, L., et al., *Quantitative neuroanatomy of all Purkinje cells with light sheet microscopy and high-throughput image analysis.* Frontiers in Neuroanatomy, 2015. **9**: p. 68.
52. Palmen, S.J.M.C., et al., *Neuropathological findings in autism.* Brain, 2004. **127**(12): p. 2572-2583.
53. Fatemi, S.H., et al., *Purkinje cell size is reduced in cerebellum of patients with autism.* Cellular and molecular neurobiology, 2002. **22**(2): p. 171-175.
54. Bauman, M.L., T.L. Kemper, and D.M. Arin, *Pervasive neuroanatomic abnormalities of the brain in three cases of Rett's syndrome.* Neurology, 1995. **45**(8): p. 1581-1586.
55. Menashe, I., et al., *Co-expression profiling of autism genes in the mouse brain.* PLoS Comput Biol, 2013. **9**(7): p. e1003128.
56. Limperopoulos, C., et al., *Does cerebellar injury in premature infants contribute to the high prevalence of long-term cognitive, learning, and behavioral disability in survivors?* Pediatrics, 2007. **120**(3): p. 584-593.

57. Wang, S.S.H., A.D. Kloth, and A. Badura, *The cerebellum, sensitive periods, and autism.* Neuron, 2014. **83**(3): p. 518-532.
58. Kanner, L., *Autistic disturbances of affective contact.* Nervous child, 1943. **2**(3): p. 217-250.
59. Asperger, H., *Die 'Autistischen Psychopathen' im Kindesalter.* Archiv fur Psychiatrie und Nervenkrankheiten, 1944. **117**: p. 76-136.
60. Fuccillo, M.V., *Striatal Circuits as a Common Node for Autism Pathophysiology.* Front Neurosci, 2016. **10**: p. 27.
61. Budimirovic, D.B. and W.E. Kaufmann, *What can we learn about autism from studying fragile X syndrome?* Developmental neuroscience, 2011. **33**(5): p. 379-394.
62. Garber, K.B., J. Visootsak, and S.T. Warren, *Fragile X syndrome.* European Journal of Human Genetics, 2008. **16**(6): p. 666-672.
63. Mostofsky, S.H., et al., *Decreased cerebellar posterior vermis size in fragile X syndrome Correlation with neurocognitive performance.* Neurology, 1998. **50**(1): p. 121-130.
64. Sabaratnam, M., *Pathological and neuropathological findings in two males with fragile-X syndrome.* Journal of Intellectual Disability Research, 2000. **44**(1): p. 81-85.
65. Greco, C.M., et al., *Neuropathologic features in the hippocampus and cerebellum of three older men with fragile X syndrome.* Mol Autism, 2011. **2**(2).
66. Koekkoek, S.K.E., et al., *Deletion of FMR1 in Purkinje cells enhances parallel fiber LTD, enlarges spines, and attenuates cerebellar eyelid conditioning in Fragile X syndrome.* Neuron, 2005. **47**(3): p. 339-352.
67. Tobia, M.J. and D.S. Woodruff-Pak, *Delay eyeblink classical conditioning is impaired in Fragile X syndrome.* Behavioral neuroscience, 2009. **123**(3): p. 665.
68. Ellegood, J., et al., *Anatomical phenotyping in a mouse model of fragile X syndrome with magnetic resonance imaging.* Neuroimage, 2010. **53**(3): p. 1023-1029.
69. Rogers, T.D., et al., *Reorganization of circuits underlying cerebellar modulation of prefrontal cortical dopamine in mouse models of autism spectrum disorder.* The Cerebellum, 2013. **12**(4): p. 547-556.
70. Broek, J.A., et al., *Synaptic vesicle dynamic changes in a model of fragile X.* Mol Autism, 2016. **7**: p. 17.
71. Pacey, L.K., et al., *Persistent astrocyte activation in the fragile X mouse cerebellum.* Brain Behav, 2015. **5**(10): p. e00400.
72. Amir, R.E., et al., *Rett syndrome is caused by mutations in X-linked MECP2, encoding methyl-CpG-binding protein 2.* Nature genetics, 1999. **23**(2): p. 185-188.
73. Segawa, M., *Early motor disturbances in Rett syndrome and its pathophysiological importance.* Brain and Development, 2005. **27**: p. S54-S58.
74. Oldfors, A., et al., *Rett syndrome: cerebellar pathology.* Pediatric neurology, 1990. **6**(5): p. 310-314.
75. Murakami, J.W., et al., *Cerebellar and cerebral abnormalities in Rett syndrome: a quantitative MR analysis.* AJR. American journal of roentgenology, 1992. **159**(1): p. 177-183.

76. Goffin, D., et al., *Rett syndrome mutation MeCP2 T158A disrupts DNA binding, protein stability and ERP responses.* Nature neuroscience, 2012. **15**(2): p. 274-283.
77. Belichenko, N.P., et al., *Comparative study of brain morphology in Mecp2 mutant mouse models of Rett syndrome.* Journal of Comparative Neurology, 2008. **508**(1): p. 184-195.
78. Chen, R.Z., et al., *Deficiency of methyl-CpG binding protein-2 in CNS neurons results in a Rett-like phenotype in mice.* Nature genetics, 2001. **27**(3): p. 327-331.
79. Mullaney, B.C., M.V. Johnston, and M.E. Blue, *Developmental expression of methyl-CpG binding protein 2 is dynamically regulated in the rodent brain.* Neuroscience, 2004. **123**(4): p. 939-949.
80. Ben-Shachar, S., et al., *Mouse models of MeCP2 disorders share gene expression changes in the cerebellum and hypothalamus.* Hum Mol Genet, 2009. **18**(13): p. 2431-42.
81. Peters, S.U., et al., *Autism in Angelman syndrome: implications for autism research.* Clinical genetics, 2004. **66**(6): p. 530-536.
82. Kim, S., et al., *Ube3a/E6AP is involved in a subset of MeCP2 functions.* Biochemical and biophysical research communications, 2013. **437**(1): p. 67-73.
83. Dan, B., et al., *From Electrophysiology to Chromatin: A Bottom-Up Approach to Angelman Syndrome.* Annals of the New York Academy of Sciences, 2004. **1030**(1): p. 599-611.
84. Holopainen, I.E., et al., *Decreased binding of [11C] flumazenil in Angelman syndrome patients with GABAA receptor β3 subunit deletions.* Annals of neurology, 2001. **49**(1): p. 110-113.
85. Miura, K., et al., *Neurobehavioral and Electroencephalographic Abnormalities in Ube3aMaternal-Deficient Mice.* Neurobiology of disease, 2002. **9**(2): p. 149-159.
86. Heck, D.H., et al., *Analysis of cerebellar function in Ube3a-deficient mice reveals novel genotype-specific behaviors.* Human molecular genetics, 2008. **17**(14): p. 2181-2189.
87. Dindot, S.V., et al., *The Angelman syndrome ubiquitin ligase localizes to the synapse and nucleus, and maternal deficiency results in abnormal dendritic spine morphology.* Hum Mol Genet, 2008. **17**(1): p. 111-8.
88. Cheron, G., et al., *Fast cerebellar oscillation associated with ataxia in a mouse model of Angelman syndrome.* Neuroscience, 2005. **130**(3): p. 631-7.
89. Bruinsma, C.F., et al., *Dissociation of locomotor and cerebellar deficits in a murine Angelman syndrome model.* J Clin Invest, 2015. **125**(11): p. 4305-15.
90. Egawa, K., et al., *Decreased tonic inhibition in cerebellar granule cells causes motor dysfunction in a mouse model of Angelman syndrome.* Science translational medicine, 2012. **4**(163): p. 163ra157-163ra157.
91. Cook Jr, E.H. and S.W. Scherer, *Copy-number variations associated with neuropsychiatric conditions.* Nature, 2008. **455**(7215): p. 919-923.
92. Nakatani, J., et al., *Abnormal behavior in a chromosome-engineered mouse model for human 15q11-13 duplication seen in autism.* Cell, 2009. **137**(7): p. 1235-1246.
93. Piochon, C., et al., *Cerebellar plasticity and motor learning deficits in a copy-number variation mouse model of autism.* Nature communications, 2014. **5**.

94. Harrison, J.E. and P.F. Bolton, *Annotation: tuberous sclerosis.* Journal of Child Psychology and Psychiatry, 1997. **38**(6): p. 603-614.
95. Eluvathingal, T.J., et al., *Cerebellar Lesions in Tuberous Sclerosis Complex Neurobehavioral and Neuroimaging Correlates.* Journal of child neurology, 2006. **21**(10): p. 846-851.
96. Gutmann, D.H., et al., *Expression of the tuberous sclerosis complex gene products, hamartin and tuberin, in central nervous system tissues.* Acta neuropathologica, 2000. **99**(3): p. 223-230.
97. Reith, R.M., et al., *Loss of Tsc2 in Purkinje cells is associated with autistic-like behavior in a mouse model of tuberous sclerosis complex.* Neurobiology of disease, 2013. **51**: p. 93-103.
98. Reith, R.M., et al., *Loss of the tuberous sclerosis complex protein tuberin causes Purkinje cell degeneration.* Neurobiology of disease, 2011. **43**(1): p. 113-122.
99. Tsai, P.T., et al., *Autistic-like behaviour and cerebellar dysfunction in Purkinje cell Tsc1 mutant mice.* Nature, 2012. **488**(7413): p. 647-651.
100. McBride, K.L., et al., *Confirmation study of PTEN mutations among individuals with autism or developmental delays/mental retardation and macrocephaly.* Autism Res, 2010. **3**(3): p. 137-41.
101. Cupolillo, D., et al., *Autistic-Like Traits and Cerebellar Dysfunction in Purkinje Cell PTEN Knock-Out Mice.* Neuropsychopharmacology, 2016. **41**(6): p. 1457-66.
102. Sheng, M. and E. Kim, *The Shank family of scaffold proteins.* Journal of cell science, 2000. **113**(11): p. 1851-1856.
103. Grabrucker, A.M., et al., *Postsynaptic ProSAP/Shank scaffolds in the cross-hair of synaptopathies.* Trends Cell Biol, 2011. **21**(10): p. 594-603.
104. Leblond, C.S., et al., *Meta-analysis of SHANK mutations in autism spectrum disorders: a gradient of severity in cognitive impairments.* 2014.
105. Ha, S., et al., *Cerebellar Shank2 Regulates Excitatory Synapse Density, Motor Coordination, and Specific Repetitive and Anxiety-Like Behaviors.* J Neurosci, 2016. **36**(48): p. 12129-12143.
106. Stoodley, C.J., *Distinct regions of the cerebellum show gray matter decreases in autism, ADHD, and developmental dyslexia.* Frontiers in systems neuroscience, 2014. **8**.
107. Südhof, T.C., *Neuroligins and neurexins link synaptic function to cognitive disease.* Nature, 2008. **455**(7215): p. 903-911.
108. Baudouin, S.J., et al., *Shared synaptic pathophysiology in syndromic and nonsyndromic rodent models of autism.* Science, 2012. **338**(6103): p. 128-132.
109. ten Brinke, M.M., et al., *Evolving Models of Pavlovian Conditioning: Cerebellar Cortical Dynamics in Awake Behaving Mice.* Cell Rep, 2015. **13**(9): p. 1977-88.
110. Kloth, A.D., et al., *Cerebellar associative sensory learning defects in five mouse autism models.* Elife, 2015. **4**: p. e06085.
111. Doya, K., *What are the computations of the cerebellum, the basal ganglia and the cerebral cortex?* Neural networks, 1999. **12**(7): p. 961-974.
112. Doya, K., *Complementary roles of basal ganglia and cerebellum in learning and motor control.* Current opinion in neurobiology, 2000. **10**(6): p. 732-739.

113. Middleton, F.A. and P.L. Strick, *Basal ganglia and cerebellar loops: motor and cognitive circuits.* Brain research reviews, 2000. **31**(2): p. 236-250.
114. M Mehmet Haznedar, M.D., et al., *Volumetric analysis and three-dimensional glucose metabolic mapping of the striatum and thalamus in patients with autism spectrum disorders.* The American journal of psychiatry, 2006. **163**(7): p. 1252-1263.
115. Hollander, E., et al., *Striatal volume on magnetic resonance imaging and repetitive behaviors in autism.* Biological psychiatry, 2005. **58**(3): p. 226-232.
116. Sears, L.L., et al., *An MRI study of the basal ganglia in autism.* Progress in Neuro-Psychopharmacology and Biological Psychiatry, 1999. **23**(4): p. 613-624.
117. Langen, M., et al., *Changes in the development of striatum are involved in repetitive behavior in autism.* Biological psychiatry, 2014. **76**(5): p. 405-411.
118. Peça, J., et al., *Shank3 mutant mice display autistic-like behaviours and striatal dysfunction.* Nature, 2011. **472**(7344): p. 437-442.
119. Wan, Y., et al., *Circuit-selective striatal synaptic dysfunction in the Sapap3 knockout mouse model of obsessive-compulsive disorder.* Biological psychiatry, 2014. **75**(8): p. 623-630.
120. Bienvenu, O.J., et al., *Sapap3 and pathological grooming in humans: Results from the OCD collaborative genetics study.* American Journal of Medical Genetics Part B: Neuropsychiatric Genetics, 2009. **150**(5): p. 710-720.
121. Abelson, J.F., et al., *Sequence variants in SLITRK1 are associated with Tourette's syndrome.* Science, 2005. **310**(5746): p. 317-320.
122. Jaramillo, T.C., et al., *Altered Striatal Synaptic Function and Abnormal Behaviour in Shank3 Exon4-9 Deletion Mouse Model of Autism.* Autism Res, 2016. **9**(3): p. 350-75.
123. Jaramillo, T.C., et al., *Novel Shank3 mutant exhibits behaviors with face validity for autism and altered striatal and hippocampal function.* Autism Res, 2016.
124. Wang, X., et al., *Altered mGluR5-Homer scaffolds and corticostriatal connectivity in a Shank3 complete knockout model of autism.* Nat Commun, 2016. **7**: p. 11459.
125. Mei, Y., et al., *Adult restoration of Shank3 expression rescues selective autistic-like phenotypes.* Nature, 2016. **530**(7591): p. 481-4.
126. Vicidomini, C., et al., *Pharmacological enhancement of mGlu5 receptors rescues behavioral deficits in SHANK3 knock-out mice.* Mol Psychiatry, 2016.
127. Won, H., et al., *Autistic-like social behaviour in Shank2-mutant mice improved by restoring NMDA receptor function.* Nature, 2012. **486**(7402): p. 261-265.
128. Schmeisser, M.J., et al., *Autistic-like behaviours and hyperactivity in mice lacking ProSAP1/Shank2.* Nature, 2012. **486**(7402): p. 256-260.
129. Peixoto, R.T., et al., *Early hyperactivity and precocious maturation of corticostriatal circuits in Shank3B(-/-) mice.* Nat Neurosci, 2016. **19**(5): p. 716-24.
130. Zhou, Y., et al., *Mice with Shank3 Mutations Associated with ASD and Schizophrenia Display Both Shared and Distinct Defects.* Neuron, 2016. **89**(1): p. 147-62.
131. Rothwell, P.E., et al., *Autism-associated neuroligin-3 mutations commonly impair striatal circuits to boost repetitive behaviors.* Cell, 2014. **158**(1): p. 198-212.

132. Chan, S.-h., L. Ryan, and T.G. Bever, *Role of the striatum in language: syntactic and conceptual sequencing.* Brain and Language, 2013. **125**(3): p. 283-294.
133. Chien, W.-H., et al., *Increased gene expression of FOXP1 in patients with autism spectrum disorders.* Molecular autism, 2013. **4**(1): p. 23.
134. Hamdan, F.F., et al., *De novo mutations in FOXP1 in cases with intellectual disability, autism, and language impairment.* The American Journal of Human Genetics, 2010. **87**(5): p. 671-678.
135. Tsang, K.M., et al., *A genome-wide survey of transgenerational genetic effects in autism.* 2013.
136. Lozano, R., et al., *A de novo FOXP1 variant in a patient with autism, intellectual disability and severe speech and language impairment.* European Journal of Human Genetics, 2015.
137. Watkins, K.E., N.F. Dronkers, and F. Vargha-Khadem, *Behavioural analysis of an inherited speech and language disorder: comparison with acquired aphasia.* Brain, 2002. **125**(3): p. 452-464.
138. Vargha-Khadem, F., et al., *Praxic and nonverbal cognitive deficits in a large family with a genetically transmitted speech and language disorder.* Proceedings of the National Academy of Sciences, 1995. **92**(3): p. 930-933.
139. Bacon, C., et al., *Brain-specific Foxp1 deletion impairs neuronal development and causes autistic-like behaviour.* Molecular psychiatry, 2015. **20**(5): p. 632-639.
140. Kurt, S., S.E. Fisher, and G. Ehret, *Foxp2 mutations impair auditory-motor association learning.* PloS one, 2012. **7**(3): p. e33130.
141. Fisher, S.E. and C. Scharff, *FOXP2 as a molecular window into speech and language.* Trends in Genetics, 2009. **25**(4): p. 166-177.
142. Groszer, M., et al., *Impaired synaptic plasticity and motor learning in mice with a point mutation implicated in human speech deficits.* Current Biology, 2008. **18**(5): p. 354-362.
143. French, C.A., et al., *An aetiological Foxp2 mutation causes aberrant striatal activity and alters plasticity during skill learning.* Molecular psychiatry, 2012. **17**(11): p. 1077-1085.
144. Ellegood, J., et al., *Clustering autism: using neuroanatomical differences in 26 mouse models to gain insight into the heterogeneity.* Mol Psychiatry, 2015. **20**(1): p. 118-25.
145. Bostan, A.C., R.P. Dum, and P.L. Strick, *Cerebellar networks with the cerebral cortex and basal ganglia.* Trends in cognitive sciences, 2013. **17**(5): p. 241-254.
146. Chen, C.H., et al., *Short latency cerebellar modulation of the basal ganglia.* Nature neuroscience, 2014. **17**(12): p. 1767-1775.
147. Khan, S., et al., *Somatosensory cortex functional connectivity abnormalities in autism show opposite trends, depending on direction and spatial scale.* Brain, 2015. **138**(Pt 5): p. 1394-409.
148. Robertson, C.E., et al., *Global motion perception deficits in autism are reflected as early as primary visual cortex.* Brain, 2014. **137**(Pt 9): p. 2588-99.
149. Carson, A.M., et al., *Electroencephalogram coherence in children with and without autism spectrum disorders: decreased interhemispheric connectivity in autism.* Autism Res, 2014. **7**(3): p. 334-43.

150. Chen, J.A., et al., *The Emerging Picture of Autism Spectrum Disorder: Genetics and Pathology.* Annual Review of Pathology: Mechanisms of Disease, 2015. **10**: p. 111-144.
151. Zwaigenbaum, L., S. Bryson, and N. Garon, *Early identification of autism spectrum disorders.* Behavioural brain research, 2013. **251**: p. 133-146.
152. Menashe, I., et al., *Co-expression profiling of autism genes in the mouse brain.* PLoS computational biology, 2013. **9**(7): p. e1003128.
153. Grabrucker, A.M., et al., *Postsynaptic ProSAP/Shank scaffolds in the cross-hair of synaptopathies.* Trends in cell biology, 2011. **21**(10): p. 594-603.
154. Zoghbi, H.Y. and M.F. Bear, *Synaptic dysfunction in neurodevelopmental disorders associated with autism and intellectual disabilities.* Cold Spring Harbor perspectives in biology, 2012. **4**(3): p. a009886.
155. Bourgeron, T., *From the genetic architecture to synaptic plasticity in autism spectrum disorder.* Nature Reviews Neuroscience, 2015. **16**(9): p. 551-563.
156. Leblond, C.S., et al., *Genetic and functional analyses of SHANK2 mutations suggest a multiple hit model of autism spectrum disorders.* PLoS Genet, 2012. **8**(2): p. e1002521.
157. Durand, C.M., et al., *Mutations in the gene encoding the synaptic scaffolding protein SHANK3 are associated with autism spectrum disorders.* Nat Genet, 2007. **39**(1): p. 25-7.
158. Berkel, S., et al., *Mutations in the SHANK2 synaptic scaffolding gene in autism spectrum disorder and mental retardation.* Nature genetics, 2010. **42**(6): p. 489-491.
159. Sato, D., et al., *SHANK1 Deletions in Males with Autism Spectrum Disorder.* Am J Hum Genet, 2012. **90**(5): p. 879-87.
160. Böckers, T.M., et al., *Differential expression and dendritic transcript localization of Shank family members: identification of a dendritic targeting element in the 3′ untranslated region of Shank1 mRNA.* Molecular and Cellular Neuroscience, 2004. **26**(1): p. 182-190.
161. Boeckers, T.M., et al., *Proline-rich synapse-associated proteins ProSAP1 and ProSAP2 interact with synaptic proteins of the SAPAP/GKAP family.* Biochemical and biophysical research communications, 1999. **264**(1): p. 247-252.
162. Leblond, C.S., et al., *Meta-analysis of SHANK mutations in autism spectrum disorders: a gradient of severity in cognitive impairments.* PLoS genetics, 2014. **10**(9): p. e1004580.
163. Sala, C., et al., *Shank synaptic scaffold proteins: keys to understanding the pathogenesis of autism and other synaptic disorders.* Journal of neurochemistry, 2015.
164. Hashimoto, K. and M. Kano, *Functional differentiation of multiple climbing fiber inputs during synapse elimination in the developing cerebellum.* Neuron, 2003. **38**(5): p. 785-96.
165. Schonewille, M., et al., *Purkinje cell-specific knockout of the protein phosphatase PP2B impairs potentiation and cerebellar motor learning.* Neuron, 2010. **67**(4): p. 618-628.

166. Wulff, P., et al., *Synaptic inhibition of Purkinje cells mediates consolidation of vestibulo-cerebellar motor learning.* Nature neuroscience, 2009. **12**(8): p. 1042-1049.
167. Häusser, M. and B.A. Clark, *Tonic synaptic inhibition modulates neuronal output pattern and spatiotemporal synaptic integration.* Neuron, 1997. **19**(3): p. 665-678.
168. Boeckers, T.M., et al., *Proline-rich synapse-associated protein-1/cortactin binding protein 1 (ProSAP1/CortBP1) is a PDZ-domain protein highly enriched in the postsynaptic density.* The Journal of neuroscience, 1999. **19**(15): p. 6506-6518.
169. Veloz, M.F.V., et al., *Cerebellar control of gait and interlimb coordination.* Brain Structure and Function, 2014: p. 1-24.
170. De Zeeuw, C.I. and M.M. Ten Brinke, *Motor Learning and the Cerebellum.* Cold Spring Harbor perspectives in biology, 2015. **7**(9): p. a021683.
171. Becker, E.B. and C.J. Stoodley, *Autism spectrum disorder and the cerebellum.* International review of neurobiology, 2013. **113**: p. 1.
172. Kloth, A.D., et al., *Cerebellar associative sensory learning defects in five mouse autism models.* eLife, 2015. **4**: p. e06085.
173. Jiang, Y.-h. and M.D. Ehlers, *Modeling Autism by< i> SHANK</i> Gene Mutations in Mice.* Neuron, 2013. **78**(1): p. 8-27.
174. De Zeeuw, C.I., et al., *Spatiotemporal firing patterns in the cerebellum.* Nature Reviews Neuroscience, 2011. **12**(6): p. 327-344.
175. van Alphen, A.M. and C.I. De Zeeuw, *Cerebellar LTD facilitates but is not essential for long-term adaptation of the vestibulo-ocular reflex.* Eur J Neurosci, 2002. **16**(3): p. 486-90.
176. Arons, M.H., et al., *Autism-associated mutations in ProSAP2/Shank3 impair synaptic transmission and neurexin-neuroligin-mediated transsynaptic signaling.* J Neurosci, 2012. **32**(43): p. 14966-78.
177. Szapiro, G. and B. Barbour, *Multiple climbing fibers signal to molecular layer interneurons exclusively via glutamate spillover.* Nat Neurosci, 2007. **10**(6): p. 735-42.
178. Badura, A., et al., *Climbing fiber input shapes reciprocity of Purkinje cell firing.* Neuron, 2013. **78**(4): p. 700-13.
179. Galliano, E., et al., *Silencing the majority of cerebellar granule cells uncovers their essential role in motor learning and consolidation.* Cell reports, 2013. **3**(4): p. 1239-1251.
180. Barski, J.J., K. Dethleffsen, and M. Meyer, *Cre recombinase expression in cerebellar Purkinje cells.* genesis, 2000. **28**(3-4): p. 93-98.
181. Schmidt-Supprian, M. and K. Rajewsky, *Vagaries of conditional gene targeting.* Nat Immunol, 2007. **8**(7): p. 665-8.
182. Kobayashi, Y. and T.K. Hensch, *Germline recombination by conditional gene targeting with Parvalbumin-Cre lines.* Front Neural Circuits, 2013. **7**: p. 168.
183. Mosconi, M.W., et al., *The role of cerebellar circuitry alterations in the pathophysiology of autism spectrum disorders.* Front Neurosci, 2015. **9**: p. 296.

184. Silva-Santos, S., et al., *Ube3a reinstatement identifies distinct developmental windows in a murine Angelman syndrome model.* J Clin Invest, 2015. **125**(5): p. 2069-76.
185. van Woerden, G.M., et al., *betaCaMKII controls the direction of plasticity at parallel fiber-Purkinje cell synapses.* Nat Neurosci, 2009. **12**(7): p. 823-5.
186. Galliano, E., et al., *Synaptic transmission and plasticity at inputs to murine cerebellar Purkinje cells are largely dispensable for standard nonmotor tasks.* J Neurosci, 2013. **33**(31): p. 12599-618.
187. Rochefort, C., et al., *Cerebellum shapes hippocampal spatial code.* Science, 2011. **334**(6054): p. 385-9.
188. Lai, C.S., et al., *A forkhead-domain gene is mutated in a severe speech and language disorder.* Nature, 2001. **413**: p. 519-23.
189. Vargha-Khadem, F., et al., *FOXP2 and the neuroanatomy of speech and language.* Nature reviews. Neuroscience, 2005. **6**: p. 131-138.
190. Watkins, K.E., N.F. Dronkers, and F. Vargha-Khadem, *Behavioural analysis of an inherited speech and language disorder: comparison with acquired aphasia.* Brain : a journal of neurology, 2002. **125**: p. 452-64.
191. Graham, S.A. and S.E. Fisher, *Understanding Language from a Genomic Perspective.* Annual review of genetics, 2015. **49**: p. 131-60.
192. Turner, S.J., et al., *Small intragenic deletion in FOXP2 associated with childhood apraxia of speech and dysarthria.* American journal of medical genetics. Part A, 2013. **161A**: p. 2321-6.
193. Reuter, M.S., et al., *FOXP2 variants in 14 individuals with developmental speech and language disorders broaden the mutational and clinical spectrum.* Journal of medical genetics, 2017. **54**: p. 64-72.
194. Morgan, A., et al., *FOXP2-Related Speech and Language Disorders.* GeneReviews(®), 1993.
195. Konopka, G., et al., *Human-specific transcriptional regulation of CNS development genes by FOXP2.* Nature, 2009. **462**: p. 213-217.
196. Spiteri, E., et al., *Identification of the transcriptional targets of FOXP2, a gene linked to speech and language, in developing human brain.* American journal of human genetics, 2007. **81**: p. 1144-1157.
197. Vernes, S.C., et al., *FOXP2 regulates gene networks implicated in neurite outgrowth in the developing brain.* PLoS Genetics, 2011. **7**.
198. Vernes, S.C., et al., *High-throughput analysis of promoter occupancy reveals direct neural targets of FOXP2, a gene mutated in speech and language disorders.* American journal of human genetics, 2007. **81**: p. 1232-1250.
199. Campbell, P., et al., *Conservation and diversity of Foxp2 expression in muroid rodents: Functional implications.* Journal of Comparative Neurology, 2009. **512**: p. 84-100.
200. Haesler, S., et al., *FoxP2 expression in avian vocal learners and non-learners.* The Journal of neuroscience : the official journal of the Society for Neuroscience, 2004. **24**: p. 3164-3175.

201. Lai, C.S.L., et al., *FOXP2 expression during brain development coincides with adult sites of pathology in a severe speech and language disorder.* Brain, 2003. **126**: p. 2455-2462.
202. Liégeois, F., et al., *Language fMRI abnormalities associated with FOXP2 gene mutation.* Nature neuroscience, 2003. **6**: p. 1230-1237.
203. French, C.A. and S.E. Fisher, *What can mice tell us about Foxp2 function?* Curr Opin Neurobiol, 2014. **28**: p. 72-9.
204. Wohlgemuth, S., I. Adam, and C. Scharff, *FoxP2 in songbirds.* Current Opinion in Neurobiology, 2014. **28**: p. 86-93.
205. French, C.A., et al., *Generation of mice with a conditional Foxp2 null allele.* Genesis (New York, N.Y. : 2000), 2007. **45**: p. 440-6.
206. Groszer, M., et al., *Impaired synaptic plasticity and motor learning in mice with a point mutation implicated in human speech deficits.* Curr Biol, 2008. **18**(5): p. 354-62.
207. Shu, W., et al., *Altered ultrasonic vocalization in mice with a disruption in the Foxp2 gene.* Proceedings of the National Academy of Sciences of the United States of America, 2005. **102**: p. 9643-9648.
208. Chabout, J., et al., *A Foxp2 Mutation Implicated in Human Speech Deficits Alters Sequencing of Ultrasonic Vocalizations in Adult Male Mice.* Frontiers in behavioral neuroscience, 2016. **10**: p. 197.
209. Haesler, S., et al., *Incomplete and inaccurate vocal imitation after knockdown of FoxP2 in songbird basal ganglia nucleus area X.* PLoS Biology, 2007. **5**: p. 2885-2897.
210. Murugan, M., et al., *Diminished FoxP2 levels affect dopaminergic modulation of corticostriatal signaling important to song variability.* Neuron, 2013. **80**: p. 1464-1476.
211. Usui, N., et al., *Sumoylation of FOXP2 Regulates Motor Function and Vocal Communication Through Purkinje Cell Development.* Biological Psychiatry, 2017. **81**: p. 220-230.
212. Graybiel, A.M., *The basal ganglia and chunking of action repertoires.* Neurobiology of learning and memory, 1998. **70**: p. 119-36.
213. Vinueza Veloz, M.F., et al., *Cerebellar control of gait and interlimb coordination.* Brain Structure and Function, 2015. **220**: p. 3513-3536.
214. Penhune, V.B. and C.J. Steele, *Parallel contributions of cerebellar, striatal and M1 mechanisms to motor sequence learning.* Behavioural brain research, 2012. **226**: p. 579-91.
215. Watkins, K.E., et al., *MRI analysis of an inherited speech and language disorder: structural brain abnormalities.* Brain : a journal of neurology, 2002. **125**: p. 465-78.
216. Ito-Ishida, A., et al., *Loss of MeCP2 in Parvalbumin-and Somatostatin-Expressing Neurons in Mice Leads to Distinct Rett Syndrome-like Phenotypes.* Neuron, 2015. **88**: p. 651-658.
217. Marino, S., et al., *PTEN is essential for cell migration but not for fate determination and tumourigenesis in the cerebellum.* Development (Cambridge, England), 2002. **129**: p. 3513-3522.

218. Dang, M.T., et al., *Disrupted motor learning and long-term synaptic plasticity in mice lacking NMDAR1 in the striatum.* Proceedings of the National Academy of Sciences of the United States of America, 2006. **103**: p. 15254-9.
219. Gorski, J.A., et al., *Cortical excitatory neurons and glia, but not GABAergic neurons, are produced in the Emx1-expressing lineage.* The Journal of neuroscience : the official journal of the Society for Neuroscience, 2002. **22**: p. 6309-6314.
220. Jin, X. and R.M. Costa, *Start/stop signals emerge in nigrostriatal circuits during sequence learning.* Nature, 2010. **466**: p. 457-462.
221. Hoogland, T.M., et al., *Role of synchronous activation of cerebellar Purkinje cell ensembles in multi-joint movement control.* Current biology : CB, 2015. **25**: p. 1157-65.
222. E.R. Kandel, Y.D., M.R. Mayford, *Learning and Memory. A Cold Spring Harbor Perspectives in Biology Collection.* 2016.
223. ten Brinke, Michiel M., et al., *Evolving Models of Pavlovian Conditioning: Cerebellar Cortical Dynamics in Awake Behaving Mice.* Cell Reports, 2015. **13**: p. 1977-1988.
224. Cullen, K.E. and J.X. Brooks, *Neural Correlates of Sensory Prediction Errors in Monkeys: Evidence for Internal Models of Voluntary Self-Motion in the Cerebellum.* The Cerebellum, 2015. **14**: p. 31-34.
225. Tian, J., et al., *Changes in Spontaneous Firing Patterns of Cerebellar Purkinje Cells in p75 Knockout Mice.* The Cerebellum, 2013. **12**: p. 300-303.
226. Tian, J., et al., *p75 Regulates Purkinje Cell Firing by Modulating SK Channel Activity through Rac1.* Journal of Biological Chemistry, 2014. **289**: p. 31458-31472.
227. Costa, R.M., *A selectionist account of de novo action learning.* Current Opinion in Neurobiology, 2011. **21**: p. 579-586.
228. Leblois, A., *Social modulation of learned behavior by dopamine in the basal ganglia: insights from songbirds.* Journal of physiology, Paris, 2013. **107**: p. 219-29.
229. Sasaki, A., et al., *Social context-dependent singing-regulated dopamine.* The Journal of neuroscience : the official journal of the Society for Neuroscience, 2006. **26**: p. 9010-4.
230. Leblois, A. and D.J. Perkel, *Striatal dopamine modulates song spectral but not temporal features through D1 receptors.* The European journal of neuroscience, 2012. **35**: p. 1771-81.
231. Schulz, S.B., et al., *Knockdown of FoxP2 alters spine density in Area X of the zebra finch.* Genes, Brain and Behavior, 2010. **9**: p. 732-740.
232. Yao, W.-D., R.D. Spealman, and J. Zhang, *Dopaminergic signaling in dendritic spines.* Biochemical pharmacology, 2008. **75**: p. 2055-69.
233. Heiman, M., et al., *A translational profiling approach for the molecular characterization of CNS cell types.* Cell, 2008. **135**: p. 738-48.
234. Enard, W., et al., *A humanized version of Foxp2 affects cortico-basal ganglia circuits in mice.* Cell, 2009. **137**: p. 961-971.

235. Costa, R.M., et al., *Rapid alterations in corticostriatal ensemble coordination during acute dopamine-dependent motor dysfunction.* Neuron, 2006. **52**: p. 359-69.
236. Pearce, T.M. and D.W. Moran, *Strategy-Dependent Encoding of Planned Arm Movements in the Dorsal Premotor Cortex.* Science, 2012. **337**: p. 984-988.
237. Shin, J.C. and R.B. Ivry, *Spatial and temporal sequence learning in patients with Parkinson's disease or cerebellar lesions.* Journal of cognitive neuroscience, 2003. **15**: p. 1232-43.
238. Aparicio, P., J. Diedrichsen, and R.B. Ivry, *Effects of focal basal ganglia lesions on timing and force control.* Brain and cognition, 2005. **58**: p. 62-74.
239. De Zeeuw, C.I., et al., *Expression of a protein kinase C inhibitor in Purkinje cells blocks cerebellar LTD and adaptation of the vestibulo-ocular reflex.* Neuron, 1998. **20**: p. 495-508.
240. Arriaga, G. and E.D. Jarvis, *Mouse vocal communication system: Are ultrasounds learned or innate?* Brain and Language, 2013. **124**: p. 96-116.
241. Wagner, M.J., et al., *Cerebellar granule cells encode the expectation of reward.* Nature, 2017.
242. De Smet, H.J., et al., *The cerebellum: Its role in language and related cognitive and affective functions.* Brain and Language, 2013. **127**: p. 334-342.
243. Mariën, P., K. van Dun, and J. Verhoeven, *Cerebellum and Apraxia.* The Cerebellum, 2014. **14**: p. 39-42.
244. Liégeois, F., et al., *Endophenotypes of FOXP2: Dysfunction within the human articulatory network.* European Journal of Paediatric Neurology, 2011. **15**: p. 283-288.
245. Greer, P.L. and M.E. Greenberg, *From synapse to nucleus: calcium-dependent gene transcription in the control of synapse development and function.* Neuron, 2008. **59**(6): p. 846-60.
246. Nabavi, S., et al., *Engineering a memory with LTD and LTP.* Nature, 2014. **511**(7509): p. 348-52.
247. Bliss, T.V. and T. Lomo, *Long-lasting potentiation of synaptic transmission in the dentate area of the anaesthetized rabbit following stimulation of the perforant path.* J Physiol, 1973. **232**(2): p. 331-56.
248. Greger, I.H., J.F. Watson, and S.G. Cull-Candy, *Structural and Functional Architecture of AMPA-Type Glutamate Receptors and Their Auxiliary Proteins.* Neuron, 2017. **94**(4): p. 713-730.
249. Pei, J. and N.V. Grishin, *Unexpected diversity in Shisa-like proteins suggests the importance of their roles as transmembrane adaptors.* Cell Signal, 2012. **24**(3): p. 758-69.
250. Huettner, J.E., *TARPs and AMPA Receptors: Function Follows Form.* Neuron, 2017. **93**(5): p. 989-991.
251. Klaassen, R.V., et al., *Shisa6 traps AMPA receptors at postsynaptic sites and prevents their desensitization during synaptic activity.* Nat Commun, 2016. **7**: p. 10682.
252. Farrow, P., et al., *Auxiliary subunits of the CKAMP family differentially modulate AMPA receptor properties.* Elife, 2015. **4**: p. e09693.

253. von Engelhardt, J., et al., *CKAMP44: a brain-specific protein attenuating short-term synaptic plasticity in the dentate gyrus.* Science, 2010. **327**(5972): p. 1518-22.
254. Schmitz, L.J.M., et al., *The AMPA receptor-associated protein Shisa7 regulates hippocampal synaptic function and contextual memory.* Elife, 2017. **6**.
255. Chen, X., et al., *CKAMP44 modulates integration of visual inputs in the lateral geniculate nucleus.* Nat Commun, 2018. **9**(1): p. 261.
256. Yamasaki, M., et al., *Glutamate receptor delta2 is essential for input pathway-dependent regulation of synaptic AMPAR contents in cerebellar Purkinje cells.* J Neurosci, 2011. **31**(9): p. 3362-74.
257. Kakegawa, W., K. Kohda, and M. Yuzaki, *The delta2 'ionotropic' glutamate receptor functions as a non-ionotropic receptor to control cerebellar synaptic plasticity.* J Physiol, 2007. **584**(Pt 1): p. 89-96.
258. Kohda, K., W. Kakegawa, and M. Yuzaki, *Unlocking the secrets of the delta2 glutamate receptor: A gatekeeper for synaptic plasticity in the cerebellum.* Commun Integr Biol, 2013. **6**(6): p. e26466.
259. Ichikawa, R., K. Sakimura, and M. Watanabe, *GluD2 Endows Parallel Fiber-Purkinje Cell Synapses with a High Regenerative Capacity.* J Neurosci, 2016. **36**(17): p. 4846-58.
260. Gonshor, A. and G.M. Jones, *Extreme vestibulo-ocular adaptation induced by prolonged optical reversal of vision.* J Physiol, 1976. **256**(2): p. 381-414.
261. Van Alphen, A.M., et al., *Motor performance and motor learning in Lurcher mice.* Ann N Y Acad Sci, 2002. **978**: p. 413-24.
262. Hashimoto, K., et al., *Impairment of AMPA receptor function in cerebellar granule cells of ataxic mutant mouse stargazer.* J Neurosci, 1999. **19**(14): p. 6027-36.
263. Chen, L., et al., *Stargazin regulates synaptic targeting of AMPA receptors by two distinct mechanisms.* Nature, 2000. **408**(6815): p. 936-43.
264. Tomita, S., et al., *Stargazin modulates AMPA receptor gating and trafficking by distinct domains.* Nature, 2005. **435**(7045): p. 1052-8.
265. Yamazaki, M., et al., *Relative contribution of TARPs gamma-2 and gamma-7 to cerebellar excitatory synaptic transmission and motor behavior.* Proc Natl Acad Sci U S A, 2015. **112**(4): p. E371-9.
266. Hirano, T., et al., *Suppression of LTD in cultured Purkinje cells deficient in the glutamate receptor delta 2 subunit.* Neuroreport, 1995. **6**(3): p. 524-6.
267. Yamashita, M., S.Y. Kawaguchi, and T. Hirano, *Contribution of postsynaptic GluD2 to presynaptic R-type Ca(2+) channel function, glutamate release and long-term potentiation at parallel fiber to Purkinje cell synapses.* Cerebellum, 2013. **12**(5): p. 657-66.
268. Heine, M., et al., *Surface mobility of postsynaptic AMPARs tunes synaptic transmission.* Science, 2008. **320**(5873): p. 201-5.
269. Makino, H. and R. Malinow, *Compartmentalized versus global synaptic plasticity on dendrites controlled by experience.* Neuron, 2011. **72**(6): p. 1001-11.
270. De Zeeuw, C.I., et al., *Expression of a protein kinase C inhibitor in Purkinje cells blocks cerebellar LTD and adaptation of the vestibulo-ocular reflex.* Neuron, 1998. **20**(3): p. 495-508.

271. Ito, M. and L. Karachot, *Protein kinases and phosphatase inhibitors mediating long-term desensitization of glutamate receptors in cerebellar Purkinje cells.* Neurosci Res, 1992. **14**(1): p. 27-38.
272. Nomura, T., et al., *Cerebellar long-term depression requires dephosphorylation of TARP in Purkinje cells.* Eur J Neurosci, 2012. **35**(3): p. 402-10.
273. van Beugen, B.J., et al., *High frequency burst firing of granule cells ensures transmission at the parallel fiber to purkinje cell synapse at the cost of temporal coding.* Front Neural Circuits, 2013. **7**: p. 95.
274. Ly, R., et al., *T-type channel blockade impairs long-term potentiation at the parallel fiber-Purkinje cell synapse and cerebellar learning.* Proc Natl Acad Sci U S A, 2013. **110**(50): p. 20302-7.
275. Wulff, P., et al., *Synaptic inhibition of Purkinje cells mediates consolidation of vestibulo-cerebellar motor learning.* Nat Neurosci, 2009. **12**(8): p. 1042-9.
276. Hoebeek, F.E., et al., *Increased noise level of purkinje cell activities minimizes impact of their modulation during sensorimotor control.* Neuron, 2005. **45**(6): p. 953-65.
277. Walter, J.T., et al., *Decreases in the precision of Purkinje cell pacemaking cause cerebellar dysfunction and ataxia.* Nat Neurosci, 2006. **9**(3): p. 389-97.
278. Nguyen-Vu, T.D., et al., *Cerebellar Purkinje cell activity drives motor learning.* Nat Neurosci, 2013. **16**(12): p. 1734-6.
279. Jirenhed, D.A., F. Bengtsson, and G. Hesslow, *Acquisition, extinction, and reacquisition of a cerebellar cortical memory trace.* J Neurosci, 2007. **27**(10): p. 2493-502.
280. Barski, J.J., K. Dethleffsen, and M. Meyer, *Cre recombinase expression in cerebellar Purkinje cells.* Genesis, 2000. **28**(3-4): p. 93-8.
281. Schindelin, J., et al., *Fiji: an open-source platform for biological-image analysis.* Nat Methods, 2012. **9**(7): p. 676-82.
282. Zhou, H., et al., *Differential Purkinje cell simple spike activity and pausing behavior related to cerebellar modules.* J Neurophysiol, 2015. **113**(7): p. 2524-36.
283. Cotman, C.W., D.T. Monaghan, and A.H. Ganong, *Excitatory amino acid neurotransmission: NMDA receptors and Hebb-type synaptic plasticity.* Annu Rev Neurosci, 1988. **11**: p. 61-80.
284. Gao, Z., B.J. van Beugen, and C.I. De Zeeuw, *Distributed synergistic plasticity and cerebellar learning.* Nat Rev Neurosci, 2012. **13**(9): p. 619-35.
285. Carey, M.R., *Synaptic mechanisms of sensorimotor learning in the cerebellum.* Curr Opin Neurobiol, 2011. **21**(4): p. 609-15.
286. Piochon, C., et al., *NMDA receptor contribution to the climbing fiber response in the adult mouse Purkinje cell.* J Neurosci, 2007. **27**(40): p. 10797-809.
287. Renzi, M., M. Farrant, and S.G. Cull-Candy, *Climbing-fibre activation of NMDA receptors in Purkinje cells of adult mice.* J Physiol, 2007. **585**(Pt 1): p. 91-101.
288. Bidoret, C., et al., *Presynaptic NR2A-containing NMDA receptors implement a high-pass filter synaptic plasticity rule.* Proc Natl Acad Sci U S A, 2009. **106**(33): p. 14126-31.
289. Bouvier, G., et al., *Burst-Dependent Bidirectional Plasticity in the Cerebellum Is Driven by Presynaptic NMDA Receptors.* Cell Rep, 2016. **15**(1): p. 104-16.

290. Nicoll, R.A. and R.C. Malenka, *Contrasting properties of two forms of long-term potentiation in the hippocampus.* Nature, 1995. **377**(6545): p. 115-8.
291. Monyer, H., et al., *Developmental and regional expression in the rat brain and functional properties of four NMDA receptors.* Neuron, 1994. **12**(3): p. 529-40.
292. Feldmeyer, D. and S. Cull-Candy, *Functional consequences of changes in NMDA receptor subunit expression during development.* J Neurocytol, 1996. **25**(12): p. 857-67.
293. Kakegawa, W., et al., *Functional NMDA receptor channels generated by NMDAR2B gene transfer in rat cerebellar Purkinje cells.* Eur J Neurosci, 2003. **17**(4): p. 887-91.
294. Wood, M.W., H.M. VanDongen, and A.M. VanDongen, *The 5'-untranslated region of the N-methyl-D-aspartate receptor NR2A subunit controls efficiency of translation.* J Biol Chem, 1996. **271**(14): p. 8115-20.
295. Di Liegro, C.M., G. Schiera, and I. Di Liegro, *Regulation of mRNA transport, localization and translation in the nervous system of mammals (Review).* Int J Mol Med, 2014. **33**(4): p. 747-62.
296. De Zeeuw, C.I. and M.M. Ten Brinke, *Motor Learning and the Cerebellum.* Cold Spring Harb Perspect Biol, 2015. **7**(9): p. a021683.
297. Voges, K., et al., *Mechanisms underlying vestibulo-cerebellar motor learning in mice depend on movement direction.* J Physiol, 2017.
298. Kessels, H.W., S. Nabavi, and R. Malinow, *Metabotropic NMDA receptor function is required for beta-amyloid-induced synaptic depression.* Proc Natl Acad Sci U S A, 2013. **110**(10): p. 4033-8.
299. Nabavi, S., et al., *Metabotropic NMDA receptor function is required for NMDA receptor-dependent long-term depression.* Proc Natl Acad Sci U S A, 2013. **110**(10): p. 4027-32.
300. Tovar, K.R. and G.L. Westbrook, *Modulating synaptic NMDA receptors.* Neuropharmacology, 2017. **112**(Pt A): p. 29-33.
301. Piochon, C., et al., *Purkinje cell NMDA receptors assume a key role in synaptic gain control in the mature cerebellum.* J Neurosci, 2010. **30**(45): p. 15330-5.
302. Wang, D.J., et al., *Long-term potentiation at cerebellar parallel fiber-Purkinje cell synapses requires presynaptic and postsynaptic signaling cascades.* Journal Neurosci., 2014. **34**(6): p. 2355-64.
303. Belmeguenai, A., et al., *Intrinsic plasticity complements long-term potentiation in parallel fiber input gain control in cerebellar Purkinje cells.* J Neurosci, 2010. **30**(41): p. 13630-43.
304. Ito, M., *Historical review of the significance of the cerebellum and the role of Purkinje cells in motor learning.* Ann N Y Acad Sci, 2002. **978**: p. 273-88.
305. Boyden, E.S., et al., *Selective engagement of plasticity mechanisms for motor memory storage.* Neuron, 2006. **51**(6): p. 823-34.
306. Badura, A., et al., *Modeled changes of cerebellar activity in mutant mice are predictive of their learning impairments.* Sci Rep, 2016. **6**: p. 36131.
307. Slemmer, J.E., C.I. De Zeeuw, and J.T. Weber, *Don't get too excited: mechanisms of glutamate-mediated Purkinje cell death.* Prog Brain Res, 2005. **148**: p. 367-90.

308. D'Angelo, E., et al., *Evidence for NMDA and mGlu receptor-dependent long-term potentiation of mossy fiber-granule cell transmission in rat cerebellum.* J Neurophysiol, 1999. **81**(1): p. 277-87.
309. Pugh, J.R. and I.M. Raman, *Potentiation of mossy fiber EPSCs in the cerebellar nuclei by NMDA receptor activation followed by postinhibitory rebound current.* Neuron, 2006. **51**(1): p. 113-23.
310. Bienenstock, E.L., L.N. Cooper, and P.W. Munro, *Theory for the development of neuron selectivity: orientation specificity and binocular interaction in visual cortex.* J Neurosci, 1982. **2**(1): p. 32-48.
311. Piochon, C., et al., *Calcium threshold shift enables frequency-independent control of plasticity by an instructive signal.* Proc Natl Acad Sci U S A. , 2016. **113**(46): p. 1091-6490.
312. Maher, B.J. and G.L. Westbrook, *SK channel regulation of dendritic excitability and dendrodendritic inhibition in the olfactory bulb.* J Neurophysiol, 2005. **94**(6): p. 3743-50.
313. Ichise, T., et al., *mGluR1 in cerebellar Purkinje cells essential for long-term depression, synapse elimination, and motor coordination.* Science, 2000. **288**(5472): p. 1832-5.
314. Galliano, E., et al., *Silencing the Majority of Cerebellar Granule Cells Uncovers Their Essential Role in Motor Learning and Consolidation.* Cell Reports, 2013.
315. De Zeeuw, C.I., et al., *Morphological correlates of bilateral synchrony in the rat cerebellar cortex.* J Neurosci, 1996. **16**(10): p. 3412-26.
316. Safo, P.K. and W.G. Regehr, *Endocannabinoids control the induction of cerebellar LTD.* Neuron, 2005. **48**(4): p. 647-59.
317. Stahl, J.S., A.M. van Alphen, and C.I. De Zeeuw, *A comparison of video and magnetic search coil recordings of mouse eye movements.* J Neurosci Methods, 2000. **99**(1-2): p. 101-10.
318. Freeman, J.H. and A.B. Steinmetz, *Neural circuitry and plasticity mechanisms underlying delay eyeblink conditioning.* Learn Mem, 2011. **18**(10): p. 666-77.
319. Mostofi, A., et al., *Electrophysiological localization of eyeblink-related microzones in rabbit cerebellar cortex.* J Neurosci, 2010. **30**(26): p. 8920-34.
320. Heiney, S.A., et al., *Precise control of movement kinematics by optogenetic inhibition of Purkinje cell activity.* J Neurosci, 2014. **34**(6): p. 2321-30.
321. Thurling, M., et al., *Cerebellar cortex and cerebellar nuclei are concomitantly activated during eyeblink conditioning: a 7T fMRI study in humans.* J Neurosci, 2015. **35**(3): p. 1228-39.
322. Steinmetz, A.B. and J.H. Freeman, *Localization of the cerebellar cortical zone mediating acquisition of eyeblink conditioning in rats.* Neurobiol Learn Mem, 2014. **114C**: p. 148-154.
323. Halverson, H.E., A. Khilkevich, and M.D. Mauk, *Relating cerebellar purkinje cell activity to the timing and amplitude of conditioned eyelid responses.* J Neurosci, 2015. **35**(20): p. 7813-32.
324. Hansel, C., D.J. Linden, and E. D'Angelo, *Beyond parallel fiber LTD: the diversity of synaptic and non-synaptic plasticity in the cerebellum.* Nat Neurosci, 2001. **4**(5):
p. 467-75.

325. Mauk, M.D. and D.V. Buonomano, *The neural basis of temporal processing.* Annu Rev Neurosci, 2004. **27**: p. 307-40.
326. Cerminara, N.L. and J.A. Rawson, *Evidence that climbing fibers control an intrinsic spike generator in cerebellar Purkinje cells.* J Neurosci, 2004. **24**(19): p. 4510-7.
327. Zhou, H., et al., *Cerebellar modules operate at different frequencies.* Elife, 2014. **3**: p. e02536.
328. Welsh, J.P., et al., *Normal motor learning during pharmacological prevention of Purkinje cell long-term depression.* Proc Natl Acad Sci U S A, 2005. **102**(47): p. 17166-71.
329. Mittmann, W., U. Koch, and M. Hausser, *Feed-forward inhibition shapes the spike output of cerebellar Purkinje cells.* J Physiol, 2005. **563**(Pt 2): p. 369-78.
330. Johansson, F., et al., *Memory trace and timing mechanism localized to cerebellar Purkinje cells.* Proc Natl Acad Sci U S A, 2014. **111**(41): p. 14930-4.
331. Steinberg, J.P., et al., *Targeted in vivo mutations of the AMPA receptor subunit GluR2 and its interacting protein PICK1 eliminate cerebellar long-term depression.* Neuron, 2006. **49**(6): p. 845-60.
332. Piochon, C., et al., *Cerebellar plasticity and motor learning deficits in a copy-number variation mouse model of autism.* Nat Commun, 2014. **5**: p. 5586.
333. Jirenhed, D.A., F. Bengtsson, and H. Jorntell, *Parallel fiber and climbing fiber responses in rat cerebellar cortical neurons in vivo.* Front Syst Neurosci, 2013. **7**: p. 16.
334. Yamaguchi, K., S. Itohara, and M. Ito, *Reassessment of long-term depression in cerebellar Purkinje cells in mice carrying mutated GluA2 C terminus.* Proc Natl Acad Sci U S A, 2016. **113**(36): p. 10192-7.
335. Gallistel, C.R., *The Coding Question.* Trends Cogn Sci, 2017. **21**(7): p. 498-508.
336. Xia, J., et al., *Cerebellar long-term depression requires PKC-regulated interactions between GluR2/3 and PDZ domain-containing proteins.* Neuron, 2000. **28**(2): p. 499-510.
337. Oberdick, J., et al., *A promoter that drives transgene expression in cerebellar Purkinje and retinal bipolar neurons.* Science, 1990. **248**(4952): p. 223-6.
338. Chettih, S.N., et al., *Adaptive timing of motor output in the mouse: the role of movement oscillations in eyelid conditioning.* Front Integr Neurosci, 2011. **5**: p. 72.
339. Koekkoek, S.K.E., et al., *Monitoring Kinetic and Frequency-Domain Properties of Eyelid Responses in Mice With Magnetic Distance Measurement Technique.* J Neurophysiol, 2002. **88**(4): p. 2124-2133.
340. Rivera, C., et al., *The K+/Cl-co-transporter KCC2 renders GABA hyperpolarizing during neuronal maturation.* Nature, 1999. **397**(6716): p. 251.
341. Glykys, J., et al., *Local impermeant anions establish the neuronal chloride concentration.* Science, 2014. **343**(6171): p. 670-675.
342. Ruffin, V.A., et al., *Intracellular pH regulation by acid-base transporters in mammalian neurons.* Frontiers in physiology, 2014. **5**.
343. Sangan, P., et al., *Cloning and expression of a chloride-dependent Na+-H+ exchanger.* Journal of Biological Chemistry, 2002. **277**(12): p. 9668-9675.

344. Deidda, G., I.F. Bozarth, and L. Cancedda, *Modulation of GABAergic transmission in development and neurodevelopmental disorders: investigating physiology and pathology to gain therapeutic perspectives.* Frontiers in cellular neuroscience, 2014. **8**.
345. Glykys, J., et al., *Chloride Dysregulation, Seizures, and Cerebral Edema: A Relationship with Therapeutic Potential.* Trends in Neurosciences, 2017.
346. Jentsch, T.J., *VRACs and other ion channels and transporters in the regulation of cell volume and beyond.* Nature Reviews Molecular Cell Biology, 2016. **17**(5): p. 293-307.
347. Branchereau, P., et al., *Depolarizing GABA/glycine synaptic events switch from excitation to inhibition during frequency increases.* Scientific reports, 2016. **6**.
348. Doyon, N., et al., *Chloride regulation: a dynamic equilibrium crucial for synaptic inhibition.* Neuron, 2016. **89**(6): p. 1157-1172.
349. Ben-Ari, Y., et al., *GABA: a pioneer transmitter that excites immature neurons and generates primitive oscillations.* Physiological reviews, 2007. **87**(4): p. 1215-1284.
350. Bormann, J., O.P. Hamill, and B. Sakmann, *Mechanism of anion permeation through channels gated by glycine and gamma-aminobutyric acid in mouse cultured spinal neurones.* The Journal of Physiology, 1987. **385**(1): p. 243-286.
351. Cohen, I., et al., *On the origin of interictal activity in human temporal lobe epilepsy in vitro.* Science, 2002. **298**(5597): p. 1418-1421.
352. Pizzarelli, R. and E. Cherubini, *Alterations of GABAergic signaling in autism spectrum disorders.* Neural plasticity, 2011. **2011**.
353. Vermeer, S., et al., *Targeted next-generation sequencing of a 12.5 Mb homozygous region reveals ANO10 mutations in patients with autosomal-recessive cerebellar ataxia.* The American Journal of Human Genetics, 2010. **87**(6): p. 813-819.
354. Jin, X., J.R. Huguenard, and D.A. Prince, *Impaired Cl− extrusion in layer V pyramidal neurons of chronically injured epileptogenic neocortex.* Journal of neurophysiology, 2005. **93**(4): p. 2117-2126.
355. Papp, E., et al., *Relationship between neuronal vulnerability and potassium-chloride cotransporter 2 immunoreactivity in hippocampus following transient forebrain ischemia.* Neuroscience, 2008. **154**(2): p. 677-689.
356. Galeffi, F., et al., *Changes in intracellular chloride after oxygen–glucose deprivation of the adult hippocampal slice: effect of diazepam.* Journal of Neuroscience, 2004. **24**(18): p. 4478-4488.
357. Pond, B.B., et al., *The chloride transporter Na+-K+-Cl− cotransporter isoform-1 contributes to intracellular chloride increases after in vitro ischemia.* Journal of Neuroscience, 2006. **26**(5): p. 1396-1406.
358. Hung, C. and J.W. Chen, *Treatment of post-traumatic epilepsy.* Current treatment options in neurology, 2012. **14**(4): p. 293-306.
359. Annegers, J.F., et al., *A population-based study of seizures after traumatic brain injuries.* New England Journal of Medicine, 1998. **338**(1): p. 20-24.
360. Rungta, R.L., et al., *The cellular mechanisms of neuronal swelling underlying cytotoxic edema.* Cell, 2015. **161**(3): p. 610-621.

361. Ben-Ari, Y., *NKCC1 Chloride Importer Antagonists Attenuate Many Neurological and Psychiatric Disorders.* Trends in Neurosciences, 2017. **40**(9): p. 536-554.
362. De Zeeuw, C., et al., *Ultrastructural study of the GABAergic, cerebellar, and mesodiencephalic innervation of the cat medial accessory olive: anterograde tracing combined with immunocytochemistry.* Journal of Comparative Neurology, 1989. **284**(1): p. 12-35.
363. Andersson, G., M. Garwicz, and G. Hesslow, *Evidence for a GABA-mediated cerebellar inhibition of the inferior olive in the cat.* Experimental brain research, 1988. **72**(3): p. 450-456.
364. Fredette, B.J. and E. Mugnaini, *The GABAergic cerebello-olivary projection in the rat.* Anatomy and embryology, 1991. **184**(3): p. 225-243.
365. Angaut, P. and C. Sotelo, *Synaptology of the cerebello-olivary pathway. Double labelling with anterograde axonal tracing and GABA immunocytochemistry in the rat.* Brain research, 1989. **479**(2): p. 361-365.
366. Lefler, Y., Y. Yarom, and M.Y. Uusisaari, *Cerebellar inhibitory input to the inferior olive decreases electrical coupling and blocks subthreshold oscillations.* Neuron, 2014. **81**(6): p. 1389-1400.
367. Ankri, L., et al., *A novel inhibitory nucleo-cortical circuit controls cerebellar Golgi cell activity.* Elife, 2015. **4**: p. e06262.
368. Szapiro, G. and B. Barbour, *Multiple climbing fibers signal to molecular layer interneurons exclusively via glutamate spillover.* Nature neuroscience, 2007. **10**(6): p. 735-742.
369. Bengtsson, F. and G. Hesslow, *Cerebellar control of the inferior olive.* The cerebellum, 2006. **5**(1): p. 7-14.
370. Seja, P., et al., *Raising cytosolic Cl− in cerebellar granule cells affects their excitability and vestibulo-ocular learning.* The EMBO journal, 2012. **31**(5): p. 1217-1230.
371. Rahmati, N., et al., *SLC26A11 (KBAT) in Purkinje cells is critical for inhibitory transmission and contributes to locomotor coordination.* eNeuro, 2016. **3**(3): p. ENEURO. 0028-16.2016.
372. Peter, S., et al., *Dysfunctional cerebellar Purkinje cells contribute to autism-like behaviour in Shank2-deficient mice.* Nature communications, 2016. **7**.
373. Wisden, W., et al., *Studying cerebellar circuits by remote control of selected neuronal types with GABAA receptors.* Frontiers in molecular neuroscience, 2009. **2**.
374. Zhang, Y., et al., *Inferior Olivary TMEM16B Mediates Cerebellar Motor Learning.* Neuron, 2017. **95**(5): p. 1103-1111. e4.
375. De Zeeuw, C.I., et al., *Spatiotemporal firing patterns in the cerebellum.* Nature reviews. Neuroscience, 2011. **12**(6): p. 327.
376. De Gruijl, J.R., et al., *Modulation of electrotonic coupling in the inferior olive by inhibitory and excitatory inputs: integration in the glomerulus.* Neuron, 2014. **81**(6): p. 1215-1217.
377. Jentsch, T.J., et al., *Molecular structure and physiological function of chloride channels.* Physiological reviews, 2002. **82**(2): p. 503-568.

378. Bi, M.M., et al., *Chloride channelopathies of ClC-2.* International journal of molecular sciences, 2013. **15**(1): p. 218-249.
379. Jentsch, T.J., *Discovery of CLC transport proteins: cloning, structure, function and pathophysiology.* The Journal of physiology, 2015. **593**(18): p. 4091-4109.
380. Jentsch, T.J., *CLC chloride channels and transporters: from genes to protein structure, pathology and physiology.* Critical reviews in biochemistry and molecular biology, 2008. **43**(1): p. 3-36.
381. Chen, T.T., et al., *Novel brain expression of ClC-1 chloride channels and enrichment of CLCN1 variants in epilepsy.* Neurology, 2013. **80**(12): p. 1078-1085.
382. Imbrici, P., et al., *ClC-1 chloride channels: state-of-the-art research and future challenges.* Frontiers in cellular neuroscience, 2015. **9**.
383. Lorenzetto, E., et al., *Genetic perturbation of postsynaptic activity regulates synapse elimination in developing cerebellum.* Proceedings of the National Academy of Sciences, 2009. **106**(38): p. 16475-16480.
384. Kros, L., et al., *Cerebellar output controls generalized spike-and-wave discharge occurrence.* Annals of neurology, 2015. **77**(6): p. 1027-1049.
385. Steinmeyer, K. and R. Klocke, *Inactivation of muscle chloride channel by transposon insertion in myotonic mice.* Nature, 1991. **354**(6351): p. 304.
386. Crepel, F., J. Mariani, and N. Delhaye-Bouchaud, *Evidence for a multiple innervation of Purkinje cells by climbing fibers in the immature rat cerebellum.* Developmental Neurobiology, 1976. **7**(6): p. 567-578.
387. Hashimoto, K. and M. Kano, *Postnatal development and synapse elimination of climbing fiber to Purkinje cell projection in the cerebellum.* Neuroscience research, 2005. **53**(3): p. 221-228.
388. Hashimoto, K., et al., *Postsynaptic P/Q-type Ca2+ channel in Purkinje cell mediates synaptic competition and elimination in developing cerebellum.* Proceedings of the National Academy of Sciences, 2011. **108**(24): p. 9987-9992.
389. Smith, R., et al., *Differential expression of an inwardly rectifying chloride conductance in rat brain neurons: a potential mechanism for cell-specific modulation of postsynaptic inhibition.* Journal of Neuroscience, 1995. **15**(5): p. 4057-4067.
390. Clayton, G.H., et al., *Developmental expression of ClC-2 in the rat nervous system.* Developmental brain research, 1998. **108**(1): p. 307-318.
391. Planells-Cases, R. and T.J. Jentsch, *Chloride channelopathies.* Biochimica et Biophysica Acta (BBA)-Molecular Basis of Disease, 2009. **1792**(3): p. 173-189.
392. Sık, A., R. Smith, and T. Freund, *Distribution of chloride channel-2-immunoreactive neuronal and astrocytic processes in the hippocampus.* Neuroscience, 2000. **101**(1): p. 51-65.
393. Blanz, J., et al., *Leukoencephalopathy upon disruption of the chloride channel ClC-2.* Journal of Neuroscience, 2007. **27**(24): p. 6581-6589.
394. Rinke, I., J. Artmann, and V. Stein, *ClC-2 voltage-gated channels constitute part of the background conductance and assist chloride extrusion.* Journal of Neuroscience, 2010. **30**(13): p. 4776-4786.

395. Weinreich, F. and T.J. Jentsch, *Pores formed by single subunits in mixed dimers of different CLC chloride channels.* Journal of Biological Chemistry, 2001. **276**(4): p. 2347-2353.
396. Staley, K., et al., *Alteration of GABA A receptor function following gene transfer of the CLC-2 chloride channel.* Neuron, 1996. **17**(3): p. 543-551.
397. Ge, Y.-X., et al., *ClC-2 contributes to tonic inhibition mediated by α5 subunit-containing GABA A receptor in experimental temporal lobe epilepsy.* Neuroscience, 2011. **186**: p. 120-127.
398. Ratté, S. and S.A. Prescott, *ClC-2 channels regulate neuronal excitability, not intracellular chloride levels.* Journal of Neuroscience, 2011. **31**(44): p. 15838-15843.
399. Madison, D.V., R.C. Malenka, and R.A. Nicoll, *Phorbol esters block a voltage-sensitive chloride current in hippocampal pyramidal cells.* Nature, 1986. **321**(6071): p. 695-697.
400. Kawasaki, M., et al., *Cloning and expression of a protein kinase C-regulated chloride channel abundantly expressed in rat brain neuronal cells.* Neuron, 1994. **12**(3): p. 597-604.
401. Borsani, G., et al., *Characterization of a human and murine gene (CLCN3) sharing similarities to voltage-gated chloride channels and to a yeast integral membrane protein.* Genomics, 1995. **27**(1): p. 131-141.
402. Stobrawa, S.M., et al., *Disruption of ClC-3, a chloride channel expressed on synaptic vesicles, leads to a loss of the hippocampus.* Neuron, 2001. **29**(1): p. 185-196.
403. Li, X., et al., *Biophysical properties of ClC-3 differentiate it from swelling-activated chloride channels in Chinese hamster ovary-K1 cells.* Journal of Biological Chemistry, 2000. **275**(46): p. 35994-35998.
404. Wang, X.Q., et al., *CLC-3 channels modulate excitatory synaptic transmission in hippocampal neurons.* Neuron, 2006. **52**(2): p. 321-333.
405. Farmer, L.M., B.N. Le, and D.J. Nelson, *CLC-3 chloride channels moderate long-term potentiation at Schaffer collateral–CA1 synapses.* The Journal of physiology, 2013. **591**(4): p. 1001-1015.
406. Greer, P.L. and M.E. Greenberg, *From synapse to nucleus: calcium-dependent gene transcription in the control of synapse development and function.* Neuron, 2008. **59**(6): p. 846-860.
407. Fakler, B. and J.P. Adelman, *Control of K Ca channels by calcium nano/microdomains.* Neuron, 2008. **59**(6): p. 873-881.
408. Picollo, A., M. Malvezzi, and A. Accardi, *TMEM16 proteins: unknown structure and confusing functions.* Journal of molecular biology, 2015. **427**(1): p. 94-105.
409. Suzuki, J., et al., *Calcium-dependent phospholipid scrambling by TMEM16F.* 2010.
410. Huang, Y., J.-J. Wang, and W.-H. Yung, *Coupling between GABA-A receptor and chloride transporter underlies ionic plasticity in cerebellar purkinje neurons.* The Cerebellum, 2013. **12**(3): p. 328-330.
411. Huang, F., et al., *TMEM16C facilitates Na+-activated K+ currents in rat sensory neurons and regulates pain processing.* Nature neuroscience, 2013. **16**(9): p. 1284-1290.

412. Duvvuri, U., et al., *TMEM16A induces MAPK and contributes directly to tumorigenesis and cancer progression.* Cancer research, 2012. **72**(13): p. 3270-3281.
413. Liu, W., et al., *Inhibition of Ca 2+-activated Cl– channel ANO1/TMEM16A expression suppresses tumor growth and invasiveness in human prostate carcinoma.* Cancer letters, 2012. **326**(1): p. 41-51.
414. Ubby, I., et al., *TMEM16A alternative splicing coordination in breast cancer.* Molecular cancer, 2013. **12**(1): p. 75.
415. Guan, L., et al., *Inhibition of calcium-activated chloride channel ANO1 suppresses proliferation and induces apoptosis of epithelium originated cancer cells.* Oncotarget, 2016. **7**(48): p. 78619.
416. Griffin, D.A., et al., *Defective membrane fusion and repair in Anoctamin5-deficient muscular dystrophy.* Human molecular genetics, 2016. **25**(10): p. 1900-1911.
417. Stephan, A.B., et al., *ANO2 is the cilial calcium-activated chloride channel that may mediate olfactory amplification.* Proceedings of the National Academy of Sciences, 2009. **106**(28): p. 11776-11781.
418. Cho, H., et al., *The calcium-activated chloride channel anoctamin 1 acts as a heat sensor in nociceptive neurons.* Nature neuroscience, 2012. **15**(7): p. 1015-1021.
419. Huang, W.C., et al., *Calcium-activated chloride channels (CaCCs) regulate action potential and synaptic response in hippocampal neurons.* Neuron, 2012. **74**(1): p. 179-192.
420. Pifferi, S., M. Dibattista, and A. Menini, *TMEM16B induces chloride currents activated by calcium in mammalian cells.* Pflügers Archiv-European Journal of Physiology, 2009. **458**(6): p. 1023-1038.
421. Grubb, S., et al., *TMEM16F (Anoctamin 6), an anion channel of delayed Ca 2+ activation.* The Journal of general physiology, 2013. **141**(5): p. 585-600.
422. Verkman, A.S. and L.J. Galietta, *Chloride channels as drug targets.* Nature reviews. Drug discovery, 2009. **8**(2): p. 153.
423. Jung, J., et al., *Dynamic modulation of ANO1/TMEM16A HCO3– permeability by Ca2+/calmodulin.* Proceedings of the National Academy of Sciences, 2013. **110**(1): p. 360-365.
424. Vocke, K., et al., *Calmodulin-dependent activation and inactivation of anoctamin calcium-gated chloride channels.* The Journal of general physiology, 2013. **142**(4): p. 381-404.
425. Jin, X., et al., *Activation of the Cl– channel ANO1 by localized calcium signals in nociceptive sensory neurons requires coupling with the IP3 receptor.* Science signaling, 2013. **6**(290): p. ra73.
426. Courjaret, R. and K. Machaca, *Mid-range Ca2+ signalling mediated by functional coupling between store-operated Ca2+ entry and IP3-dependent Ca2+ release.* Nature communications, 2014. **5**.
427. Ha, G.E., et al., *The Ca2+-activated chloride channel anoctamin-2 mediates spike-frequency adaptation and regulates sensory transmission in thalamocortical neurons.* Nature communications, 2016. **7**.

428. Llinas, R. and Y. Yarom, *Electrophysiology of mammalian inferior olivary neurones in vitro. Different types of voltage-dependent ionic conductances.* The Journal of physiology, 1981. **315**(1): p. 549-567.
429. Llinás, R. and Y. Yarom, *Properties and distribution of ionic conductances generating electroresponsiveness of mammalian inferior olivary neurones in vitro.* The Journal of Physiology, 1981. **315**(1): p. 569-584.
430. Zhang, W., et al., *Anoctamin calcium-activated chloride channels may modulate inhibitory transmission in the cerebellar cortex.* PloS one, 2015. **10**(11): p. e0142160.
431. Satoh, H., et al., *Depolarization-induced depression of inhibitory transmission in cerebellar Purkinje cells.* Physiological reports, 2013. **1**(3): p. e00061.
432. Neureither, F., et al., *Impaired Motor Coordination and Learning in Mice Lacking Anoctamin 2 Calcium-Gated Chloride Channels.* The Cerebellum, 2017: p. 1-9.
433. Alka, K. and J.R. Casey, *Bicarbonate transport in health and disease.* IUBMB life, 2014. **66**(9): p. 596-615.
434. Tombaugh, G.C. and G.G. Somjen, *Effects of extracellular pH on voltage-gated Na+, K+ and Ca2+ currents in isolated rat CA1 neurons.* The Journal of physiology, 1996. **493**(3): p. 719-732.
435. Balestrino, M. and G. Somjen, *Concentration of carbon dioxide, interstitial pH and synaptic transmission in hippocampal formation of the rat.* The Journal of Physiology, 1988. **396**(1): p. 247-266.
436. Majumdar, D. and M.O. Bevensee, *Na-coupled bicarbonate transporters of the solute carrier 4 family in the nervous system: function, localization, and relevance to neurologic function.* Neuroscience, 2010. **171**(4): p. 951-972.
437. Tang, C.-M., M. Dichter, and M. Morad, *Modulation of the N-methyl-D-aspartate channel by extracellular H+.* Proceedings of the National Academy of Sciences, 1990. **87**(16): p. 6445-6449.
438. Traynelis, S.F. and S.G. Cull-Candy, *Proton inhibition of N-methyl-D-aspartate receptors in cerebellar neurons.* Nature, 1990. **345**(6273): p. 347-350.
439. Hentschke, M., et al., *Mice with a targeted disruption of the Cl−/HCO3− exchanger AE3 display a reduced seizure threshold.* Molecular and Cellular Biology, 2006. **26**(1): p. 182-191.
440. Jacobs, S., et al., *Mice with targeted Slc4a10 gene disruption have small brain ventricles and show reduced neuronal excitability.* Proceedings of the National Academy of Sciences, 2008. **105**(1): p. 311-316.
441. Burette, A.C., et al., *The sodium-driven chloride/bicarbonate exchanger in presynaptic terminals.* Journal of Comparative Neurology, 2012. **520**(7): p. 1481-1492.
442. Chen, L.-M., et al., *Expression and localization of Na-driven Cl-HCO 3− exchanger (SLC4A8) in rodent CNS.* Neuroscience, 2008. **153**(1): p. 162-174.
443. Romero, M.F., et al., *The SLC4 family of bicarbonate transporters.* Molecular aspects of medicine, 2013. **34**(2): p. 159-182.
444. Sander, T., et al., *Association of the 867Asp variant of the human anion exchanger 3 gene with common subtypes of idiopathic generalized epilepsy.* Epilepsy research, 2002. **51**(3): p. 249-255.

445. Liu, Y., et al., *Expression and distribution of NBCn2 (Slc4a10) splice variants in mouse brain: Cloning of novel variant NBCn2-D.* Brain research, 2011. **1390**: p. 33-40.
446. Chesler, M. and K. Kaila, *Modulation of pH by neuronal activity.* Trends in neurosciences, 1992. **15**(10): p. 396-402.
447. Tong, C.-K. and M. Chesler, *Activity-evoked extracellular pH shifts in slices of rat dorsal lateral geniculate nucleus.* Brain research, 1999. **815**(2): p. 373-381.
448. Zhan, R.-Z., et al., *Intracellular acidification induced by membrane depolarization in rat hippocampal slices: roles of intracellular Ca 2+ and glycolysis.* Brain research, 1998. **780**(1): p. 86-94.
449. Allen, N.J. and D. Attwell, *Modulation of ASIC channels in rat cerebellar Purkinje neurons by ischaemia-related signals.* The Journal of physiology, 2002. **543**(2): p. 521-529.
450. Jovov, B., et al., *Immunolocalization of the acid-sensing ion channel 2a in the rat cerebellum.* Histochemistry and cell biology, 2003. **119**(6): p. 437-446.
451. Rahmati, N., et al., *Slc26a11 is prominently expressed in the brain and functions as a chloride channel: expression in Purkinje cells and stimulation of V H+-ATPase.* Pflügers Archiv-European Journal of Physiology, 2013. **465**(11): p. 1583-1597.
452. Soleimani, M., *SLC26 Cl-/HCO3-exchangers in the kidney: roles in health and disease.* Kidney international, 2013. **84**(4): p. 657-666.
453. Everett, L.A., et al., *Pendred syndrome is caused by mutations in a putative sulphate transporter gene (PDS).* Nature genetics, 1997. **17**(4): p. 411-422.
454. Hästbacka, J., et al., *The diastrophic dysplasia gene encodes a novel sulfate transporter: positional cloning by fine-structure linkage disequilibrium mapping.* Cell, 1994. **78**(6): p. 1073-1087.
455. Kim, K.H., et al., *SLC26A7 is a Cl–channel regulated by intracellular pH.* Journal of Biological Chemistry, 2005. **280**(8): p. 6463-6470.
456. Petrovic, S., et al., *SLC26A7: a basolateral Cl-/HCO 3-exchanger specific to intercalated cells of the outer medullary collecting duct.* American Journal of Physiology-Renal Physiology, 2004. **286**(1): p. F161-F169.
457. Petrovic, S., et al., *Identification of a basolateral Cl−/HCO 3− exchanger specific to gastric parietal cells.* American Journal of Physiology-Gastrointestinal and Liver Physiology, 2003. **284**(6): p. G1093-G1103.
458. Rahmati, N., *The Role of Chloride Homeostasis in the Olivocerebellar System.* 2015.
459. Xu, J., et al., *Slc26a11, a chloride transporter, localizes with the vacuolar H+-ATPase of A-intercalated cells of the kidney.* Kidney international, 2011. **80**(9): p. 926-937.
460. Hebert, S.C., D.B. Mount, and G. Gamba, *Molecular physiology of cation-coupled Cl − cotransport: the SLC12 family.* Pflügers Archiv, 2004. **447**(5): p. 580-593.
461. Kawakita, I., et al., *Type 2 K+−Cl− cotransporter is preferentially recruited to climbing fiber synapses during development and the stellate cell-targeting dendritic zone at adulthood in cerebellar Purkinje cells.* European Journal of Neuroscience, 2013. **37**(4): p. 532-543.

462. Takayama, C. and Y. Inoue, *Developmental localization of potassium chloride co-transporter 2 (KCC2) in the Purkinje cells of embryonic mouse cerebellum.* Neuroscience research, 2007. **57**(2): p. 322-325.
463. Plotkin, M., et al., *Expression of the Na-K-2Cl cotransporter is developmentally regulated in postnatal rat brains: a possible mechanism underlying GABA's excitatory role in immature brain.* Journal of neurobiology, 1997. **33**(6): p. 781-795.
464. Dzhala, V.I., et al., *NKCC1 transporter facilitates seizures in the developing brain.* Nature medicine, 2005. **11**(11): p. 1205.
465. Stein, V., et al., *Expression of the KCl cotransporter KCC2 parallels neuronal maturation and the emergence of low intracellular chloride.* Journal of Comparative Neurology, 2004. **468**(1): p. 57-64.
466. Lu, J., M. Karadsheh, and E. Delpire, *Developmental regulation of the neuronal-specific isoform of K-Cl cotransporter KCC2 in postnatal rat brains.* Developmental Neurobiology, 1999. **39**(4): p. 558-568.
467. Sedmak, G., et al., *Developmental expression patterns of KCC2 and functionally associated molecules in the human brain.* Cerebral Cortex, 2016. **26**(12): p. 4574-4589.
468. Friedel, P., et al., *WNK1-regulated inhibitory phosphorylation of the KCC2 cotransporter maintains the depolarizing action of GABA in immature neurons.* Sci Signal, 2015. **8**(383): p. ra65.
469. Rinehart, J., et al., *Sites of regulated phosphorylation that control K-Cl cotransporter activity.* Cell, 2009. **138**(3): p. 525-536.
470. Zeuthen, T., *Water-transporting proteins.* Journal of Membrane Biology, 2010. **234**(2): p. 57-73.
471. Jourdain, P., et al., *Determination of transmembrane water fluxes in neurons elicited by glutamate ionotropic receptors and by the cotransporters KCC2 and NKCC1: a digital holographic microscopy study.* Journal of Neuroscience, 2011. **31**(33): p. 11846-11854.
472. MacAulay, N., S. Hamann, and T. Zeuthen, *Water transport in the brain: role of cotransporters.* Neuroscience, 2004. **129**(4): p. 1029-1042.
473. Dzhala, V.I., A.C. Brumback, and K.J. Staley, *Bumetanide enhances phenobarbital efficacy in a neonatal seizure model.* Annals of neurology, 2008. **63**(2): p. 222-235.
474. Kahle, K.T., et al., *Decreased seizure activity in a human neonate treated with bumetanide, an inhibitor of the Na+-K+-2Cl-cotransporter NKCC1.* Journal of child neurology, 2009. **24**(5): p. 572-576.
475. Mikawa, S., et al., *Developmental changes in KCC1, KCC2 and NKCC1 mRNAs in the rat cerebellum.* Developmental brain research, 2002. **136**(2): p. 93-100.
476. Kanaka, C., et al., *The differential expression patterns of messenger RNAs encoding K-Cl cotransporters (KCC1, 2) and Na-K-2Cl cotransporter (NKCC1) in the rat nervous system.* Neuroscience, 2001. **104**(4): p. 933-946.
477. Brumback, A.C. and K.J. Staley, *Thermodynamic regulation of NKCC1-mediated Cl − cotransport underlies plasticity of GABAA signaling in neonatal neurons.* Journal of Neuroscience, 2008. **28**(6): p. 1301-1312.

478. Evans, R.L., et al., *Severe impairment of salivation in Na+/K+/2Cl– cotransporter (NKCC1)-deficient mice.* Journal of Biological Chemistry, 2000. **275**(35): p. 26720-26726.
479. Delpire, E., et al., *Deafness and imbalance associated with inactivation of the secretory Na-K-2Cl co-transporter.* Nature genetics, 1999. **22**(2).
480. Sung, K.-W., et al., *Abnormal GABAA receptor-mediated currents in dorsal root ganglion neurons isolated from Na–K–2Cl cotransporter null mice.* Journal of Neuroscience, 2000. **20**(20): p. 7531-7538.
481. Dixon, M.J., et al., *Mutation of the Na-K-Cl co-transporter gene Slc12a2 results in deafness in mice.* Human molecular genetics, 1999. **8**(8): p. 1579-1584.
482. Pace, A.J., et al., *Failure of spermatogenesis in mouse lines deficient in the Na+-K+-2Cl–cotransporter.* Journal of Clinical Investigation, 2000. **105**(4): p. 441.
483. Li, H., et al., *Patterns of cation-chloride cotransporter expression during embryonic rodent CNS development.* European Journal of Neuroscience, 2002. **16**(12): p. 2358-2370.
484. Hübner, C.A., D.E. Lorke, and I. Hermans-Borgmeyer, *Expression of the Na-K-2Cl-cotransporter NKCC1 during mouse development.* Mechanisms of development, 2001. **102**(1): p. 267-269.
485. Russell, J.M., *Sodium-potassium-chloride cotransport.* Physiological Reviews, 2000. **80**(1): p. 211-276.
486. Friedrich, B., I. Matskevich, and F. Lang, *Cell volume regulatory mechanisms*, in *Mechanisms and Significance of Cell Volume Regulation*. 2006, Karger Publishers. p. 1-8.
487. Haas, M., *The Na-K-Cl cotransporters.* American Journal of Physiology-Cell Physiology, 1994. **267**(4): p. C869-C885.
488. Lytle, C., *Activation of the avian erythrocyte Na-K-Cl cotransport protein by cell shrinkage, cAMP, fluoride, and calyculin-A involves phosphorylation at common sites.* Journal of Biological Chemistry, 1997. **272**(24): p. 15069-15077.
489. Payne, J.A., et al., *Cation–chloride co-transporters in neuronal communication, development and trauma.* Trends in neurosciences, 2003. **26**(4): p. 199-206.
490. Kahle, K.T., et al., *K-Cl cotransporters, cell volume homeostasis, and neurological disease.* Trends in molecular medicine, 2015. **21**(8): p. 513-523.
491. Song, L., et al., *Molecular, functional, and genomic characterization of human KCC2, the neuronal K–Cl cotransporter.* Molecular brain research, 2002. **103**(1): p. 91-105.
492. Williams, J.R., et al., *The neuron-specific K-Cl cotransporter, KCC2 antibody development and initial characterization of the protein.* Journal of Biological Chemistry, 1999. **274**(18): p. 12656-12664.
493. Pearson, M., et al., *Localization of the K+–Cl– cotransporter, KCC3, in the central and peripheral nervous systems: expression in the choroid plexus, large neurons and white matter tracts.* Neuroscience, 2001. **103**(2): p. 481-491.
494. Boettger, T., et al., *Loss of K-Cl co-transporter KCC3 causes deafness, neurodegeneration and reduced seizure threshold.* The EMBO journal, 2003. **22**(20): p. 5422-5434.

495. Brock, L., J. Coombs, and J. Eccles. *Action potentials of motoneurones with intracellular electrode*. in *Proc. Univ. Otago Med. Sch*. 1951.
496. Farrant, M. and K. Kaila, *The cellular, molecular and ionic basis of GABA A receptor signalling.* Progress in brain research, 2007. **160**: p. 59-87.
497. McBain, C.J. and A. Fisahn, *Interneurons unbound.* Nature reviews. Neuroscience, 2001. **2**(1): p. 11.
498. Whittington, M.A. and R.D. Traub, *Interneuron diversity series: inhibitory interneurons and network oscillations in vitro.* Trends in neurosciences, 2003. **26**(12): p. 676-682.
499. Staley, K., *Carts, Horses, and Push-Pull Regulation of EGABA in Neonatal Seizures.* Epilepsy currents, 2011. **11**(6): p. 205-208.
500. Kaila, K. and J. Voipio, *Postsynaptic fall in intracellular pH induced by GABA-activated bicarbonate conductance.* Nature, 1987. **330**(6144): p. 163-165.
501. Carlson, B.X., L. Elster, and A. Schousboe, *Pharmacological and functional implications of developmentally-regulated changes in GABA A receptor subunit expression in the cerebellum.* European journal of pharmacology, 1998. **352**(1): p. 1-14.
502. Sigel, E. and M.E. Steinmann, *Structure, function, and modulation of GABAA receptors.* Journal of Biological Chemistry, 2012. **287**(48): p. 40224-40231.
503. Succol, F., et al., *Intracellular chloride concentration influences the GABAA receptor subunit composition.* Nature communications, 2012. **3**: p. 738.
504. Ortinski, P.I., et al., *Expression of distinct α subunits of GABA A receptor regulates inhibitory synaptic strength.* Journal of neurophysiology, 2004. **92**(3): p. 1718-1727.
505. Wisden, W., *Structure and distribution of multiple GABAA receptor subunits with special reference to the cerebellum.* Annals of the New York Academy of Sciences, 1995. **757**(1): p. 506-515.
506. Angelotti, T. and R. Macdonald, *Assembly of GABAA receptor subunits: alpha 1 beta 1 and alpha 1 beta 1 gamma 2S subunits produce unique ion channels with dissimilar single-channel properties.* Journal of Neuroscience, 1993. **13**(4): p. 1429-1440.
507. Porter, N.M., et al., *Kinetic properties of alpha 1 beta 1 gamma-aminobutyric acidA receptor channels expressed in Chinese hamster ovary cells: regulation by pentobarbital and picrotoxin.* Molecular pharmacology, 1992. **42**(5): p. 872-881.
508. Verdoorn, T.A., et al., *Functional properties of recombinant rat GABA A receptors depend upon subunit composition.* Neuron, 1990. **4**(6): p. 919-928.
509. Farrant, M. and Z. Nusser, *Variations on an inhibitory theme: phasic and tonic activation of GABAA receptors.* Nature reviews. Neuroscience, 2005. **6**(3): p. 215.
510. Pirker, S., et al., *GABA A receptors: immunocytochemical distribution of 13 subunits in the adult rat brain.* Neuroscience, 2000. **101**(4): p. 815-850.
511. Schweizer, C., et al., *The γ2 subunit of GABAA receptors is required for maintenance of receptors at mature synapses.* Molecular and Cellular Neuroscience, 2003. **24**(2): p. 442-450.
512. Brickley, S.G. and I. Mody, *Extrasynaptic GABAA receptors: their function in the CNS and implications for disease.* Neuron, 2012. **73**(1): p. 23-34.

513. Brickley, S.G., et al., *The contribution of δ subunit-containing GABAA receptors to phasic and tonic conductance changes in cerebellum, thalamus and neocortex.* Frontiers in neural circuits, 2013. **7**: p. 203.
514. Rossi, D.J. and M. Hamann, *Spillover-mediated transmission at inhibitory synapses promoted by high affinity α6 subunit GABAA receptors and glomerular geometry.* Neuron, 1998. **20**(4): p. 783-795.
515. Mitchell, S.J. and R.A. Silver, *GABA spillover from single inhibitory axons suppresses low-frequency excitatory transmission at the cerebellar glomerulus.* Journal of Neuroscience, 2000. **20**(23): p. 8651-8658.
516. Sieghart, W. and G. Sperk, *Subunit composition, distribution and function of GABA-A receptor subtypes.* Current topics in medicinal chemistry, 2002. **2**(8): p. 795-816.
517. Laurie, D.J., P. Seeburg, and W. Wisden, *The distribution of 13 GABAA receptor subunit mRNAs in the rat brain. II. Olfactory bulb and cerebellum.* Journal of Neuroscience, 1992. **12**(3): p. 1063-1076.
518. Gonzalez-Burgos, G., K.N. Fish, and D.A. Lewis, *GABA neuron alterations, cortical circuit dysfunction and cognitive deficits in schizophrenia.* Neural plasticity, 2011. **2011**.
519. Hoebeek, F.E., et al., *Differential olivo-cerebellar cortical control of rebound activity in the cerebellar nuclei.* Proceedings of the National Academy of Sciences, 2010. **107**(18): p. 8410-8415.
520. Person, A.L. and I.M. Raman, *Purkinje neuron synchrony elicits time-locked spiking in the cerebellar nuclei.* Nature, 2012. **481**(7382): p. 502-505.
521. Buzsáki, G. and X.-J. Wang, *Mechanisms of gamma oscillations.* Annual review of neuroscience, 2012. **35**: p. 203-225.
522. Veloz, M.F.V., et al., *Cerebellar control of gait and interlimb coordination.* Brain Structure and Function, 2015. **220**(6): p. 3513-3536.
523. Watanabe, D., et al., *Ablation of cerebellar Golgi cells disrupts synaptic integration involving GABA inhibition and NMDA receptor activation in motor coordination.* Cell, 1998. **95**(1): p. 17-27.
524. Bazzigaluppi, P., et al., *Olivary subthreshold oscillations and burst activity revisited.* Frontiers in neural circuits, 2012. **6**.
525. De Gruijl, J.R., et al., *Climbing fiber burst size and olivary sub-threshold oscillations in a network setting.* PLoS computational biology, 2012. **8**(12): p. e1002814.
526. Kano, M., et al., *Synaptic excitation produces a long-lasting rebound potentiation of inhibitory synaptic signals in cerebellar Purkinje cells.* Nature, 1992. **356**(6370): p. 601-604.
527. Hirano, T. and S.-y. Kawaguchi, *Regulation and functional roles of rebound potentiation at cerebellar stellate cell—Purkinje cell synapses.* Frontiers in cellular neuroscience, 2014. **8**.
528. Ito, M., *The cerebellum: brain for an implicit self.* 2012: FT press.
529. Gao, Z., B.J. Van Beugen, and C.I. De Zeeuw, *Distributed synergistic plasticity and cerebellar learning.* Nature reviews. Neuroscience, 2012. **13**(9): p. 619.

530. Curtis, D., et al., *The hyperpolarization of spinal motoneurones by glycine and related amino acids.* Experimental Brain Research, 1968. **5**(3): p. 235-258.
531. Werman, R., R. Davidoff, and M. Aprison, *Inhibitory of glycine on spinal neurons in the cat.* Journal of Neurophysiology, 1968. **31**(1): p. 81-95.
532. Zarbin, M.A., J.K. Wamsley, and M.J. Kuhar, *Glycine receptor: light microscopic autoradiographic localization with [3H] strychnine.* Journal of Neuroscience, 1981. **1**(5): p. 532-547.
533. Ye, J.-H., *Regulation of excitation by glycine receptors*, in *Inhibitory Regulation of Excitatory Neurotransmission*. 2007, Springer. p. 123-143.
534. Flint, A.C., X. Liu, and A.R. Kriegstein, *Nonsynaptic glycine receptor activation during early neocortical development.* Neuron, 1998. **20**(1): p. 43-53.
535. Ye, J.H., et al., *Inhibitory effect of ondansetron on glycine response of dissociated rat hippocampal neurons.* Journal of Pharmacology and Experimental Therapeutics, 1999. **290**(1): p. 104-111.
536. Chattipakorn, S.C. and L.L. McMahon, *Pharmacological characterization of glycine-gated chloride currents recorded in rat hippocampal slices.* Journal of neurophysiology, 2002. **87**(3): p. 1515-1525.
537. McCool, B.A. and S.K. Botting, *Characterization of strychnine-sensitive glycine receptors in acutely isolated adult rat basolateral amygdala neurons.* Brain research, 2000. **859**(2): p. 341-351.
538. Mangin, J., et al., *Functional glycine receptor maturation in the absence of glycinergic input in dopaminergic neurones of the rat substantia nigra.* The Journal of physiology, 2002. **542**(3): p. 685-697.
539. Gaiarsa, J.-L., O. Caillard, and Y. Ben-Ari, *Long-term plasticity at GABAergic and glycinergic synapses: mechanisms and functional significance.* Trends in neurosciences, 2002. **25**(11): p. 564-570.
540. Lynch, J.W., *Molecular structure and function of the glycine receptor chloride channel.* Physiological reviews, 2004. **84**(4): p. 1051-1095.
541. Grudzinska, J., et al., *The β subunit determines the ligand binding properties of synaptic glycine receptors.* Neuron, 2005. **45**(5): p. 727-739.
542. Becker, C.-M., W. Hoch, and H. Betz, *Glycine receptor heterogeneity in rat spinal cord during postnatal development.* The EMBO Journal, 1988. **7**(12): p. 3717.
543. Dumoulin, A., A. Triller, and S. Dieudonné, *IPSC kinetics at identified GABAergic and mixed GABAergic and glycinergic synapses onto cerebellar Golgi cells.* Journal of Neuroscience, 2001. **21**(16): p. 6045-6057.
544. Chan-Palay, V., *The cerebellar dentate nucleus*, in *Cerebellar Dentate Nucleus*. 1977, Springer. p. 1-24.
545. Zeeuw, C. and A. Berrebi, *Postsynaptic targets of Purkinje cell terminals in the cerebellar and vestibular nuclei of the rat.* European Journal of Neuroscience, 1995. **7**(11): p. 2322-2333.
546. Husson, Z., et al., *Differential GABAergic and glycinergic inputs of inhibitory interneurons and purkinje cells to principal cells of the cerebellar nuclei.* Journal of Neuroscience, 2014. **34**(28): p. 9418-9431.
547. Bagnall, M.W., et al., *Glycinergic projection neurons of the cerebellum.* Journal of Neuroscience, 2009. **29**(32): p. 10104-10110.

548. Shiang, R., et al., *Mutations in the α1 subunit of the inhibitory glycine receptor cause the dominant neurologic disorder, hyperekplexia.* Nature genetics, 1993. **5**(4): p. 351-358.
549. Kawa, K., *Glycine facilitates transmitter release at developing synapses: a patch clamp study from Purkinje neurons of the newborn rat.* Developmental brain research, 2003. **144**(1): p. 57-71.
550. Dehnes, Y., et al., *The glutamate transporter EAAT4 in rat cerebellar Purkinje cells: a glutamate-gated chloride channel concentrated near the synapse in parts of the dendritic membrane facing astroglia.* Journal of Neuroscience, 1998. **18**(10): p. 3606-3619.
551. Robinson, M.B. and L.A. Dowd, *Heterogeneity and functional properties of subtypes of sodium-dependent glutamate transporters in the mammalian central nervous system.* Advances in pharmacology, 1996. **37**: p. 69-115.
552. Fairman, W., et al., *An excitatory amino-acid transporter with properties of a ligand-gated chloride channel.* Nature, 1995. **375**(6532): p. 599.
553. Wadiche, J.I., S.G. Amara, and M.P. Kavanaugh, *Ion fluxes associated with excitatory amino acid transport.* Neuron, 1995. **15**(3): p. 721-728.
554. Nagao, S., S. Kwak, and I. Kanazawa, *EAAT4, a glutamate transporter with properties of a chloride channel, is predominantly localized in Purkinje cell dendrites, and forms parasagittal compartments in rat cerebellum.* Neuroscience, 1997. **78**(4): p. 929-933.
555. Brochu, G., L. Maler, and R. Hawkes, *Zebrin II: a polypeptide antigen expressed selectively by Purkinje cells reveals compartments in rat and fish cerebellum.* Journal of Comparative Neurology, 1990. **291**(4): p. 538-552.
556. Takahashi, M., M. Sarantis, and D. Attwell, *Postsynaptic glutamate uptake in rat cerebellar Purkinje cells.* The Journal of Physiology, 1996. **497**(2): p. 523-530.
557. Otis, T.S., M.P. Kavanaugh, and C.E. Jahr, *Postsynaptic glutamate transport at the climbing fiber-Purkinje cell synapse.* Science, 1997. **277**(5331): p. 1515-1518.
558. Tanaka, J., et al., *Extra-junctional localization of glutamate transporter EAAT4 at excitatory Purkinje cell synapses.* Neuroreport, 1997. **8**(11): p. 2461-2464.
559. Zhou, H., et al., *Cerebellar modules operate at different frequencies.* Elife, 2014. **3**.
560. Llinas, R. and Y. Yarom, *Electrophysiology of mammalian inferior olivary neurones in vitro. Different types of voltage-dependent ionic conductances.* J Physiol, 1981. **315**: p. 549-67.
561. Llinas, R. and Y. Yarom, *Properties and distribution of ionic conductances generating electroresponsiveness of mammalian inferior olivary neurones in vitro.* J Physiol, 1981. **315**: p. 569-84.
562. Lang, E.J., I. Sugihara, and R. Llinas, *Differential roles of apamin- and charybdotoxin-sensitive K+ conductances in the generation of inferior olive rhythmicity in vivo.* J Neurosci, 1997. **17**(8): p. 2825-38.
563. Choi, S., et al., *Subthreshold membrane potential oscillations in inferior olive neurons are dynamically regulated by P/Q- and T-type calcium channels: a study in mutant mice.* J Physiol, 2010. **588**(Pt 16): p. 3031-43.

564. Ha, G.E., et al., *The Ca2+-activated chloride channel anoctamin-2 mediates spike-frequency adaptation and regulates sensory transmission in thalamocortical neurons.* Nat Commun, 2016. **7**: p. 13791.
565. Billig, G.M., et al., *Ca2+-activated Cl- currents are dispensable for olfaction.* Nat Neurosci, 2011. **14**(6): p. 763-9.
566. Skefos, J., et al., *Regional alterations in purkinje cell density in patients with autism.* PLoS One, 2014. **9**(2): p. e81255.
567. Whitney, E.R., et al., *Cerebellar Purkinje cells are reduced in a subpopulation of autistic brains: a stereological experiment using calbindin-D28k.* Cerebellum, 2008. **7**(3): p. 406-16.
568. Limperopoulos, C., et al., *Does cerebellar injury in premature infants contribute to the high prevalence of long-term cognitive, learning, and behavioral disability in survivors?* Pediatrics, 2007. **120**(3): p. 584-93.
569. Bolduc, M.E. and C. Limperopoulos, *Neurodevelopmental outcomes in children with cerebellar malformations: a systematic review.* Dev Med Child Neurol, 2009. **51**(4): p. 256-67.
570. Stoodley, C.J., et al., *Altered cerebellar connectivity in autism and cerebellar-mediated rescue of autism-related behaviors in mice.* Nat Neurosci, 2017. **20**(12): p. 1744-1751.
571. Gottlieb, J., *From thought to action: the parietal cortex as a bridge between perception, action, and cognition.* Neuron, 2007. **53**(1): p. 9-16.
572. Marko, M.K., et al., *Behavioural and neural basis of anomalous motor learning in children with autism.* Brain, 2015. **138**(Pt 3): p. 784-97.
573. Nebel, M.B., et al., *Intrinsic Visual-Motor Synchrony Correlates With Social Deficits in Autism.* Biol Psychiatry, 2016. **79**(8): p. 633-41.
574. Hsu, P.D., E.S. Lander, and F. Zhang, *Development and applications of CRISPR-Cas9 for genome engineering.* Cell, 2014. **157**(6): p. 1262-78.

Appendix

Summary

The majority of experimental work discussed in this dissertation is devoted to the study of Purkinje cell physiology. For that purpose I have used different mutant mouse models, which have specific mutations that affected the ability of the Purkinje cell to processes input and generate appropriate output to facilitate a type of behaviour.

In **chapter 2.1** we reviewed ASD mouse models and discussed the anatomical, morphological and physiological abnormalities that underlie changes in the striatum and cerebellum in ASD. We now appreciate that different genetic mutations can cause similar behavioural phenotypes related to ASD, but can lead to very different phenotypes in cellular physiology and morphology of the same population of cells. From the studies reviewed, it is clear that the cerebellum and striatum both play a major role in ASD and that the next challenge is in the unravelling of the sensitivity of circuit dysfunction during development. In the following **chapter 2.2** we explore the involvement of the cerebellum in ASD and present results on cerebellar dysfunction induced with the removal of shank2 in Purkinje cells. These results are in support of the hypothesized significance of cerebellum dysfunction in ASD and that impairment of Purkinje cell physiology might play a role in ASD like symptoms. In **chapter 2.3** we discuss results relevant for language deficit caused by the mutation of the transcription factor Foxp2. By specifically removing the *Foxp2* gene from the Purkinje cells in mice we observe motor coordination as well as timing difficulties. These phenotypes might be caused by Purkinje cell increased excitability and as a consequence aberrant Purkinje cell modulation activity and correlation with motor output. These results reveal possible contributions of the cerebellum to behaviour seen in humans affected by *Foxp2* mutations. In **chapter 3.1** we report how the absence of shisa6, an AMPA receptor auxiliary protein, leads to lower spontaneous as well as evoked post synaptic responses at the parallel fibre to Purkinje cell synapse. Further investigation revealed that Shisa6 effectively interacts with AMPA receptor subunits but also the non-AMPA glutamate receptor GluD2. The downregulation of GluA2 and GluA3 is hypothesized to be the main reason for the reduced potentiation as well as LTP. Furthermore, these strong physiological impairments result in motor baseline as well as learning phenotypes. We show in **chapter 3.2** that long-term potentiation at the parallel fibre to Purkinje cell synapse can be affected by adding NMDA receptors that facilitate additional calcium influx. The impaired LTP but intact LTD that we observed is in support of the hypothesis that precise calcium threshold regulations are crucial for the kind of synaptic plasticity that is

modulated at the parallel fibre to Purkinje cell synapse. In **chapter 3.3** we combine two genetic modifications that individually result in low behavioural abnormalities, in mice that lack either LTD or feed forward inhibitory input, and combine these two genetic modifications in a double conditional KO for the Purkinje cells. These mice present with worse behavioural phenotypes than would be expected from a simple add-on of the individual genetic modifications. These results are in line with the synergistic plasticity hypothesis which describes that more than one site of information processing need to be affected in order for the severity of the behavioural learning deficiencies to increase. In **chapter 4.1** we review the current state of chloride mediated function in the central nervous system. What is clear from the papers reviewed here is that little is understood about the chloride mediated function in many different neurons. To give an example: the family of calcium activated chloride channels have only recently been identified and are now characterized in many different neuronal types where their significance in neuronal excitability is found to play a significant role. In **chapter 4.2** we present preliminary results of an ongoing study on chloride currents in the inferior olive. Here, we reveal that these currents are gated through Ano2, a calcium activated chloride channel. In this chapter evidence is presented for a role of Ano2 in the high threshold spike of inferior olive cells as well as motor related function.

Samenvatting

Het merendeel van het experimentele werk dat in dit proefschrift wordt besproken is gewijd aan de studie van Purkinje celfysiologie. Om dit te bewerkstelligen hebben we verschillende mutaties in muismodellen gebruikt. Deze specifieke mutaties hebben invloed op het vermogen van de Purkinje-cel om elektrische input te verwerken en de juiste output te genereren waarmee gedrag kan worden beïnvloed.

In **hoofdstuk 2.1** hebben we recente ASD-muismodellen besproken en de anatomische, morfologische en fysiologische afwijkingen uitgelicht die ten grondslag liggen aan veranderingen in het striatum en het cerebellum in ASD. We zien nu dat verschillende genetische mutaties vergelijkbare gedragsfenotypen kunnen veroorzaken die gerelateerd zijn aan ASD, maar toch verschillende fenotypes in cellulaire fysiologie en morfologie van dezelfde populatie van cellen kunnen laten zien. Uit de resultaten van de onderzochte studies is het duidelijk dat het cerebellum en striatum beide een belangrijke rol spelen in de etiologie van ASD en dat de volgende uitdaging ligt in het ontrafelen van de gevoeligheid van circuitstoornissen tijdens de ontwikkeling. In het volgende **hoofdstuk 2.2** onderzoeken we de betrokkenheid van het cerebellum bij ASD en presenteren we de resultaten van cerebellaire dysfunctie geïnduceerd door het verwijderen van shank2 in Purkinje-cellen. Deze resultaten ondersteunen de veronderstelde significantie van cerebellum disfunctie bij ASD en dat verstoring van Purkinje-celfysiologie een rol kan spelen bij ASD-achtige symptomen. In **hoofdstuk 2.3** bespreken we de resultaten die relevant zijn voor spraakproblemen veroorzaakt door de mutatie van de transcriptiefactor Foxp2. Door specifiek het Foxp2-gen uit de Purkinje-cellen in muizen te verwijderen, ontstaan er fenotypen in motorcoördinatie en timing mogelijkheden. Deze fenotypen kunnen worden veroorzaakt door de verhoogde excitatie van Purkinje-cellen en als gevolg afwijkende Purkinje-cel modulatie activiteit en correlatie met motor gedrag. Deze resultaten tonen mogelijke bijdragen van het cerebellum aan gedrag afwijkingen bij mensen die Foxp2-mutaties hebben. In **hoofdstuk 3.1** beschrijven we hoe de afwezigheid van shisa6, een AMPA-receptor-gerelateerd eiwit, leidt tot lagere spontane en opgewekte post-synaptische responsen bij de Purkinje cel-synaps. In ons onderzoek onthullen we dat shisa6 effectief interacteert met AMPA-receptor sub eenheden maar ook met de niet-AMPA-glutamaat receptor GluD2. De neerwaartse regulatie van GluA2 en GluA3 wordt verondersteld de belangrijkste reden te zijn voor de verminderde potentiëring en de dysfunctionele LTP-

inductie. Bovendien resulteerden deze sterke fysiologische abnormaliteiten ook voor dysfunctie in de basis motoriek en motorisch leren. We laten in **hoofdstuk 3.2** zien dat potentiatie op de lange termijn bij de Purkinje-cel synaps kan worden beïnvloed door NMDA-receptoren toe te voegen die onder andere extra calciumtoevoer vergemakkelijken. De aangetaste LTP, maar intacte LTD die we waarnamen, ondersteunt de hypothese dat precieze calcium drempel reguleringen cruciaal is voor het soort synaptische plasticiteit dat gemoduleerd is in de Purkinje cel synaps. In **hoofdstuk 3.3** combineren we twee genetische modificaties die afzonderlijk resulteren in lage gedragsafwijkingen, bij muizen die LTD of feed forward inhibitorische input missen en combineren deze twee genetische modificaties in een dubbele conditionele KO voor de Purkinje-cellen. Deze muizen vertonen slechter gedragsfenotypen dan zou worden verwacht van een eenvoudige toevoeging van de individuele genetische modificaties. Deze resultaten zijn in overeenstemming met de synergetische plasticiteitshypothese die beschrijft dat meer dan één plaats van informatieverwerking moet worden beïnvloed om de ernst van de gedragsfenotypen te vergroten. In **hoofdstuk 4.1** bespreken we de huidige literatuur van chloride-gemedieerde functie in het centrale zenuwstelsel. Wat duidelijk is uit de hier besproken artikelen is dat we vooralsnog weinig inzicht hebben in de chloride-gemedieerde functie in veel verschillende neuronen. Om een voorbeeld te geven, de familie van de calcium geactiveerde chloridekanalen is pas recent geïdentificeerd en wordt nu in veel verschillende neuronale typen gekarakteriseerd. In **hoofdstuk 4.2** presenteren we resultaten van een lopend onderzoek naar chloridestromen in de inferieure olijf. Hier onthullen we dat deze chloride stromen door Ano2, een calcium geactiveerd chloridekanaal, gefaciliteerd worden. In dit hoofdstuk wordt bewijs gepresenteerd voor een rol van Ano2 in de hoogdrempelige calcium potentialen van inferieure olijfcellen en hierdoor ook motor gerelateerde functie.

Curriculum Vitae

Name: Saša Peter

Date of birth: 28-09-1986

Place of birth: Zenica

Nationality: Dutch

Education

PhD candidate, Neuroscience

Erasmus MC Department of Neuroscience, Rotterdam; 2012-2018

Netherlands Institute for Neuroscience, Amsterdam; 2012-2017

Master of Science, Cum Laude, Neuroscience; 2012

University of Amsterdam

Bachelor of Science, Psychobiology; 2009

University of Amsterdam

Teaching experience

Brain anatomy VO medical students, Erasmus MC, Rotterdam; 2017-2018

Supervision of neuroscience master students, Erasmus MC, Rotterdam; 2015-2018

StudentPLUS 'bijlessen' in physics, chemistry and biology, Amsterdam; 2009-2010

List of Publications

Saša Peter*, Michiel M. ten Brinke*, Jeffrey Stedehouder, Claudia M. Reinelt, Bin Wu, Haibo Zhou, Kuikui Zhou, Henk-Jan Boele, Steven A. Kushner, Min Goo Lee, Michael J. Schmeisser, Tobias M. Boeckers, Martijn Schonewille, Freek E. Hoebeek and Chris I. De Zeeuw *"Dysfunctional cerebellar Purkinje cells contribute to autism-like behaviour in Shank2-deficient mice."* (***Nature Communications, 2016***)

Saša Peter, Chris I. De Zeeuw, Tobias M. Boeckers, Michael J. Schmeisser "*Cerebellar and striatal pathologies in mouse models of autism spectrum disorder." (**Advances in Anatomy, Embryology and Cell Biology, 2017**)*

H.J. Boele*, **Saša Peter***, M.M. Ten Brinke*, L. Verdonschot, A.H.C. Ypelaar, Z. Gao, S.K.E. Koekkoek, C.I. De Zeeuw *"Impact of parallel fiber to Purkinje cell long-term depression is unmasked in absence of inhibitory input." (**Science Advances, 2018**)*

Catherine A. French*, María F. Vinueza Veloz*, Kuikui Zhou*, **Saša Peter***, Simon E. Fisher, Rui M. Cost and Chris I. De Zeeuw *"Differential effects of Foxp2 disruption in distinct motor circuits." (**Molecular Psychiatry, 2018**)*

Lin-Chien Huang, Meagan Barclay, Kevin Lee, **Saša Peter**, Gary D Housley, Peter R Thorne and Johanna M Montgomery *"Synaptic profiles during neurite extension, refinement and retraction in the developing cochlea"* (***Neural development, 2012***)

Elisa Galliano*, Martijn Schonewille*, **Saša Peter**, Mandy Rutteman, María Fernanda Vinueza Veloz, Marco Marconi, Ype Elgersma, Dick Jaarsma, Simone Houtman, Freek E. Hoebeek and Chris I. De Zeeuw. *"Impact of NMDA receptors at the parallel fiber to Purkinje cell synapse on plasticity and motor learning."* (***eNeuro, 2018***)

Negah Rahmati, Freek E. Hoebeek, **Saša Peter** and Chris I. De Zeeuw. *"Chloride Homeostasis in Neurons With Special Emphasis on the Olivocerebellar System: Differential Roles for Transporters and Channels."* (***Frontiers in cellular Neuroscience, 2018***)

Saša Peter*, Bastiaan H.A. Urbanus*, Remco V. Klaassen*, Bin Wu, Henk-Jan Boele, Sameha Azizi, Johan A. Slotman, Adriaan B. Houtsmuller, Martijn Schonewille, Freek E. Hoebeek, Sabine Spijker, August B. Smit¶ and Chris I. De Zeeuw¶ *"AMPA-receptor auxiliary protein Shisa6 is essential for Purkinje cell synaptic potentiation and motor learning" (**Submitted, 2018**)*

Saša Peter*, Leonoor Schonebaum*, Vincenzo Romano, Maria Fernanda Vinueza Veloz, Negah Rahmati, Maurizio Cundari, Marcel de Jeu, Thomas J. Jentsch, Freek E. Hoebeek and Chris I. De Zeeuw "*Anoctamin2/TMEM16B is important for Inferior Olive cell physiology and motor performance." (**In preparation, 2018**)*

* Co-first authors

Dankwoord

Het is nu zes jaar geleden dat ik aan mijn promotieonderzoek begon. Ik kan met gemak zeggen dat promoveren mijn zwaarste onderneming is geweest tot nu toe. Mijn bijdrage aan de publicaties in dit proefschrift waren niet mogelijk geweest zonder de collega's die betrokken zijn geweest bij het onderzoek en mijn familie en vrienden die mij hebben gesteund buiten het onderzoek om.

Beste Chris, beste promotor: allereerst wil ik jou bedanken dat je mij hebt aangenomen als PhD student. Jij hebt mij de middelen en ruimte gegeven om mijzelf te ontwikkelen en mijn interesses in het onderzoek van het cerebellum te verkennen. De afgelopen zes jaar zijn zeker niet helemaal soepel verlopen. Als het onderzoek minder ging, de resultaten niet meezaten, of ik iets te cynisch was over de aanpak, wist je mij te motiveren om door te blijven zoeken naar een andere invalshoek en naar iets dat wel werkte. Chris, dank hiervoor.

Beste Freek, beste copromotor: bloed, zweet en tranen. Jij hebt mij zien ontwikkelen de afgelopen jaren, maar voor jou is er ook veel veranderd. Van zelfstandig en principieel onderzoeker nu hoogleraar en afdelingshoofd in Utrecht. Sommige dingen veranderen niet: jij bent iemand die altijd door pusht en resultaat weet te behalen. Jij wist mij op cruciale momenten in de elektrofysiologie door te pushen en te motiveren om weer op een andere manier naar de data te kijken. Ik heb op een bepaalde manier onderdeel uitgemaakt van het Hoebeek-lab, maar jij had vanzelfsprekend jouw eigen agenda en projecten die niet gerelateerd waren aan mijn werk. Toch kon ik al die jaren zonder moeite bij jou aankloppen en je om hulp vragen. Je was er altijd, zonder uitzondering, op zoek naar een oplossing. Freek, dank hiervoor.

Ik begon mijn PhD op het NIN waar Laurens en Cathrin mij hebben leren in vivo patchen, dank voor deze 'first trials'. Hier in Rotterdam wil ik allereerst de technici bedanken die het werk mede mogelijk hebben gemaakt. Mandy, Laura, Ilja en recent Stephanie: bedankt voor het verzorgen van de muis-lijnen en het genotyperen. Zonder jullie waren de experimenten die in dit proefschrift beschreven zijn niet mogelijk geweest. Erika, dank voor al je tips gedurende onze immuno pogingen in de inferieure olijf. Elize, jij hebt heel veel uren besteed aan de immuno en EM coupes. Dank dat je altijd klaar stond om te helpen en nieuwe pogingen te doen als het weer eens niet ging zoals we dat hadden gehoopt.

Martijn, bedankt dat jouw deur altijd open staat voor discussie. Ik heb veel van jou geleerd. Ik ben er trots op dat we de projecten, beschreven in dit proefschrift, tot een goed einde hebben kunnen brengen en natuurlijk bedankt dat je in mijn PhD commissie zit. Bin, dank voor je inzet met de in vivo experimenten voor onze papers. Ik wens je veel succes met het afronden van je PhD.

Gao, dank voor alle discussies. Ik wens je veel succes met je groep in de toekomst. Bibi veel succes nog met het afronden komende tijd. Hana, zelim ti puno srece ovih iducih godina. Dick, (oud) buurman, bedankt voor de grappen en de interessante (soms bizarre) discussies. Tom, ik heb nu twee jaar met jou in de snijzaal mogen staan voor het hersenen practicum. Dank voor je begeleiding en de kans om anatomie les te geven: het blijft leuk om aan anderen uitleg te geven en zelf ook meer anatomisch inzicht te krijgen. Laurens, dank voor alle hulp tijdens de chaos van de muizen protocollen transitie. Ook wil ik je bedanken voor al je inzet voor het Ano2 project.

Bastiaan, ik heb je de laatste paar jaar sterk zien ontwikkelen als master student en nu als PhD student. Jij hebt inmiddels een breed arsenaal aan skills verworven om de komende jaren goed aan de slag te kunnen gaan. Ik weet zeker dat jij alles in je mars hebt om een uitstekende wetenschapper te worden. Bedankt voor je inzet voor ons project en natuurlijk de gezelligheid en alle muziek tips! Leonoor, jij hebt ondanks de moeilijkheden in ons Ano2-project hard doorgepushd voor extra data. Dank voor al je inzet en de gezellige momenten op onze oude kamer. Ik wens je heel veel succes tijdens je coschappen en hopelijk tot binnenkort wanneer we ons Ano2 verhaal afronden.

Michiel, je bent een van de meest energieke personen die ik ken. Onze korte reis in NYC is een blijvende herinnering. Dank voor de samenwerking en heel veel succes in je nieuwe consultancy rol. Henk Jan, we hebben inmiddels een aantal projecten samengewerkt. Dank voor alle leuke en interessante gesprekken. Ik heb veel over 'eye blink' geleerd van jou en ik ben blij dat onze papers succesvol zijn afgerond. Heel veel plezier en succes op Princeton, dat het een mooie ervaring mag zijn!

Carmen, dankjewel voor de gezelligheid in en buiten het lab om gedurende de afgelopen jaren. Ik vond onze discussies altijd waardevol en ik ben blij om te zien dat je je plek in Rotterdam gevonden hebt! Je bent een uitstekende wetenschapper en ik wens je heel veel succes in de nabije toekomst. Vincenzo, jouw onuitputtelijke positieve houding is dat wat me het meeste bijstaat. We hebben veel goede discussies gehad door de jaren heen. Succes met het afronden van je PhD en dank voor je contributie aan het Ano2 project.

Martijn, het was een gezellige en leuke trip naar San Diego. Dank voor alle discussies en ik hoop dat je een leuke tijd hebt voor je post-doc in Parijs. François, dank voor alle discussies die we met en zonder bier hebben gehad. Ik wens je nog veel succes met het afmaken van je PhD. Mario, bedankt voor de vele wetenschappelijke en niet wetenschappelijke gesprekken. Ik heb veel van jou geleerd over de olijf. Ik kijk er naar uit om weer af te spreken. Aleksandra, ik heb in de korte tijd dat we elkaar hebben gezien sinds je terug bent veel van je geleerd. Bedankt voor de goede discussies en dat je onderdeel uitmaakt van mijn PhD commissie. Ik wens je veel succes bij het opbouwen van je eigen lab!

Gerard, dank dat ik altijd bij je binnen kon vallen voor vragen omtrent mijn ephys experimenten, ik heb tijdens deze en andere momenten veel van je geleerd. En natuurlijk bedankt dat je de secretaris rol op je nam voor mijn PhD commissie.

Steven, dank voor onze samenwerking voor het Shank2 project. Ik heb je input zeer gewaardeerd en ik blijf veel van je leren. Bedankt dat je mijn proefschrift hebt gelezen en dat je onderdeel uitmaakt van mijn PhD commissie.

Sabine, bedankt voor onze samenwerking voor het Shisa6 project. Ik ben blij dat deze nu is uitgezonden en hopelijk binnenkort gepubliceerd. Ook bedankt dat je in mijn PhD commissie zit en de tijd nam om mijn proefschrift te lezen.

Michael, I was very happy to hear you could make it to Rotterdam to be part of my PhD committee. Of course many thanks for our Shank2 and review collaborations. I look forward to seeing you again.

Dr. Kasri, we did not get a chance to talk yet. Many thanks in advance that you are willing to be part of my PhD committee.

Loes en Elise, dank jullie wel voor het draaiende houden van de afdeling en het werk dat zit in het organiseren van de neuroscience master en PhD programma's.

Farnaz, Licia, Lorenzo, Lieke, Martina, George, Andy, Mohammed, Johan, Aaron, Geeske, Oscar, Jochen, Mafer, Sander, Bas, Shashini, Catarina, Joshua, Gerco, Malik, Zhanmin dank jullie wel voor de leuke gesprekken en de gezelligheid in en buiten het lab om gedurende de afgelopen jaren.

Negah, je bent al een tijdje weg maar ik heb hele fijne herinneringen aan onze tijd in het lab

en de moeilijke tijd tijdens het patchen. Het was heel leuk om jou en Ace te bezoeken in Boston. Ik hoop dat het Harvard avontuur nog steeds goed bevalt. Ik kijk er naar uit je snel weer te zien!

Simo! Ik kan me nog goed herinneren dat ik net een half jaar bij het Erasmus werkzaam was toen jij bij het Hoebeek-lab kwam solliciteren. We hebben door de jaren heen veel gelachen, gefeest en gereisd, maar ook veel "troubleshooting" en muziek gedeeld tijdens het patchen. Jouw energie, vrolijkheid en zuid europese mentaliteit heeft voor mij de PhD een stuk leuker gemaakt, dank je hiervoor. Ik mis je al een tijdje in het lab, en buiten het werk om mis ik je vriendschap. Hopelijk zien we elkaar snel weer.

En natuurlijk de rest van mijn Italiaanse familie: dank jullie wel Costi, Tommy (en Ottavia) en Ilir voor jullie vriendschap, de gezellige avonden, BBQ's en reisjes samen. De Italiaanse avond soep… iets dat ik altijd zal blijven missen (haha). Tot binnenkort in Florence!

Dank aan alle vrienden buiten het onderzoek om, jullie weten wie jullie zijn! Zonder jullie waren de afgelopen jaren een stuk zwaarder geweest. Extra veertje voor Frank en Tadzio omdat ze als paranimfen achter mij staan. Dank mannen.

Harrie, bedankt voor je steun door de jaren heen. Ondanks alle drukte kijk ik ernaar uit om samen weer een goede detective te kijken. Lieve Oda, bedankt voor de goede zorgen en je steun.

Dragi braco i seko, bile su ovo lude godine drago mi je da smo se dogovarali i našli kad smo mogli. Volio bi samo da se još češće nađemo i družimo.

Dragi tata, hvala što si bio tu za mene na svoj način i kada si mogao. Uvjek smo dobro pričali zajedno i to je nešto što mi je uvjek bilo do srca.

Lieve mama, door de oorlog in Bosnië heb jij alles achtergelaten om met mij naar Nederland te vluchten. Alles was onzeker; wat we hier zouden doen, waar we zouden terechtkomen. Jij hebt mij van jongs af aan gemotiveerd om te blijven leren. Dank voor jouw onvoorwaardelijke liefde.

Als laatste, mijn steun en liefde, Chrisje. In de laatste drie jaar heb jij veel gezeur van mijn kant moeten aanhoren terwijl je het zelf ook niet altijd makkelijk had. We hebben samen al behoorlijk veel gezien en meegemaakt. Ik ben heel blij dat jij er voor koos naar Rotterdam te verhuizen. Ik kijk uit naar onze avonturen in de toekomst.